Iron Deficiency Uniquely Reprograms the Amino Acid and Lipid Metabolism of Red Pulp Macrophages to Support Enhanced Iron Recycling Functions

by

Raghunandan Mahadeva

Doctoral dissertation
Laboratory of Iron Homeostasis
International Institute of Molecular and Cell Biology in Warsaw
Warsaw PhD School in Natural and BioMedical Sciences

Supervisor: **Dr hab. Wojciech Pokrzywa**

Auxiliary Supervisor: **Dr Katarzyna Mleczko-Sanecka**

Warsaw, March 2026

THANK YOU | DZIĘKUJĘ | ಧನ್ಯವಾದಗಳು

*I would like to express my deepest gratitude to my supervisor, **Dr. Katarzyna Mleczko-Sanecka**. Your guidance has been central to shaping the way I think as a scientist. Your clarity of thought, scientific rigor, and structured approach to problem solving have had a lasting impact on me. And your kindness and support meant a great deal, especially while being far away from home. I will carry everything I have learned from you throughout my career.*

*I am deeply grateful to my family, who mean everything to me. To my father, **Mahadeva H J**, and my mother, **Sumithra S R**, your courage, trust, and encouragement made it possible for me to come this far. Your belief in me continues to drive me to achieve something meaningful.*

*To my sisters, **Shilpa M** and **Shwetha M**, thank you for being such a strong support system for our family and for taking care of our parents while I am away. That strength gives me the confidence to keep pushing forward.*

*To my wife, **Nisarga H D**, you are my whole world. Your love, care, and support have been unmatched. You made this journey easier in every possible way, taking on responsibilities and always standing by me through everything. Thank you for being not just my support, but also my closest friend.*

*I would also like to extend my sincere thanks to my in-laws, **Dhananjaya, Saroja,** and **Nishanth**, for their constant encouragement and support throughout this journey.*

*I am sincerely thankful to my mentors who have guided me at different stages of my journey. I would like to thank **Prof. Elizabeta Nemeth** and **Prof. Tomas Ganz** for hosting me at UCLA and for their generous guidance and support during my research visit and beyond, which had a strong influence on my scientific thinking. I am also grateful to **Prof. Elizabeta Nemeth** and **Prof. Grzegorz Sumara** for their support as members of my Thesis Advisory Committee, where their insights, suggestions, and discussions helped improve the quality and direction of my work. I would also like to thank my previous supervisor, **Dr. Bibha Choudhary**, and **Prof. Yathindra**, under whom I first learned how to approach research, and whose guidance laid the foundation for everything I have done since.*

*I would like to thank my colleagues **Aneta, Pratik, Komal, Marta, Gabriela, Patryk, Patrycja, Iwona, Krzysiek**, and **Ania** for their support, for all the discussions, and for helping me learn many valuable things along the way. I am also grateful to **Dr. hab. Wojciech Pokrzywa** and to all members of the **Laboratory of Protein Metabolism** for creating a positive and collaborative environment.*

*I would also like to thank my **friends** for their support and for making this journey more enjoyable. I am grateful to the **International Institute of Molecular and Cell Biology** for providing me with the opportunity and environment to carry out this work. Finally, I am deeply grateful to **God** for all that has been given to me and for guiding me along the right path.*

ABSTRACT

Iron deficiency is the most common nutritional disorder worldwide, yet the ways in which specialized cell types adapt to limited iron availability remain incompletely understood. Splenic red pulp macrophages (RPMs) play a crucial role in systemic iron homeostasis. They continuously remove aged red blood cells (RBCs) through a process known as erythrophagocytosis (EP) and recycle iron back into the circulation. However, the impact of iron-deficient (ID) conditions on the function and metabolic programs of RPMs has not been clearly established.

This dissertation builds on previous findings to demonstrate that ID conditions do not impair the function of RPMs; rather, they induce a coordinated adaptive state characterized by enhanced EP, increased mitochondrial activity, and significant metabolic remodeling that supports heightened oxidative metabolism. More specifically, this thesis leverages proteomic analyses and functional approaches to demonstrate that this adaptive state relies on the selective activation of oxidative metabolic pathways, particularly branched-chain amino acid (BCAA) catabolism and fatty acid β-oxidation. This coordinated response is highly specific to this cell type and is not observed in other macrophage populations. Notably, BCAA metabolism emerges as a crucial aspect of the metabolic adaptation observed in ID RPMs. The rate-limiting enzyme branched-chain α-ketoacid dehydrogenase subunit B (BCKDHB) is selectively upregulated, and pharmacological inhibition of BCAA catabolism reverses the heightened EP and mitochondrial activity that occur under ID conditions, both *in vitro* and *in vivo*. Meanwhile, lipid metabolism shifts toward increased β-oxidation and decreased lipid storage; inhibiting fatty acid oxidation similarly disrupts EP. Together, these findings identify BCAA- and lipid-derived substrates as key drivers of the increased bioenergetic demands associated with sustained RBC clearance.

Additionally, this metabolic reprogramming is linked to the systemic regulation of iron homeostasis. The low hepcidin-high ferroportin (FPN) axis, along with spleen tyrosine kinase (SYK) signaling, establishes a regulatory framework that connects iron export to these metabolic adaptations and increased mitochondrial respiration in ID RPMs. Within this framework, the data presented here define how these conditions are accompanied by the selective engagement of metabolic pathways, including BCAA catabolism and fatty acid β-oxidation, that support increased mitochondrial activity and sustained EP.

In summary, this thesis defines how the coordinated activation of amino acid and lipid metabolic pathways supports RPM function under ID conditions. Specifically, the data demonstrate that BCAA catabolism and fatty acid β-oxidation contribute to sustaining mitochondrial activity and EP, thereby supporting RBC clearance during iron limitation. These findings establish a functional link between metabolic pathway engagement and the capacity of RPMs to maintain iron-recycling activity under conditions of restricted iron availability.

STRESZCZENIE

Niedobór żelaza jest najczęstszym zaburzeniem żywieniowym na świecie. Jednak sposoby, w jakie wyspecjalizowane typy komórek adaptują się do ograniczonej dostępności żelaza, pozostają nie w pełni poznane. Śledzionowe makrofagi czerwonej miazgi (ang. red pulp macrophages; RPMs) odgrywają kluczową rolę w ogólnoustrojowej homeostazie żelaza. Nieustannie usuwają stare erytrocyty w procesie zwanym erytrofagocytozą i odzyskują żelazo z powrotem do krążenia. Niemniej jednak wpływ warunków niedoboru żelaza na funkcję i programy metaboliczne RPMs nie został dotąd jednoznacznie określony.

Niniejsza rozprawa doktorska, opierając się na wcześniejszych badaniach, wykazuje, że warunki niedoboru żelaza w diecie nie upośledzają funkcji RPMs; przeciwnie, indukują skoordynowany stan adaptacyjny charakteryzujący się nasileniem erytrofagocytozy, zwiększoną aktywnością mitochondrialną oraz istotnymi zmianami metabolicznymi. W szczególności praca ta wykorzystuje analizy proteomiczne oraz badania funkcjonalne, aby wykazać, że stan ten opiera się na selektywnej aktywacji szlaków metabolicznych o charakterze oksydacyjnym, w szczególności katabolizmu aminokwasów rozgałęzionych (BCAAs) oraz β-oksydacji kwasów tłuszczowych. Odpowiedź ta jest wysoce specyficzna dla tego typu komórek i nie jest obserwowana w innych populacjach makrofagów. Co istotne, metabolizm BCAAs wyłania się jako kluczowy element adaptacji metabolicznej obserwowanej w RPMs w warunkach niedoboru żelaza. Enzym ograniczający szybkość reakcji, podjednostka B dehydrogenazy α-ketokwasów rozgałęzionych (BCKDHB), ulega selektywnej indukcji, a farmakologiczne hamowanie katabolizmu BCAAs odwraca nasiloną erytrofagocytozę oraz zwiększoną aktywność mitochondrialną obserwowaną w warunkach ograniczonej dostępności żelaza, zarówno *in vitro*, jak i *in vivo*. Równocześnie metabolizm lipidów ulega przesunięciu w kierunku zwiększonej β-oksydacji i zmniejszonego magazynowania lipidów; hamowanie utleniania kwasów tłuszczowych w podobny sposób zaburza erytrofagocytozę. Łącznie wyniki te wskazują na substraty pochodzące z BCAAs i lipidów jako kluczowe czynniki napędzające zwiększone zapotrzebowanie bioenergetyczne związane ze wzmożonym usuwaniem erytrocytów.

Ponadto, to przeprogramowanie metaboliczne jest powiązane z ogólnoustrojową regulacją homeostazy żelaza. Oś niska hepcydyna–wysoka ferroportyna (FPN), wraz z sygnalizacją kinazy tyrozynowej śledziony (SYK), tworzy ramy regulacyjne łączące eksport żelaza z tymi adaptacjami metabolicznymi oraz zwiększonym oddychaniem mitochondrialnym w RPMs w warunkach niedoboru żelaza. W ramach tego układu przedstawione dane definiują, w jaki sposób warunki te wiążą się z selektywnym zaangażowaniem szlaków metabolicznych, w tym katabolizmu BCAAs i β-oksydacji kwasów tłuszczowych, które wspierają zwiększoną aktywność mitochondrialną i erytrofagocytozę.

Podsumowując, niniejsza rozprawa określa, w jaki sposób skoordynowana aktywacja szlaków metabolicznych aminokwasów i lipidów wspiera funkcję RPMs w warunkach niedoboru żelaza. W szczególności przedstawione dane pokazują, że katabolizm BCAAs oraz β-oksydacja kwasów tłuszczowych przyczyniają się do utrzymania aktywności mitochondrialnej i erytrofagocytozy, wspierając tym samym usuwanie erytrocytów w warunkach ograniczonej dostępności żelaza. Wyniki te ustanawiają funkcjonalny związek między aktywacją szlaków metabolicznych a zdolnością RPMs do podtrzymania aktywności recyklingu żelaza w warunkach jego deficytu w diecie.

TABLE OF CONTENTS

Contents

1. INTRODUCTION

1.1 Iron as an Essential and Constrained Resource in Mammals

Iron is one of several transition metals essential for biological systems, along with zinc, manganese, copper, and molybdenum[1]. Most organisms rely on iron as an essential cofactor for enzymes that support mitochondrial metabolism, energy production, redox reactions, and nucleotide metabolism, as well as DNA replication and repair[2,3]. Its ability to alternate between ferrous (Fe^{2+}) and ferric (Fe^{3+}) oxidation states under physiological conditions is central to its function in oxygen transport, electron transfer, and a wide range of enzymatic reactions[4,5]. These same chemical properties, however, necessitate precise regulatory mechanisms because excess or mislocalized iron can promote the formation of reactive oxygen species, leading to cellular damage[2,6]. As a result, biological systems have evolved sophisticated strategies to maintain adequate iron availability while simultaneously preventing iron-mediated toxicity[5].

In mammals, maintaining iron balance is uniquely challenging due to the lack of a regulated pathway for iron excretion[7,8]. Approximately 70–80% of body iron is sequestered in hemoglobin within circulating erythrocytes, underpinning systemic oxygen delivery and metabolic function[2,9]. This compartmentalization makes the daily iron requirement for erythropoiesis, the production of new RBCs, substantial and typically far exceeds the amount of iron absorbed from dietary sources[10]. As a result, disruptions in iron availability often disproportionately affect erythropoiesis, making iron deficiency the leading cause of anemia worldwide[11,12]. Iron deficiency anemia impacts more than one billion individuals globally, while subclinical iron deficiency is even more prevalent[13]. Because iron is indispensable for a broad range of cellular processes, insufficient iron can impair physiological processes beyond erythropoiesis, including those affecting neuronal, muscle, or immune cell function. Iron deficiency can result from inadequate dietary intake, impaired absorption, chronic blood loss, or iron sequestration during inflammation[13,14]. These physiological constraints require coordinated regulation of iron absorption, distribution, storage, and utilization at both systemic and cellular levels, with internal iron recycling providing the major source of iron for erythropoiesis[15].

1.2 Cellular and Systemic Iron Balance in Mammals

Iron metabolism in mammals is a tightly regulated process that ensures both systemic and cellular iron homeostasis while minimizing the risks posed by reactive iron species. In the circulation, most iron exists as ferric (Fe^{3+}) iron bound to transferrin, which is taken up by cells predominantly through transferrin receptor 1 (TFR1) mediated endocytosis[16]. Within endosomes, acidification facilitates iron release, reduction to the ferrous state by STEAP3[17], and subsequent transport into the cytosol through divalent metal transporter 1[18,19]. The resulting cytosolic labile iron pool (LIP)[20] serves as a readily accessible reservoir of iron for essential processes, including mitochondrial respiration, heme synthesis, and iron-sulfur cluster assembly[21]. Because labile Fe^{2+} iron can promote oxidative stress, the size and distribution of

the LIP are tightly regulated. To prevent LIP expansion beyond safe limits, cells partition iron into storage, export, and targeted delivery pathways.

Iron is sequestered within ferritin, a multimeric protein complex composed of heavy and light chains that stores iron in a largely redox-inert form under physiological conditions[22–24]. The heavy chain subunit of ferritin plays a critical role in catalyzing the oxidation of iron to the ferric form and facilitating its safe incorporation into the ferritin core, thereby limiting cellular oxidative stress[24]. When iron is required, it can be released from ferritin via lysosomal degradation in a process known as ferritinophagy, which is mediated by the autophagy receptor NCOA4[25]. Consistent with a functional role for ferritinophagy in systemic iron supply, genetic studies have demonstrated that NCOA4-mediated ferritinophagy in macrophages is required to mobilize stored iron for erythropoiesis, as conditional *Ncoa4* deletion in this cell type increases susceptibility to iron deficiency anemia and promotes splenic iron retention under low-iron conditions[26]. Cellular iron export is accomplished exclusively by FPN, the only identified iron exporter in mammals[27–29], which releases iron in the ferrous form. Following export, iron is oxidized by extracellular ferroxidases, such as hephaestin on enterocytes and ceruloplasmin in plasma and at the macrophage surface, allowing it to reassociate with transferrin and complete the iron trafficking cycle[30]. Intracellular iron distribution is further coordinated by iron chaperones, including PCBP1 and PCBP2, which deliver iron to ferritin and selected non-heme iron enzymes, ensuring proper storage and supporting essential metabolic pathways[31–33].

Cellular iron homeostasis is maintained through a highly regulated post-transcriptional mechanism involving the iron-responsive element (IRE)/iron-regulatory protein (IRP) system[34–36]. IREs are conserved stem–loop motifs located in the untranslated regions of mRNAs encoding proteins critical for iron acquisition, storage, and export. In conditions of iron deficiency, IRPs bind to IREs, inhibiting the translation of ferritin and FPN mRNAs while stabilizing TFR1 mRNA, thereby enhancing cellular iron uptake and restricting iron storage and export. In contrast, when iron is abundant, IRP1 acquires an iron-sulfur cluster and functions as cytosolic aconitase[37,38], losing its RNA-binding ability, while IRP2 is targeted for ubiquitin-mediated degradation via FBXL5[39]. This regulatory shift induces ferritin synthesis and FPN expression while decreasing TFR1 levels. Through these dynamic mechanisms, cells effectively modulate iron flux to maintain homeostasis and minimize the accumulation of labile iron. These processes are particularly crucial in cells with specialized iron-handling roles, such as macrophages.

At the systemic level, iron metabolism is primarily determined by erythropoietic demand. Humans synthesize an estimated 200 billion RBCs each day, collectively containing 2–3 grams of iron[5]. In mammals, iron balance is constrained by the absence of a regulated excretory pathway. Consequently, iron is lost only through passive and relatively inefficient processes, amounting to approximately 1–2 mg per day, primarily via epithelial shedding, with additional losses in premenopausal females due to menstruation. Although intestinal absorption compensates for these losses by providing a similar amount of iron, it remains insufficient to meet the total daily physiological requirement of 20–25 mg. The majority of this iron is supplied through highly efficient recycling from senescent erythrocytes, a process mediated predominantly by splenic and hepatic macrophages[40,41]. This mechanism effectively returns

20–25 mg of iron to the circulation each day, sustaining a small but critical pool of transferrin-bound iron (3–4 mg) for tissue use. Among tissue macrophages, splenic RPMs play a particularly significant role in erythrocyte recycling[42,43].

Systemic regulation of iron homeostasis primarily operates by controlling iron flux rather than total body iron content, thereby imposing variable functional demands on iron-recycling macrophages[7]. For RPMs, whose physiological role is continuous erythrocyte clearance and iron export, such regulation is expected to directly shape intracellular iron load, impacting their metabolism and cellular functions[41]. However, these concepts have not been systematically investigated previously. Hepcidin is the central endocrine signal that sets the rate of iron entry into plasma by controlling FPN-dependent export from enterocytes, hepatocytes, and iron-recycling macrophages[44,45]. It was identified in 2001 as a small, cysteine-rich peptide produced predominantly by hepatocytes, and *in vivo* genetic studies established that decreasing Hamp expression is sufficient to drive systemic iron overload, whereas increasing Hamp expression induces systemic iron restriction[46–48].

Hepcidin transcription is regulated by three principal physiological inputs, each mediated by distinct signaling modules. First, iron loading activates a BMP–SMAD pathway in the liver in which endothelial cells produce BMP ligands that stimulate hepatocyte BMP receptors, with BMP6 acting as an iron-inducible signal and BMP2 providing a more constitutive component of the response[49,50]. This activation leads to phosphorylation of SMAD1/5/8[51], followed by assembly with SMAD4, and transcriptional activation of Hamp; this axis is further tuned by membrane components such as hemojuvelin, a BMP co-receptor[52], and interaction between the hemochromatosis proteins HFE and TFR2, which is promoted as transferrin saturation rises and HFE is displaced from TFR1[53]. Second, inflammation induces hepcidin chiefly via IL-6–JAK/STAT3, and this response functionally cooperates with intact BMP–SMAD signaling, providing a mechanistic basis for inflammatory hypoferremia[54,55]. Third, erythropoietic demand suppresses hepcidin through erythron-derived factors, most prominently erythroferrone, which is induced in erythroid progenitors downstream of EPO–JAK2/STAT5 and dampens BMP-dependent signaling to increase iron availability for erythropoiesis[56–58]. In addition, the hepatokine fibrinogen-like 1 (FGL1), induced in the liver by hypoxia during recovery from anemia, acts as a BMP6 antagonist that further represses hepcidin and promotes iron mobilization[59].

At the effector level, hepcidin controls iron recycling by directly targeting FPN at the cell surface, thereby determining whether iron is retained within macrophages or released into the circulation to feed the transferrin-bound plasma iron pool[28,44]. Hepcidin binding triggers FPN inactivation through coupled processes that include endocytosis[60] and lysosomal degradation driven by ubiquitination-dependent trafficking[61]. There is also evidence for rapid channel occlusion that can inhibit export before degradation is complete[45]. In iron-recycling macrophages, this endocrine switch is not only a flux controller but also a likely metabolic determinant, because changes in FPN activity are expected to modify intracellular iron burden, influence redox balance, and potentially alter the capacity for sustained erythrocyte clearance[15,62,63].

While the overall core principles of iron metabolism are conserved among mammals, notable species-specific differences exist in iron turnover and absorption[64]. In humans, daily iron requirements are met predominantly through the efficient recycling of heme-derived iron, with intestinal absorption primarily compensating for unavoidable losses[2]. In contrast, mice demonstrate higher fractional absorption rates of dietary non-heme iron and, as a result, are more sensitive to variations in dietary iron intake. This heightened sensitivity makes mice susceptible to rapid transitions between iron deficiency and overload under experimental conditions[65]. Such interspecies differences must be carefully considered when extrapolating results from murine models to human iron physiology, particularly in research focused on macrophage-driven iron recycling[66].

1.3 Red Pulp Macrophages as Specialized Iron-Recycling Cells

RBCs constitute the body's most abundant cell population and contain approximately 2–3 g of iron in the form of hemoglobin. Throughout their approximately 115–120-day lifespan in humans[67] or roughly a 40-day lifespan in mice[68], RBCs endure constant mechanical stress and exposure to high oxygen levels. These conditions lead to the gradual accumulation of oxidative damage to membrane lipids and proteins[69–71]. Although erythrocytes are equipped with antioxidant enzymes such as superoxide dismutase, catalase, and glutathione reductase, these systems are insufficient to counteract oxidative injury during prolonged circulation[72]. Additionally, the absence of nuclei and most organelles in mature erythrocytes prevents them from repairing or replacing damaged cellular structures. As a result, aging RBCs progressively lose membrane integrity and functionality. The removal of these senescent or damaged cells from circulation occurs through EP, predominantly performed by splenic RPMs and hepatic Kupffer cells (KCs)[73]. Given that dietary iron absorption is limited, and erythropoiesis relies on a steady supply of iron, mammals rely largely on the recovery of iron from aged RBCs, making macrophage-mediated erythrocyte clearance a central pillar of systemic iron homeostasis[74].

Within the splenic red pulp, the clearance of senescent or damaged erythrocytes is carried out predominantly by RPMs[75], a specialized population that exhibits a substantially higher erythrophagocytic capacity than other resident splenic macrophage subsets[43]. Consistent with this, *in vivo* analyses have shown that within the spleen, predominantly RPMs, and to a much smaller extent Ly6C-high monocytes, can engulf senescent RBCs, whereas other immune cell types, including granulocytes, dendritic cells, and lymphocytes, exhibit little or no erythrophagocytic capacity[75]. In addition, comparative analyses of splenic macrophage subsets demonstrate that RPMs are the most efficient phagocytes of RBCs when compared with other populations such as marginal zone and metallophilic macrophages[43]. The central role of the spleen in erythrocyte quality control has long been recognized[76], supported by classical observations that splenectomized individuals accumulate structurally abnormal erythrocytes containing nuclear remnants, denatured hemoglobin inclusions, and iron-rich granules[77]. These findings underscore the requirement for an intact splenic environment to ensure efficient removal of damaged RBCs. The splenic red pulp provides such an environment through its open circulation and narrow endothelial slits, which impose stringent biomechanical

constraints on circulating erythrocytes[78–80]. RBCs with reduced deformability are retained within the red pulp, creating the necessary conditions for macrophage-mediated recognition. Recognition of aged or stressed erythrocytes involves the integration of multiple surface cues, including reduced cellular deformability, exposure of phosphatidylserine[70], and opsonization by naturally occurring antibodies that bind modified membrane proteins such as clustered Band 3, which forms when oxidized or denatured hemoglobin associates with the membrane[81]. These pro-clearance signals are detected by receptors expressed on RPMs, as indicated by analysis of the available transcriptomics data[41], including TIM4[82], the TAM family receptors MERTK and AXL[83], and Fc receptors such as CD16[84]. In parallel, inhibitory signaling through the interaction between CD47 on erythrocytes and SIRPα on macrophages[43], which normally suppresses phagocytosis of healthy cells, becomes less effective as erythrocytes age or sustain mechanical damage, thereby permitting their removal.

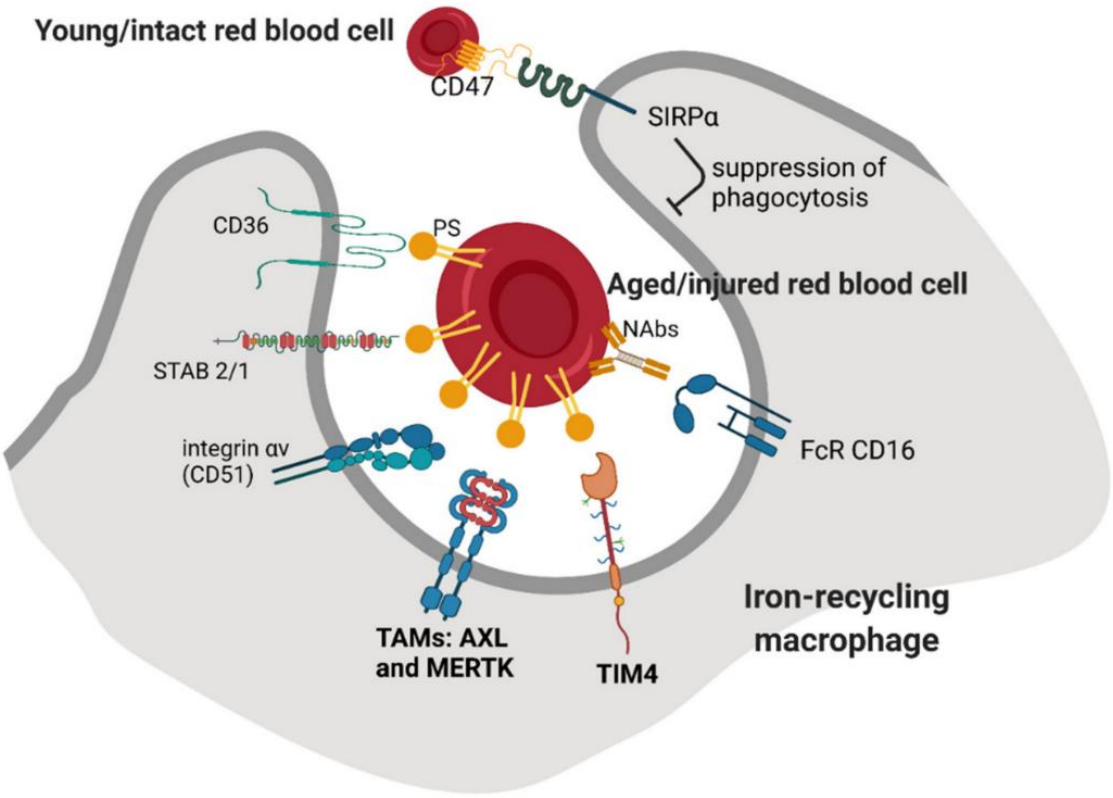

Figure 1: Recognition of aged or injured erythrocytes by iron-recycling macrophages.

Adapted from [41]. Aged or damaged RBCs acquire surface changes, including phosphatidylserine exposure and antibody opsonization, that promote their recognition by iron-recycling macrophages. These signals are sensed by receptors such as TIM4, AXL, MERTK, and Fc receptor CD16, whereas intact erythrocytes are protected from clearance through inhibitory CD47–SIRPα signaling.

Following uptake of senescent or stressed erythrocytes, RPMs initiate a tightly coordinated intracellular degradation program. Internalized erythrocytes are enclosed within phagosomes that subsequently fuse with lysosomal compartments, forming phagolysosomes in which erythrocyte constituents are dismantled[85]. Hemoglobin is hydrolyzed, and liberated heme must be rapidly extracted from the phagolysosomal lumen to prevent heme-mediated toxicity. This transport step is mediated primarily by the heme transporter HRG1[86,87], whose expression is

particularly high in iron-recycling macrophages, including RPMs and KCs. Once delivered to the cytosol, heme is degraded by heme oxygenase 1 (HO-1), yielding biliverdin, carbon monoxide, and ferrous iron[88–90]. The essential role of this pathway is underscored by genetic evidence demonstrating that impaired HO-1 activity is associated with macrophage loss and severe disturbances in iron homeostasis, highlighting the requirement for efficient heme detoxification to sustain erythrophagocytic capacity[89].

Iron released from heme degradation is expected to replenish the cytosolic LIP and then be partitioned between cellular metabolic use, temporary storage in ferritin, and export via FPN for systemic redistribution, as has been shown in other cell types[5]. In iron-recycling macrophages such as RPMs, however, the precise quantitative balance between these fates remains to be defined. Excess iron can be safely sequestered within ferritin[23,91], whereas iron destined for erythropoiesis is exported through the FPN[28,44,62], thereby restoring transferrin-bound iron in the circulation. This export process is tightly regulated by hepcidin, a liver-derived peptide hormone that responds to systemic iron needs[15,44,45]. During iron excess or inflammation, hepcidin binds to FPN, triggering its occlusion and subsequent lysosomal degradation, thereby retaining iron within macrophages and limiting plasma iron availability[92]. In contrast, states of iron deficiency or increased erythropoietic demand are associated with hepcidin suppression, which stabilizes FPN at the macrophage surface and facilitates enhanced iron release from RPMs to support ongoing erythropoiesis[56,93,94].

In parallel with EP of intact cells, recent studies have proposed that hemolysis-driven pathways contribute to iron recycling within the spleen[95]. This model suggests that a subset of erythrocytes undergo localized hemolysis, generating hemoglobin-depleted erythrocyte remnants that macrophages may preferentially capture. This model further proposed, but did not demonstrate, that RPMs clear free hemoglobin via CD163-mediated uptake of the hemoglobin-haptoglobin complex. However, prior to the work to which this thesis contributed, the relative quantitative contribution of hemolysis-derived *versus* phagocytosis-derived iron recycling remained unresolved. Moreover, the cellular contribution to hemolysis-derived iron handling and its distribution across splenic and hepatic compartments were incompletely defined, and it was unclear how these pathways are engaged under physiological *versus* stress conditions. Together, these gaps indicated that while hemolysis-associated mechanisms may complement EP, their quantitative relevance and cell-type specificity still needed to be established.

1.4 Metabolic Organization of Efferocytic Macrophages and RPMs

Macrophages are highly specialized phagocytes that continuously adjust their metabolic profile to match tissue localization, cargo load, and functional demands[96]. In contrast to short-lived, rapidly recruited inflammatory monocyte-derived cells, many tissue-resident macrophage populations support lifelong organ homeostasis through sustained, high-capacity clearance of apoptotic or senescent cells. It is estimated that efferocytosis, the engulfment and degradation of apoptotic cells[97,98], contributes to the daily recycling of an estimated 1–2% of the total cellular biomass[99]. This continuous clearance is energetically demanding. Macrophages

engaged in efferocytosis undergo extensive metabolic rewiring, with a prominent reliance on oxidative phosphorylation (OXPHOS)[100,101], as well as coordinated adjustments in glucose, lipid, and amino acid metabolism to meet the combined energetic and biosynthetic burden imposed by cargo processing. ATP produced through OXPHOS supports actin remodeling and membrane dynamics required for engulfment, while lysosomal degradation of internalized material further increases metabolic demand. Importantly, metabolites liberated from the internalized cargo can feed back on macrophage metabolic state and function, thereby influencing subsequent phagocytic activity and associated homeostatic programs. This metabolite-driven feedback framework has motivated the view that, to a substantial extent, phagocytes adapt to and are instructed by the nature of the material they engulf, including apoptotic cells and microbes[102–104].

During sustained clearance of apoptotic cells, macrophages do not simply increase ATP production; instead, they redistribute carbon flux and redox handling across core metabolic pathways to accommodate cargo degradation, membrane remodeling, and the need to avoid inflammatory activation[96,105]. A consistent theme across efferocytosis models is an increased reliance on mitochondrial metabolism, including higher electron transport chain activity and OXPHOS, supported by the routing of apoptotic cell-derived lipids into fatty acid oxidation[106]. In parallel, sterols derived from apoptotic membranes engage lipid-sensing transcriptional programs, particularly LXR and PPAR signaling, which promote cholesterol efflux via transporters such as ABCA1 and ABCG1 and reduce the risk of intracellular lipid overload[107,108]. These mitochondrial- and lipid-centered adaptations are not incompatible with glycolytic engagement. In efferocytic macrophages, apoptotic cell uptake has been shown to increase glucose uptake[109] and lactate production, with lactate export through the monocarboxylate transporter SLC16A1 facilitating the release of glycolytic by-products from engulfing phagocytes. In this setting, SLC16A1-dependent lactate export helps maintain intracellular metabolic homeostasis and supports continued efferocytosis[109,110]. Cargo digestion also generates substantial amino acid flux, implicating amino acid metabolism as a particularly prominent mode for regulation of anti-inflammatory polarization of macrophages and their sustained clearance capacity[111–114]. Together, these observations support the view that mitochondrial respiration, lipid catabolism, and selected amino acid-dependent pathways are coordinately engaged to power engulfment while buffering the biochemical burden of digestion, and that metabolites released from cargo can feed back to stabilize continued clearance behavior.

For RPMs, these general metabolic organizations are directly relevant but remain far less well defined than for canonical efferocytic macrophages. RPMs are distinctive as their dominant physiological cargo consists of senescent erythrocytes, which deliver a highly specialized biochemical load enriched in protein, predominantly hemoglobin, and heme iron, with comparatively limited lipid content[41]. This unusual cargo composition imposes stringent demands on mitochondrial function, redox control, and substrate utilization, suggesting that EP may require a metabolic configuration distinct from that supporting apoptotic cell clearance in other tissues[5]. Despite the central role of RPMs in erythrocyte turnover and systemic iron recycling, their metabolism has largely been examined through the lens of iron handling rather than as an integrated, pathway-level program supporting sustained phagocytic activity. In

particular, how mitochondrial respiration, amino acid metabolism, and lipid utilization are coordinated to maintain continuous EP under physiological conditions, and in response to altered body iron balance, remains poorly understood. Elucidating this metabolic organization is therefore essential for understanding how RPMs preserve lifelong clearance capacity and systemic iron homeostasis, and it defines the central conceptual focus of this thesis.

Iron deficiency provides a uniquely informative context for interrogating RPM metabolism, as it imposes a systemic constraint that is expected to directly impair mitochondrial function and may also reshape iron recycling[15,94]. In most cell types, iron restriction limits oxidative metabolism by impairing iron–sulfur cluster biogenesis and the activity of respiratory chain complexes and other mitochondrial enzymes[115,116]; accordingly, experimental models of iron deficiency or impaired iron utilization typically show reduced mitochondrial respiration and OXPHOS, often accompanied by a compensatory increase in glycolytic activity[117–119]. Against this background, results from our laboratory identified RPMs as a paradox: findings underlying this thesis showed that, rather than collapsing into an energetically compromised state, RPMs adapt to iron deficiency by increasing mitochondrial activity and mass, lysosomal function, and phagocytic throughput. These observations raise the question of whether iron deficiency reprograms specific metabolic pathways in RPMs to sustain high mitochondrial function. In this thesis, I therefore focused on defining which amino acid and lipid-dependent pathways underlie this adaptation, how they intersect with mitochondrial function, and how they ultimately regulate erythrocyte clearance and iron homeostasis.

1.5 Amino Acid Metabolism as a Functional Axis in Efferocytic Macrophages

Phagocytosis imposes a substantial protein-handling burden on macrophages, making amino acid metabolism an integral component of their sustained clearance programs. During efferocytosis, engulfed cells are degraded within phagolysosomes, releasing large quantities of amino acids that must be efficiently reutilized, catabolized, or redistributed to maintain metabolic balance. Emerging evidence indicates that this amino acid flux is not simply a byproduct of digestion but actively contributes to shaping the metabolic state and functional phenotype of macrophages. Metabolites derived from this process can act as signaling molecules, influencing key cellular programs[100,111,120]. Macrophages engaged in continuous clearance must coordinate lysosomal degradation with mitochondrial activity, biosynthetic demands, and signaling pathways that support repeated rounds of engulfment and pro-resolving immunosuppressive behavior[110,121]. For RPMs, which specialize in the clearance of hemoglobin-dense erythrocytes rather than classical apoptotic cells, the magnitude and composition of this amino acid influx are expected to differ substantially, raising the question of how specific amino acid pathways are organized to sustain EP and iron recycling.

Among amino acids, the metabolism of arginine, methionine, tryptophan, and glutamine has emerged to date as particularly important in efferocytosis-fuelled macrophages[100,111,120]. These examples illustrate how lysosome-released nitrogen and carbon can be repurposed to sustain continual clearance. For instance, arginine from apoptotic cells is metabolized by arginase 1 and ornithine decarboxylase into polyamines like putrescine, which are necessary for Rac1-

dependent actin remodeling and repeated rounds of phagocytosis[111]. Methionine derived from engulfed cells contributes to S-adenosylmethionine production and supports epigenetic programs that reinforce pro-resolving macrophage states, including increased TGFβ expression[113,122]. In parallel, tryptophan catabolism through indoleamine 2,3-dioxygenase generates kynurenine metabolites that stabilize anti-inflammatory macrophage phenotypes, while glutamine utilization through GLS1-dependent non-canonical glutaminolysis supports mitochondrial redox balance and sustained oxidative metabolism[112,114]. Collectively, these findings underscore that efferocytosis is intrinsically linked to coordinated metabolic reprogramming, with amino acid metabolism emerging as a core determinant of macrophage clearance capacity and functional state.

BCAAs, namely leucine, isoleucine, and valine, constitute a distinct class of amino acids whose catabolism directly interfaces with mitochondrial energy metabolism. Their degradation is initiated by branched-chain aminotransferases (BCAT), with BCAT1 operating in the cytosol and BCAT2 within mitochondria, producing branched-chain α-ketoacids that are subsequently oxidized by the mitochondrial BCKDH complex[123,124]. This enzymatic step represents the principal rate-limiting control point of BCAA oxidation[125] and channels carbon skeletons into acetyl-CoA and succinyl-CoA, thereby supplying substrates to the tricarboxylic acid (TCA) cycle and OXPHOS[126,127]. In macrophages, BCAA metabolism has been shown to exert context-dependent effects on mitochondrial function and activation state. During inflammatory activation, BCAT1 activity has been linked to mitochondrial metabolic remodeling and the induction of early pro-inflammatory gene expression[126], whereas in alternative activation settings, enhanced BCAA availability or catabolic flux, as well as leucine-mTORC1 signaling, have been associated with increased oxidative metabolism and anti-inflammatory polarization[128,129]. Together, these observations underscore the context-dependent role of BCAA metabolism in regulating macrophage bioenergetics and function. However, whether BCAA catabolism contributes directly to phagocytic functions such as efferocytosis or EP, particularly in iron-recycling macrophages with exceptionally high and continuous clearance demands, has not yet been systematically explored.

These considerations are particularly relevant for RPMs, whose dominant physiological cargo differs fundamentally from that encountered during canonical efferocytosis. Senescent erythrocytes are composed largely of densely-packed hemoglobin, whose globin chains are enriched in neutral and hydrophobic amino acids, including valine and leucine, members of the BCAA family[130]. Consequently, EP is expected to deliver a quantitatively large and compositionally biased amino acid load to RPMs, with a relative enrichment in BCAAs compared with other phagocytic contexts. Although clinical and metabolic studies have reported associations between circulating BCAA levels, hemoglobin concentration, and iron indices[131], these observations remain correlative and do not address macrophage-intrinsic metabolic organization. Whether BCAA catabolism contributes functionally to the metabolic configuration of iron-recycling macrophages, particularly under conditions of altered systemic iron availability, remains unexplored. Addressing this question and defining the role of amino acid metabolism in the adaptive program of RPMs constitutes the central objective of this thesis.

1.6 Lipid Metabolism and Cooperative Fuel Utilization in Efferocytic Macrophages

Sustained phagocytosis exposes macrophages to a substantial flux of membrane-derived lipids in parallel with protein-derived substrates. Accumulating evidence indicates that fatty acid metabolism is a central component of the metabolic program supporting continuous clearance[100]. During efferocytosis, lysosomal degradation of apoptotic cells liberates long-chain fatty acids that are routed into mitochondrial β-oxidation. These fatty acids are oxidized via β-oxidation to boost electron transport chain activity and OXPHOS, thereby increasing ATP production and enhancing the spare respiratory capacity of mitochondria to respond to increased energetic demand under stress conditions. In concert with glucose and other nutrient pathways, this metabolic shift drives reprogramming toward a proresolving phenotype[106,120]. The resulting enhancement in mitochondrial performance supports IL-10 production and tissue repair–associated transcriptional programs, while coordinating with glucose and amino acid metabolism to sustain ATP supply and redox balance during repeated rounds of engulfment.

Mitochondrial β-oxidation has therefore emerged as a cooperative fuel axis in efferocytic macrophages rather than a redundant pathway. Genetic or pharmacological disruption of fatty acid oxidation compromises oxidative metabolism and impairs acquisition of resolution-associated phenotypes, underscoring its importance for sustaining the energetic and anabolic requirements imposed by apoptotic cell clearance. Long-chain fatty acids derived from engulfed cargo feed into carnitine-dependent transport and oxidation pathways, increasing delivery of reducing equivalents to the respiratory chain and reinforcing mitochondrial resilience under sustained phagocytic load. At the same time, lipid handling in macrophages remains tightly regulated, with triacylglycerol synthesis and lipid droplet formation providing a buffering system that can sequester excess fatty acids and modulate inflammatory output in a context-dependent manner[106,132–134].

Although senescent erythrocytes are composed predominantly of hemoglobin, they also retain a membrane enriched in phospholipids and cholesterol, which constitutes a potential source of fatty acids during EP[41,135]. In this setting, mitochondrial β-oxidation is likely fuelled by a combination of erythrocyte-derived fatty acids and mobilization of endogenous lipid stores, with the balance between fatty acid oxidation and triacylglycerol storage shaping how RPMs meet the energetic demands of continuous EP.

In addition to the critical role of β-oxidation in supporting efferocytosis, important links between lipid and iron metabolism have also been reported. Beyond serving as substrates, lipid-handling pathways intersect with iron biology. Recent work indicates that iron availability in macrophages can remodel lipid storage programs, with iron depletion driving Diacylglycerol O-acyltransferase 1(DGAT1) dependent triacylglycerol synthesis and lipid droplet biogenesis, thereby supporting mitophagy, mitochondrial quality control, and cellular stress responses[136]. In macrophages, lipid droplet formation can act as a protective sink for excess fatty acids, thereby limiting lipotoxic stress[132,134,137]. While fatty acid oxidation, lipid storage, and lipolysis have been studied extensively in canonical efferocytic macrophages, how these pathways are configured in iron-recycling macrophages remains poorly defined. In RPMs, which need to integrate continuous erythrocyte clearance with FPN-mediated iron export under conditions of

fluctuating systemic iron availability, the balance between lipid utilization and storage is likely to represent a critical determinant of metabolic resilience.

Iron deficiency provides a particularly informative context for interrogating this organization, as it imposes simultaneous constraints on mitochondrial function and on iron flux. Understanding how fatty acid oxidation is integrated with amino acid metabolism and iron export in RPMs is therefore essential for defining how systemic iron status reshapes macrophage metabolism and, in turn, regulates erythrocyte clearance and iron homeostasis. The work presented in this thesis addresses this question by delineating the metabolic adaptations that enable RPMs to sustain iron recycling under iron-restricted conditions.

1.7 Research Objectives

The primary objective of this thesis was to define how ID conditions reprogram the metabolic state of RPMs to support enhanced EP and iron recycling functions. Building on previous observations that ID RPMs exhibit increased EP, expanded lysosomal and mitochondrial networks, this work sought to identify the specific metabolic pathways and upstream signals that sustain this adaptive state.

To address this, the following specific objectives were pursued:

- To characterize the metabolic adaptations of RPMs under ID conditions, with a focus on defining changes in mitochondrial respiration, substrate utilization, and identifying key metabolic pathways associated with enhanced erythrophagocytic activity.
- To define the role of BCAA catabolism as a central metabolic pathway supporting mitochondrial function and sustained EP.
- To investigate the contribution of lipid metabolism, particularly fatty acid β-oxidation and altered lipid storage, to the bioenergetic adaptation of RPMs.
- To determine how metabolic pathways are functionally integrated with upstream iron-dependent signaling, with emphasis on the hepcidin–FPN axis and SYK-mediated regulation.

2. RESULTS

2.1 Iron Deficiency Drives Metabolic Adaptation of Red Pulp Macrophages via FPN-SYK Signaling and BCAA Catabolism to Enhance Erythrophagocytosis (Manuscript 1)

2.1.1. The following section summarizes key observations generated in the laboratory, including those to which this thesis contributed, that laid the conceptual and mechanistic foundation for the principal part of my doctoral project. While the earliest datasets defining the systemic consequences of nutritional iron deficiency were obtained prior to the start of my doctoral work, the subsequent experiments were carried out collaboratively within the laboratory. Within this collaborative work, my contributions included Seahorse metabolic flux analyses, participation in the design and execution of FPN-overexpression experiments together with Pratik Mandal, selected flow-cytometric analyses, and data processing and interpretation. I also contributed to animal work, tissue collection, and downstream sample preparation. Together, these studies established a framework linking FPN stabilization, intracellular signaling pathways, and metabolic adaptation to enhanced EP during iron deficiency.

As outlined in the introduction, the project was motivated by the hypothesis that nutritional iron deficiency may pose a significant challenge to iron-recycling macrophages. However, it remained unclear whether and how dietary iron restriction reshapes the essential erythrocyte-clearance function of splenic RPMs. To address this question, the laboratory employed a nutritional iron restriction model in mice that reduced iron stores in the spleen and liver, decreased transferrin saturation, and induced mild microcytic hypochromic anemia, consistent with the expected consequences of systemic iron deficiency. Within this context, subsequent analyses revealed that, despite systemic iron depletion, RPMs from ID mice displayed enhanced EP activity. Importantly, this phenotype was not explained by increased susceptibility of RBCs from ID mice to phagocytosis, indicating that nutritional iron deficiency is associated with enhanced RPM clearance function rather than the emergence of “eat-me” signals on RBCs.

At the molecular level, RPMs from ID mice displayed features consistent with cellular iron depletion, including increased TFR1 expression and reduced ferritin levels. In parallel, expression of the iron exporter FPN was elevated, consistent with reduced systemic hepcidin levels during iron deficiency. Notably, total iron content in RPMs was reduced, yet these cells exhibited a modest but significant increase in the intracellular LIP together with elevated levels of reactive oxygen species. These observations are consistent with increased intracellular iron flux rather than simple iron deprivation and together with the enhanced erythrophagocytic activity observed in RPMs from ID mice, indicate that RPMs in iron deficiency operate in a state of elevated iron turnover that may help sustain systemic iron recycling.

To further define the molecular programs underlying enhanced erythrophagocytic activity in ID RPMs, transcriptomic and quantitative proteomic analyses were performed. Surprisingly,

transcriptional changes induced by iron deficiency were relatively limited, arguing against the activation of a broad inflammatory or stress-driven transcriptional program. In contrast, quantitative proteomic profiling revealed extensive remodeling at the protein level, with substantially broader alterations and only minimal overlap with the transcriptomic dataset. Functional enrichment analysis identified mitochondrial and lysosomal proteins as the most significantly represented categories among upregulated hits, suggesting that iron deficiency induces pronounced post-transcriptional metabolic reprogramming in RPMs.

Consistent with this proteomic signature, RPMs from ID mice exhibited clear evidence of enhanced mitochondrial activity. Measurements of mitochondrial membrane potential and mitochondrial mass indicated expansion of the mitochondrial compartment and increased oxidative capacity in these cells. In parallel, multiple components of the lysosomal system were upregulated, including proteins associated with the CLEAR lysosomal regulatory network. Functional measurements further demonstrated increased lysosomal mass and lysosomal activity, indicating enhanced degradative capacity.

This coordinated expansion of mitochondrial and lysosomal systems was accompanied by increased glucose uptake and elevated protein synthesis, reflecting increased bioenergetic demand in RPMs under ID conditions. Notably, steady-state ATP levels were modestly reduced, yet activation of the energy deficit sensor, AMPK, was not increased. These observations suggest that RPMs during iron deficiency are not energy-depleted but instead operate in a state of elevated metabolic flux that supports sustained EP.

Having established that RPMs in iron deficiency display enhanced erythrophagocytic activity together with evidence of increased intracellular iron turnover and metabolic remodeling, the next question was whether this phenotype is driven directly by cellular iron depletion or instead by systemic regulatory signals. To address this, the effect of pharmacological iron chelation was examined *in vitro* using primary macrophages differentiated under heme-rich conditions to resemble RPMs (iRPMs). Iron removal alone did not enhance erythrocyte clearance in these cells, indicating that reduced intracellular iron levels *per se* are insufficient to induce the adaptive erythrophagocytic phenotype.

Given that systemic iron deficiency is accompanied by alterations in circulating iron-regulatory signals, the potential contribution of serum-derived factors was next examined. When iRPMs were cultured in serum obtained from ID mice, the *in vivo* phenotype was recapitulated, including increased expression of the iron exporter FPN and enhanced erythrophagocytic activity without changes in total cellular iron levels. Importantly, short-term treatment with the hepcidin mimetic PR73 reversed the enhanced EP induced by ID serum and abolished the associated increase in mitochondrial activity. Consistent with these observations, administration of PR73 *in vivo* reduced surface FPN levels on RPMs and selectively suppressed their elevated erythrophagocytic activity in ID mice, while producing minimal effects under control iron-balanced (IB) conditions.

To assess whether FPN stabilization also contributes to the increased oxidative metabolism of RPMs, I performed Seahorse extracellular flux analysis on magnetically separated RPMs isolated from IB and ID mice after short-term *ex vivo* treatment with PR73. This assay measures

oxygen consumption rate (OCR) as a proxy for mitochondrial respiration and was optimized to reliably assess the bioenergetic state of freshly isolated RPMs. Using sequential addition of oligomycin, FCCP, and rotenone/antimycin A, I quantified basal respiration, maximal respiration, and spare respiratory capacity. RPMs from ID mice displayed elevated mitochondrial respiration across these parameters, and PR73 treatment reduced this heightened oxidative state. These findings indicate that FPN-dependent signaling contributes directly to the metabolic adaptation of RPMs.

Further supporting a role for the hepcidin–FPN axis, Tmprss6-deficient mice, which maintain elevated hepcidin levels despite features of systemic iron restriction, did not exhibit the increase in EP observed under nutritional iron deficiency. Together, these observations indicate that reduced hepcidin levels and the resulting stabilization of FPN, rather than systemic iron restriction alone, are key drivers of the enhanced erythrophagocytic activity and metabolic adaptation of RPMs during nutritional iron deficiency.

Having established that reduced hepcidin levels and consequent stabilization of FPN are key drivers of RPM adaptation during nutritional iron deficiency, we next asked whether increased FPN expression itself is sufficient to induce the functional and metabolic features observed in ID RPMs. To address this, together with Pratik Mandal, we generated iRPMs with enforced FPN overexpression and compared them with mock-transduced controls. To better mimic the splenic microenvironment, transduced iRPMs were also exposed to stressed RBCs during culture. We found that increased surface FPN did not alter total iron levels, but increased labile iron levels were observed only in conditions with stressed RBC exposure, consistent with our observations in ID RPMs *in vivo*. FPN overexpression reproduced key features of the ID-like state, including elevated TFR1 and enhanced EP. Notably, the FPN-driven control of EP was independent of continuous exposure to stressed RBCs and was reversed by pharmacological inhibition of FPN with vamifeport. Together, these observations indicate that increased FPN activity and the resulting rise in intracellular iron flux, rather than changes in total cellular iron content, are sufficient to stimulate erythrophagocytic activity.

We further found that FPN overexpression in iRPMs recapitulated the metabolic characteristics of ID RPMs. They displayed increased mitochondrial activity and mitochondrial mass, together with elevated glucose uptake and increased protein synthesis. These responses were suppressed by vamifeport, indicating that they depend on active FPN function. Importantly, these changes were independent of the presence of stressed RBCs during culture and did not correlate with altered intracellular labile iron levels, suggesting that FPN regulates RPM metabolism through mechanisms that extend beyond its classical role in controlling iron abundance. Thus, increased FPN expression is not only sufficient to enhance EP but also to induce a broader bioenergetic adaptation characteristic of RPMs under ID conditions.

We next addressed how increased FPN expression is translated into functional rewiring. Because calcium signaling is a known regulator of macrophage phagocytic activity, intracellular Ca^{2+} dynamics were examined in both RPMs and iRPM-based models. RPMs from ID mice exhibited increased intracellular Ca^{2+} levels compared with IB controls, and this elevation was selectively reversed by PR73 treatment. Similarly, iRPMs exposed to ID serum showed increased Ca^{2+} levels that were likewise suppressed by PR73. FPN-overexpressing

iRPMs also displayed higher intracellular Ca^{2+} levels than mock controls. Functionally, both intracellular and extracellular Ca^{2+} chelation reduced overall EP and importantly, abolished the enhanced RBC uptake observed under high-FPN conditions. These data place Ca^{2+} signaling downstream of the low hepcidin-high FPN state and indicate that it is required for the increased erythrophagocytic capacity of RPMs in iron deficiency.

An important mechanistic question was whether this effect reflected direct Ca^{2+} transport by FPN itself. To test this, iRPMs overexpressing the FPN D39A mutant, expected to disrupt Ca^{2+} import while preserving Fe^{2+} transport, were compared with cells expressing wild-type FPN. No significant differences were observed in either erythrophagocytic activity or intracellular Ca^{2+} levels between the two FPN variants. This finding argues against a simple model in which FPN directly drives functional adaptation through its own Ca^{2+} transport activity and instead supports the view that FPN promotes Ca^{2+}-dependent rewiring through an indirect signaling mechanism.

The next step was to identify the Ca^{2+}-dependent signaling pathway responsible for this response. PIEZO1, a mechanosensitive regulator of EP described previously in RPMs, was first examined, but inhibition of PIEZO1 did not suppress the enhanced erythrophagocytic capacity induced by ID serum, arguing against a major role in this specific adaptation. A broader pharmacological screen similarly excluded several Ca^{2+}-associated pathways, including CaMKK, calmodulin-mediated signaling, purinergic receptor signaling, macropinocytosis, and protein kinase C, as critical mediators of the FPN-driven EP regulation. In contrast, inhibition of SYK abolished the increase in EP observed in FPN-overexpressing iRPMs. This result was reproduced with the more selective SYK inhibitor entospletinib, which also suppressed the increased EP induced by ID serum. In parallel, SYK inhibition prevented the increase in intracellular Ca^{2+} associated with FPN overexpression. My investigation further showed that entospletinib reversed mitochondrial activity and mass to the control levels of mock-transduced cells. Together, these findings identify SYK as the key downstream effector linking FPN-dependent Ca^{2+} signaling to both metabolic and phagocytic rewiring.

Next, the role of SYK in RPM iron recycling was investigated *in vivo*. In RPMs from ID mice, acute PR73 treatment reduced levels of phosphorylated SYK, whereas RPMs from IB mice showed no significant change, placing SYK activation downstream of the low hepcidin-high FPN state. Oral entospletinib administration *in vivo* reduced phospho-SYK levels in both IB and ID mice, but its functional effects were selective for the ID condition. In ID mice, SYK inhibition markedly reduced erythrophagocytic activity, partially reversed the increase in intracellular Ca^{2+}, and attenuated the induction of FPN. These effects were accompanied by evidence of compensatory erythropoietic adaptation, including increased reticulocyte counts, expansion of splenic proerythroblasts and EryA erythroblasts, and increased plasma EPO levels. These observations may indicate less effective iron delivery from RPMs to support extramedullary erythropoiesis. Together, these data establish SYK as a possible central mediator of the FPN-dependent adaptation of RPMs to iron deficiency and define the FPN-Ca^{2+}-SYK axis as the signaling framework that controls the metabolic specialization described in the following section.

2.1.2. The following section describes the part of the study to which I made the primary conceptual and experimental contribution. Building on the identification of the hepcidin-FPN-SYK signaling axis as a key driver of RPM adaptation to iron deficiency, I set out to define the metabolic pathways that sustain this adaptive state. In particular, I focused on elucidating how iron deficiency reshapes the metabolic circuitry of RPMs, ultimately identifying BCAA catabolism and fatty acid β-oxidation as key pathways driving RPM reprogramming. To this end, I designed and performed a series of metabolic and pharmacological perturbation experiments in primary cells and in mice, combined with functional assays. These studies allowed me to define how specific metabolic pathways contribute to the enhanced erythrophagocytic capacity of RPMs during iron deficiency.

Having established that ID RPMs undergo FPN and SYK-dependent functional and metabolic rewiring, I next asked which downstream metabolic pathways enable these cells to sustain enhanced EP. This question was particularly important because RPMs process hemoglobin-rich RBCs and therefore face a metabolic burden that is distinct from other efferocytic macrophages.

To determine whether the metabolic rewiring of RPMs in iron deficiency resembles previously described efferocytic programs or instead reflects a more specialized adaptation, I revisited the transcriptomic and proteomic datasets of RPMs from ID *versus* IB mice with a specific focus on nutrient-handling pathways. Canonical efferocytic programs described in other macrophage systems have been linked to defined SLC transporter signatures and to the use of pathways such as arginine, tryptophan, and glutamine metabolism[109]. In contrast, RPMs from ID mice did not show coordinated transcriptional induction of the genes from the SLC family, previously associated with the response to apoptotic cell clearance. Likewise, canonical amino acid associated efferocytic pathways were not supported in RPMs from ID mice. Notably, RPMs failed to display detectable protein levels of key efferocytosis-associated enzymes, including ARG1 and ODC1 (arginine–polyamine metabolism) and IDO1 (tryptophan catabolism). At the same time, GLS1, a key enzyme in non-canonical glutaminolysis[109], did not exhibit the upregulation characteristic of canonical efferocytic programs[111]. Instead, the dominant metabolic pattern that emerged from the proteomic analysis was the enrichment of proteins linked to lipid utilization and BCAA catabolism.

Among the proteins elevated in RPMs from ID mice, the proteomic dataset revealed a coordinated enrichment of enzymes associated with mitochondrial fatty acid β-oxidation, BCAA catabolism, and lipid handling. Within the BCAA catabolic pathway, several key enzymes were upregulated, including BCAT1, which catalyzes the initial step of BCAA transamination, as well as downstream components such as BCKDHB, aldehyde dehydrogenases (ALDH family members), methylcrotonoyl-CoA carboxylase (MCCC), and short-chain acyl-CoA dehydrogenases (ACADs), indicating enhanced capacity for BCAA-derived carbon entry into mitochondrial metabolism.

In parallel, enzymes involved in mitochondrial fatty acid β-oxidation were enriched, including CPT2, which controls mitochondrial fatty acid import, together with downstream β-oxidation enzymes such as HADH, ECHS1, and medium-chain ACADs. In addition, proteins linked to lipid mobilization, including the lipase ABHD12B, were increased, whereas DGAT1, a key

enzyme involved in triacylglycerol synthesis and lipid storage, was reduced, consistent with a shift away from lipid storage toward oxidative substrate utilization. Amino acid transporters, including SLC7A7 and SLC7A8, were also upregulated at the protein level.

Based on this global proteomic analysis, I selected a subset of representative proteins from these pathways for further validation and functional characterization. Flow cytometric analyses were then performed not only to validate the differential expression of these proteins, but also to assess whether these metabolic adaptations were specific to RPMs or shared across other macrophage populations. To this end, expression of BCKDHB, CPT2, ACADSB, citrate synthase, ABHD12B, and SLC7A7 was compared across RPMs, KCs, and peritoneal macrophages, enabling both confirmation of the proteomic findings and evaluation of the cell-type specificity of the observed metabolic program. Together, these data indicate that RPMs in ID conditions do not simply increase overall metabolic activity, but instead adopt a selective oxidative state favoring the mobilization and catabolism of amino acid- and lipid-derived substrates.

To validate the proteomic data and determine whether these changes were specific to RPMs or reflected a broader macrophage response to iron restriction, I quantified selected metabolic proteins across other tissue-resident macrophage populations, including KCs and peritoneal macrophages. The former contribute to RBC clearance, albeit to a lesser extent, whereas the latter do not play a role in iron recycling. This analysis showed that BCKDHB, SLC7A7, CPT2, ACADSB, citrate synthase, and the lipase ABHD12B were selectively increased in RPMs from ID mice, while remaining unchanged or being reduced in KCs and peritoneal macrophages. In parallel, DGAT1 expression and lipid droplet content were decreased, consistent with a shift away from lipid storage toward oxidative substrate utilization. These findings demonstrate that ID imposes a cell-type-specific metabolic state in RPMs, characterized by coordinated enhancement of pathways supporting mitochondrial respiration.

Because BCAA metabolism had not previously been implicated in sustaining enhanced EP in this setting, I next investigated this pathway in more detail. Baseline measurements showed that RPMs contain high intracellular levels of BCAAs relative to other splenic immune cell populations. Next, I observed that BCAA abundance in RPMs was lower than in KCs and similar to that in peritoneal macrophages. However, pharmacological inhibition of the first step of BCAA catabolism, mediated by BCATs, using the inhibitor ERG240 led to intracellular accumulation of BCAAs, confirming their active utilization in RPMs. I then asked whether erythrophagocytic cargo uptake activates this pathway. Prolonged exposure of iRPMs to stressed RBCs strongly induced BCKDHB expression, the enzyme involved in the rate-limiting step in BCAA breakdown, whereas exposure to RBC ghosts failed to elicit a comparable response. This induction was more pronounced in iRPMs than in conventional bone marrow-derived macrophages, consistent with the notion that the erythrophagocytic specialization of RPM-like cells is coupled to more robust activation of BCAA catabolism. This suggested that processing of intact, hemoglobin-rich erythrocytes specifically promotes activation of the BCAA catabolic machinery. In parallel, stressed RBC exposure did not cause intracellular BCAA accumulation, further supporting active substrate consumption under conditions that mimic erythrophagocytic load. Notably, total intracellular BCAA levels remained unchanged

despite the increased erythrophagocytic activity of RPMs from ID mice *in vivo*. This suggests that under ID conditions, RPMs achieve a new metabolic equilibrium, with balanced enhancement of both BCAA supply and utilization.

To determine whether this pathway lies downstream of FPN-driven rewiring, I examined BCKDHB expression in iRPMs overexpressing FPN. FPN overexpression increased BCKDHB abundance, and this effect depended on both FPN activity and SYK signaling. The same regulatory pattern was observed *in vivo*, where inhibition of SYK reduced BCKDHB levels in RPMs from ID mice. Functionally, inhibition of BCAT activity with ERG240 abolished the enhancement of EP caused by FPN overexpression in iRPMs, demonstrating that BCAA catabolism is required for the adaptive increase in phagocytic capacity. In the reciprocal direction, leucine supplementation enhanced EP, and this effect was attenuated when BCAT activity was blocked. BCAT inhibition also reversed the induction of BCKDHB itself and reduced mitochondrial mass and mitochondrial activity in FPN-overexpressing cells. Importantly, the reversal of the enhanced phagocytic and metabolic phenotype of ID-like RPMs was reproduced with the second BCAT inhibitor Bay-069, providing additional support that this effect reflected inhibition of BCAA catabolism rather than an isolated compound-specific response. Together, these findings showed that BCAA catabolism is not merely associated with the ID RPM state but functions as a downstream metabolic effector required to sustain FPN-driven mitochondrial remodeling and enhanced EP.

In parallel, I assessed the contribution of fatty acid β-oxidation. CPT2 upregulation in RPMs under ID conditions also depended on FPN and SYK activity, and this SYK dependence was confirmed both *in vitro* and *in vivo*. Pharmacological inhibition of CPT2 abolished the FPN-driven increase in EP. Thus, β-oxidation, like BCAA catabolism, did not simply correlate with the ID-like state but was functionally required for the enhanced phagocytic program downstream of FPN-SYK signaling. These data indicate that β-oxidation acts together with BCAA catabolism within the FPN-SYK regulatory framework. Together, my analyses identified two cooperative oxidative pathways, BCAA breakdown and fatty acid β-oxidation, as central components of the metabolic program that supports enhanced EP in ID RPMs.

Having established *in vitro* that BCAA catabolism contributes to the FPN-driven enhancement of EP, I next examined whether this pathway is also required *in vivo* to sustain the metabolic and functional phenotype of RPMs during iron deficiency. To address this question, I first assessed mitochondrial respiratory activity in freshly isolated RPMs following pharmacological inhibition of BCAT activity. *Ex vivo* inhibition of BCAT markedly reduced the elevated respiratory capacity observed in RPMs from ID animals, directly linking BCAA metabolism to the enhanced oxidative phenotype of these cells.

To determine whether BCAA catabolism is functionally required for RPM adaptation *in vivo*, I next inhibited BCAT activity pharmacologically in ID mice over a three-week period. This intervention significantly reduced the elevated erythrophagocytic activity of RPMs and prevented the expansion of mitochondrial mass previously observed under ID conditions. In parallel, inhibition of BCAA catabolism suppressed the induction of key mitochondrial metabolic enzymes, including BCKDHB and citrate synthase, indicating impaired support of the TCA cycle. Notably, mitochondrial membrane potential remained elevated in ID RPMs of

ERG240-supplemented mice despite the reduction in mitochondrial mass, suggesting that mitochondrial polarization and mitochondrial biogenesis can become partially uncoupled when BCAA-derived substrates are limited.

At the systemic level, inhibition of BCAA catabolism produced measurable consequences for erythropoietic homeostasis. Mice treated with the BCAT inhibitor displayed increased circulating reticulocyte numbers together with expansion of splenic erythroid progenitors and elevated erythropoietin levels compared to untreated ID mice. These findings are consistent with a compensatory erythropoietic response likely triggered by impaired iron delivery from RPMs when BCAA-dependent metabolic support for EP is disrupted. Importantly, transferrin saturation remained comparably reduced in these animals, indicating that the erythropoietic response did not arise from global alterations in systemic iron availability but rather from altered efficiency of iron recycling. This interpretation was further supported by increased renal Epo and Tfrc expression following ERG240 supplementation in ID mice, the latter indicating increased iron demand in the kidney. Similarly, an increase in cardiac Tfrc expression indicated enhanced iron-demand signaling in the heart, whereas corresponding hepatic iron-responsive changes were not further altered by BCAT inhibition. Together, these findings suggest that suppression of BCAA catabolism exacerbates the functional consequences of iron restriction in selected tissues without uniformly worsening systemic iron availability.

To further define how BCAA catabolism contributes to the metabolic state of RPMs during iron deficiency, I next performed mitochondrial substrate utilization profiling using Mitoplates. This colorimetric, high-throughput assay measures mitochondrial respiration across a panel of defined substrates to reveal pathway-specific metabolic preferences. I found that RPMs isolated from ID mice exhibited increased oxidation of a broad range of metabolic substrates, including glycolytic intermediates, amino acid-derived fuels, fatty acid–associated substrates, and TCA cycle intermediates. This pattern is consistent with the elevated oxidative capacity previously observed in these cells. Inhibition of BCAT activity partially attenuated this metabolic shift, with the most pronounced reductions observed in the utilization of TCA cycle substrates and fatty acid-linked fuels. At the same time, utilization of selected amino acid-associated substrates, including leucine, malic acid, tryptamine, and ornithine, remained elevated relative to IB RPMs, indicating that BCAT-dependent BCAA metabolism accounts for an important component, but not the entirety, of the heightened respiratory phenotype. Together, these findings show that BCAA catabolism contributes significantly to the metabolic rewiring of ID RPMs, likely by providing anaplerotic carbon that supports mitochondrial metabolism and cooperates with other oxidative pathways.

Collectively, my results demonstrate that BCAA catabolism is not merely associated with the ID RPM state but is functionally required to sustain the metabolic and functional adaptations that enable enhanced EP. While earlier sections of the study established that ID RPMs exhibit enhanced EP and undergo FPN-SYK-dependent functional rewiring, the experiments described here show that this adaptive state is maintained by the coordinated activation of BCAA catabolism and fatty acid β-oxidation. These pathways provide metabolic support for mitochondrial function and erythrophagocytic activity, thereby enabling RPMs to preserve efficient iron recycling under conditions of systemic iron restriction.

2.2 Liver Sinusoidal Endothelial Cells Constitute a Major Route for Hemoglobin Clearance (Manuscript 2)

The work described in Chapter 2.1 established that splenic RPMs undergo functional and metabolic adaptation during iron deficiency to sustain efficient EP. However, erythrocyte turnover *in vivo* generates multiple forms of erythrocyte-derived material, including aged but still intact erythrocytes, membrane remnants, and hemoglobin released through local hemolysis in the spleen, as proposed by Klei et al.[95]. How these distinct substrates are distributed among iron-handling cell types across organs had remained incompletely understood. Manuscript 2 addressed this question by systematically defining the cellular pathways responsible for the clearance of erythrocyte-derived material within the spleen and liver. In particular, the study aimed to determine how splenic and hepatic cell populations contribute to the uptake of intact erythrocytes, erythrocyte membrane remnants (RBC ghosts), and circulating hemoglobin.

To dissect these processes *in vivo*, erythrocytes isolated from donor mice constitutively expressing GFP were additionally fluorescently membrane-labeled and transfused into recipient animals. This experimental approach enabled the simultaneous tracking of intact erythrocytes and erythrocyte membrane fragments following circulation and tissue uptake. Subsequent flow cytometric analyses were used to quantify substrate uptake across splenic and hepatic myeloid and endothelial cell populations, including RPMs, KCs, and liver sinusoidal endothelial cells (LSECs). Through these experiments, the study established that erythrocyte-derived substrates are processed through a distributed cellular network involving both organs rather than a single dominant cell type.

Consistent with their established physiological role, RPMs emerged as the primary cell population responsible for the uptake of intact erythrocytes, with a substantial fraction internalizing dual-labeled erythrocytes. Importantly, RPMs were similarly efficient at internalizing erythrocyte membrane remnants, indicating that they process not only intact cells, but also partially degraded erythrocyte material generated during splenic hemolysis. In contrast, other splenic myeloid cell populations, such as pre-RPMs, dendritic cells, and monocytes, as well as splenic endothelial cells, showed no capacity for the uptake of intact RBCs, and except for pre-RPMs, markedly lower capacity for the internalization of RBC ghosts.

The liver displayed a distinct pattern of substrate handling. KCs, the resident macrophages of the liver, contributed significantly to the uptake of erythrocyte membrane fragments but showed relatively lower capacity for engulfing intact erythrocytes. Dendritic cells or LSECs were negative for the uptake of intact RBCs, but appeared positive for tethering or uptake of RBC ghosts, albeit to a much lower extent than KCs. We next examined the handling of free hemoglobin released from lysed erythrocytes. In contrast to the pattern observed for intact RBCs and RBC ghosts, hemoglobin scavenging was executed predominantly by LSECs, with a supporting contribution from KCs, whereas splenic RPMs and splenic endothelial cells contributed only minimally. LSECs, therefore, exhibited very limited erythrophagocytic activity but high efficiency in scavenging free hemoglobin, identifying them as a functionally

distinct component of the iron-recycling network. These findings revealed an unexpected cellular specialization in which LSECs participate directly in erythrocyte-derived iron recycling by removing circulating hemoglobin and engaging downstream heme-processing pathways.

Together, these findings defined a division of labor between splenic and hepatic compartments in the processing of erythrocyte-derived substrates. While splenic RPMs remain the primary mediators of EP, the liver acts as a complementary organ that clears erythrocyte remnants and hemoglobin released during erythrocyte turnover. In this coordinated system, KCs preferentially internalize membrane components, whereas LSECs serve as efficient scavengers of circulating hemoglobin. Together, these results indicate a cooperative spleen-liver axis that ensures the safe detoxification of hemoglobin and the efficient recycling of iron derived from senescent erythrocytes.

My contribution to this study focused on supporting the experimental work that delineated and quantified the uptake of erythrocyte-derived substrates across splenic and hepatic cell populations. In particular, I assisted in the methodological optimization and execution of the experiments used to measure the uptake of intact erythrocytes, erythrocyte ghosts, and free hemoglobin by myeloid and endothelial cells. I also participated in the analysis and visualization of the resulting datasets, which helped clarify the relative contributions of different cell types to erythrocyte-derived iron recycling. These experiments were essential for establishing the cellular framework that links splenic EP with hepatic scavenging pathways.

Importantly, this study provides a broader physiological context for the findings described in the previous manuscript. While the earlier work demonstrated that RPMs metabolically adapt to sustain enhanced EP during iron deficiency, the results presented here reveal how erythrocyte-derived material is subsequently handled by additional cellular components of the iron-recycling network. Furthermore, the work described here provided a methodological basis for transfusion assays of dual-stained stressed RBCs, which were instrumental in demonstrating that ID RPMs are more efficient in the clearance of both intact RBCs and RBC ghosts compared to IB RPMs. Together, these studies define complementary layers of regulation in systemic iron recycling: metabolic adaptation of splenic macrophages to process erythrocytes efficiently and coordinated hepatic scavenging pathways that remove hemoglobin and membrane remnants generated during erythrocyte turnover.

3. DISCUSSION

Iron deficiency is a complex physiological state with broad systemic consequences, yet the cellular logic by which individual tissues adapt to limited iron availability remains incompletely understood[13,15,94]. Because the majority of body iron is contained within RBCs, efficient recycling of iron from senescent RBCs becomes particularly important under these conditions[2,5,41,74]. RPMs are central to this process, as they represent the principal splenic cell population responsible for the uptake and processing of aged RBCs and for the return of recycled iron to the circulation[41,42,73–75]. Despite this central role, it has remained unclear whether ID conditions compromise this function, elicit adaptive responses that preserve systemic iron recycling, or leave it largely unaffected.

This question is particularly relevant because iron restriction has been associated with impaired function in several cell types. Previous work has shown that iron deficiency can suppress proliferation and mitochondrial activity in immune cells, perturb neuronal and muscle physiology, and alter macrophage inflammatory responses in a context-dependent manner[3,14,117,138–140]. At the level of macrophage biology, however, the consequences of low iron availability have remained difficult to generalize, as different experimental systems have produced apparently divergent results[3,15,139]. These observations underscore the need for a cell-type-specific understanding of how iron limitation affects specialized macrophage populations. In this context, RPMs are of particular interest because they continuously process hemoglobin-rich cargo and are therefore exposed to metabolic demands that are distinct from those of other tissue-resident macrophages[41,73,74,101].

The work presented in this thesis shows that ID conditions do not impair the core iron-recycling function of RPMs. Instead, they induce a coordinated adaptive state in which enhanced EP is coupled to increased mitochondrial activity and selective engagement of oxidative metabolic pathways, including BCAA catabolism and fatty acid β-oxidation. These findings indicate that ID conditions are not solely associated with impaired cellular function but can also induce adaptive reprogramming in selected cell types that supports maintenance of organismal homeostasis[15,94]. In the case of RPMs, this adaptive state enables sustained or increased RBC clearance despite reduced systemic iron availability, thereby helping to maintain iron delivery under conditions in which iron becomes especially limiting[41,74]. This response appears to be highly cell-type specific. Unlike KCs, which also contribute to iron recycling[41,73,141], RPMs undergo coordinated metabolic and functional rewiring under ID conditions. This specificity likely reflects the distinct microenvironmental and functional context of RPMs[96,100]. RPMs reside in the splenic red pulp, where they are continuously exposed to retained senescent RBCs[41,73,74] and high heme burden. In addition, under ID conditions, they operate within a milieu shaped by stress erythropoiesis. These local features may impose a metabolic demand that is not reproduced in hepatic macrophages despite their contribution to iron recycling.

A central mechanistic conclusion of this work is that the adaptive state of RPMs in ID conditions is not defined solely by reduced intracellular iron content, but rather by altered iron flux through FPN. Although RPMs exhibit classical features of cellular iron restriction, the

concurrent increase in FPN expression together with elevated labile iron and enhanced EP suggests that these cells do not operate solely in a state of passive iron depletion. Instead, the data support a framework in which low systemic hepcidin stabilizes FPN, thereby promoting iron export while sustained RBC processing maintains intracellular iron balance[44,45,62]. In this context, RPMs operate in a high iron-flux state that supports continued iron recycling despite limited systemic availability. Consistent with this interpretation, perturbation of the hepcidin-FPN axis alters both EP and metabolic activation, indicating that FPN functions as an important regulatory component in the RPM response to ID.

The data presented here further indicate that the adaptive state of RPMs under ID conditions is functionally linked to SYK signaling. In addition to its established role in phagocytic signaling[43,142,143], SYK inhibition in this study attenuated not only enhanced EP but also the associated increase in mitochondrial activity and mitochondrial mass, linking SYK to the bioenergetic adaptation of RPMs. This point is important because it places SYK within the same functional framework as the metabolic changes that sustain RBC processing, rather than restricting its role to cargo uptake alone. In this context, the present findings extend the earlier identification of the FPN-SYK axis by showing that SYK is also connected to the mitochondrial component of RPM adaptation.

This connection is particularly relevant in light of previous studies showing that altered iron handling can have context-dependent effects on cellular respiration. In myeloid cells, FPN deletion or iron accumulation reduced mitochondrial respiration in BMDMs and liver leukocytes[144], whereas iron chelation with Deferoxamine (DFO) restored mitochondrial oxygen consumption, indicating that excess intracellular iron can suppress macrophage bioenergetics. In contrast, in colorectal cancer cells, DFO-mediated iron chelation reduced oxygen consumption[145] and impaired mitochondrial metabolism, showing that iron deprivation can also limit respiration in a distinct cellular context. Together with these reports, the findings presented here indicate that the effect of altered iron handling on mitochondrial function is not uniform, but depends on cell type, iron state, and physiological context. In RPMs exposed to ID conditions, SYK-dependent signaling is associated with increased, rather than decreased, mitochondrial activity, supporting the view that the FPN–SYK axis contributes to a context-specific bioenergetic adaptation that sustains enhanced EP.

A major implication of these findings is that EP in RPMs must be considered within the broader framework of metabolically demanding phagocytic processes. Sustained clearance of cellular material is not a passive degradative event, but requires continuous metabolic adaptation[100,105]. It supports ATP production to power cytoskeletal remodeling, phagosome–lysosome fusion, and ion transport; drives biosynthesis of membrane lipids, nucleotides, and amino acids needed for phagosome turnover and anti-inflammatory mediators; and maintains redox balance by fueling NADPH and glutathione regeneration, which protects mitochondria from oxidative damage and allows safe handling of cargo-derived reactive oxygen species[100,106,111,120].

While previous studies have shown that efferocytosis in macrophages is associated with increased mitochondrial activity and engagement of specific metabolic pathways, existing studies have largely focused on apoptotic cells as a model cargo and tend to generalize these metabolic requirements across efferocytosis. Thus, it remains unclear whether these

dependencies can be extrapolated to other forms of cargo, such as hemoglobin-rich erythrocytes, where the metabolic demands and by-products may differ substantially. Moreover, the metabolic pathways described in efferocytosis are functionally heterogeneous and do not uniformly support mitochondrial metabolism. For example, glutamine metabolism can directly fuel the TCA cycle and oxidative phosphorylation, whereas arginine and tryptophan metabolism primarily contribute to cytoskeletal remodeling or signaling programs associated with resolution and tolerance rather than serving as major mitochondrial substrates [100,106,111,120].

Within this framework, the data presented here indicate that RPMs under ID conditions adopt a metabolic state that is distinct from previously described efferocytic programs[100,111,114,120]. Although increased mitochondrial activity and enhanced β-oxidation, together with augmented glucose uptake, represent shared features, the transcriptional and proteomic analyses do not support a dominant role for pathways such as arginine, tryptophan, or glutamine metabolism, which have been implicated in other macrophage contexts[111–114]. Instead, the most prominent metabolic changes point toward selective engagement of BCAA catabolism. These findings indicate that RPMs establish a distinct metabolic configuration aligned with the biochemical composition of RBC-derived cargo rather than amplifying a generic efferocytic program[41,100].

The identification of BCAA catabolism as a central component of this adaptive state is particularly notable. BCAAs represent a major source of carbon that can feed into the TCA cycle through anaplerotic reactions, thereby supporting sustained mitochondrial respiration[125–127]. In the context of RPMs, which continuously process hemoglobin-rich RBCs, it is plausible that amino acids liberated during globin degradation contribute to this metabolic configuration[73,130]. The relatively high leucine and valine content of hemoglobin, together with the enrichment of BCAA catabolic enzymes and the functional dependence on BCAT activity, support the interpretation that this pathway is not merely associated with the ID state but contributes directly to sustaining the elevated bioenergetic demands imposed by enhanced EP. In addition, two amino acid transporters, SLC7A7 and SLC7A8, were identified as upregulated in the proteomic dataset, with SLC7A7 further validated by flow cytometry. Both transporters mediate the transport of large neutral amino acids, including BCAAs, and were primarily associated with amino acid import rather than export[146]. This implies that ID RPMs, in addition to enhanced EP, may meet their BCAA demand from the extracellular pool. However, SLC7A7 and SLC7A8 may also export these substrates depending on concentration gradients across the plasma membrane. Thus, it is important to emphasize that the present data do not directly trace the origin of the BCAA substrates supporting their enhanced catabolism. While the data are consistent with a contribution of RBC-derived amino acids, definitive demonstration of substrate flux will require dedicated metabolic tracing approaches.

My *in vivo* data indicate that inhibition of BCAT in ID mice does not markedly exacerbate systemic iron deficiency, but it does provide the first evidence for more pronounced extramedullary erythropoiesis, accompanied by elevated EPO and increased iron-demand signaling in the heart and kidney. This pattern resembles the constellation recently described in individuals with post-acute sequelae of SARS-CoV-2 infection (“long COVID”), where a multivariate signature of persistent inflammation, low serum iron, anemia, ID reticulocytosis,

and stress erythropoiesis was identified as an early correlate of later symptom burden, independent of initial disease severity[147]. These parallels raise the possibility that chronic post-infectious iron dysregulation and impaired iron recycling, potentially including defective RBC handling by macrophage populations such as RPMs, constitute a shared axis contributing to inefficient oxygen transport, and some of the clinical manifestations observed in long COVID[147].

A complementary feature of the metabolic adaptation in ID RPMs is the engagement of fatty acid β-oxidation, as implicated previously for efferocytosis[106,120,133]. Lipid oxidation is a well-established mechanism for supporting mitochondrial ATP production in conditions of sustained cellular activity[96,100,106]. In RPMs under ID conditions, the enrichment of β-oxidation-associated enzymes, together with the sensitivity of EP to CPT2 inhibition, indicates that lipid-derived substrates contribute alongside amino acids to fuel mitochondrial metabolism.

Notably, this pattern differs from observations in *in vitro* models of ID macrophages, where iron restriction has been associated with increased DGAT1-dependent triacylglycerol synthesis and lipid accumulation, consistent with a shift toward lipid sequestration rather than oxidation[137]. In contrast, RPMs under ID conditions exhibit reduced DGAT1 expression and decreased lipid droplet content, indicating preferential engagement of fatty acid utilization. This discrepancy likely reflects differences in cellular context, as RPMs function *in vivo* under conditions of sustained EP and continuous exposure to hemoglobin-rich cargo, whereas *in vitro* systems do not recapitulate these features. Rather than acting independently, BCAA catabolism and β-oxidation appear to operate as coordinated inputs into the TCA cycle, together supporting the elevated oxidative state required for continuous RBC clearance. Thus, the engagement of lipid oxidation in ID RPMs likely represents a specialized adaptation to sustained EP rather than a generalizable response of macrophages to iron restriction. This organization of metabolic pathways suggests that RPMs utilize multiple nutrient sources to sustain function under conditions of limited systemic iron availability.

Importantly, this metabolic configuration appears to be closely linked to the upstream FPN-SYK regulatory axis. The dependence of both BCAA catabolism and β-oxidation on FPN activity and SYK signaling suggests that metabolic adaptation in RPMs is not a secondary consequence of increased phagocytic activity but is instead an integral component of the signaling program that defines the ID state of RPMs. In this context, altered iron flux through FPN is coupled to signaling pathways that coordinate both cellular function and metabolic state, thereby aligning substrate utilization with the demands of enhanced EP. This integration of iron handling, signaling, and metabolism represents a regulatory framework within which the metabolic adaptations described here are established.

An important aspect of these findings is their cell-type specificity. The metabolic pathways identified here were not similarly induced in other macrophage populations, indicating that the observed adaptation is not a general response to systemic iron restriction. Instead, it likely reflects the unique functional niche of RPMs within the spleen, where continuous exposure to RBC-derived material imposes distinct metabolic requirements. This interpretation is consistent with the idea that macrophage metabolic programs are shaped by both environmental cues and the biochemical properties of the material they process[96,100,102–105]. In this context,

RPMs emerge as a specialized macrophage population that is uniquely adapted to couple substrate availability to functional demand. This uniqueness may be driven by high heme burden in the splenic microenvironment, and/or by paracrine signals from adjacent cells, including erythroid cells or lymphocytes. The exact contribution of such external signals in shaping RPMs' responses would need to be investigated.

The broader physiological relevance of this specialization becomes clearer when considered together with the findings of the second study included in this thesis. That work demonstrates that the processing of RBC-derived material is distributed across multiple cell types, with RPMs primarily responsible for the clearance of intact RBCs, while hepatic cell populations contribute to the handling of RBC-derived lipid remnants and circulating hemoglobin[95,141]. This division of labor does not diminish the central role of RPMs in EP. Rather, it defines a coordinated system in which distinct cell types contribute to different stages of RBC turnover. Within this framework, the metabolic adaptation described here can be understood as a mechanism that enables RPMs to sustain their specific role in this process under ID conditions.

Several questions arise from these findings. First, the mechanism by which FPN-dependent changes in iron flux are translated into downstream signaling events remains to be fully defined. In particular, the relationship between FPN activity, intracellular Ca^{2+} dynamics, and SYK activation warrants further investigation. Second, while the functional importance of BCAA catabolism is clearly established, the precise contribution of different nutrient sources to mitochondrial metabolism in RPMs remains unresolved. Third, it will be important to determine whether similar metabolic programs operate in other contexts characterized by increased RBC turnover or whether this adaptation is specific to ID conditions.

Taken together, the results presented in this thesis support a model in which ID conditions induce a coordinated adaptive program in RPMs that integrates iron handling, signaling, and metabolism. Stabilization of FPN and engagement of SYK-dependent signaling are coupled to the activation of oxidative metabolic pathways, including BCAA catabolism and fatty acid β-oxidation, which together sustain mitochondrial function and enhance EP. In this framework, RPMs are not passive responders to iron limitations but actively reprogram their metabolic circuitry to maintain iron recycling. More broadly, these findings highlight how tissue-resident macrophages can adapt their metabolic state to the biochemical demands imposed by their functional niche, thereby preserving systemic homeostasis under conditions of nutritional stress.

4. FUTURE DIRECTIONS

The work presented in this thesis establishes that iron deficiency induces a coordinated functional and metabolic adaptation in RPMs, characterized by enhanced EP and a shift toward mitochondrial oxidative metabolism supported by BCAA catabolism and fatty acid β-oxidation. While these findings define a framework linking iron handling to metabolic rewiring, several mechanistic and physiological questions remain unresolved.

A first key question concerns the physiological significance of enhanced EP under ID conditions. The observed coupling between increased RBC uptake and augmented iron export raises the possibility that RPM adaptation contributes to the maintenance of systemic iron distribution during ID. In addition to the data presented in this thesis, to address this directly, future studies should trace the fate of RBC-derived iron *in vivo*. Stable or radioactive iron isotope-based approaches, in which RBCs are labeled and their clearance followed over time, would allow quantitative assessment of iron redistribution to the erythroid compartment of the bone marrow and spleen and peripheral organs such as the heart, brain, or skeletal muscle. Such experiments will be important to determine whether increased EP primarily supports local RPM function, directly feeds erythropoietic expansion, or contributes to sustaining iron availability in non-erythroid tissues that are particularly sensitive to iron limitations.

A second unresolved issue relates to the metabolic fate of substrates that sustain the elevated oxidative state of ID RPMs. The data presented here identify BCAA catabolism and fatty acid β-oxidation as contributors to enhanced mitochondrial activity, yet the precise fate of these substrates within central carbon metabolism remains unclear. In particular, it is not known to what extent BCAA-derived carbon directly enters the TCA cycle and supports the heightened respiratory activity of ID RPMs. This could be addressed using stable isotope tracing with ^{13}C-labeled BCAAs (for example ^{13}C-leucine), incorporated into hemoglobin by expanding erythrocytes from fetal liver–derived erythroid progenitors in labeled culture media. These labeled RBCs could then be subjected to *in vitro* EP by iRPMs overexpressing FPN, followed by LC–MS–based metabolite tracing. Such analyses will allow direct assessment of whether BCAA catabolism provides anaplerotic input into mitochondrial metabolism and how this integrates with fatty acid β-oxidation to sustain oxidative phosphorylation. More broadly, these experiments should clarify how amino acid-derived carbons are coordinated within the metabolic network that supports enhanced EP in ID RPMs.

A third priority is to establish the causal requirement of BCAA catabolism in RPM adaptation using genetic approaches. While the present work shows that pharmacological inhibition of BCAT activity suppresses mitochondrial activation and EP, these experiments do not exclude off-target effects and therefore do not establish a definitive causal requirement for BCAA catabolism in this setting. Conditional deletion of BCAT1 and BCAT2 in RPMs will therefore be required to define the contribution of the initial transamination step to the observed phenotype. In addition, genetic perturbation of the BCKDH complex may provide a more direct assessment of the requirement for BCAA-derived carbon entry into mitochondrial metabolism. Such models will allow evaluation of whether disruption of BCAA catabolism impairs

mitochondrial respiration, limits the induction of oxidative metabolism, and attenuates EP under ID conditions. They will also help refine the positioning of BCAA catabolism within the FPN–SYK-dependent regulatory framework and determine whether this pathway functions primarily as an anaplerotic input into the TCA cycle or contributes more broadly to the metabolic state that sustains enhanced EP. Importantly, these models will also enable assessment of the physiological consequences of disrupting BCAA catabolism during ID, including whether combined impairment of iron availability and BCAA utilization compromises RPM function sufficiently to affect systemic iron homeostasis, erythropoietic responses, or organismal viability.

A fourth area that requires further development is the broader metabolic characterization of RPMs. While functional enrichment of proteomic data identified key pathways, including BCAA catabolism and fatty acid β-oxidation, initial attempts to perform untargeted metabolomics and lipidomics revealed some technical limitations. Although pilot analyses suggested trends toward altered amino acid- and lipid-associated metabolites, the data were compromised by high inter-sample variation and lacked sufficient resolution to fully support confident pathway-level conclusions. These limitations likely reflect a combination of low cell numbers, rapid metabolite turnover, and insufficient analytical sensitivity, indicating that standard metabolomic workflows are not readily applicable to RPMs and require optimization tailored to this cell type. Future studies will therefore need to improve sample preparation, metabolite extraction, and detection sensitivity to enable reliable profiling of low-abundance intermediates. In particular, approaches that minimize metabolite loss and preserve the metabolic state during cell isolation will be critical. Integration of optimized metabolomic and lipidomic datasets with existing proteomic and functional data should allow a more precise definition of the metabolic networks that support RPM adaptation to ID, rather than inference based primarily on enzyme expression. In addition, functional assays that directly quantify BCKDH complex activity in ID RPMs *in vivo* or in their *in vitro* counterparts would provide an elegant complement to the data obtained so far.

Another unresolved aspect is the relationship between RPM metabolic adaptation and erythropoietic responses. ID is associated with compensatory erythropoiesis, including splenic erythroid expansion, and the data presented here indicate that disruption of RPM metabolic pathways, such as BCAA catabolism, is accompanied by increased erythropoietic drive. However, it remains unclear whether these effects arise solely from altered iron availability or whether RPM-derived metabolic or signaling changes can directly influence erythroid differentiation. *In vitro* systems based on fetal liver-derived erythroid progenitors provide a controlled platform to address this question. By modulating iron availability and perturbing pathways identified in RPMs, including BCAA catabolism, it should be possible to determine whether these pathways influence erythroid maturation independently of systemic iron redistribution. Such experiments may help distinguish between indirect effects mediated by iron supply and direct regulatory interactions between macrophage metabolic states and erythropoietic programs.

Finally, it will be important to determine whether the metabolic program identified in RPMs is specific to EP or can also be engaged by other forms of phagocytic cargo. The data presented

here show that BCAA catabolism is induced in association with RBC processing, as indicated by increased BCKDHB expression following exposure to stressed RBCs but not RBC ghosts, and by the functional requirement for BCAT activity in sustaining enhanced EP. However, it remains unclear whether this response reflects a specific adaptation to hemoglobin-rich erythrocyte cargo or a more general metabolic requirement of macrophages exposed to sustained phagocytic load. This question can be addressed by systematically comparing the effects of distinct cargos, including apoptotic cells and bacterial particles, on the induction of BCAA catabolism and related metabolic pathways. In particular, it will be important to assess whether exposure to apoptotic cells or heat-inactivated *E. coli* induces enzymes such as BCKDHB, alters BCAT-dependent metabolic activity, or engages the broader oxidative program that in RPMs includes fatty acid β-oxidation. Such analyses will help determine whether the FPN–SYK–BCAA axis defined here represents a cargo-specific adaptation linked to RBC clearance or a broader metabolic module that supports macrophage phagocytic function during sustained substrate processing. In addition, the proteomic data suggest that other amino acid–associated pathways beyond BCAA catabolism may contribute to the control of EP, warranting future investigation of these candidate circuits at both functional and mechanistic levels.

Together, these future directions will refine the mechanistic understanding of RPM adaptation to ID and help define its physiological relevance at both cellular and systemic levels.

5. REFERENCES

1. Zoroddu, M. A. *et al.* The essential metals for humans: a brief overview. *J Inorg Biochem* **195**, 120–129 (2019).
2. Ganz, T. Systemic Iron Homeostasis. *Physiological Reviews* **93**, 1721–1741 (2013).
3. Cronin, S. J. F., Woolf, C. J., Weiss, G. & Penninger, J. M. The Role of Iron Regulation in Immunometabolism and Immune-Related Disease. *Front. Mol. Biosci.* **6**, (2019).
4. Andreini, C., Banci, L., Bertini, I., Elmi, S. & Rosato, A. Non-heme iron through the three domains of life. *Proteins: Structure, Function, and Bioinformatics* **67**, 317–324 (2007).
5. Muckenthaler, M. U., Rivella, S., Hentze, M. W. & Galy, B. A Red Carpet for Iron Metabolism. *Cell* **168**, 344–361 (2017).
6. Steele, S. L. *et al.* Daily Oral Supplementation with 60 mg of Elemental Iron for 12 Weeks Alters Blood Mitochondrial DNA Content, but Not Leukocyte Telomere Length in Cambodian Women. *Nutrients* **13**, (2021).
7. Hentze, M. W., Muckenthaler, M. U., Galy, B. & Camaschella, C. Two to Tango: Regulation of Mammalian Iron Metabolism. *Cell* **142**, 24–38 (2010).
8. Wang, J. & Pantopoulos, K. Regulation of cellular iron metabolism. *Biochem J* **434**, 365–381 (2011).
9. Wilson, M. T. & Reeder, B. J. Oxygen-binding haem proteins. *Experimental Physiology* **93**, 128–132 (2008).
10. Muñoz, M., Villar, I. & García-Erce, J. A. An update on iron physiology. *World J Gastroenterol* **15**, 4617–4626 (2009).
11. Kyu, H. H. *et al.* Global, regional, and national disability-adjusted life-years (DALYs) for 359 diseases and injuries and healthy life expectancy (HALE) for 195 countries and territories, 1990–2017: a systematic analysis for the Global Burden of Disease Study 2017. *The Lancet* **392**, 1859–1922 (2018).
12. Gardner, W. M. *et al.* Prevalence, years lived with disability, and trends in anaemia burden by severity and cause, 1990–2021: findings from the Global Burden of Disease Study 2021. *The Lancet Haematology* **10**, e713–e734 (2023).
13. Pasricha, S.-R., Tye-Din, J., Muckenthaler, M. U. & Swinkels, D. W. Iron deficiency. *The Lancet* **397**, 233–248 (2021).
14. More, S., Shivkumar, V. B., Gangane, N. & Shende, S. Effects of iron deficiency on cognitive function in school going adolescent females in rural area of central India. *Anemia* **2013**, 819136 (2013).
15. Mleczko-Sanecka, K. & Silvestri, L. Cell-type-specific insights into iron regulatory processes. *American Journal of Hematology* **96**, 110–127 (2021).
16. Gammella, E., Buratti, P., Cairo, G. & Recalcati, S. The transferrin receptor: the cellular iron gate. *Metallomics.* **9**, 1367–1375 (2017).
17. Ohgami, R. S. *et al.* Identification of a ferrireductase required for efficient transferrin-dependent iron uptake in erythroid cells. *Nat Genet* **37**, 1264–1269 (2005).
18. Fleming, M. D. *et al.* Nramp2 is mutated in the anemic Belgrade (b) rat: Evidence of a role for Nramp2 in endosomal iron transport. *Proceedings of the National Academy of Sciences* **95**, 1148–1153 (1998).

19. Xu, H., Jin, J., DeFelice, L. J., Andrews, N. C. & Clapham, D. E. A Spontaneous, Recurrent Mutation in Divalent Metal Transporter-1 Exposes a Calcium Entry Pathway. *PLOS Biology* **2**, e50 (2004).
20. Lv, H. & Shang, P. The significance, trafficking and determination of labile iron in cytosol, mitochondria and lysosomes. *Metallomics.* **10**, 899–916 (2018).
21. Kakhlon, O. & Cabantchik, Z. I. The labile iron pool: characterization, measurement, and participation in cellular processes1. *Free Radical Biology and Medicine* **33**, 1037–1046 (2002).
22. Levi, S. *et al.* Mechanism of ferritin iron uptake: activity of the H-chain and deletion mapping of the ferro-oxidase site. A study of iron uptake and ferro-oxidase activity of human liver, recombinant H-chain ferritins, and of two H-chain deletion mutants. *J Biol Chem* **263**, 18086–18092 (1988).
23. Harrison, P. M. & Arosio, P. The ferritins: molecular properties, iron storage function and cellular regulation. *Biochimica et Biophysica Acta (BBA) - Bioenergetics* **1275**, 161–203 (1996).
24. Rucker, P., Torti, F. M. & Torti, S. V. Role of H and L Subunits in Mouse Ferritin". *Journal of Biological Chemistry* **271**, 33352–33357 (1996).
25. Mancias, J. D., Wang, X., Gygi, S. P., Harper, J. W. & Kimmelman, A. C. Quantitative proteomics identifies NCOA4 as the cargo receptor mediating ferritinophagy. *Nature* **509**, 105–109 (2014).
26. Nai, A. *et al.* NCOA4-mediated ferritinophagy in macrophages is crucial to sustain erythropoiesis in mice. *Haematologica* **106**, 795–805 (2021).
27. Donovan, A. *et al.* Positional cloning of zebrafish ferroportin1 identifies a conserved vertebrate iron exporter. *Nature* **403**, 776–781 (2000).
28. Donovan, A. *et al.* The iron exporter ferroportin/Slc40a1 is essential for iron homeostasis. *Cell Metabolism* **1**, 191–200 (2005).
29. McKie, A. T. *et al.* A Novel Duodenal Iron-Regulated Transporter, IREG1, Implicated in the Basolateral Transfer of Iron to the Circulation. *Molecular Cell* **5**, 299–309 (2000).
30. Vulpe, C. D. *et al.* Hephaestin, a ceruloplasmin homologue implicated in intestinal iron transport, is defective in the sla mouse. *Nat Genet* **21**, 195–199 (1999).
31. Shi, H., Bencze, K. Z., Stemmler, T. L. & Philpott, C. C. A Cytosolic Iron Chaperone That Delivers Iron to Ferritin. *Science* **320**, 1207–1210 (2008).
32. Nandal, A. *et al.* Activation of the HIF Prolyl Hydroxylase by the Iron Chaperones PCBP1 and PCBP2. *Cell Metab* **14**, 647–657 (2011).
33. Philpott, C. C. *et al.* Iron-tracking strategies: Chaperones capture iron in the cytosolic labile iron pool. *Front. Mol. Biosci.* **10**, (2023).
34. Casey, J. L., Koeller, D. M., Ramin, V. C., Klausner, R. D. & Harford, J. B. Iron regulation of transferrin receptor mRNA levels requires iron-responsive elements and a rapid turnover determinant in the 3' untranslated region of the mRNA. *EMBO J* **8**, 3693–3699 (1989).
35. Kim, H.-Y., LaVaute, T., Iwai, K., Klausner, R. D. & Rouault, T. A. Identification of a Conserved and Functional Iron-responsive Element in the 5′-Untranslated Region of Mammalian Mitochondrial Aconitase*. *Journal of Biological Chemistry* **271**, 24226–24230 (1996).

36. Wilkinson, N. & Pantopoulos, K. The IRP/IRE system in vivo: insights from mouse models. *Front Pharmacol* **5**, 176 (2014).
37. Phillips, J. D., Guo, B., Yu, Y., Brown, F. M. & Leibold, E. A. Expression and biochemical characterization of iron regulatory proteins 1 and 2 in Saccharomyces cerevisiae. *Biochemistry* **35**, 15704–15714 (1996).
38. Haile, D. J. *et al.* Cellular regulation of the iron-responsive element binding protein: disassembly of the cubane iron-sulfur cluster results in high-affinity RNA binding. *Proc. Natl. Acad. Sci. U.S.A.* **89**, 11735–11739 (1992).
39. Vashisht, A. A. *et al.* Control of Iron Homeostasis by an Iron-Regulated Ubiquitin Ligase. *Science* **326**, 718–721 (2009).
40. Ganz, T. Macrophages and Iron Metabolism. *Microbiol Spectr* **4**, (2016).
41. Slusarczyk, P. & Mleczko-Sanecka, K. The Multiple Facets of Iron Recycling. *Genes (Basel)* **12**, 1364 (2021).
42. Ganz, T. Macrophages and systemic iron homeostasis. *J Innate Immun* **4**, 446–453 (2012).
43. Bian, Z. *et al.* Cd47-Sirpα interaction and IL-10 constrain inflammation-induced macrophage phagocytosis of healthy self-cells. *Proc Natl Acad Sci U S A* **113**, E5434–E5443 (2016).
44. Nemeth, E. *et al.* Hepcidin Regulates Cellular Iron Efflux by Binding to Ferroportin and Inducing Its Internalization. *Science* **306**, 2090–2093 (2004).
45. Aschemeyer, S. *et al.* Structure-function analysis of ferroportin defines the binding site and an alternative mechanism of action of hepcidin. *Blood* **131**, 899–910 (2018).
46. Nicolas, G. *et al.* Lack of hepcidin gene expression and severe tissue iron overload in upstream stimulatory factor 2 (USF2) knockout mice. *Proc Natl Acad Sci U S A* **98**, 8780–8785 (2001).
47. Park, C. H., Valore, E. V., Waring, A. J. & Ganz, T. Hepcidin, a Urinary Antimicrobial Peptide Synthesized in the Liver*. *Journal of Biological Chemistry* **276**, 7806–7810 (2001).
48. Pigeon, C. *et al.* A new mouse liver-specific gene, encoding a protein homologous to human antimicrobial peptide hepcidin, is overexpressed during iron overload. *J Biol Chem* **276**, 7811–7819 (2001).
49. Canali, S., Wang, C.-Y., Zumbrennen-Bullough, K. B., Bayer, A. & Babitt, J. L. Bone morphogenetic protein 2 controls iron homeostasis in mice independent of Bmp6. *Am J Hematol* **92**, 1204–1213 (2017).
50. Koch, P.-S. *et al.* Angiocrine Bmp2 signaling in murine liver controls normal iron homeostasis. *Blood* **129**, 415–419 (2017).
51. Kautz, L. *et al.* Iron regulates phosphorylation of Smad1/5/8 and gene expression of *Bmp6, Smad7, Id1*, and *Atoh8* in the mouse liver. *Blood* **112**, 1503–1509 (2008).
52. Babitt, J. L. *et al.* Bone morphogenetic protein signaling by hemojuvelin regulates hepcidin expression. *Nat Genet* **38**, 531–539 (2006).
53. Schmidt, P. J., Toran, P. T., Giannetti, A. M., Bjorkman, P. J. & Andrews, N. C. The Transferrin Receptor Modulates Hfe-Dependent Regulation of Hepcidin Expression. *Cell Metabolism* **7**, 205–214 (2008).
54. Nemeth, E. *et al.* IL-6 mediates hypoferremia of inflammation by inducing the synthesis of the iron regulatory hormone hepcidin. *J Clin Invest* **113**, 1271–1276 (2004).

55. Ganz, T. Anemia of Inflammation. *New England Journal of Medicine* **381**, 1148–1157 (2019).
56. Kautz, L. *et al.* IDENTIFICATION OF ERYTHROFERRONE AS AN ERYTHROID REGULATOR OF IRON METABOLISM. *Nat Genet* **46**, 678–684 (2014).
57. Wang, C.-Y. *et al.* Smad1/5 is required for erythropoietin-mediated suppression of hepcidin in mice. *Blood* **130**, 73–83 (2017).
58. Wang, C.-Y. *et al.* Erythroferrone lowers hepcidin by sequestering BMP2/6 heterodimer from binding to the BMP type I receptor ALK3. *Blood* **135**, 453–456 (2020).
59. Sardo, U. *et al.* The hepatokine FGL1 regulates hepcidin and iron metabolism during anemia in mice by antagonizing BMP signaling. *Blood* **143**, 1282–1292 (2024).
60. Qiao, B. *et al.* Hepcidin-Induced Endocytosis of Ferroportin Is Dependent on Ferroportin Ubiquitination. *Cell Metabolism* **15**, 918–924 (2012).
61. Traeger, L. *et al.* UBA6 and NDFIP1 regulate the degradation of ferroportin. *Haematologica* **107**, 478–488 (2022).
62. Knutson, M. D., Oukka, M., Koss, L. M., Aydemir, F. & Wessling-Resnick, M. Iron release from macrophages after erythrophagocytosis is up-regulated by ferroportin 1 overexpression and down-regulated by hepcidin. *Proc Natl Acad Sci U S A* **102**, 1324–1328 (2005).
63. Slusarczyk, P. *et al.* Impaired iron recycling from erythrocytes is an early hallmark of aging. *eLife* **12**, e79196 (2023).
64. Finch, C. Regulators of Iron Balance in Humans. *Blood* **84**, 1697–1702 (1994).
65. Ha, J.-H., Doguer, C. & Collins, J. F. Consumption of a high-iron diet disrupts homeostatic regulation of intestinal copper absorption in adolescent mice. *Am J Physiol Gastrointest Liver Physiol* **313**, G353–G360 (2017).
66. Fillebeen, C. *et al.* Mice are poor heme absorbers and do not require intestinal Hmox1 for dietary heme iron assimilation. *Haematologica* **100**, e334–e337 (2015).
67. Franco, R. S. Measurement of Red Cell Lifespan and Aging. *Transfus Med Hemother* **39**, 302–307 (2012).
68. Dholakia, U., Bandyopadhyay, S., Hod, E. A. & Prestia, K. A. Determination of RBC Survival in C57BL/6 and C57BL/6-Tg(UBC–GFP) Mice. *Comp Med* **65**, 196–201 (2015).
69. Waugh, R. E. *et al.* Rheologic Properties of Senescent Erythrocytes: Loss of Surface Area and Volume With Red Blood Cell Age. *Blood* **79**, 1351–1358 (1992).
70. Bratosin, D. *et al.* Cellular and molecular mechanisms of senescent erythrocyte phagocytosis by macrophages. A review. *Biochimie* **80**, 173–195 (1998).
71. Mohanty, J. G., Nagababu, E. & Rifkind, J. M. Red blood cell oxidative stress impairs oxygen delivery and induces red blood cell aging. *Front Physiol* **5**, 84 (2014).
72. Suzuki, T. & Agar, N. S. Glutathione peroxidase, superoxide dismutase and catalase in the red blood cells of GSH-normal and GSH-deficient sheep. *Experientia* **39**, 103–104 (1983).
73. Klei, T. R. L., Meinderts, S. M., van den Berg, T. K. & van Bruggen, R. From the Cradle to the Grave: The Role of Macrophages in Erythropoiesis and Erythrophagocytosis. *Front Immunol* **8**, 73 (2017).

74. Knutson, M. & Wessling-Resnick, M. Iron Metabolism in the Reticuloendothelial System. *Critical Reviews in Biochemistry and Molecular Biology* **38**, 61–88 (2003).
75. Youssef, L. A. *et al.* Increased erythrophagocytosis induces ferroptosis in red pulp macrophages in a mouse model of transfusion. *Blood* **131**, 2581–2593 (2018).
76. Crosby, W. H. & Benjamin, N. R. Siderocytes and the Spleen. *Blood* **12**, 165–170 (1957).
77. Vargas, A. Illustrated Pathology of the Spleen. *J Clin Pathol* **54**, 255 (2001).
78. Mebius, R. E. & Kraal, G. Structure and function of the spleen. *Nat Rev Immunol* **5**, 606–616 (2005).
79. Duez, J. *et al.* Mechanical clearance of red blood cells by the human spleen: Potential therapeutic applications of a biomimetic RBC filtration method. *Transfusion Clinique et Biologique* **22**, 151–157 (2015).
80. Meinderts, S. M. *et al.* Human and murine splenic neutrophils are potent phagocytes of IgG-opsonized red blood cells. *Blood Adv* **1**, 875–886 (2017).
81. Kannan, R., Yuan, J. & Low, P. S. Isolation and partial characterization of antibody- and globin-enriched complexes from membranes of dense human erythrocytes. *Biochem J* **278**, 57–62 (1991).
82. Oh, M.-H. *et al.* mTORC2 signaling selectively regulates generation and function of tissue-resident peritoneal macrophages. *Cell Rep* **20**, 2439–2454 (2017).
83. Zagórska, A. *et al.* Differential regulation of hepatic physiology and injury by the TAM receptors Axl and Mer. *Life Sci Alliance* **3**, e202000694 (2020).
84. Lutz, H. U. Naturally occurring antibodies. *Adv Exp Med Biol* **750**, vii–x (2012).
85. Delaby, C. *et al.* Subcellular Localization of Iron and Heme Metabolism Related Proteins at Early Stages of Erythrophagocytosis. *PLoS One* **7**, e42199 (2012).
86. Rajagopal, A. *et al.* Haem homeostasis is regulated by the conserved and concerted functions of HRG-1 proteins. *Nature* **453**, 1127–1131 (2008).
87. White, C. *et al.* HRG1 is essential for heme transport from the phagolysosome of macrophages during erythrophagocytosis. *Cell Metab* **17**, 261–270 (2013).
88. Poss, K. D. & Tonegawa, S. Heme oxygenase 1 is required for mammalian iron reutilization. *Proc Natl Acad Sci U S A* **94**, 10919–10924 (1997).
89. Kovtunovych, G., Eckhaus, M. A., Ghosh, M. C., Ollivierre-Wilson, H. & Rouault, T. A. Dysfunction of the heme recycling system in heme oxygenase 1–deficient mice: effects on macrophage viability and tissue iron distribution. *Blood* **116**, 6054–6062 (2010).
90. Wegiel, B., Nemeth, Z., Correa-Costa, M., Bulmer, A. C. & Otterbein, L. E. Heme Oxygenase-1: A Metabolic Nike. *Antioxid Redox Signal* **20**, 1709–1722 (2014).
91. Delaby, C. *et al.* A physiological model to study iron recycling in macrophages. *Experimental Cell Research* **310**, 43–53 (2005).
92. Kim, A. *et al.* A mouse model of anemia of inflammation: complex pathogenesis with partial dependence on hepcidin. *Blood* **123**, 1129–1136 (2014).
93. Pasricha, S.-R. *et al.* Hepcidin is regulated by promoter-associated histone acetylation and HDAC3. *Nat Commun* **8**, 403 (2017).
94. Camaschella, C. Iron deficiency. *Blood* **133**, 30–39 (2019).
95. Klei, T. R. L. *et al.* Hemolysis in the spleen drives erythrocyte turnover. *Blood* **136**, 1579–1589 (2020).

96. Van den Bossche, J., O'Neill, L. A. & Menon, D. Macrophage Immunometabolism: Where Are We (Going)? *Trends in Immunology* **38**, 395–406 (2017).
97. Arandjelovic, S. & Ravichandran, K. S. Phagocytosis of apoptotic cells in homeostasis. *Nat Immunol* **16**, 907–917 (2015).
98. Doran, A. C., Yurdagul, A. & Tabas, I. Efferocytosis in health and disease. *Nat Rev Immunol* **20**, 254–267 (2020).
99. Sender, R. & Milo, R. The distribution of cellular turnover in the human body. *Nat Med* **27**, 45–48 (2021).
100. Schilperoort, M. *et al.* The role of efferocytosis-fueled macrophage metabolism in the resolution of inflammation. *Immunological Reviews* **319**, 65–80 (2023).
101. Wculek, S. K. *et al.* Oxidative phosphorylation selectively orchestrates tissue macrophage homeostasis. *Immunity* **56**, 516-530.e9 (2023).
102. Yurdagul, A. Metabolic Consequences of Efferocytosis and its Impact on Atherosclerosis. *Immunometabolism* **3**, e210017 (2021).
103. Basu, S. & Rossol, M. You are what you eat: metabolic recycling of phagocytosed bacteria modulates macrophage immunity. *Sig Transduct Target Ther* **10**, 133 (2025).
104. Lesbats, J. *et al.* Macrophages recycle phagocytosed bacteria to fuel immunometabolic responses. *Nature* **640**, 524–533 (2025).
105. Wculek, S. K., Dunphy, G., Heras-Murillo, I., Mastrangelo, A. & Sancho, D. Metabolism of tissue macrophages in homeostasis and pathology. *Cell Mol Immunol* **19**, 384–408 (2022).
106. Zhang, S. *et al.* Efferocytosis Fuels Requirements of Fatty Acid Oxidation and the Electron Transport Chain to Polarize Macrophages for Tissue Repair. *Cell Metab* **29**, 443-456.e5 (2019).
107. A-Gonzalez, N. *et al.* Apoptotic cells promote their own clearance and immune tolerance through activation of LXR. *Immunity* **31**, 245–258 (2009).
108. Ogata, M. *et al.* On the mechanism for PPAR agonists to enhance ABCA1 gene expression. *Atherosclerosis* **205**, 413–419 (2009).
109. Morioka, S. *et al.* Efferocytosis induces a novel SLC program to promote glucose uptake and lactate release. *Nature* **563**, 714–718 (2018).
110. Trzeciak, A., Wang, Y.-T. & Perry, J. S. A. First we eat, then we do everything else: The dynamic metabolic regulation of efferocytosis. *Cell Metabolism* **33**, 2126–2141 (2021).
111. Yurdagul, A. *et al.* Macrophage Metabolism of Apoptotic Cell-Derived Arginine Promotes Continual Efferocytosis and Resolution of Injury. *Cell Metab* **31**, 518-533.e10 (2020).
112. Merlin, J. *et al.* Non-canonical glutamine transamination sustains efferocytosis by coupling redox buffering to oxidative phosphorylation. *Nat Metab* **3**, 1313–1326 (2021).
113. Ampomah, P. B. *et al.* Macrophages use apoptotic cell-derived methionine and DNMT3A during efferocytosis to promote tissue resolution. *Nat Metab* **4**, 444–457 (2022).
114. Sukka, S. R. *et al.* Efferocytosis drives a tryptophan metabolism pathway in macrophages to promote tissue resolution. *Nat Metab* **6**, 1736–1755 (2024).
115. Rouault, T. A. & Tong, W.-H. Iron–sulphur cluster biogenesis and mitochondrial iron homeostasis. *Nat Rev Mol Cell Biol* **6**, 345–351 (2005).

116. Read, A. D., Bentley, R. ET., Archer, S. L. & Dunham-Snary, K. J. Mitochondrial iron–sulfur clusters: Structure, function, and an emerging role in vascular biology. *Redox Biol* **47**, 102164 (2021).
117. Hoes, M. F. *et al.* Iron deficiency impairs contractility of human cardiomyocytes through decreased mitochondrial function. *Eur J Heart Fail* **20**, 910–919 (2018).
118. Li, H. *et al.* Iron regulatory protein 2 modulates the switch from aerobic glycolysis to oxidative phosphorylation in mouse embryonic fibroblasts. *Proc. Natl. Acad. Sci. U.S.A.* **116**, 9871–9876 (2019).
119. Wang, R., Hussain, A., Guo, Q. Q., Jin, X. W. & Wang, M. M. Oxygen and Iron Availability Shapes Metabolic Adaptations of Cancer Cells. *World J Oncol* **15**, 28–37 (2024).
120. Yan, Q. *et al.* Metabolic reprogramming in efferocytosis. *Front. Cell Dev. Biol.* **13**, (2025).
121. Pandit, R., Hillman, H., Williams, J. W. & Yurdagul, A. More Than a Cleanup Crew: The Expanding Biology of Efferocytosis. *Arterioscler Thromb Vasc Biol* **46**, e323211 (2026).
122. McCubbrey, A. L. *et al.* Polyamine import and accumulation causes immunomodulation in macrophages engulfing apoptotic cells. *Cell Rep* **38**, 110222 (2022).
123. Bonvini, A., Coqueiro, A. Y., Tirapegui, J., Calder, P. C. & Rogero, M. M. Immunomodulatory role of branched-chain amino acids. *Nutr Rev* **76**, 840–856 (2018).
124. Lu, M. *et al.* Branched-chain amino acid catabolism promotes M2 macrophage polarization. *Front Immunol* **15**, 1469163 (2024).
125. Shimomura, Y. *et al.* Branched-Chain Amino Acid Catabolism in Exercise and Liver Disease, ,. *The Journal of Nutrition* **136**, 250S-253S (2006).
126. Papathanassiu, A. E. *et al.* BCAT1 controls metabolic reprogramming in activated human macrophages and is associated with inflammatory diseases. *Nat Commun* **8**, 16040 (2017).
127. Neinast, M., Murashige, D. & Arany, Z. Branched Chain Amino Acids. *Annu Rev Physiol* **81**, 139–164 (2019).
128. Lu, M. *et al.* Branched-chain amino acid catabolism promotes M2 macrophage polarization. *Front. Immunol.* **15**, (2024).
129. Yan, H. *et al.* Leucine alleviates cytokine storm syndrome by regulating macrophage polarization via the mTORC1/LXRα signaling pathway. *Elife* **12**, RP89750 (2024).
130. Chernoff, A. I., Liu, J. C., Battle, E. & Bond, M. The Amino Acid Composition of Hemoglobin.II. Analytical Technics. *Blood* **17**, 54–70 (1961).
131. Enko, D. *et al.* Branched-chain amino acids are linked with iron metabolism. *Ann Transl Med* **8**, 1569 (2020).
132. Castoldi, A. *et al.* Triacylglycerol synthesis enhances macrophage inflammatory function. *Nat Commun* **11**, 4107 (2020).
133. Nakayama, Y. *et al.* A long noncoding RNA regulates inflammation resolution by mouse macrophages through fatty acid oxidation activation. *Proceedings of the National Academy of Sciences* **117**, 14365–14375 (2020).
134. Wang, Y. *et al.* Lipid droplet accumulation mediates macrophage survival and Treg recruitment via the CCL20/CCR6 axis in human hepatocellular carcinoma. *Cell Mol Immunol* **21**, 1120–1130 (2024).

135. Kaza, N., Ojaghi, A. & Robles, F. E. Hemoglobin quantification in red blood cells via dry mass mapping based on UV absorption. *J Biomed Opt* **26**, 086501 (2021).
136. Long, M. *et al.* DGAT1 activity synchronises with mitophagy to protect cells from metabolic rewiring by iron depletion. *EMBO J* **41**, EMBJ2021109390 (2022).
137. Koliwad, S. K. *et al.* DGAT1-dependent triacylglycerol storage by macrophages protects mice from diet-induced insulin resistance and inflammation. *J Clin Invest* **120**, 756–767 (2010).
138. Jiang, Y. *et al.* Iron-dependent histone 3 lysine 9 demethylation controls B cell proliferation and humoral immune responses. *Nat Commun* **10**, 2935 (2019).
139. Wang, L. *et al.* Attenuated inflammatory responses in hemochromatosis reveal a role for iron in the regulation of macrophage cytokine translation. *J Immunol* **181**, 2723–2731 (2008).
140. Agoro, R., Taleb, M., Quesniaux, V. F. J. & Mura, C. Cell iron status influences macrophage polarization. *PLOS ONE* **13**, e0196921 (2018).
141. Zurawska, G. *et al.* Liver sinusoidal endothelial cells constitute a major route for hemoglobin clearance. *EMBO Rep* https://doi.org/10.1038/s44319-025-00673-5 (2026) doi:10.1038/s44319-025-00673-5.
142. Mócsai, A., Ruland, J. & Tybulewicz, V. L. J. The SYK tyrosine kinase: a crucial player in diverse biological functions. *Nat Rev Immunol* **10**, 387–402 (2010).
143. Underhill, D. M. & Goodridge, H. S. Information processing during phagocytosis. *Nat Rev Immunol* **12**, 492–502 (2012).
144. Winn, N. C., Wolf, E. M., Cottam, M. A., Bhanot, M. & Hasty, A. H. Myeloid-specific deletion of ferroportin impairs macrophage bioenergetics but is disconnected from systemic insulin action in adult mice. *Am J Physiol Endocrinol Metab* **321**, E376–E391 (2021).
145. Schwartz, A. J. *et al.* Hepcidin sequesters iron to sustain nucleotide metabolism and mitochondrial function in colorectal cancer epithelial cells. *Nat Metab* **3**, 969–982 (2021).
146. Bhutia, Y. D. & Ganapathy, V. Glutamine Transporters in Mammalian Cells and Their Functions in Physiology and Cancer. *Biochim Biophys Acta* **1863**, 2531–2539 (2016).
147. Hanson, A. L. *et al.* Iron dysregulation and inflammatory stress erythropoiesis associates with long-term outcome of COVID-19. *Nat Immunol* **25**, 471–482 (2024).

Appendix 1

Manuscript 1:

Pratik Kumar Mandal*, **Raghunandan Mahadeva***, Komal Chouhan*, Patryk Slusarczyk*, Gabriela Zurawska, Marta Niklewicz, Matylda Macias, Aleksandra Szybińska, Aneta Jończy, Zhaoyuan Liu, Florent Ginhoux, Małgorzata Lenartowicz, Wojciech Pokrzywa, Elizabeta Nemeth and Katarzyna Mleczko-Sanecka. Iron deficiency drives metabolic adaptation of red pulp macrophages via FPN-SYK signaling and BCAA catabolism to enhance erythrophagocytosis. bioRxiv (2026). DOI: https://doi.org/10.1101/2025.06.13.659526

*Authors contributed equally

Warsaw, 19-12-2025

Raghunandan Mahadeva

Laboratory of Iron Homeostasis

International Institute of Molecular
and Cell Biology in Warsaw
Ks. Trojdena 4 Street
02-109 Warsaw

Candidate's Contribution Statement

Article's title: Iron deficiency drives metabolic adaptation of red pulp macrophages via FPN–SYK signaling and BCAA catabolism to enhance erythrophagocytosis

Authors: Pratik Kumar Mandal#, **Raghunandan Mahadeva#**, Komal Chouhan#, Patryk Slusarczyk#, Gabriela Zurawska, Marta Niklewicz, Matylda Macias, Aleksandra Szybińska, Aneta Jończy, Zhaoyuan Liu, Florent Ginhoux, Małgorzata Lenartowicz, Wojciech Pokrzywa, Delphine Meynard, Elizabeta Nemeth and Katarzyna Mleczko-Sanecka#

# - equal contribution

Journal: bioRxiv

Date of publishing: 15/06/2025 (first version); 05/12/2025 (latest version)

DOI: https://doi.org/10.1101/2025.06.13.659526

I hereby declare that I, Raghunandan Mahadeva, made a substantive contribution to the development of this publication. My contribution consisted of:

I was responsible for the conceptual, experimental, and analytical work defining how iron deficiency alters metabolic circuitries in red pulp macrophages, with a particular focus on branched-chain amino-acid catabolism, β-oxidation pathways, and their functional relevance to erythrophagocytosis. This included designing and executing metabolic and pharmacological perturbation experiments in primary cells and in mice; establishing and performing ferroportin-overexpression assays; conducting *ex vivo* functional assays; generating Seahorse and Mitoplate metabolic profiles; and analyzing protein and metabolite expression patterns

associated with metabolic rewiring. Altogether, I solely generated the data for Figures 6 and 7 of the above-mentioned preprint and contributed to several earlier panels, including Figures 3–5. Specifically, for Figure 3, I performed the Seahorse metabolic flux analyses and contributed to the processing and interpretation of these datasets. For Figure 4, I helped establish and carry out the ferroportin-overexpression experiments together with the first author. For Figure 5, I performed selected flow-cytometric assays and assisted with data interpretation. Across these figures, I also supported the team in animal procedures, including sacrifice, tissue collection, and subsequent assay preparation, and contributed to performing several downstream experiments. I co-conceived the overall flow of the study, participated in data interpretation, created scientific visualizations, and contributed to the writing of the manuscript.

Candidate's Signature

Signature of the Corresponding Author

Iron deficiency drives metabolic adaptation of red pulp macrophages via ferroportin-SYK signaling and BCAA catabolism to enhance erythrophagocytosis

Pratik Kumar Mandal[1#], Raghunandan Mahadeva[1#], Komal Chouhan[1#], Patryk Slusarczyk[1#], Gabriela Zurawska[1], Marta Niklewicz[1], Matylda Macias[1], Aleksandra Szybińska[1], Aneta Jończy[1], Zhaoyuan Liu[2], Florent Ginhoux[3], Małgorzata Lenartowicz[4], Wojciech Pokrzywa[1], Elizabeta Nemeth[5] and Katarzyna Mleczko-Sanecka[1]

1 International Institute of Molecular and Cell Biology in Warsaw, Poland.

2 Shanghai Institute of Immunology, Department of Immunology and Microbiology, Shanghai Jiao Tong University School of Medicine, Shanghai 200025, China.

3 Shanghai Institute of Immunology, Department of Immunology and Microbiology, Shanghai Jiao Tong University School of Medicine, Shanghai 200025, China; Singapore Immunology Network, Agency for Science, Technology and Research, Singapore 138648, Singapore; Translational Immunology Institute, SingHealth Duke-NUS Academic Medical Centre, Singapore, Singapore.

4 Laboratory of Genetics and Evolution, Institute of Zoology and Biomedical Research, Jagiellonian University, Cracow, Poland.

5 David Geffen School of Medicine at UCLA, Los Angeles, California, United States.

# - equal contribution

To whom correspondence may be addressed: Katarzyna Mleczko-Sanecka, International Institute of Molecular and Cell Biology in Warsaw, 4 Ks. Trojdena Street, 02-109 Warsaw, Poland, E-mail: kmsanecka@iimcb.gov.pl

Abstract

Iron deficiency is the most common nutritional disorder worldwide, yet how individual cell types adjust to iron scarcity remains unclear. Splenic red pulp macrophages (RPMs) are essential for systemic iron homeostasis. They manage exceptionally high iron flux by recycling aged red blood cells through erythrophagocytosis, a specialized form of efferocytosis. However, how RPMs adapt their clearance and metabolic programs to iron deficiency remains unexplored. Here, we show that RPMs from mildly anemic, iron-deficient mice exhibit enhanced erythrophagocytic capacity. Proteomic profiling and flow cytometry revealed expansion and activation of lysosomal and mitochondrial networks, accompanied by elevated mitochondrial respiration. This metabolic rewiring and the increase in erythrophagocytosis depended on branched-chain amino acid (BCAA) catabolism. These responses were distinct from alternative macrophage activation states and absent in liver and peritoneal macrophages. Mechanistically, the low hepcidin-high ferroportin axis and SYK kinase activity emerged as drivers of this functional rewiring. Pharmacological inhibition of SYK or BCAA catabolism blunted iron-deficiency-induced erythrophagocytic and mitochondrial adaptations of RPMs. Together, these findings reveal a non-canonical metabolic reprogramming of RPMs that enhances their specialized clearance functions during systemic iron scarcity, raising possiblity that similar signaling circuits may operate in other efferocytic macrophage subsets under altered ferroportin-SYK axis activity.

Introduction

Efficient clearance of apoptotic cells, termed efferocytosis, is fundamental to tissue homeostasis and the prevention of inflammation by averting the release of potentially damaging intracellular components into the surrounding microenvironment[1–4]. Macrophages, the primary phagocytes responsible for efferocytosis, undergo profound metabolic reprogramming to sustain this process[5]. Lipid metabolite-driven receptor activation (e.g., PPARδ, LXR) promotes continual efferocytosis[6–8] coupled with enhanced glycolysis[9,10], fatty acid oxidation[11], mitochondrial respiration and dynamics[12,13], and an upregulated pentose phosphate pathway[14,15,61]. Among amino acids, the metabolism of arginine [via arginase 1 (ARG1) and ornithine decarboxylase (ODC1)][16], methionine (leading to modulation of DNA methylation)[17], tryptophan [by indoleamine 2,3-dioxygenase 1 (IDO1)][18], and glutamine [via glutaminase-1 (GLS1)-mediated glutaminolysis][19] have well-characterized roles in regulating macrophage function during efferocytosis. However, a critical gap remains in our understanding of how diverse metabolic changes are integrated and regulated across macrophage subsets and specialized efferocytic processes. In particular, very little is known about the metabolic or signaling control of erythrophagocytosis (EP), the process of clearing physiologically aged or damaged red blood cells (RBCs), which is predominantly carried out by red pulp macrophages (RPMs) in the spleen[20–22]. As RBCs constitute the body's largest iron store, their efficient removal and subsequent iron recovery are critical for supporting erythropoiesis[21,22]. Upon engulfment, RBCs are processed within phagolysosomes, releasing heme, which is catabolized by heme oxygenase 1 (HO-1) into ferrous iron (Fe^{2+}) that feeds the cellular labile iron pool (LIP). Within RPMs, iron from the LIP is either stored within ferritin or exported via ferroportin (FPN) to replenish circulating transferrin-bound iron. The iron export capacity of FPN is tightly regulated by hepcidin, a liver-derived hormone that provokes occlusion and/or degradation of FPN, thus ensuring systemic iron homeostasis[23–25]. The central role of RPMs in the maintenance of iron homeostasis is underscored by the functional attenuation in RBC clearance, accompanied by progressive splenic iron accumulation, observed in mice lacking genes essential for RPM development and during physiological aging[26–28]. Emerging evidence indicates that EP is regulated by such factors as pro-inflammatory signals[29–31], the mechanosensitive channel PIEZO1[32] via calcium (Ca^{2+}) signaling[27,32], and iron accumulation[27]. How these or other factors interact to fine-tune EP in response to varying physiological demands, particularly in states of altered iron bioavailability, remains a key unanswered question.

The critical nature of the RPM-driven recycling system takes on new significance in the face of the global burden of iron deficiency, the main cause of anemia, which impacts approximately 1.8 billion people (approximately 30% of the population)[33–36]. According to the 2021 Global Burden of Disease study, anemia ranks as the third leading contributor to years lived with disability worldwide, and, despite its multifactorial origins, dietary iron deficiency remains the primary cause[35,37]. Critically, the prevalence of iron deficiency itself significantly exceeds that of clinically diagnosed anemia and represents a crucial intersection between cellular iron metabolism and public health outcomes, particularly in resource-constrained developing regions[36–38]. Yet, the specific cellular vulnerabilities and the molecular mechanisms orchestrating adaptation to iron deficiency, including those operating within iron-recycling splenic RPMs, remain poorly defined.

Here, we demonstrate that RPMs in iron-deficient (ID) mice exhibit enhanced EP, and we explore how this functional adjustment is regulated by cellular signaling and metabolic rewiring. We reveal that the hepcidin-FPN axis, via regulating Ca^{2+} and spleen tyrosine kinase (SYK) signaling, enhances the EP capacity of RPMs together with their mitochondrial respiration to optimize iron recycling during iron deficiency. Furthermore, we show that RPMs uniquely rely on efficient catabolism of branched-chain amino acids (BCAAs), rich in RBCs, to enhance their EP capacity, and that this metabolic requirement remains under the control of high FPN and SYK. In sum, our findings highlight novel signaling and metabolite-driven mechanisms that shape the functional plasticity of RPMs during limited iron supplies. These insights not only deepen our understanding of RPM biology but may also inform how other macrophage populations adapt to metabolic stress or iron fluctuations in diverse physiological and pathological contexts.

Results

Nutritional iron deficiency increases the EP capacity of RPMs

To investigate the impact of low systemic iron availability on EP and, more broadly, the iron-recycling capacity of RPMs, we employed a murine model of nutritional iron deficiency. To this end, four-week-old female mice were subjected to either an ID diet (<5 ppm iron) or an iron-balanced (IB) control diet (200 ppm iron) for five weeks. Dietary iron restriction resulted in significantly decreased splenic (Figure 1A) and hepatic (Figure 1B) non-heme iron concentrations in the ID group compared to the IB group, confirmed by reduced iron deposition within the splenic red pulp via Perl's staining (Figure S1A). A subtle but significant reduction in cardiac (Figure S1B)

non-heme iron was also observed in the ID group, while muscle (Figure S1C) tissue iron content remained unaffected. These data suggested a tissue-specific response to dietary iron restriction, with the spleen and the liver, the organs for iron recycling and storage, being the most affected. Consistent with limited iron delivery, transferrin saturation (Figure 1C) was markedly reduced in ID mice, leading to mild microcytic hypochromic anemia (Figure 1D, S1D, and S1E), which hallmarks iron deficiency. Expectedly, ID mice displayed compensatory mechanisms manifested by splenic stress erythropoiesis, as evidenced by elevated serum erythropoietin (EPO) (Figure S1F) and increased percentage of splenic, but not bone marrow, $CD71^{+}/TER119^{+}$ progenitor cells (Figure 1E and S1G).

Next, we aimed to precisely characterize cell-intrinsic iron parameters of RPMs in response to iron-restricted feeding. Consistent with the drop in serum levels of the iron-regulatory hormone hepcidin (Figure 1F), FPN expression in RPMs was significantly elevated in ID mice, as shown by F4/80 immunofluorescence in splenic red pulp and by flow cytometric analysis of $F4/80^{high}$ $CD11b^{dim}$ RPMs[27] (Figure 1G and 1H). In agreement with boosted iron-export capacity, a marked decrease in total iron content was observed in the magnetically sorted RPMs from ID mice (Figure 1I), along with reduced protein expression of both L- and H-ferritin as assessed by flow cytometry (FTL and FTH1; Figure 1J and 1K), indicating depletion of intracellular iron stores. Furthermore, we detected upregulated levels of transferrin receptor 1 (TFR1) surface expression (Figure 1L), implying a cellular response to iron deficiency. However, paradoxically, despite enhanced iron export, RPMs in ID mice unexpectedly displayed a mild but significant elevation of LIP, as assessed using the Fe^{2+}-specific fluorescent probe FerroOrange (Figure 1M). Consistent with this finding, we also detected mildly elevated reactive oxygen species (ROS) levels in RPMs of ID versus IB mice (Figure 1N).

Intrigued by the increased LIP in RPMs of ID mice, we investigated the capacity of EP, the major route for RPM iron acquisition. To this end, following well-established procedures[27,39], we transfused mice with PKH67-labeled RBCs. Strikingly, flow cytometry analysis revealed significantly enhanced phagocytosis of temperature-stressed RBCs (sRBC) by RPMs from ID compared to IB mice, a phenomenon not observed for non-stressed fresh RBCs that were engulfed at comparably negligible levels (Figure 1O). In addition, we evaluated EP capacity across other myeloid populations, including Kupffer cells (KCs) in the liver, macrophages in the bone marrow, and circulating monocytes (Figure 1O). Among these, only KCs showed a statistically significant,

albeit modest, increase in EP capacity in iron-restricted mice. Previous work has shown that splenic red pulp sinuses trap aged RBCs, leading to partial hemolysis and subsequent phagocytosis of membrane remnants (RBC ghosts) by RPMs[40]. To distinguish between the clearance of intact sRBCs and RBC ghosts in our model, we intravenously injected mice with sRBCs ubiquitously expressing GFP and stained with PKH26 membrane dye, as described previously[41]. Consistent with our prior results, RPMs from ID mice exhibited increased EP of GFP^+ $PKH26^+$ and GFP-$PKH26^+$ sRBCs compared to control IB animals, confirming their enhanced capability for the uptake of both intact RBCs and RBC ghosts (Figure 1P). Likewise, splenic clearance of transfused GFP-positive sRBCs was accelerated in ID mice compared to IB controls (Figure 1Q), further supporting enhanced sRBC removal by RPMs within the low-iron splenic microenvironment. To validate sRBC transfusion assay results, we next assessed intracellular levels of the erythrocyte marker TER119 in RPMs as a measure of endogenous EP capacity[27,42], confirming its elevation in ID mice (Figure 1R). Finally, we verified whether increased EP in low-iron mice is solely driven by macrophage-intrinsic mechanisms or could result from erythrocyte-derived signals. RBC lifespan remained comparable between IB and ID mice (Figure 1S), suggesting that iron restriction did not compromise RBC integrity. Next, exposure of the apoptotic cell marker phosphatidylserine in splenic RBCs was not enhanced in ID compared to IB mice (Figure 1T). Finally, using a co-culture assay of magnetically isolated splenic and circulating RBCs with primary macrophages, we found that while aged splenic RBCs are preferentially sequestered compared to circulating RBCs (Figure 1U), iron deficiency does not increase splenic RBC susceptibility to phagocytosis (Figure 1V), implying no induction of RBC "eat-me" signals by iron restriction. Taken together, we uncovered that systemic iron restriction potentiates the cell-intrinsic RBC clearance capacity of RPMs, likely aimed at balancing the increased replenishment of the plasma iron pool by FPN-mediated export.

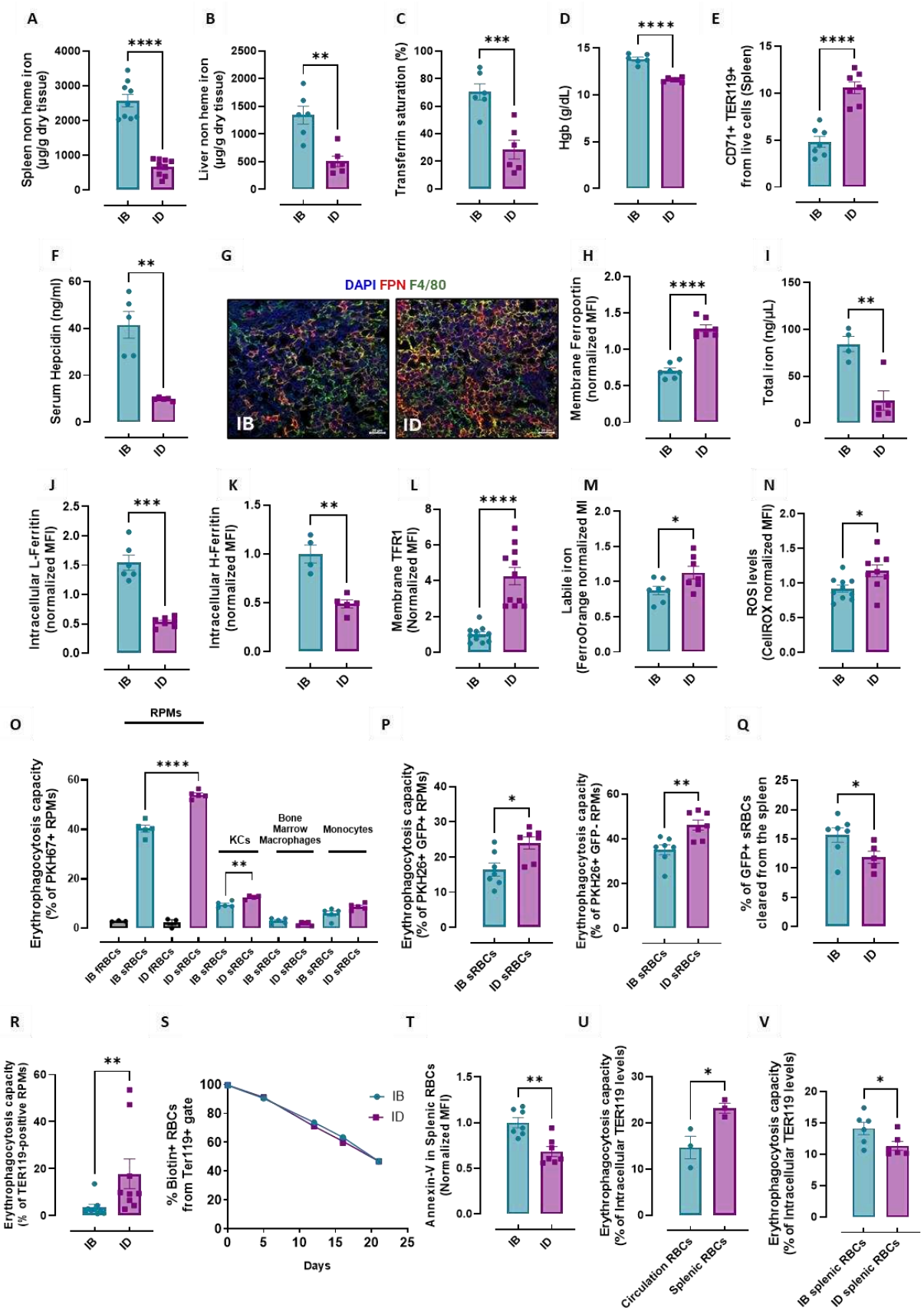

Figure 1. Nutritional iron deficiency increases the erythrophagocytic capacity of RPMs.

(A) Spleen and (B) liver non-heme iron levels, (C) plasma transferrin saturation, and (D) blood hemoglobin (Hgb) were measured in iron-balanced (IB) and iron-deficient (ID) mice. (E) Shown is the percentage of erythroid progenitor cells ($TER119^+$ $CD71^+$) present in the spleen of IB and ID mice. (F) Serum hepcidin levels were measured in IB and ID mice with the Hepcidin-Murine Compete ELISA Kit. (G) Representative confocal microscopy images of ferroportin (FPN) protein localization in the splenic red pulp of IB and ID mice. Frozen spleen slices were processed and stained for RPMs (F4/80, green), FPN (red), and nuclei (blue). (H) Expression of FPN on the cell membrane of RPMs derived from IB and ID mice, gated as $F4/80^{high}$, $CD11b^{dim}$, was assessed by flow cytometry. (I) The total intracellular iron content in magnetically sorted RPMs from IB and ID mice was assessed using the Iron Assay Kit. (J) Intracellular L-ferritin and (K) H-ferritin protein levels in RPMs of IB and ID mice were quantified by flow cytometry. (L) Expression of TFR1 on the cell membrane of RPMs derived from IB and ID mice was assessed by flow cytometry. (M) Cytosolic ferrous iron (Fe^{2+}) levels in RPMs of IB and ID mice were measured using the FerroOrange probe with flow cytometry. (N) The cytosolic ROS levels in RPMs of IB and ID mice were assessed by determining CellROX Deep Red fluorescence intensity with flow cytometry. (O) The erythrophagocytosis (EP) capacity in RPMs and other myeloid populations of IB and ID mice was determined using flow cytometry by measuring the percentage of cells that phagocytosed transfused PKH67-labeled RBCs. fRBCs indicate fresh RBCs, sRBCs - stressed RBCs (shown only for RPMs; in other indicated populations, fRBCs uptake was negligibly low). (P) IB and ID mice were transfused with GFP-expressing and PKH26-stained sRBCs. The percentage of RPMs positive for intact RBCs ($PKH26^+GFP^+$) and RBC ghosts ($PKH26^+GFP^-$) was determined. (Q) Flow cytometric analysis of splenic GFP-sRBC percentage in ID vs IB mice. (R) The endogenous EP capacity of RPMs derived from IB and ID mice was determined by intracellular staining of the RBC marker TER119 in RPMs and flow cytometry. (S) The RBC biotinylation lifespan assay was performed on circulating RBCs from IB and ID mice. (T) Flow cytometry assessment of phosphatidylserine exposure (Annexin V staining) in splenic RBCs of ID vs IB mice. (U) EP capacity by primary cultured macrophages (iRPM) was determined using splenic and circulating RBCs of IB mice. (V) EP capacity of iRPMs exposed to RBCs derived from the spleens of IB and ID mice. Each dot represents one mouse or an independent cell-based experiment. Each dot in the graph (S) represents n=9. Data are represented as mean ± SEM. Welch's unpaired t-test determined statistical significance between the two groups. ns $p>0.05$, *$p<0.05$, **$p<0.01$, ***$p<0.001$ and ****$p<0.0001$.

Iron deficiency drives metabolic reprogramming and enhanced lysosomal activity of RPMs via the non-canonical type of polarization

To decipher the molecular mechanisms of enhanced EP capacity in RPMs of ID mice and explore potential accompanying functional changes, we first investigated the transcriptome of FACS-isolated RPMs. Surprisingly, only 145 genes were differentially expressed between RPMs derived from ID and IB mice (Figure 2A, Table S1). Bioinformatic analysis revealed significant enrichment of cell cycle regulators (e.g., *Mki67, Plk1, Plk2, Aurka, E2f7, Sgo1, Kif4, Cenpf, Bub1, Ccnb1, Ccnb2*) among genes upregulated by iron deficiency. This suggested increased pro-mitotic signaling in RPM of ID mice, which was corroborated by elevated protein levels of the proliferation marker Ki67 (Figure 2B). However, this response was not reflected by any significant change in the representation of total RPMs within $CD45^+$ splenic cells (Figure 2C). Likewise, using the Ms4a3Cre-RosaTdT reporter mice[43], we found no significant differences in the relative

representation of residual embryonically-derived RPMs within the RPM population (Figure 2D), suggesting the absence of their proliferation. The percentage of monocyte-derived RPMs also remained constant at approximately 15% in both IB and ID mice (Figure 2D), implying that the EP enhancement was not driven by *de novo* monocyte recruitment.

To further explore the adaptation of RPMs to systemic iron deficiency, we employed TMT-based quantitative proteomics of magnetically-sorted F4/80-high RPMs. This analysis identified 420 proteins significantly more abundant and 282 decreased in RPMs of ID mice compared to IB mice (Figure 2E, Table S2). Confirming the quality of the proteomics analysis, we found FTH1 and FTL as the top downregulated hits, and TFR1 as the most induced protein in RPMs of iron-restricted mice. Consistent with this expression pattern, IRP2, a regulator of cellular iron balance, was stabilized in RPMs of ID mice. In agreement with RNA-seq data, we also detected an increase in several regulators of cell cycle progression, such as AURKA, AURKB, PLK1, and CDK1 in RPMs of low-iron mice. Intriguingly, proteomic analysis revealed a pronounced functional rewiring of RPMs in ID mice, highlighting significant post-transcriptional regulation, with far more protein-level alterations and minimal overlap between transcriptomic and proteomic datasets (Figure 2F). First, we observed upregulation of the phosphatidylserine-recognizing phagocytic receptors MERTK and TIM4 (significant hits), and a trend towards induction of AXL and STAB2, along with the Fc receptor CD16 in RPMs of ID mice, responses that were all confirmed by flow cytometry (Figure 2G-H, Figure S2.1A-C). Interestingly, this elevated capacity for recognizing "eat me" signals was accompanied by the induction of the "don't eat me" receptor SIRPα on RPMs in ID mice (Figure S2.1D), hinting at a mechanism that promotes the clearance of aged dysfunctional RBCs, sparing those that are intact. Next, to gain unbiased insights into processes supporting the enhanced EP capacity of RPMs in ID mice, we performed functional enrichment analyses on the differentially expressed proteins. Notably, mitochondrial proteins emerged as the most significantly enriched category among hits upregulated in RPMs of ID compared to IB mice (Figure 2I), including factors involved in ATP synthesis (ATP5S), metabolite transport (SLC25A5, VDAC1), mitochondrial protein import (SAMM50), iron-sulfur cluster assembly (SFXN2), cristae remodeling (MCCC1, PMPCB), and coenzyme Q-10 biosynthesis (COQ9, COQ5). Flow cytometric analysis confirmed these expanded mitochondrial functions by demonstrating a significant increase in both mitochondrial membrane potential (a proxy for mitochondrial activity) (Figure 2J) and mitochondrial mass (Figure 2K) in RPMs of ID mice. Consistently, RPMs of ID

versus IB mice exhibited increased uptake of fluorescently labeled glucose analog (Figure 2L) and showed a significant upregulation of protein synthesis (Figure 2M), a major ATP-consuming process reflective of enhanced cellular bioenergetics. Interestingly, ATP levels in FACS-sorted RPMs revealed a mild depletion in ID compared to IB mice (Figure 2N), but the activation status of AMPK, a key sensor of cellular energy stress, was not enhanced (Figure 2O). This suggests that RPMs of ID mice did not exhibit energy deficit, but rather a state where increased ATP production is insufficient to meet the high ATP demand driven by accelerated EP and protein synthesis. Importantly, in contrast to RPMs, neither peritoneal macrophages (not involved in iron recycling) nor iron-recycling KCs show hallmarks of metabolic rewiring in ID mice, as exemplified by unaltered mitochondrial activity and mass (Figure S2.1E-H).

Further analysis of the proteomic data revealed another major category, encompassing proteins associated with lysosomal functions, as enriched in RPMs of ID compared to IB mice (Figure 2I). In total, RPMs of iron-restricted mice increased the protein levels of 25 key components of the Coordinated Lysosomal Expression and Regulation (CLEAR) network, a transcriptional program that drives lysosomal biogenesis and function[44] (Figure S2.2A). This included integral lysosomal membrane proteins, LAMP1 and LAMP2, vacuolar ATPase subunits (ATP6V0D1, ATP6V0A1), essential for lysosomal acidification, and a diverse array of lysosomal hydrolases, including cathepsins B, D, and S; α-glucosidase (GAA); β-glucosidase (GBA); N-acetylglucosaminidase (NAGA); and sialidase 1 (NEU1). Flow cytometric analysis confirmed elevated intracellular LAMP1 levels (Figure 2P), indicating increased lysosomal mass in RPMs of ID mice. Consistent with this, we observed enhanced lysosomal activity in RPMs of ID mice using a fluorescent probe (Figure 2R). Further ultrastructural analysis of RPMs within splenic sections with TEM revealed that while the number of regular lysosomes, autophagolysosomes, autophagosomes, and peroxisomes remained unaltered between control and low-iron mice, large lysosomes were more abundant in RPMs of iron-restricted mice (Figure S2.2B and S2.2C). While lysosomal size is dynamic and influenced by nutrient availability, emerging evidence, for instance, from senescent cells suggests that a higher proportion of enlarged lysosomes correlates with increased proteolytic activity and lysosomal mass[45,46], remaining consistent with our observations. Taken together, these data suggest that enhanced lysosomal function in RPMs of ID mice is coordinated with heightened RBC clearance, extending the spectrum of RPMs reprogramming in iron deficiency.

Erythrocytic heme and iron loading, as well as systemic or cell-intrinsic iron deficiency, have been shown to influence macrophage polarization, promoting either pro-inflammatory or anti-inflammatory profiles, though findings have often been contradictory[47–50]. Since metabolic reprogramming is closely linked to macrophage polarization, which in turn shapes the outcome of infections and inflammatory diseases[51], we assessed the polarization state of RPMs from iron-restricted mice. Our RNA-seq and proteomics data revealed no clear induction of either pro- or anti-inflammatory mediators, alongside a mixed expression pattern of surface signals identified by flow cytometry. While some markers typically associated with M1 (MHCII, CD74) and M2 (CD206) polarization were decreased in RPMs of ID *versus* IB mice, others, such as the pro-inflammatory CD38 and the anti-inflammatory CD163, were increased (Figure S2.3). This atypical combination of features suggests that augmented RBC clearance in nutritionally iron-restricted mice leads to the activation state of RPMs distinct from the canonical M1 or M2 type of profile.

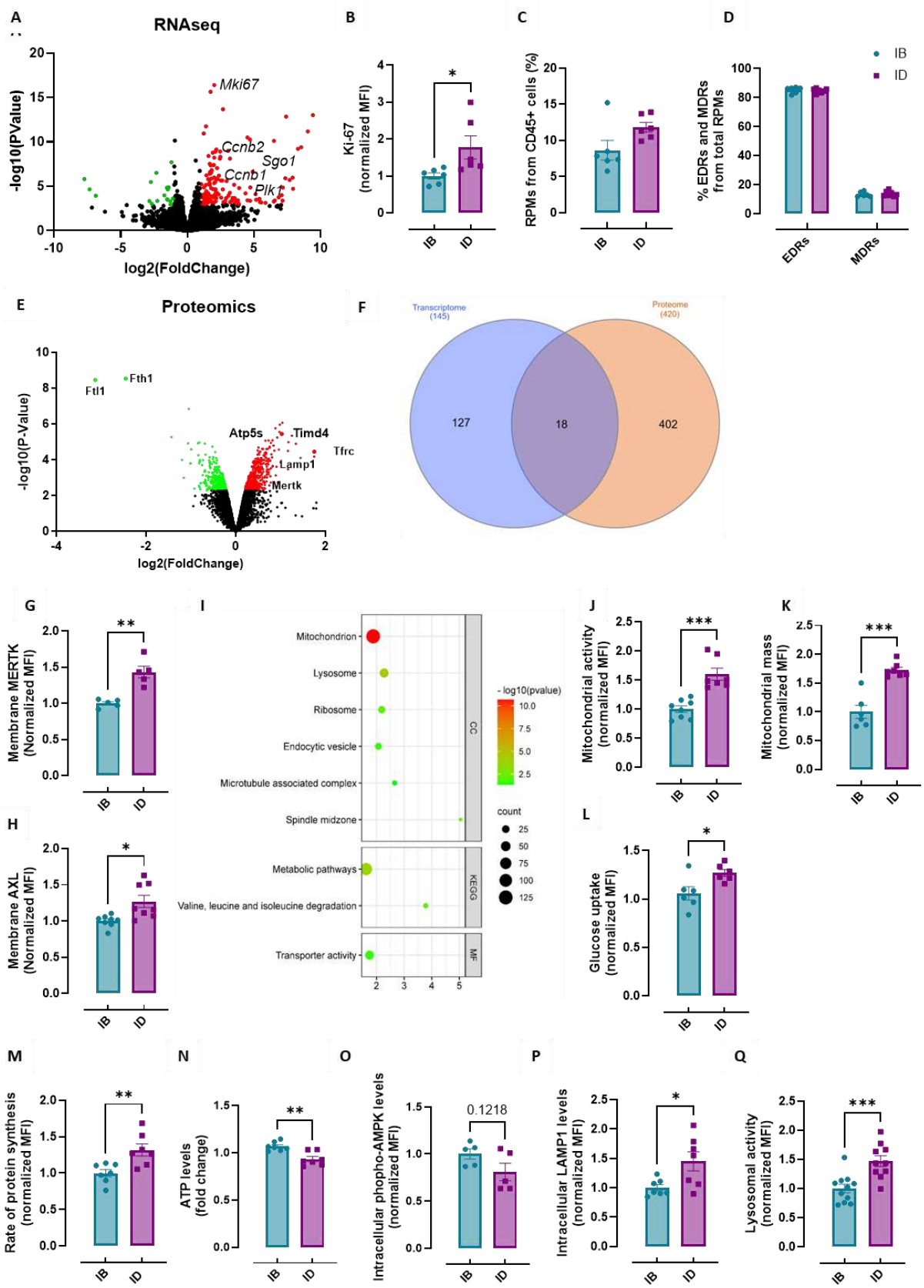

232

Figure 2. Iron deficiency drives metabolic reprogramming and enhanced lysosomal activity of RPMs.

(A) A volcano plot of differentially regulated genes identified by the RNA-Seq transcriptomic analysis in FACS-sorted RPMs derived from IB and ID mice. (B) Intracellular Ki-67 protein levels in RPMs derived from IB and ID mice were assessed by flow cytometry. (C and D) Percentage of (C) total RPMs and (D) embryonic-derived RPMs (EDRs) and monocyte-derived RPMs (MDRs) among total RPMs in IB and ID mice. (E) Volcano plot visualizing the proteomic landscape of RPMs in response to iron deficiency, depicting differentially expressed proteins in IB and ID mice. (F) Venn diagram comparing the differentially expressed genes (transcriptome) and proteins (proteome) in RPMs from ID mice. (G and H) Cell membrane expression levels of (G) MERTK and (H) AXL of RPMs in IB and ID mice were determined by using fluorescently labeled antibodies and flow cytometry. (I) Enriched functional categories among significantly increased protein hits in magnetically sorted RPMs derived from ID versus IB spleen. (J) Mitochondrial membrane potential/activity and (K) mitochondrial mass were determined in RPMs derived from IB and ID mice using TMRE probe and MitoTracker Green, respectively, with flow cytometry. (L) Quantification of glucose uptake via flow cytometry in RPMs from IB and ID mice using a fluorescent glucose analog. (M) Flow cytometric detection of newly synthesized proteins in RPMs of IB and ID mice using Click-iT Plus OPP Alexa Fluor 488 Protein Synthesis Assay. (N) Quantification of ATP levels in FACS-sorted RPMs (10,000 cells) from IB and ID mice using a chemiluminescence-based assay. (O) Intracellular phosphorylated AMPK protein levels in RPMs derived from IB and ID mice were assessed by flow cytometry. (P) Intracellular expression levels of the core lysosomal protein LAMP1 in RPMs of IB and ID mice were determined by flow cytometry. (Q) Flow cytometric assessment of lysosomal activity in RPMs of IB and ID mice using the Lysosomal Intracellular Activity Assay Kit. Each dot represents one mouse. Data are represented as mean ± SEM. Welch's unpaired t-test determined statistical significance between the two groups. ns $p>0.05$, *$p<0.05$, **$p<0.01$, ***$p<0.001$ and ****$p<0.0001$.

Low hepcidin levels are critical for functional adaptations of RPMs during iron deficiency

To elucidate the mechanisms driving the enhanced EP capacity of RPMs in iron deficiency, we first investigated whether these adaptations were directly dependent on intracellular iron levels. Iron depletion *in vitro* using deferiprone (Figure 3A) or DFO[27] did not alter the RBC clearance capacity of primary BMDM macrophages cultured with hemin (iRPM)[27]. Furthermore, our *in vivo* data demonstrated that despite systemic iron deficiency, RPMs in ID mice exhibited elevated LIP (Figure 1M), likely due to their increased EP activity, indicating that iron chelation *in vitro* might not fully recapitulate the complex cellular interactions and signaling pathways present in RPMs *in vivo*. These findings suggested that factors beyond simple iron availability may be critical drivers of enhanced RPM phagocytic activity during iron deficiency. To address this possibility mechanistically, we developed an *in vitro* system using iRPMs cultured in serum derived from IB and ID mice, instead of bovine serum. This system recapitulated increased FPN and TFR1 expressions in iRPMs exposed to ID serum, without a significant change in total iron levels (Figure 3B-D). Notably, cells cultured in ID serum exhibited enhanced EP (Figure S3A), suggesting that serum-borne factor is sufficient to rewire the phagocytic capacity of iRPMs towards RBCs. We first excluded the contribution of EPO, the cytokine previously implicated as a stimulator of efferocytosis[52]. We showed that iRPMs, in contrast to BMDMs cultured without hemin, which is

critical to mimic the heme and iron-rich nature of RPMs, did not enhance EP even under high EPO doses (Figure S3B-C). Moreover, PPARγ, a factor proposed to act downstream of EPO[52], failed to alter the EP capacity of iRPMs (Figure S3C). Next, inspired by a study that revealed low hepcidin, rather than iron deficiency itself, as a key driver of pro-inflammatory responses in iron-restricted mice[50], we hypothesized that reduced serum hepcidin levels and enhanced FPN stabilization in RPMs might play a critical role in the adaptive reprogramming of these cells. Strikingly, a 4-h treatment with the hepcidin mimetic PR73 reversed the enhanced EP phenotype in iRPMs exposed to ID, but not to IB serum (Figure 3E and S3D). Likewise, we conducted live imaging of EP by cultured iRPMs incubated with serum from IB and ID mice, and exposed to sRBCs labeled with a dedicated pHrodo™ dye that remains non-fluorescent at neutral pH but emits fluorescence in acidic environments, indicating sequestrations in phagolysosomes. In line with our flow cytometry results, we observed enhanced pHrodo signal in real time in iRPMs treated with ID serum, reflecting their enhanced EP capacity (Figure 3F). This boost of RBC clearance capacity was significantly abrogated upon 4 h of PR73 treatment (Figure 3F). Consistent with our *in vivo* observations, ID serum induced a significant increase in both mitochondrial and lysosomal activity, which was likewise abrogated by PR73 treatment (Figure S3E-H).

To follow these *in vitro* observations, we next administered IB and ID mice with PR73 via intraperitoneal injection 4 h before analysis. PR73 administration effectively reduced cell-surface FPN expression and induced hypoferremia in both dietary groups (Figure 3G-H). However, total RPM iron content remained unchanged in both IB and ID mice following PR73 treatment (Figure 3I). PR73 administration did not reverse the increased cell surface expression of TFR1 on RPMs of ID mice but instead led to its further elevation, in contrast to IB mice, where TFR1 levels remained unaltered (Figure 3J). Interestingly, PR73 elicited similarly distinct effects on the LIP in RPMs depending on the dietary regimen: it expectedly increased LIP levels in IB mice, but led to a mild decrease in ID mice (Figure 3K). The latter pattern was, strikingly, closely reflected by the pronounced reversal of the elevated EP capacity of RPMs from ID mice by PR73 injection (Figure 3L). Likewise, PR73 abrogated most of the other hallmarks of RPM adaptation to iron deficiency, including elevated mitochondrial activity, increased glucose uptake, and heightened protein synthesis (Figure 3M-O). Intriguingly, these modulating effects of PR73 were absent in IB mice. Furthermore, *ex vivo* freshly isolated RPMs exhibited substantially elevated oxidative phosphorylation (OXPHOS), as assessed by oxygen consumption rate measurement with Seahorse

(Figure 3P). Strikingly, a 4-h preincubation of the *ex vivo* RPMs of ID mice with PR73 completely abolished their activated oxygen consumption (Figure 3P). Of note, these rapid effects of PR73 did not include changes in the mitochondrial mass of RPMs, remaining elevated regardless of PR73 injection in ID mice (Figure S3I). Similarly, lysosomal activity of RPMs of ID mice remained higher than in IB mice despite PR73 supplementation, suggesting either distinct regulatory mechanisms or differential kinetics governing these responses (Figure S3J). To support the key role of the hepcidin-FPN axis in modulating the iron-recycling activity of RPMs, we employed *Tmprss6* knockout (KO) mice, a model of iron-refractory iron deficiency anemia (IRIDA)[53–55]. This model exhibits some characteristics of the nutritional ID model, including reduced transferrin saturation, decreased hepatic iron stores (Figure S3K-L), and anemia. However, in contrast to dietary ID conditions, *Tmprss6* KO mice display elevated hepcidin levels, and their splenic iron stores remain largely unchanged[56,57], with no significant depletion observed, consistent with our findings (Figure S3M). Importantly, we observed no significant difference in RPMs' EP capacity between *Tmprss6* KO mice and wild-type controls (Figure 3Q). Likewise, *in vitro* cultured iRPMs showed no difference in RBC clearance when exposed to serum from either *Tmprss6* KO or wild-type mice (Figure 3R). In sum, these data implied that deficient hepcidin levels and FPN stabilization, hallmarks of nutritional ID, are key driving factors for enhanced RPM erythrophagocytic capacity and their metabolic adaptation to low systemic iron levels.

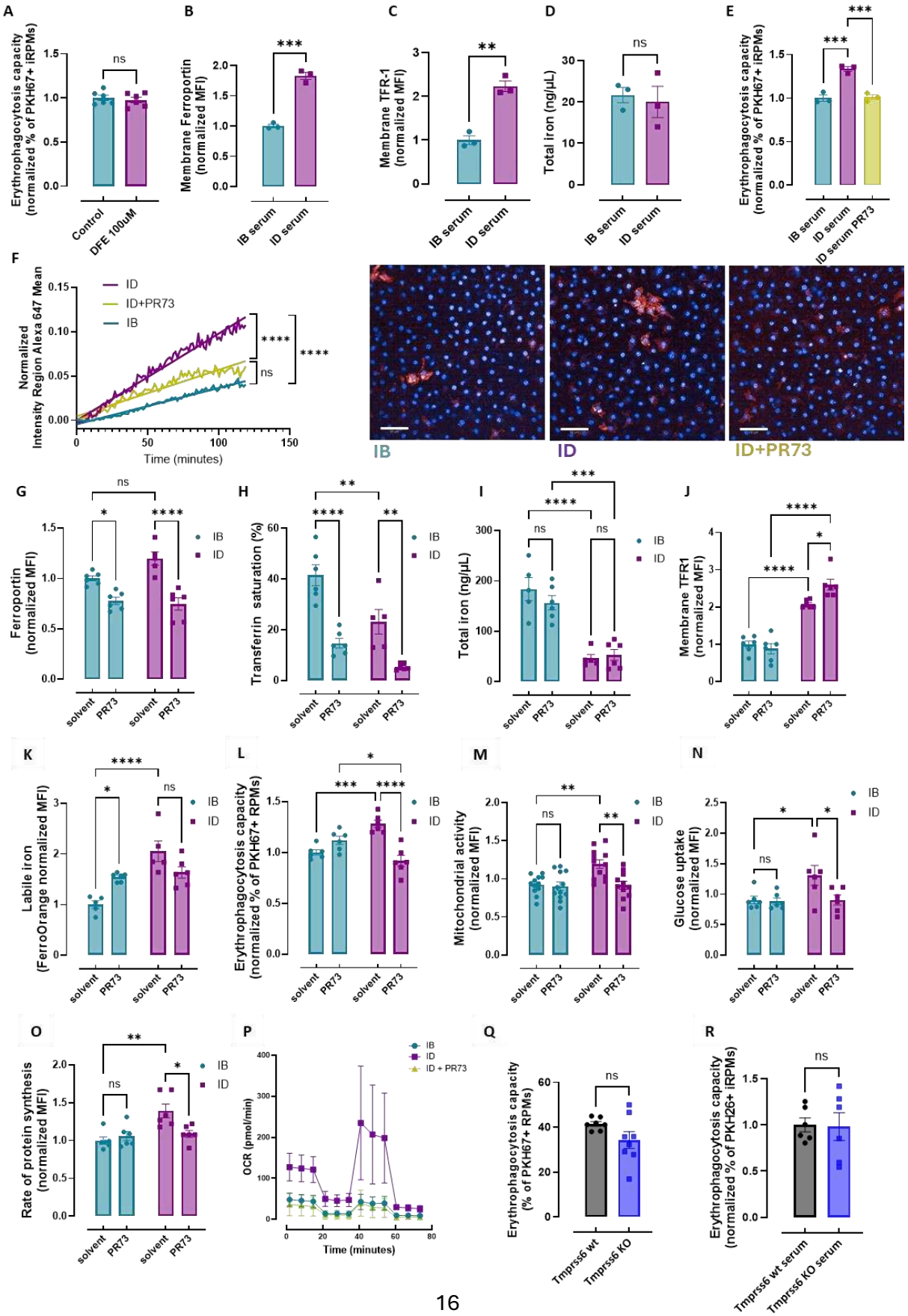

Figure 3. Low hepcidin levels are critical for functional adaptations of RPMs during iron deficiency. (A) Normalized EP capacity of PKH67-stained sRBCs by cultured iRPMs treated with an iron chelator DFE (100 µM, 18 h). (B-C) Flow cytometry analysis of (B) surface FPN and (C) TFR1 expression on iRPMs cultured with serum from IB or ID mice. (D) The total intracellular iron content in iRPMs cultured with serum from IB or ID mice was assessed using the Iron Assay Kit. (E) The EP capacity in iRPMs cultured with serum from IB or ID mice, and serum from ID mice supplemented with the hepcidin agonist PR73 (2 µg/mL, 4 h) determined using flow cytometry by measuring the percentage of cells that phagocytosed PKH67-labeled RBCs. (F) Time-lapse imaging of the EP progression in iRPMs, exposed to pHrodo-stained sRBCs and cultured with the serum from IB and ID mice (with and without 4 h pretreatment with PR73). The left panel shows the quantification of the RBC fluorescent signal over time, normalized to the number of macrophages. The right panel shows example images at the endpoint of the assay. Scale bar=50 µm. (G) Flow cytometric analysis of FPN cell surface expression on RPMs from IB and ID mice following intraperitoneal administration of the hepcidin agonist PR73 (50 nmol/mouse, 4 h). (H) Plasma transferrin saturation was determined in IB and ID mice following PR73 administration. (I) Intracellular iron content in magnetically sorted RPMs from IB and ID mice post-PR73 treatment as determined using the Iron Assay Kit. (J) Flow cytometric evaluation of TFR1 surface expression on RPMs derived from IB and ID mice post-PR73 administration. (K) Flow cytometric measurement of cytosolic ferrous iron (Fe^{2+}) levels in RPMs from IB and ID mice using FerroOrange following PR73 administration. (L) Normalized EP capacity of PKH67-sRBCs by RPMs from IB and ID mice after PR73 administration. (M) Mitochondrial activity was determined in RPMs derived from IB and ID mice using the TMRE probe post-PR73 administration, with flow cytometry. (N) Quantification of glucose uptake via flow cytometry in RPMs from IB and ID mice upon PR73 administration using a fluorescent glucose analog. (O) Flow cytometric detection of newly synthesized proteins in RPMs of IB and ID mice using Click-iT Plus OPP Alexa Fluor 488 Protein Synthesis Assay after PR73 administration. (P) Seahorse analysis of *ex vivo* RPMs from IB and ID mice, with or without 4 h PR73 preincubation for RPMs from ID mice. (Q) Flow cytometric assessment of EP capacity in RPMs of *Tmprss6* wt and *Tmprss6* KO mice was quantified as the percentage of cells engulfing PKH67-labeled sRBCs. (R) Normalized EP capacity of PKH26 sRBCs by cultured iRPMs treated with serum from *Tmprss6* wt and *Tmprss6* KO mice was determined using flow cytometry. Each dot represents one mouse or an independent cell-based experiment. Data are represented as mean ± SEM. Welch's unpaired t-test determined statistical significance in A-D and Q-R, while two-way ANOVA with Tukey's Multiple Comparison tests was used in G-O. A one-way ANOVA test with Dunnett's or Tukey's Multiple Comparison tests was used in E. In F, the significant differences between the slopes of simple linear regression lines are shown. ns $p>0.05$, *$p<0.05$, **$p<0.01$, ***$p<0.001$ and ****$p<0.0001$.

Elevated FPN regulates RPM rewiring in ID conditions via Ca^2-dependent signaling

To further assess the role of FPN upregulation in RPM rewiring under systemic ID conditions, we used lentiviral transduction to create iRPMs with enforced FPN overexpression (FPN OE; FPN-iRPMs) and assessed whether this mimics RPM adaptation to iron deficiency. Control iRPMs were generated using an empty vector without the *Slc40a1* gene, encoding FPN (mock-iRPMs). We confirmed significant FPN elevation on the surface of FPN-iRPMs compared to control cells (Figure 4A). This further led to the elevation of TFR1 surface expression but did not significantly change the total iron levels (Figure 4B-C), thus resembling the iRPMs exposed to ID vs IB serum. Under basal conditions, we quantified the LIP in both FPN-iRPMs and mock-iRPMs, finding no significant difference (Figure 4D). In an attempt to recapitulate the mildly elevated LIP observed in RPMs of ID mice during enhanced *in vivo* EP, we next sought to mimic the splenic

microenvironment by continuously exposing iRPMs to sRBCs during culture. Strikingly, sRBC-exposed FPN-iRPMs exhibited a significant increase in LIP compared to mock-iRPMs (Figure 4D), mirroring the *in vivo* RPM response (Figure 1M). Most importantly, FPN-iRPMs displayed enhanced RBC clearance regardless of sRBC exposure during culture (Figure 4E), a response that was efficiently reversed by suppression of FPN by a potent specific inhibitor vamifeport[58] (Figure 4F). These findings demonstrate that forced FPN expression and consequent increased cellular iron flux, rather than overall iron content, specifically stimulate EP.

We next investigated in more detail the potential metabolic consequences of increased FPN expression. FPN overexpression led to a significant increase in both mitochondrial activity and mass compared to mock-transduced iRPMs in a manner that was likewise blocked by vamifeport (Figure 4G-H). This response was reflected by a vamifeport-controlled increase in glucose uptake and protein synthesis rate in FPN-overexpressing iRPMs (Figure 4I-J), suggesting a coordinated metabolic adaptation. Importantly, these responses were independent of the presence of sRBCs in the culture media and intracellular iRPM LIP levels (Figure S4A-D), indicating a regulatory effect of FPN on mitochondrial functions that may reach beyond its role as a regulator of intracellular iron status.

We next set out to elucidate the signaling mechanisms underlying the functional rewiring of RPMs in response to increased FPN expression during systemic iron deficiency. Our previous work demonstrated that age-related iron overload, likely due to low FPN expression, suppressed RPM's RBC clearance capacity[27]. This phenomenon was recapitulated in iron-loaded *in vitro* iRPMs and was reflected by reduced intracellular Ca^{2+} levels[27], a key regulatory signal for macrophage phagocytosis[32,59]. Extending this observation, we found a significant increase in intracellular Ca^{2+} levels within RPMs of ID mice compared to IB mice (Figure 4K), mirroring the enhanced RBC clearance capacity. Notably, PR73 administration reversed the elevated intracellular Ca^{2+} levels specifically in RPMs of ID mice, with no effect observed in RPMs of IB mice (Figure 4L). In parallel, iRPMs exposed to ID serum also displayed increased Ca^{2+} levels, a response likewise suppressed by PR73 treatment (Figure 4M). This demonstrates that intracellular Ca^{2+} signaling, like phagocytic and mitochondrial activities, is uniquely reprogrammed in RPMs of iron-deficient mice in a manner dependent on low hepcidin/high FPN. Consistently, FPN-iRPMs exhibited increased intracellular Ca^{2+} levels compared to mock-iRPMs, independent of the presence of stressed RBCs during culture and cellular LIP levels, further implying the role of Ca^{2+} signaling in

RPM functional rewiring driven by high FPN (Figure 4N). To further examine whether enhanced Ca^{2+} signaling may support increased EP in iRPMs, we employed both intracellular (BAPTA-AM) and/or extracellular (EGTA) Ca^{2+} chelators in the FPN-iRPM model and iRPMs exposed to ID and IB serum (Figure 4O-P). Both chelation strategies not only reduced the overall EP capacity of iRPMs but also effectively suppressed the enhancement of RBC clearance in FPN-high conditions. Recent findings implied that FPN may have the capacity for Ca^{2+} import[60]. To test whether FPN-mediated Ca^{2+} influx directly drives their functional rewiring, we employed overexpression of the FPN variant harboring a specific aspartate-to-alanine mutation (D39A), expected to disrupt the unidirectional movement of Ca^{2+} into the cell while preserving Fe^{2+} transport function[54]. Interestingly, we found no significant differences in the enhancement of EP or intracellular Ca^{2+} levels between iRPMs overexpressing mutant D39A and wild-type FPN (Figure 4Q-R). In sum, our findings suggested that FPN-mediated activation of Ca^{2+} signaling, likely through an indirect mechanism, contributes to enhanced phagocytic capacity of RPMs.

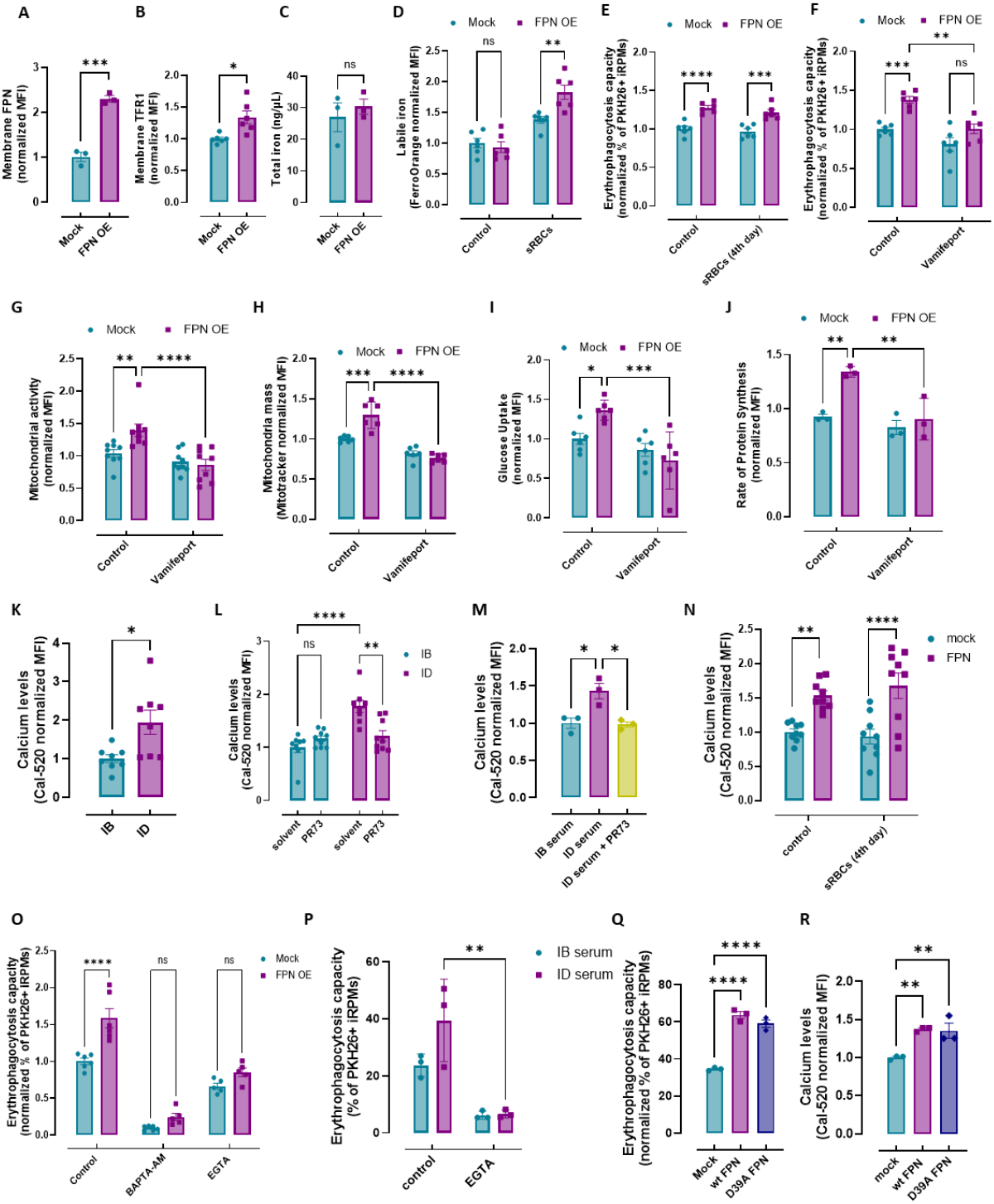

Figure 4. Elevated FPN regulates RPM rewiring in ID conditions via Ca²-dependent signaling.

(A-J) Lentiviral transduction was used to generate iRPMs overexpressing FPN (FPN OE; FPN-iRPMs) or expressing an empty vector (mock). (A-C) Flow cytometric analysis of (A) FPN and (B) TFR1 cell surface expression, and (C) intracellular iron content in mock and FPN-iRPMs determined using the Iron Assay Kit. (D) Flow cytometric measurement of cytosolic ferrous iron (Fe^{2+}) levels in mock and FPN-iRPMs with and

without sRBC exposure during culture. (E) Normalized EP capacity towards PKH26-sRBCs by mock and FPN-iRPMs with and without sRBC exposure during culture was determined with flow cytometry. (F-J) iRPMs were cultured with sRBCs and treated with vamifeport (20 μM, 15 h). (F) Normalized EP capacity towards PKH26-sRBCs was determined by flow cytometry. (G) Mitochondrial activity and (H) mass were determined by the TMRE and MitoTracker Green probes, respectively, and flow cytometry. (I) Quantification of glucose uptake via flow cytometry using a fluorescent glucose analog. (J) Flow cytometric detection of newly synthesized proteins using Click-iT Plus OPP Alexa Fluor 488 Protein Synthesis Assay and flow cytometry. (K) Cytosolic calcium iron (Ca^{2+}) levels in RPMs of IB and ID mice were measured using Cal-520 fluorescent probe with flow cytometry. (L) Cytosolic Ca^{2+} levels in RPMs of IB and ID mice were measured with flow cytometry post-PR73 administration using Cal-520 fluorescent probe with flow cytometry. (M) Cytosolic Ca^{2+} levels in iRPMs cultured with serum from IB or ID mice and serum from ID mice treated with the hepcidin agonist PR73 (2 μg/mL, 4 h) were determined using Cal-520 fluorescent probe with flow cytometry. (N) Flow cytometric measurement of cytosolic Ca^{2+} levels in mock and FPN-iRPMs with and without sRBC exposure using Cal-520 fluorescent probe with flow cytometry. (O) Normalized EP capacity of PKH26-sRBCs by mock and FPN-iRPMs treated with an intracellular (BAPTA-AM; 10 μM, 1 h) and extracellular (EGTA; 3 mM, 30 min) calcium chelator. (P) The EP capacity in iRPMs cultured with serum from IB and ID mice, and treated with extracellular (EGTA; 3 mM, 30 min) calcium chelator, was determined using flow cytometry by measuring the percentage of cells that phagocytosed PKH26-labeled sRBCs. (Q) Flow cytometric assessment of EP capacity in mock-transduced iRPMs and iRPMs overexpressing wild-type FPN and FPN mutant D39A was quantified as the percentage of cells engulfing PKH26-labeled RBCs. (R) Flow cytometric measurement of cytosolic Ca^{2+} levels in mock, FPN, and D39A-iRPMs using Cal-520 fluorescent probe with flow cytometry. Each dot represents one mouse or an independent cell-based experiment. Data are represented as mean ± SEM. Welch's unpaired t-test determined statistical significance in A-C and K. Two-way ANOVA with Tukey's Multiple Comparison tests was used in D-J, N, and N-P. A one-way ANOVA test with Dunnett's or Tukey's Multiple Comparison tests was used in M and Q-R. ns $p>0.05$, *$p<0.05$, **$p<0.01$, ***$p<0.001$ and ****$p<0.0001$.

SYK kinase mediates the FPN-dependent adaptation of RPMs to ID conditions

Expanding on prior knowledge, we next sought to identify the genetic mediators of Ca^{2+}-dependent signaling underlying the functional rewiring of RPMs in ID mice. First, we examined the involvement of PIEZO1, a mechanoreceptor identified to modulate Ca^{2+} signaling and EP in RPMs[32]. Indeed, under basal conditions, treatment of iRPMs *in vitro* with the PIEZO1 activator YODA1 and the inhibitor GsMTx1 mildly affected EP (Figure S5.1A-B). However, GsMTx1 did not significantly affect the enhanced EP capacity observed in iRPMs exposed to ID serum (Figure S5.1C). These findings excluded a major role for PIEZO1 in mediating the functional acceleration of RPMs in response to iron deficiency.

To further dissect the Ca^{2+}-dependent signaling pathways responsible for the enhanced EP observed in RPMs during iron deficiency, we performed a targeted pharmacological screen. Inhibitors of CaMKK (STO-609), calmodulin-mediated signaling (W7), P2 receptor-mediated Ca^{2+} signaling (Apyrase)[59], and macropinocytosis (EIPA) had no discernible impact on EP in either mock or FPN-iRPMs (Figure 5A). Likewise, despite its well-established role in Ca^{2+}-dependent signaling, inhibition of protein kinase C (PKC) with Bisindolylmaleimide I did not reduce EP in either mock-

or FPN-iRPMs (Figure 5A). However, the inhibition of the spleen tyrosine kinase (SYK), a downstream effector of PKC-dependent signaling, with piceatannol completely abolished the increased EP in FPN-iRPMs *versus* mock-transduced iRPMs (Figure 5A). To mitigate the potential off-target effects of piceatannol, we next employed the highly selective SYK inhibitor entospletinib (ENTO; also known as GS-9973) in mock- and FPN-iRPM cultures. Consistently, ENTO effectively suppressed FPN-driven EP enhancement in FPN-iRPMs and iRPMs cultured in ID versus IB serum (Figure 5B-C). Furthermore, we observed that ENTO prevented an increase in Ca^{2+} levels upon FPN overexpression (Figure 5D). Interestingly, supplementation with ENTO was sufficient to reduce both the mitochondrial activity and mass of iRPMs overexpressing FPN to the control levels of mock-transduced cells (Figure 5E-F).

Next, we sought to investigate the role of SYK in RPM iron recycling *in vivo.* First, we found that a 4 h treatment of ID mice with PR73 markedly reduced levels of the active form of SYK, phospho-SYK (Y525/526), in RPMs, whereas no significant effect of the hepcidin agonist was observed in RPMs from IB mice (Figure 5G), similarly to all previous ID-specific suppressive effects of PR73 on RPM rewiring phenotypes. We further assessed the impact of the SYK inhibition with ENTO in both IB and ID mice. Oral daily ENTO administration for the last 2 weeks of the iron-modified diet (5 mg/kg/day; with flavored jellies) effectively reduced phospho-SYK (Y525/526) levels in RPMs from both IB and ID mice compared to vehicle controls (Figure 5H). Strikingly, ENTO administration led to a marked reduction in the EP capacity of RPMs, specifically in ID mice, while EP in IB mice remained unaffected by ENTO treatment (Figure 5I). Furthermore, ENTO treatment partially reversed the increase in Ca^{2+} levels in RPMs observed between ID and IB mice (Figure 5J). Interestingly, ENTO also suppressed FPN induction associated with iron deficiency (Figure 5K), suggesting that EP capacity and FPN expression may be bidirectionally linked. The modulation of FPN appeared independent of liver hepcidin mRNA expression, with no hepcidin induction observed by ENTO supplementation (Figure 5L). Instead, hepcidin expression in ENTO-treated ID mice dropped approximately 50-fold compared to placebo-ID mice. This may indicate that ENTO treatment promotes hepcidin-suppressing signals, such as increased hypoxia or erythropoietic drive, but the exact mechanism by which SYK regulates hepcidin remains to be determined. On systemic levels, a 2-week ENTO treatment did not affect liver iron content within IB or ID groups (Figure S5.2A) or circulating hematological parameters (Figure S5.2B-C), and it only showed some tendency for the more pronounced decrease in the transferrin saturation levels

(Figure 5M). Therefore, we extended the period of ENTO administration for 3 weeks and evaluated the systemic blood parameters. While we observed no significant difference in hemoglobin or MCH between iron-restricted mice supplemented with ENTO *versus* placebo (Figure 5N, S5.2D), we noticed an increase in reticulocyte counts and reduction of reticulocyte hemoglobin content (Figure 5O-P), indicating the onset of systemic hematological effects of ENTO treatment. Consistently, whereas erythroid progenitors' expansion was not affected by ID in the bone marrow, we detected a more pronounced expansion of immature EPO-responsive splenic progenitors, proerythroblasts, and EryA erythroblasts, in ENTO-treated *versus* control mice (Figure 5Q-R). Consistently, plasma EPO levels were elevated in a more pronounced manner between ID and IB mice following ENTO supplementation compared to placebo-exposed mice (Figure 5S). Interestingly, the saturation of transferrin in the circulation was not significantly different between ID mice treated with ENTO and placebo (Figure S5.2E). This suggests that a more pronounced compensatory extramedullary erythropoietic response is initiated by ENTO, likely due to less effective direct iron delivery from iron-recycling RPMs. Taken together, SYK activity emerged as critical for the enhanced RBC-clearance capacity of RPMs in ID mice, with SYK inhibition triggering compensatory erythropoietic responses that are consistent with a possible reduction in iron delivery from RPMs.

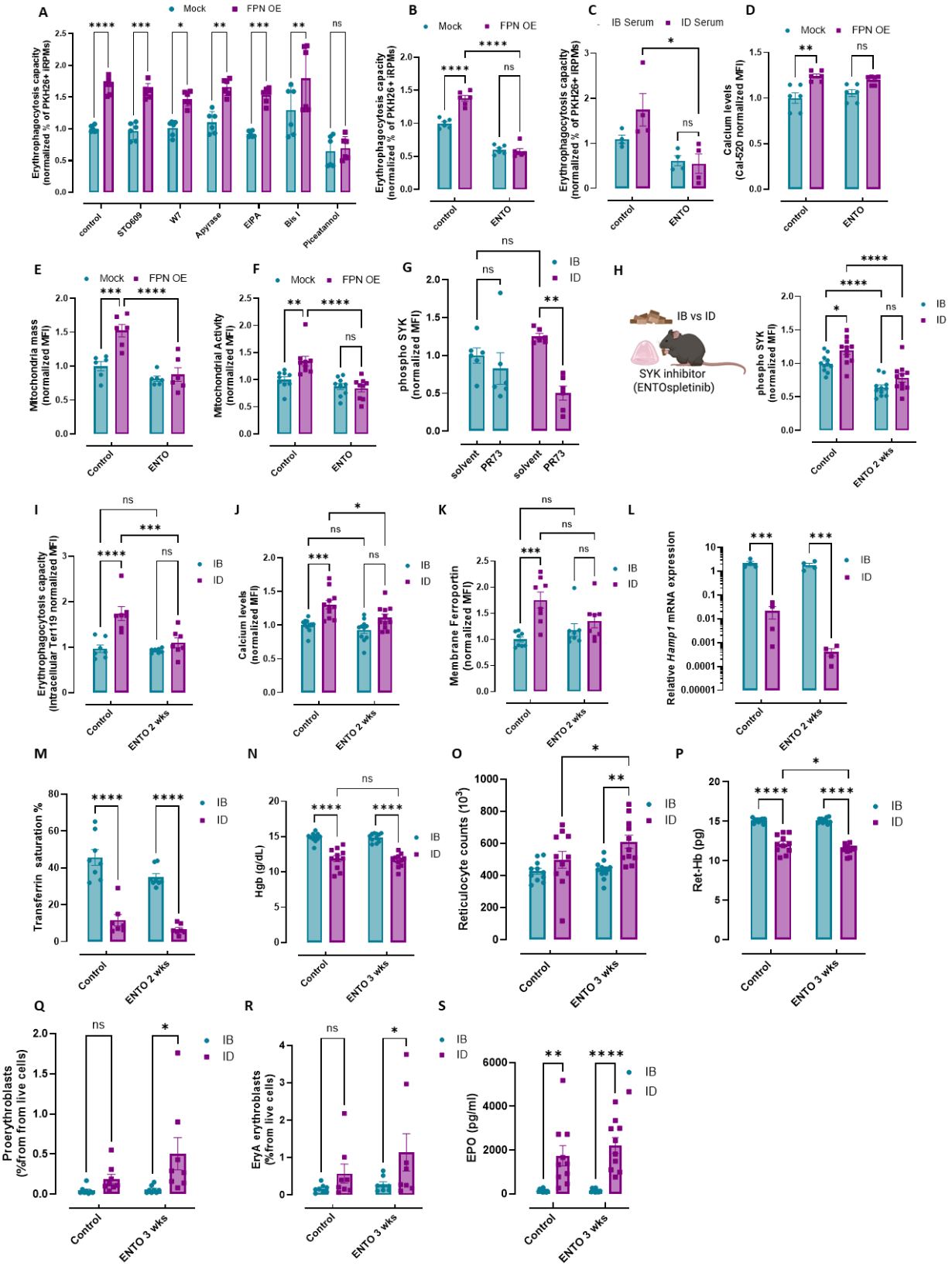

506

Figure 5. SYK kinase mediates the FPN-dependent adaptation of RPMs to ID conditions.

(A) Normalized EP capacity of mock and FPN-iRPMs, measured by uptake of PKH26-labeled sRBCs with flow cytometry. iRPMs were cultured with sRBC for 4 days before analysis and treated with inhibitors targeting CaMKK (STO-609; 2.5 μM, 16 h), ATP-triggered purinergic receptor-mediated Ca^{2+} signaling (Apyrase; 5U/ml, 30 min), calmodulin (W7; 20 μM, 30 min), macropinocytosis (EIPA; 25 μM, 30 min), protein kinase C (Bisindolylmaleimide I, BIS I; 10 μM, 1 h), and spleen tyrosine kinase (SYK; Piceatannol; 100 μM, 30 min). (B) Normalized EP capacity of mock and FPN-iRPMs upon treatment with the SYK inhibitor Entospletinib (ENTO) measured by uptake of PKH26-labeled sRBCs. (C) Normalized EP capacity of iRPMs cultured with serum from IB or ID mice upon treatment with ENTO was measured by uptake of PKH26-labeled sRBCs with flow cytometry. (D) Flow cytometric measurement of cytosolic Ca^{2+} levels in mock and FPN-iRPMs upon treatment with ENTO using Cal-520 fluorescent probe. (E) Mitochondrial mass was determined in mock and FPN-iRPMs upon ENTO treatment using MitoTracker Green and flow cytometry. (F) Mitochondrial activity was measured in mock and FPN-iRPMs with and without treatment with ENTO using the TMRE probe and flow cytometry. (G) Flow cytometric analysis of phosphorylated SYK (phospho-SYK) in RPMs isolated from IB and ID mice, 4 h after intraperitoneal administration of the hepcidin agonist PR73 (50 nmol/mouse). (H). IB and ID mice were supplemented with the orally bioavailable SYK inhibitor ENTO via daily jelly feeding for 2 or 3 weeks before analysis (5 mg/kg/day). Phospho-SYK levels in RPMs were assessed by flow cytometry in IB and ID mice supplemented with ENTO. (I) EP capacity of RPMs from IB and ID mice supplemented with ENTO was determined by intracellular staining for the erythrocyte marker TER119, followed by flow cytometry. (J) Cytosolic Ca^{2+} levels in RPMs from IB and ID mice supplemented with ENTO were measured by flow cytometry using the Cal-520 fluorescent probe. (K) Surface expression of FPN on RPMs was assessed by flow cytometry in IB and ID mice supplemented with ENTO. (L) Relative mRNA expression of the Hamp gene in RPMs from IB and ID mice supplemented with ENTO. (M) Plasma transferrin saturation levels were measured in IB and ID mice supplemented with ENTO. (N) Blood hemoglobin (Hgb) concentration was determined in IB and ID mice supplemented with ENTO. (O) Reticulocyte counts in IB and ID mice supplemented with ENTO. (P) Reticulocyte hemoglobin content in IB and ID mice supplemented with ENTO. (Q and R) Proerythroblast (Q) and EryA erythroblasts (R) representations in the spleens of IB and ID mice supplemented with ENTO. (S) Plasma EPO levels were measured in IB and ID mice supplemented with ENTO. Each dot represents either an independent cell-based experiment or one mouse. Data are represented as mean ± SEM. Two-way ANOVA with Tukey's Multiple Comparison tests was used to determine statistical significance. ns $p>0.05$, *$p<0.05$, **$p<0.01$, ***$p<0.001$ and ****$p<0.0001$.

Functional adaptation of RPMs to iron deficiency involves enhanced BCAA catabolism and β-oxidation pathways

Efferocytosis is a continuous, energy-intensive process that demands extensive metabolic resources and reprogramming[5]. Enhanced glucose uptake and potentiated OXPHOS of ID *versus* IB RPMs, processes regulated in part by FPN (Figure 3N and P), have been previously reported to support efferocytosis[10,11]. However, we questioned whether the metabolic reprogramming observed in RPMs of ID mice reflects a unique adaptation to the challenge of processing hemoglobin-rich RBCs or if it shares features with other macrophage efferocytic programs. To address this, we revisited our transcriptomic and proteomic datasets. Morioka *et al*. identified nineteen solute carrier (SLC) transporter genes that are transcriptionally upregulated during apoptotic cell clearance, establishing a canonical efferocytosis signature[10]. Strikingly, RPMs in ID mice diverge from this

model: none of these nineteen SLC transporters were upregulated at the mRNA level. Similarly, we observed no clear signature of hypoxia-driven programs, pentose phosphate pathway activation, or increased lactate production[9,61]. Notably, RPMs also failed to display detectable protein levels of key enzymes associated with amino acid signaling that support efferocytosis, including ARG1 and ODC1 (crucial for arginine-to-putrescine conversion), or IDO1 (the tryptophan-catabolizing enzyme), and did not express SLC36A4, the principal tryptophan transporter[16,18]. While GLS1, the enzyme responsible for non-canonical glutaminolysis[19], was detected through proteomic analysis, its levels were unaltered under iron-deficient conditions. Conversely, the enriched category of metabolic proteins differentially regulated in RPMs of ID mice revealed consistent alterations of lipid metabolism, resembling other efferocytic macrophages[11]. This includes elevated enrichment expression of β-oxidation enzymes, most notably the rate-limiting CPT2, induction of lipases, and concurrent downregulation of DGAT1 (diacylglycerol O-acyltransferase 1), which mediates triacylglyceride synthesis. Interestingly, we also observed significant enrichment of enzymes involved in branched-chain amino acid (BCAA) breakdown. In parallel, two upregulated proteomic hits, SLC7A7 and SLC7A8, represent antiporters that transport cationic and large neutral amino acids, including BCAAs[62].

To validate these metabolic adaptations in RPMs of ID mice and assess whether they are specific to this subset, we profiled selected proteomic hits by flow cytometry across tissue-resident macrophage populations. We found that BCKDHB, the rate-limiting enzyme of BCAA catabolism, the BCAA exporter SLC7A7, β-oxidation enzymes CPT2 and ACADSB, the TCA enzyme citrate synthase, and the lipase ABHD12B were all significantly elevated in ID RPMs compared to iron-balanced controls, while remaining unchanged or reduced in KCs and peritoneal macrophages (Figure 6A). Consistently, both DGAT1 and lipid droplet levels were specifically downregulated in RPMs of ID mice, suggesting a unique skewing toward energy-consuming pathways under iron deficiency (Figure 6A). Next, we focused on BCAA metabolism, a pathway not previously linked to enhanced efferocytosis. Baseline BCAA levels were exceptionally high in RPMs compared to other splenic cell types, though still lower than in KCs and similar to peritoneal macrophages (Figure 6B-C). BCAA content increased significantly in RPMs treated *ex vivo* with ERG240, a pharmacologic blocker of BCAA catabolism at the stage of the first reaction catalyzed by the BCAT enzyme (Figure 6C). Prolonged exposure of iRPMs to stressed RBCs, but not RBC ghosts, induced strong BCKDHB expression, more robust than in standard BMDMs, and appeared to prevent

BCAA accumulation in RBC-exposed cells (Figure 6D-E). Notably, BCAA content remained unchanged in RPMs from ID mice (Figure 6F), despite elevated EP, suggesting that BCAA metabolism is tightly regulated. This implied that ID conditions impose a new metabolic equilibrium necessary to maintain enhanced iron recycling by RPMs. Further exploring this concept, BCKDHB levels were elevated in iRPMs overexpressing FPN, a response that, like EP, depended on both FPN and SYK kinase activity (Figure 6G). The SYK dependency of BCKDHB was also evident *in vivo* in RPMs derived from ID *versus* IB mice (Figure 6H). Strikingly, inhibition of BCAT enzymatic activity using ERG240 abolished the EP boost caused by FPN overexpression (Figure 6I), indicating that enhanced BCAA catabolism is essential for reprogramming RPM phagocytic function. Similarly, exposure to leucine increased EP capacity in iRPMs in a manner diminished by ERG240 pre-treatment (Figure 6J). Interestingly, BCAT inhibition also reversed BCKDH induction and reduced mitochondrial mass and activity, specifically in FPN-overexpressing iRPMs (Figure 6K-M). We confirmed the reversal of the enhanced phagocytic and metabolic function of ID-like RPMs by BCAT suppression using another inhibitor, BAY069 (Figure S6.1A-C). We next looked at the requirement of β-oxidation for the RPM ID-like adaptation. Like BCKDHB, CPT2 upregulation was dependent on both FPN and SYK activity (Figure S6.2A). This SYK dependence was further validated *in vivo*, where ENTO reversed CPT2 induction in RPMs from ID mice (Figure S6.2B). Finally, inhibition of CPT2 activity with trimetazidine (TMZ) abolished the enhanced EP observed with FPN overexpression, demonstrating that increased β-oxidation is a key component of the metabolic programming driving augmented phagocytic function in RPMs (Figure S6.2C). Taken together, both BCAA catabolism and β-oxidation emerged in our study as FPN/SYK-controlled pathways that maintain enhanced phagocytosis and metabolic activities of RPMs in iron deficiency.

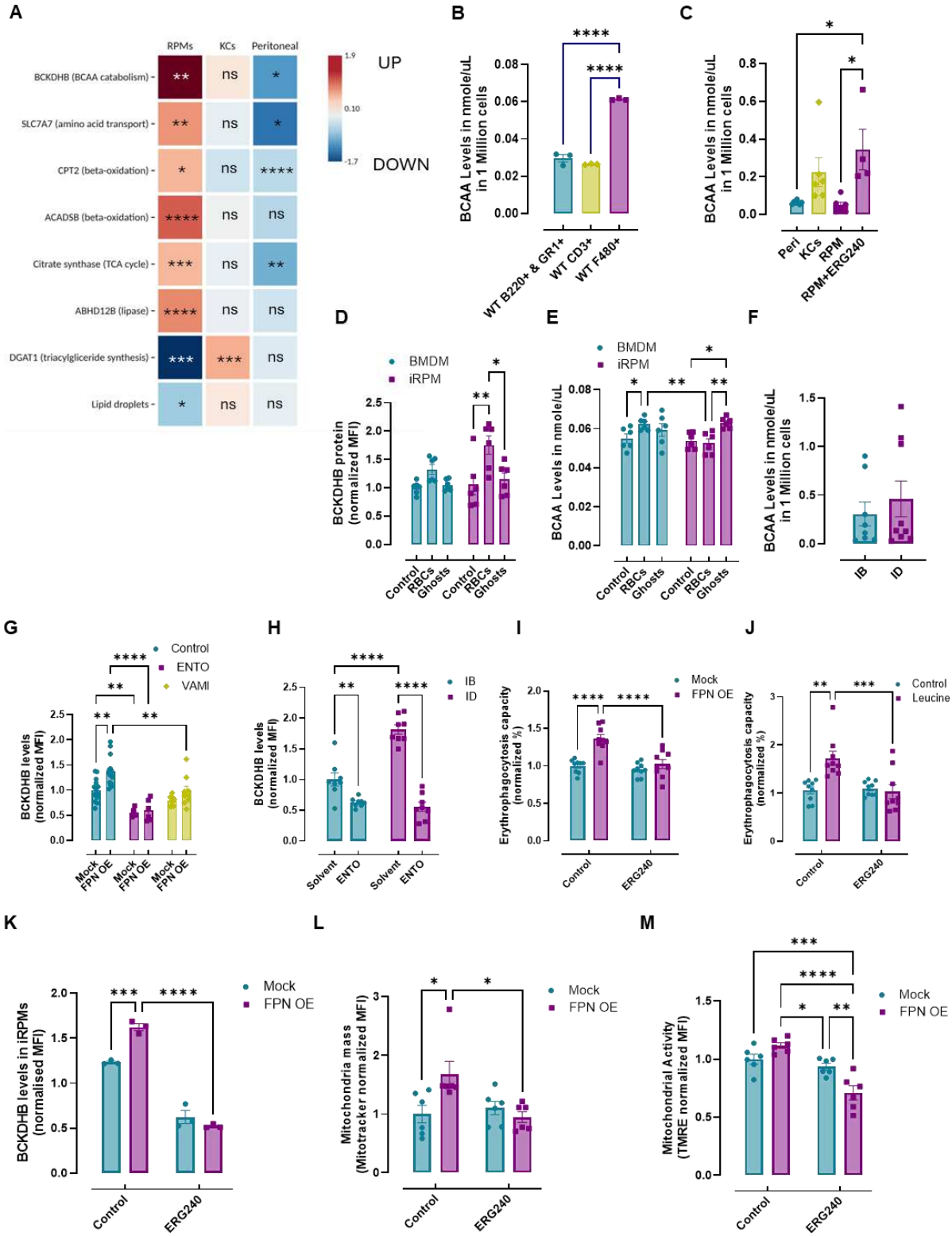

Figure 6. Functional adaptation of RPMs to iron deficiency involves enhanced BCAA catabolism.

(A) Heatmap showing levels of BCKDHB, SLC7A7, CPT2, ACADSB, citrate synthase, ABHD12B, DGAT1, and lipid droplet levels across RPMs, KCs, and peritoneal macrophages measured by flow cytometry. Data represent log2-transformed fold changes in cells of ID mice vs IB mice, with significant changes marked by asterisks. (B) Quantification of BCAA levels in different splenic immune cell populations - F4/80$^+$ RPMs, CD3$^+$ T cells, and other splenocytes, measured using a colorimetric BCAA assay. (C) Quantification of BCAA levels of *ex vivo* magnetically-sorted peritoneal macrophages, KCs, and RPMs (untreated and treated with ERG240). (D) Intracellular BCKDHB levels and (E) BCAA levels in iRPMs and BMDMs treated with stressed RBCs and RBC ghosts compared to untreated control. (F) BCAA levels in magnetically-isolated RPMs from IB and ID mice (G). Intracellular BCKDHB levels in mock and FPN overexpressing (OE) iRPMs upon treatment with entospletinib (ENTO) (10 μM, 1 h) and vamifeport (VAMI) (20 μM, 15 h), determined using flow cytometry (H). Intracellular BCKDHB levels in RPMs from IB and ID mice supplemented with ENTO via jelly feeding (3 weeks) were determined using flow cytometry. (I) Normalized EP capacity towards PKH26-sRBCs by mock and FPN overexpressing iRPMs upon ERG240 treatment (10 μM, 15 h). (J) Normalized EP capacity towards PKH26-sRBCs by iRPMs upon leucine exposure. (K) Intracellular BCKDHB levels in mock and FPN OE iRPMs upon treatment with ERG240. (L) Mitochondrial mass was determined in mock and FPN OE iRPMs upon treatment with ERG240 using MitoTracker Green and flow cytometry. (M) Mitochondrial activity was determined in mock and FPN OE iRPMs upon treatment with ERG240 using the TMRE probe and flow cytometry. Each dot represents one mouse or an independent cell-based experiment. Data are represented as mean ± SEM. Two-way ANOVA with Tukey's Multiple Comparison tests was used in D, E, and G-M, while one-way ANOVA test with Dunnett's or Tukey's Multiple Comparison tests was used in B and C, A Welch's unpaired t-test determined statistical significance in A and F. ns $p>0.05$, *$p<0.05$, **$p<0.01$, ***$p<0.001$ and ****$p<0.0001$.

In vivo inhibition of BCAA catabolism alters erythrophagocytic capacity and metabolic remodeling of RPMs in ID mice

We next sought to dissect the functional relevance of BCAA metabolism in regulating erythrophagocytic capacity and mitochondrial remodeling *in vivo*. First, we found that enhanced OXPHOS of freshly isolated RPMs from ID mice, as measured using a Seahorse analyzer, was abrogated by *ex vivo* treatment with ERG240 (Figure 7A), indicating its critical dependence on BCAA catabolism. Next, we administered ERG240, a bioavailable BCAT inhibitor, to ID mice via daily jelly feeding for three weeks. Consistent with our *in vitro* observations, ERG240 treatment significantly suppressed the enhanced EP activity of RPMs in ID mice (Figure 7B). In parallel, ERG240 administration prevented the increase of mitochondrial mass and the upregulation of BCKDHB and citrate synthase protein levels, a proxy for TCA cycle capacity (Figure 7C-E). Interestingly, despite this reduction in mitochondrial mass and citrate synthase, mitochondrial membrane potential was not suppressed and remained comparable to untreated ID controls (Figure 7F), suggesting a partial uncoupling between mitochondrial polarization state and respiratory functions under conditions of BCAT inhibition *in vivo*. Notably, FPN protein abundance remained

unchanged in ERG240-treated mice subjected to ID feeding (Figure 7G), indicating that, as in ENTO-supplemented animals, reduced RPM erythrophagocytic activity is linked to diminished exposure of FPN at the plasma membrane. At the systemic level, ERG240 treatment very modestly affected the degree of anemia, as evidenced by a slightly more pronounced reduction in hematocrit, while hemoglobin levels, MCV, and MCH values remained unchanged in ID mice receiving the drug relative to untreated ID controls (Figure 7H and S7A). However, circulating reticulocyte counts were significantly elevated specifically in ERG240-treated animals (Figure 7I), indicating a heightened stress erythropoietic response aimed at restoring circulating red cell mass, likely reflecting enhanced sensing of iron deficiency. In line with this, ERG240-treated mice displayed a significant expansion of splenic erythroid progenitors, with both proerythroblasts and EryB erythroblasts (Figure S7D) showing elevated representation relative to untreated ID mice. Consistently, plasma EPO levels were significantly elevated in ERG240-treated ID mice (Figure 7J), aligning with the observed expansion of splenic erythroid progenitors. Interestingly, not only were *Epo* mRNA levels elevated in the kidney of ID mice upon ERG240 supplementation as compared to placebo controls, but also *Tfrc* transcription was increased (Fig. 7K and L). Similarly, cardiac *Tfrc* appeared as more significantly induced in ID mice upon ERG240 treatment compared with untreated ID controls, reflecting a slightly more pronounced drop in the heart non-heme iron content (Fig. S7E-F). However, liver *Tfrc* induction and a decrease in iron levels upon ID diet were not modified by ERG240 supplementation (Fig. S7G-H), and transferrin saturation remained comparably reduced in ERG240- and placebo groups (Fig. S7I). These observations may suggest sensing of more pronounced hypoxia by the kidney, and of tissue iron deficiency in some, but not all, organs.

Finally, to assess how systemic iron deficiency alters mitochondrial fuel use *in vivo*, and how these changes depend on BCAT activity, we performed MitoPlate S1 substrate profiling on freshly isolated RPMs. Relative to IB controls, RPMs from ID mice exhibited broadly increased utilization of glycolytic, amino-acid–derived, fatty-acid/carnitine-linked, and TCA cycle substrates, consistent with their heightened OXPHOS phenotype (Figure 7M). BCAT inhibition with ERG240 partially attenuated this shift, most notably reducing oxidation of several TCA cycle and fatty-acid–linked fuels, in line with the decrease in global mitochondrial respiration measured by Seahorse. In contrast, several amino-acid substrates, such as leucine+L-malic acid, tryptamine, and ornithine, remained more highly utilized than in RPMs of IB mice, indicating that while BCAT-dependent

677 BCAA metabolism contributes to the enhanced respiratory capacity of RPMs in ID mice, additional
678 metabolic pathways support the full extent of their increased mitochondrial activity.

679 Collectively, these data demonstrate that BCAA catabolism is required for sustaining increased EP
680 functions, with implications for the body's adaptation to dietary iron restriction.

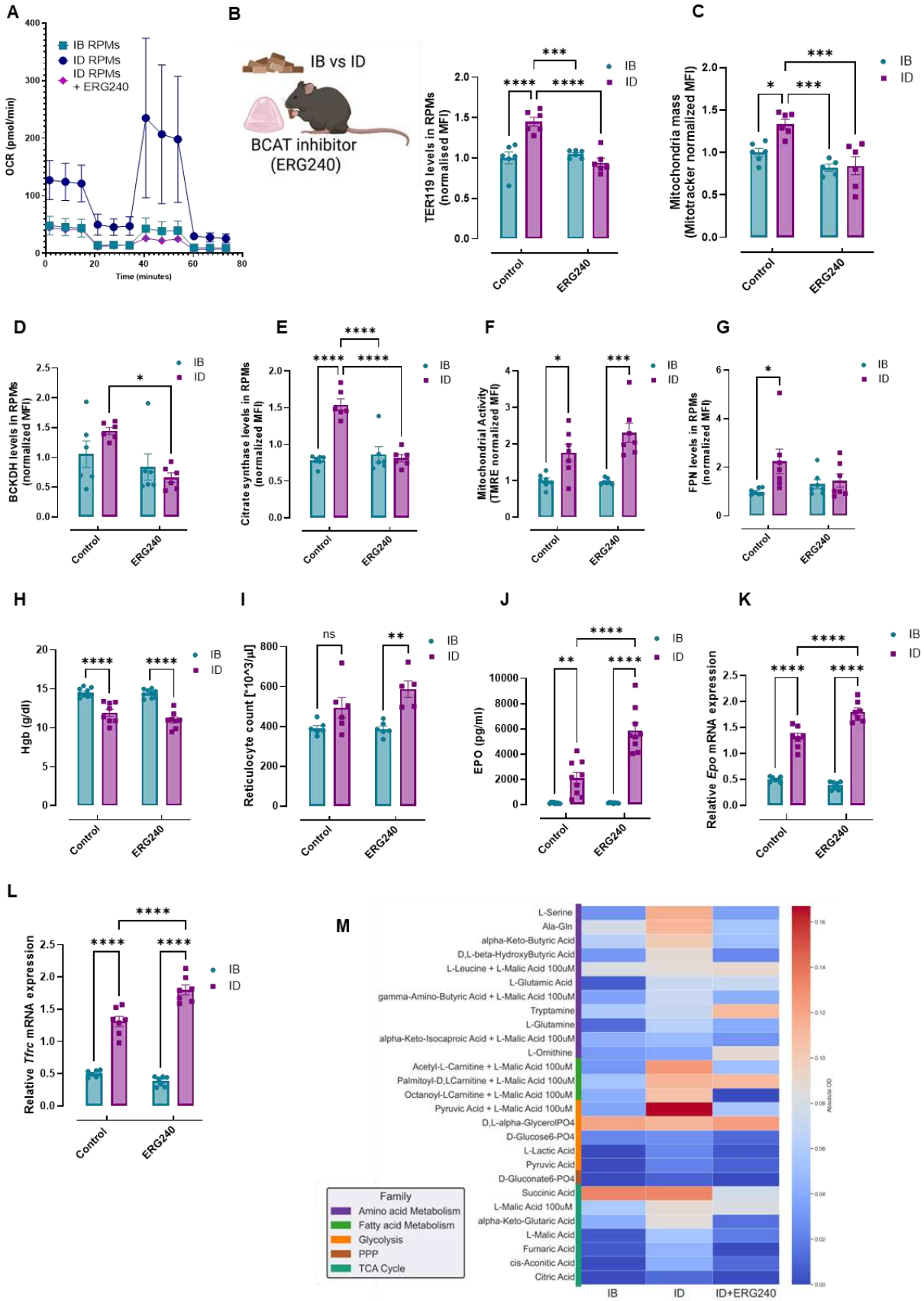

Figure 7. *In vivo* inhibition of BCAA catabolism alters erythrophagocytic capacity and metabolic remodeling of RPMs in ID mice.

(A) Seahorse analysis of *ex vivo* magnetically-isolated RPMs from IB and ID mice, including 4 h ERG240 preincubation for RPMs from ID mice. (B) IB and ID mice were supplemented with the orally bioavailable BCAT inhibitor ERG240 via daily jelly feeding for 3 weeks before analysis (5 mg/kg/day). EP capacity of RPMs from IB and ID mice supplemented with ERG240, determined by intracellular staining for the erythrocyte marker TER119, followed by flow cytometry. (C) Mitochondrial mass of RPMs from IB and ID mice supplemented with ERG240 was determined using MitoTracker Green, followed by flow cytometry. (D) Intracellular BCKDHB levels of RPMs from IB and ID mice supplemented with ERG240 (E). Intracellular citrate synthase levels of RPMs from IB and ID mice supplemented with ERG240 (F). Mitochondrial activity of RPMs from IB and ID mice supplemented with ERG240 was determined using the TMRE probe, followed by flow cytometry. (G) FPN levels of RPMs from IB and ID mice supplemented with ERG240 were determined by flow cytometry. (H) Blood hemoglobin (Hgb) and reticulocyte count (I) were determined in IB and ID mice supplemented with ERG240. (J) Plasma EPO levels were measured in IB and ID mice supplemented with ERG240. (K and L) Relative mRNA expression of the (K). Relative mRNA expression of *Epo* and (L) *Tfrc* genes in the kidneys of IB and ID mice supplemented with ERG240 (M). Absolute mitochondrial substrate utilization profiles of RPMs from IB, ID, and ID mice supplemented with ERG240, measured using the MitoPlate S1 assay. Blank-corrected OD values for all metabolites with detectable activity in ID RPMs (n = 27) are shown and grouped by metabolic pathway. Each dot represents one mouse or an independent cell-based experiment. Data are represented as mean ± SEM. Two-way ANOVA with Tukey's Multiple Comparison tests was used in B-L. ns $p>0.05$, *$p<0.05$, **$p<0.01$, ***$p<0.001$ and ****$p<0.0001$.

Discussion

Iron deficiency is a complex physiological state with multifaceted implications. The precise quantitative thresholds that trigger cellular or organismal functional consequences, and the cell-type-specific molecular consequences, including the identification of the most vulnerable cell types and the sequence of cellular dysfunction triggered by iron deficiency, remain poorly understood. Beyond its well-known erythropoietic effects leading to anemia, iron deficits impair neuronal and muscle functions[33,63,64], suppress immune cell activity and proliferation[65–68], and dysregulate macrophage responses[49,50,69,70]. However, the seemingly contradictory findings regarding the effects of iron depletion on macrophage inflammatory cytokine production *in vitro* versus *in vivo*[49,50,69,70] highlight the critical need for a more precise, cell-type-specific, and context-dependent understanding of how low iron status affects macrophage functions. Specifically, how RPMs, specialized iron-recycling cells central to the maintenance of systemic iron homeostasis, adapt to the metabolic stress of systemic iron deficiency remains a key open question. Here, we address this gap by defining a signaling-metabolic circuit through which systemic iron deficiency reprograms RPMs to enhance erythrophagocytosis and sustain iron recycling (Fig. 8).

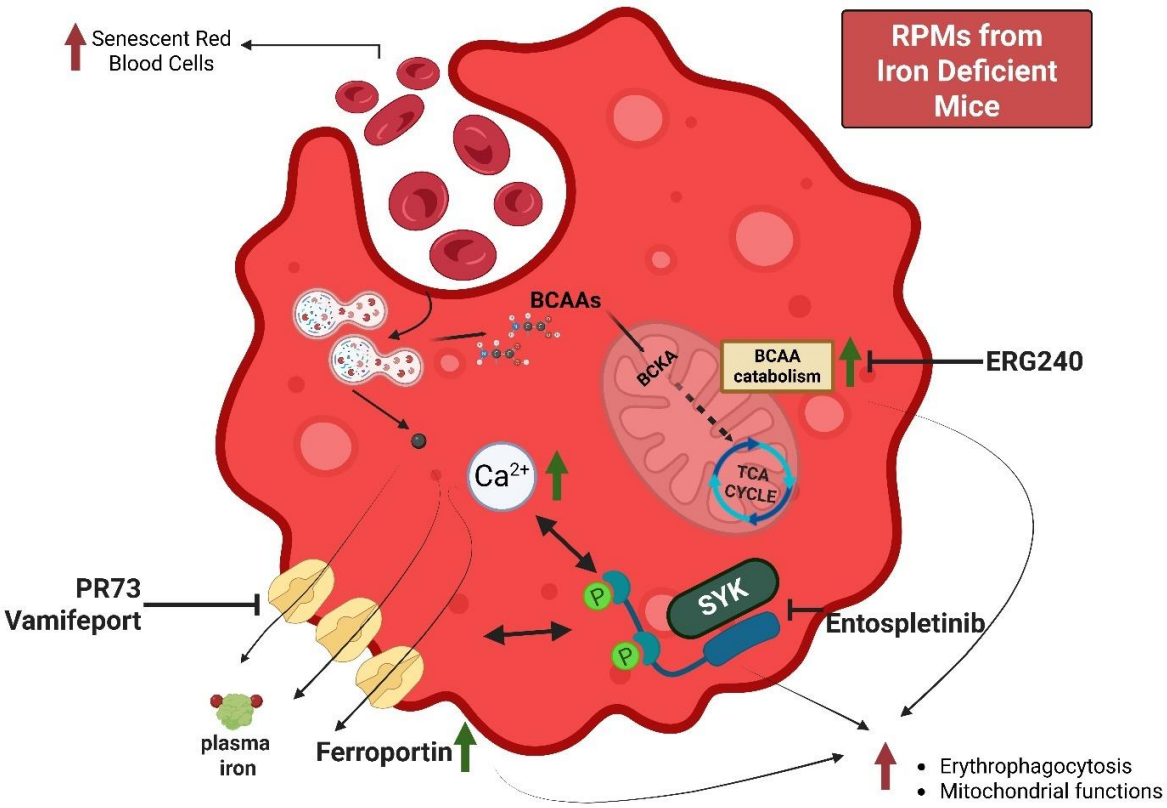

Figure 8. Iron deficiency induces metabolic rewiring of red pulp macrophages to enhance erythrophagocytosis.

Model illustrating how systemic iron deficiency reprograms RPMs to sustain iron recycling. Increased FPN-mediated iron export activates SYK-dependent signaling, promoting mitochondrial metabolic adaptation, including BCAA catabolism, which supports enhanced erythrophagocytosis of senescent RBCs. Pharmacological inhibition of FPN, SYK, or BCAA catabolism disrupts this adaptive program.

RPMs from ID mice displayed classical markers of cellular iron depletion (increased TFR1, decreased ferritin), reflecting activation of the iron-responsive element/iron regulatory protein (IRE/IRP) system, a post-transcriptional regulatory mechanism that normally increases iron uptake and reduces iron storage and FPN-mediated export under iron-limiting conditions[20,25]. However, we observed increased FPN expression in RPMs of ID mice, despite proteomic analysis showing elevated IRP2 levels. This implies that suppressed hepcidin levels in iron deficiency, which relieve the dominant negative regulation of FPN, override any potential IRP2-mediated repression. Although RPM iron stores were low in ID mice, increased LIP and oxidative stress were observed relative to IB controls, consistent with enhanced EP activity and a likely increase in cellular iron flux. Intriguingly, this observation suggests that other iron-related signals beyond LIP contribute to IRP2 stabilization in RPMs. The elevated FPN expression facilitates the export of iron derived

737 from engulfed RBCs, likely supporting the accelerated stress erythropoiesis in the spleen and the
738 iron needs of other cell types during iron deficiency. These results reveal an adaptive mechanism
739 in RPMs that prioritizes systemic iron delivery while promoting more efficient clearance of
740 senescent RBCs in the spleen in response to dietary iron deficiency. Importantly, by demonstrating
741 that the RBC clearance capacity of RPMs in ID mice depends on functional FPN, our findings
742 highlight a tight coordination between iron export and its delivery through erythrophagocytosis,
743 representing, to the best of our knowledge, a previously unrecognized concept. The relatively mild
744 systemic effects observed upon disruption of these adaptive mechanisms may reflect the short-term
745 nature of their experimental inhibition in RPMs. Nevertheless, our findings underscore the need to
746 determine how RPM rewiring and increased EP during iron deficiency reshape tissue iron
747 distribution, and how these metabolic and functional adaptations ultimately influence organismal
748 physiology, including immune competence, neuronal function, and muscle performance.

749 The established cellular response to iron deficiency, observed in iron-deprived macrophages *in*
750 *vitro* and in TFR1-null cardiomyocytes, involves a metabolic shift toward glycolysis accompanied
751 by mitochondrial dysfunction and impaired electron transport chain activity[49,71]. In contrast, RPMs
752 from ID mice show enhanced mitochondrial function, with increased mitochondrial mass and
753 elevated OXPHOS activity confirmed by Seahorse and proteomic analyses, accompanied by an
754 increase in mitochondrial membrane potential. This unique, cell-type-specific metabolic
755 adaptation, absent in Kupffer cells and peritoneal macrophages, suggests that RPMs are exceptional
756 in adjusting their physiology to increased bioenergetic demand, imposed by boosted iron recycling
757 capability. Whether these responses are driven by the spleen's unique microenvironment,
758 potentially via signals from extramedullary erythropoiesis, remains to be understood. Importantly,
759 this exceptional metabolic state of highly enhanced mitochondrial respiration was acutely shut
760 down by inhibition of FPN with PR73, and mirrored by suppressed glucose uptake and protein
761 synthesis *in vivo*, pointing to a novel relationship between FPN functionality and cellular
762 metabolism in the context of heightened efferocytic activity. These findings were further supported
763 by the similar metabolic features induced solely by FPN overexpression in the RPM *in vitro* model.

764 Emerging evidence links substantial metabolic reprogramming to efferocytosis. This is hallmarked
765 by altered amino acid utilization, particularly of arginine[16], methionine[17], tryptophan[18], and
766 glutamine[19], lactate production[9,10], boosted pentose phosphate pathway[14,15], increased glucose
767 uptake and glycolysis[9,10], fatty acid oxidation[11], and, critically, enhanced mitochondrial

768 respiration[12,13], acting in concert to sustain energetically demanding efferocytosis and promote an
769 anti-inflammatory milieu[12,13]. While RPMs of ID mice retain some of these metabolic traits,
770 particularly enhanced OXPHOS, our omics analyses reveal a distinct divergence from canonical
771 efferocytic programs. For example, key transporters and enzymes involved in arginine, tryptophan,
772 and glutamine metabolism are absent or uninduced. BCAAs represent important metabolic
773 substrates for macrophages, fueling the TCA cycle and supporting both pro-inflammatory and anti-
774 inflammatory polarization in a context-dependent manner[72–74]. However, the relevance of BCAA
775 catabolism in promoting efferocytosis and controlling the functions of iron-recycling macrophages
776 has remained largely unexplored. Our study demonstrates that RPMs of ID mice uniquely
777 upregulate BCKDHB in a manner controlled by both FPN and SYK, identifying the new
778 mechanistic link between the capacity of BCAA breakdown and these regulators. We further show
779 that enhanced RBC clearance in RPMs relies on BCAA-driven bioenergetics, reflected by the
780 dependence of their heightened OXPHOS on BCAT activity. The MitoPlate profiling further
781 clarifies this metabolic specialization. Although RPMs from ID mice display broadly elevated
782 mitochondrial substrate use, BCAT inhibition led to a marked divergence between fuel classes:
783 oxidation of several key TCA cycle and fatty-acid-linked substrates was substantially reduced by
784 ERG240, whereas utilization of select amino-acid-derived fuels, particularly leucine, malic acid,
785 tryptamine, and ornithine, remained comparatively resilient. This pattern points to a reliance on
786 non-canonical transamination-linked anaplerosis that sustains the α-ketoglutarate (α-KG) pool.
787 When BCAT is suppressed, the diminished α-KG supply limits TCA cycle flux, making
788 conventional carbon inputs more vulnerable, while specific amino acid pathways able to restore or
789 utilize α-KG through distinct enzymatic routes can still support the elevated mitochondrial state
790 characteristic of RPMs in ID mice. Altogether, these findings reveal either a previously
791 unrecognized specialization of RPMs for processing BCAA-rich RBCs or suggest a more general,
792 therapeutically exploitable metabolic dependency in efferocytic macrophages. Future work will
793 clarify whether this pathway is restricted to RPMs or is required for efficient or increased clearance
794 of apoptotic cells in other macrophage subtypes.

795 Our work further identified significantly elevated intracellular Ca^{2+} levels in RPMs of ID mice,
796 closely dependent on functional FPN and correlating with their enhanced EP capacity. While recent
797 studies have demonstrated that PKC activity can promote FPN exposure on the cell surface in type
798 2 diabetes and as a response to iron loading[75], our findings suggest that, in the context of iron

deficiency, increased FPN expression and elevated intracellular Ca^{2+} may represent parallel or intersecting pathways that together facilitate enhanced EP. It is also plausible that RPMs of ID mice, characterized by low iron stores but elevated LIP, additionally regulate FPN exposure on the surface via Ca^{2+}-stimulated high PKC activity. Our data suggest no direct involvement of PKC in mediating FPN-dependent and Ca^{2+}-triggered regulation of EP, at least using the cellular model of RPMs. However, RPMs of ID mice treated by ENTO not only downmodulate EP but also FPN surface levels and Ca^{2+}, which may represent a secondary response, possibly mediated by PKC activity.

Our discovery that SYK drives EP in RPMs aligns with its emerging roles in diverse phagocytic processes. Bian *et al*. demonstrated that SYK activation overrides Cd47-SIRPα-mediated "don't eat me" signals to enable inflammation-driven clearance of "self" RBC[30]. Recent studies highlight SYK as a critical mediator of microglial responses to amyloid-β (Aβ) plaques in Alzheimer's disease, where SYK deficiency impairs Aβ phagocytosis[76,77]. Our work extends this observation by identifying iron deficiency as a physiological trigger for SYK activation in RPMs, with upstream regulation by the low hepcidin-high FPN. Furthermore, our work reveals SYK-dependent metabolic-phagocytic coupling. Whereas previous findings link high SYK activity to inhibition of mitochondrial respiration[78], we show that mitochondrial membrane potential and mass, heightened by FPN overexpression, critically depend on SYK activity. Critically, our data imply that SYK may represent a novel molecular switch for the regulation of efferocytic capacity, a concept that requires further work.

Finally, the FPN–SYK-mediated rewiring of RPMs in iron deficiency does not resemble M1/M2-like polarization. RPMs from ID mice exhibited an ambiguous pattern of surface marker alterations, indicating no consistent pro- or anti-inflammatory skewing, and no clear regulation of immune-linked mediators in omics data. They also employed a mixed functional phenotype: elevated ROS production, driven by increased labile iron, characteristic of M1 macrophages, alongside enhanced oxidative phosphorylation, mitochondrial biogenesis, and lysosomal activity, features typically associated with M2 macrophages[79–85]. Likewise, SYK has emerged as a context-dependent regulator of macrophage polarization and function, promoting fibrotic and proinflammatory programs in diabetic kidney disease and ulcerative colitis, respecitvely and enabling immunosuppressive reprogramming of tumor-associated macrophages[86,87,88]. Together with the notion that enhanced EP in RPMs only partially resembles previously reported adaptation

mechanisms to efferocytosis, our work proposes that the polarization state of RPMs in iron deficiency represents a new type of adaptation, whose resemblance in other macrophage types/environmental conditions opens an avenue for future investigations.

Methods

Mice

Female C57BL/6 J mice were utilized for the experiments and housed under specific pathogen-free (SPF) conditions at the Experimental Medicine Centre in Bialystok, Poland. These mice were provided with either a standard iron-balanced diet (200 mg/kg, SAFE U8958P; IB diet) or an iron-deficient diet (5.9 mg/kg, SAFE U8958P; ID diet) for 5 weeks, commencing at 4 weeks of age. 9-week-old *Tmprss6* wild-type and KO mice were provided by Dr. Delphine Meynard from INSERM, Toulouse, France. Upon arrival at the local facility at the International Institute of Molecular and Cell Biology (IIMCB), mice were acclimatized briefly before being sacrificed or subjected to further procedures, if required. Ms4a3-Cre mice were obtained from Florent Ginhoux[43], and RosaTdT reporter mice [B6;129S6-Gt(ROSA)26Sortm9(CAG-tdTomato)Hze/J JAX#: 007905] were a kind gift of Agnieszka Kobielak. Female C57BL/6-Tg(UBC-GFP)30Scha/J (UBI-GFP/BL6) mice were kindly provided by Aneta Suwińska (Faculty of Biology, University of Warsaw, Poland). For primary cell cultures, C57BL/6 J mice were maintained in the SPF facility at the Mossakowski Medical Research Institute in Warsaw, Poland.All animal experiments and protocols were approved by the respective local ethical committees in Olsztyn and Warsaw, including the decisions: Uchwala 026, WAW2/015/2019, and WAW2/048/2020). Usage of Ms4a3Cre-RosaTdT reporter mice was approved by WAW2/126/2023. For PR73 administration, mice were intraperitoneally injected with 50 nmol of PR73 for 4 h before being sacrificed. The procedure was approved by the local ethical committee in Warsaw (WAW2/150/2019). Experiments including SYK and BCAA catabolism suppression were covered by the permissions: WAW2/068/2024 and WAW2/029/2025.

Isolation of Single-Cell Suspensions from Murine Organs

Bone marrow cells were obtained by flushing the femurs and tibias with sterile HBSS (Gibco, 14025092) using a 25G needle. Following centrifugation at 600 x g for 10 min at 4°C, the pellet containing the isolated cells was collected for further processing. The spleen was harvested and homogenized by passage through a 70 µm cell strainer (pluriSelect, 43-50070-51). Before FACS sorting, the spleen was enzymatically digested with HBSS containing 1 mg/mL Collagenase D

(Roche, 11088882001) and 50 U/mL DNase I for 30 min at 37°C to facilitate cell dissociation. The resulting cell suspension was then washed with cold HBSS and centrifuged at 600 x g for 10 min at 4°C. The harvested liver was perfused using Liver Perfusion Medium (Gibco, 17701038), followed by mincing and enzymatic digestion in Liver Digest Medium (Gibco, 17703034) at 37°C for 30 min. The digested liver tissue was then pressed through a 70 μm strainer into HBSS. The resulting cell suspension was centrifuged at 50 g for 3 min to separate the hepatocyte-enriched pellet, which was discarded. The supernatant, containing non-parenchymal cells, was further centrifuged at 700 g for 15 min at 4°C. The resulting cell pellet was resuspended in a solution of 5 mL PBS with 0.5% BSA and 5 mL of 50% Percoll (Cytiva, 17-0891-01) diluted in PBS. This suspension underwent Percoll gradient centrifugation at 700 g for 30 min at 20°C to enrich specific cell populations. The peritoneal cavity was lavaged with HBSS to collect peritoneal fluid. The retrieved fluid was then passed through a 70 μm strainer to remove debris, followed by centrifugation at 600 x g for 10 min at 4°C to pellet the peritoneal cells. Blood was collected via cardiac puncture into a heparin-coated tube. The cells were separated by centrifugation at 400 g for 10 min at 4°C following a wash with HBSS. RBCs present in a single-cell suspension were lysed using 1X RBC Lysis buffer (BioLegend, 420302) for 3 min at room temperature. However, this step was excluded when analyzing erythroid cells and RBCs. Following that, the cells were washed with 1X HBSS and centrifuged at 600g for 10 min at 4°C. The resulting pellet was processed for subsequent functional assays and antibody labeling.

Generation of iRPMs

Mononuclear cells were aseptically harvested from the femurs and tibias of mice and subsequently cultured at a concentration of 0.5×10^6/1mL in RPMI-1640 medium (Gibco, 61870036) supplemented with 10% FBS (Cytiva, SV30160.03), 1X Penicillin-Streptomycin (Gibco, 15140122), and 20 ng/mL of macrophage colony-stimulating factor (MCSF, BioLegend, 576406) in a 5% CO_2 incubator at 37°C. On days 4 and 6 of culture, the medium was replaced with fresh complete medium supplemented with 20 μM hemin (Sigma-Aldrich, 51280). In the initial experiments, we also included 10 ng/mL interleukin-33, which was later omitted as it was not critical for mimicking RPM-like phenotypes. All experiments were performed on day 8 of culture. For treatments, hemin (Sigma-Aldrich, 51280) solution was prepared with 0.15 M NaCl containing 10% NH_4OH. For the phagocytosis assay, iRPMs were treated for 1 h with 10 μM Entospletinib (Selleck, S7523), 15 h with 10 μM ERG240 (MedChemExpress, HY-W193545A), 15 h with 10μM BAY-069 (MedChemExpress, HY-148242), 15 h with 10 mM leucine (Sigma-

Aldrich, L8000), 24 h with 100 µM deferoxamine (DFE, Sigma-Aldrich, D9533), 30 min with 10 µM BAPTA/AM (CALBIOCHEM, 196419), 1 h with 3 mM EGTA (Sigma, E8145), 16 h with 2.5 µM STO609 (Sigma-Aldrich, S1318), 30 min with 20 µM W7 (Sigma-Aldrich, 681629), 30 min with 5U/ml apyrase (Sigma-Aldrich, A6535), 30 min with 25 µM EIPA (Selleckchem, S9849), 1 h with 10 µM BisindolylmaleimideI (Sigma-Aldrich, 203290), 30 min with 100 µM Piceatannol (Sigma-Aldrich, P0453). Vamifeport was a kind gift from CSL Vifor and was purchased from MedChem Express (VIT-2763), and was used for 15 h at 20 µM concentration.

Flow Cytometric Analysis and Cell Sorting

Cell suspensions of spleens and livers at a concentration of approximately 1×10^7, along with iRPMs, were stained with LIVE/DEAD Fixable Aqua/Violet (Invitrogen, L34966/L34964) following the manufacturer's instructions to identify dead cells. After extensive washing, Fc block was added to the cells at a 1:100 dilution in FACS buffer and incubated at 4˚C for 10 min. The cells were then stained with fluorophore-conjugated antibodies at a dilution of 1:100 to 1:400, depending on the titration, in FACS buffer for 30 min at 4˚C. The cells were washed thoroughly with FACS buffer and analyzed using flow cytometry. For the analysis of splenic RPM populations, cells were initially identified as $CD45^+$ $F4/80^{high}$ $CD11b^{dim}$ $TREML4^+$ after excluding lineage-positive cells ($CD3^+$ T cells, $B220^+$ B cells, $Gr\text{-}1^+$ neutrophils/monocytes), as previously described[27]. However, since we observed that the majority of RPMs were $TREML4^+$, we omitted TREML4 from the panel in further analyses. Surface antibodies against CD45 (Biolegend, 30-F11), CD45R/B220 (Biolegend, RA3-6B2), Ly-6G/Ly-6C (Gr-1) (Biolegend, RB6-8C5), CD3 (Biolegend, 17A2), F4/80 (Biolegend, BM8), CD11b (Biolegend, M1/70), and TREML4 (Biolegend, 16E5) were used. For erythroid cell analysis, TER-119 (Biolegend) and CD71 (Biolegend, RI7217) were included. Staining for proteins linked to amino acid and lipid metabolism utilized antibodies against BCKDHB (Santa Cruz Biotechnology, sc-374630), SLC7A7 (Invitrogen, PA5-113527), CPT2 (Novus Biologicals, NBP1-85471), ACADSB (Proteintech, 13122-1-AP), ABHD12B (Proteintech, 20623-1-AP), citrate synthase (Proteintech, 16131-1-AP), and DGAT1 (Novus Biologicals, NB110-41487). The analysis of liver KCs and iRPM populations involved the use of surface antibodies, including CD45 (Biolegend, 30-F11), F4/80 (Biolegend, BM8), and CD11b (Biolegend, M1/70). FPN detection was performed using a non-commercial antibody that recognizes the extracellular loop of mouse FPN (rat monoclonal, Amgen, clone 1C7) directly conjugated with Alexa488 (Alexa Fluor 488 Labeling Kit ab236553). To analyze RBCs, surface antibodies such as CD45 (Biolegend, 30-F11), TER-119 (Biolegend), and CD71 (Biolegend,

RI7217) were used. Lastly, the analysis of peritoneal macrophages involved the use of surface antibodies, including CD45 (Biolegend, 30-F11), F4/80 (Biolegend, BM8), MHCII (Biolegend, M5/114.15.2), and CD11b (Biolegend, M1/70). Events were acquired using Aria II (BD Biosciences) or CytoFLEX (Beckman Coulter) and were analyzed using FlowJo or CytExpert, respectively. For RNA sequencing (RNA-seq) and ATP levels quantification, RPMs were sorted into Trizol-LS (Invitrogen, 10296010) or assay buffer, respectively, using an Aria II cell sorter (BD Biosciences) with an 85 µm nozzle.

Functional Assays and Detection of Intracellular Fe^{2+} Iron

To assess intracellular ROS levels, CellROX Deep Red Reagent (Invitrogen, C10422) was used, and fluorescence was measured in the APC channel following the manufacturer's protocol. The lysosomal activity was evaluated using the Lysosomal Intracellular Activity Assay Kit (Biovision, K448) and fluorescence was measured in the FITC channel as directed by the manufacturer. To measure mitochondrial activity, the tetramethylrhodamine ethyl ester (TMRE) fluorescent probe (Sigma-Aldrich, 87917) was utilized at a concentration of 400 nM for 30 min at 37 °C, and the fluorescence was measured in the PE channel. Mitochondrial mass was measured by fluorescence levels upon staining with MitoTracker Green (Invitrogen, M7514) at 100 nM for 30 min at 37 °C in the FITC channel. Intracellular calcium (Ca^{2+}) levels were assessed using the Cal-520 AM probe (Abcam, ab171868) at 5 µM for 1 h at 37 °C. Briefly, surface-stained cells were incubated with the probe in HBSS, followed by immediate flow cytometric analysis in the FITC channel without further washing. Intracellular ferrous iron (Fe^{2+}) was quantified using FerroOrange (Dojindo, F374) with detection in the PE channel by flow cytometry. Surface-stained cells were incubated in HBSS containing 1 µM FerroOrange for 30 min at 37 °C and immediately analyzed without further wash steps. Lipid droplet content was quantified using the Lipid Droplet Assay Kit Deep Red (Dojindo, LD06-10) following the manufacturer's protocol, with fluorescence recorded in the APC channel. Glucose uptake was measured using the Glucose Uptake Capacity Assay Kit (Dojindo, UP03), and fluorescence was measured in the APC channel as per the manufacturer's protocol. To perform intracellular staining, cells that had already been surface-stained were fixed using 4% PFA and permeabilized with 0.5% Triton-X in PBS. The cells were then stained with appropriate primary antibodies for 1 h at 4°C, followed by a 30-minute incubation with Alexa Fluor 488 or Alexa Fluor 647 conjugated anti-Rabbit IgG (1:1000 Thermo Fisher, A-21206). Afterward, the geometric mean fluorescence intensities (MFI) of the probes/target protein levels were measured by flow cytometry using Aria II (BD Biosciences) or CytoFLEX (Beckman Coulter). Data were then analyzed using

FlowJo or CytExpert software, respectively. The MFI of the adequate fluorescence minus one (FMO) control was subtracted from the samples' MFI to quantify the data. The data were further normalized for analysis.

ATP levels

The levels of cellular ATP in FACS-sorted RPMs (10000 cells per sample) were measured using the ATP Assay Kit (Sigma-Aldrich, MAK473) according to the manufacturer's instructions.

Magnetic Sorting of RPMs

60 x 10^6 cells were incubated for 15 min at 4°C in PBS containing 5% Normal Rat Serum (Thermo Scientific, 10710C) and anti-CD16/32 antibody (Biolegend, 101320) in a 5 mL round-bottom tube. The cells were then labeled with anti-F4/80 (APC, Biolegend, 123116), anti-Ly-6G/Ly-6C (Gr-1) (Biotin, Biolegend, 108403), anti-CD3 (Biotin, Biolegend, 100243), anti-mouse Ly-6C (Biotin, Biolegend, 128003), and anti-B220 (Biotin, Biolegend, 103204) for 20 min at 4°C in the dark. The cells were washed with a cold PBS solution containing 2 mM EDTA and 0.5% BSA (hereafter referred to as "sorting buffer") and centrifuged at 600 g for 10 min. The pellet was resuspended in 400 µL of sorting buffer containing 50 µL of MojoSort Streptavidin Nanobeads (Biolegend, 480016) and kept in the cold and dark for 15 min. After incubation, an additional 400 µL of sorting buffer was added to the cells, and the tube was placed on an EasyEights EasySep Magnet (STEMCELL, 18103) for 7 min. The supernatant was transferred to a fresh 5 mL tube and centrifuged at 600 g for 10 min. The pellet was resuspended in 100 µL of sorting buffer, and 10 µL of MojoSort Mouse anti-APC Nanobeads (Biolegend, 480072) were added. The suspension was gently pipetted and incubated for 15 min at 4°C in the dark. The tube was then placed on a magnet for 7 min, and the supernatant was saved for analysis. The beads with attached F4/80+ cells were washed with sorting buffer and counted under a light microscope with a Neubauer chamber. The cells were pelleted and frozen in liquid nitrogen for further analysis.

Magnetic Sorting of RBCs, T Cells, B Cells, Granulocytes, Peritoneal Macrophages, and Kupffer Cells

RBCs, T cells, B cells, and granulocytes were magnetically isolated from spleen using the same general workflow as described for splenic RPM isolation, with modified antibody labeling and bead combinations. Single-cell suspensions were incubated with anti-CD16/32 to block Fcγ receptors on leukocytes prior to staining. Cells were stained with biotinylated antibodies against TER-119 (RBCs), B220 (B cells), and Gr-1 (granulocytes) and a PE-conjugated anti-CD3 antibody

(T cells) Biotin-labeled RBCs, B cells, and granulocytes were isolated using streptavidin Nanobeads, and $CD3^+$ T cells using anti-PE Nanobeads. This strategy yielded highly purified fractions of RBCs, T cells, B cells, and granulocytes for downstream analyses. Peritoneal macrophages were isolated using the same marker and bead strategy as splenic macrophages, with biotinylated antibodies against CD3, B220, and Gr-1 for lineage depletion, followed by positive selection of $F4/80^+$ cells using anti-APC nanobeads.

Magnetic sorting of Kupffer cells was performed according to a two-step liver perfusion protocol with minor modifications. Briefly, mice were euthanized, and livers were perfused in situ through the inferior vena cava with Liver Perfusion Medium for 3 min, followed by perfusion with prewarmed Liver Digest Medium for 15–20 min after transection of the portal vein. Digested livers were gently dissociated in RPMI 1640, filtered through a 100-µm strainer, and subjected to two rounds of low-speed centrifugation (50 g, 3 min) to remove hepatocytes. The resulting non-parenchymal cell fraction was centrifuged at 650 g for 15 min at 4 °C, treated with red blood cell lysis buffer, and further purified using a two-layer Percoll gradient. Cells collected from the interphase between 25% and 50% Percoll were washed, Fc-blocked, and incubated with anti-F4/80 MicroBeads UltraPure. $F4/80^+$ Kupffer cells were isolated using magnetized LS separation columns, washed, and prepared for downstream analyses. All cell isolations were performed at 4 °C, and purified cells were counted, pelleted, and snap-frozen in liquid nitrogen prior to intracellular BCAA quantification.

Measurement of Cellular Iron Levels

To determine the levels of total iron in magnetically sorted RPMs, the Iron Assay Kit from Sigma-Aldrich (MAK025) was employed by following the manufacturer's instructions. The volume of buffers and reagents used in the measurement of total iron in RPMs was adjusted accordingly. The absorbance at 593 nm was recorded using a Nanodrop ND-1000 Spectrophotometer from Thermo Fisher Scientific. Iron concentrations in RPMs (ng/µL) were calculated from the standard curve and then normalized to the number of cells in each sample.

***In Vivo* RBC Lifespan**

A sterile solution of EZ-Link Sulfo-NHS Biotin (Thermo Fisher Scientific, 21217) was prepared in PBS with a final concentration of 1 mg per 100 µL. The solution was then filtered through a 0.1 µm filter (Millipore, SLVV033RS). One day before the first blood collection, 100 µL of the sterile Biotin solution was intravenously injected into the mice. Blood samples were collected from the

tail vein on days 0, 5, 12, 16, and 21, using heparinized capillaries to prevent clotting. RBCs were separated by centrifugation at 400 g for 5 min at 4°C, and each sample was resuspended in 250 µL of HBSS containing 5% normal rat serum (Thermo Fisher Scientific). The suspension was then mixed with 2 µL of fluorescently labeled anti-TER-119 and streptavidin, except for the fluorescence minus one (FMO) sample in each group, where fluorescent streptavidin was omitted. After incubation at 4℃ for 30 min, the samples were centrifuged and resuspended in HBSS. Flow cytometry was used to determine the percentage of biotinylated erythrocytes.

Preparation of Stressed RBCs for Erythrophagocytosis Assays

The preparation and staining of stressed RBCs followed a previously outlined procedure[27,39]. To obtain the RBCs, mice were humanely euthanized, and whole blood was aseptically collected via cardiac puncture into CPDA-1 solution (Sigma-Aldrich, C4431) with a final concentration of 10%. The collected whole blood was combined, and plasma was separated by centrifugation at 400 g for 15 min at 4℃, then filtered through a 0.1 µm filter and stored at 4℃. The RBCs were then suspended in HBSS, and leukocytes were eliminated using Lymphosep (Biowest, L0560-500). Following this, the cells were subjected to a 30-minute heating period at 48℃ with continuous agitation to generate stressed RBCs. To stain the sRBCs, 1×10^{10} RBCs were resuspended in 1 ml of diluent C and mixed with 1 ml of diluent C containing 4 µM of PKH-67 (Sigma-Aldrich, MINI67) or PKH-26 (Sigma-Aldrich, MINI26). The mixture was then incubated in the dark for 5 min at 37℃, and the reaction was stopped by adding 10 mL of HBSS containing 2% FCS and 0.5% BSA. Staining was followed by two washing steps with HBSS. For *in vitro* EP assays, the cells were resuspended in RPMI-1640 and counted. For the *in vivo* approach, RBCs were resuspended to 50% hematocrit in previously collected and filtered plasma.

***In Vitro* Erythrophagocytosis**

On the 8th day post-seeding, stained, and counted sRBCs were added to iRPMs on 12-well plates in 10-fold excess for 1.5 h at 37 °C and 5% CO_2. After incubation, the cells were extensively washed with cold HBSS to eliminate any non-engulfed sRBCs. Subsequently, the cells were detached using Accutase (BioLegend, 423201), which were then transferred to a round-bottom FACS tube, washed with HBSS, and centrifuged at 600 g for 5 min. The cells were labeled with antibodies and analyzed using flow cytometry. For time-lapse confocal imaging of the execution of RBC uptake by iRPMs, sRBCs were stained with pH-sensitive pHrodo™ Deep Red Mammalian and Bacterial Cell Labeling Kit. The imaging was performed using the Opera Phenix

(PerkinElmer), an automated confocal spinning disk microscope. Imaging was conducted for 120 min, with acquisition every 1.3 min.

***In Vivo* Erythrophagocytosis**

The mice were intravenously transfused with 100 µL of RBCs resuspended in plasma to 50% hematocrit. The animals were kept in cages with ad libitum access to food and water for 1.5 h before being sacrificed for organ isolation.

Mini-Hepcidin (PR73) Preparation

An optimized protocol was developed for preparing mini-Hepcidin (PR73, a kind gift from Elizabeta Nemeth, UCLA, USA) for intraperitoneal injection in mice. Commercially available PR73 powder may not represent the pure peptide, so we adjusted the preparation based on the estimated active component content (80%). The process began by precisely weighing the PR73 powder to account for the estimated 80% active component. This powder was then dissolved in 80% ethanol to ensure complete extraction of the peptide. The solution was thoroughly mixed using a vortex mixer to achieve a homogenous suspension. Next, the solution was carefully transferred to a sterile, low-bind vial (SL-220) to minimize potential losses due to adsorption during incubation. A brief heat treatment at 37°C for a few seconds facilitated the complete dissolution of any undissolved particles. Following the heat treatment, the vial cap was removed, and the solution was aliquoted into designated culture tubes for individual injections. A Speedvac concentrator was then used to evaporate the ethanol, resulting in a concentrated PR73 gel within each tube. To achieve a final working concentration of 0.5 nmol/µl, 2 ml of sterile, injectable-grade water was added to each tube containing the PR73 gel. The tubes were vigorously vortexed to ensure complete dissolution of the gel and homogenization of the solution. For *in vivo* experiments, 100 µl of the prepared PR73 stock solution was administered per mouse via intraperitoneal injection. A solvent control solution was prepared by following the same steps outlined above but substituting the PR73 solution with only 80% ethanol. This control solution served as a baseline for comparison with the PR73-treated mice in subsequent experiments.

Live-Cell Imaging of Erythrophagocytosis in iRPMs

To assess erythrophagocytic capacity, iRPMs were seeded in Greiner Bio-One CELLSTAR µClear™ 96-well, Cell Culture-Treated, Flat-Bottom Microplate and cultured with IB versus ID serum. iRPMs with ID serum were treated with PR73 for 4 h. Following PR73 treatment, iRPMs were exposed to temperature-stressed, pHrodo-labeled RBCs, prepared using the pHrodo™ Deep

Red Mammalian and Bacterial Cell Labeling Kit (Thermo Fisher Scientific). The stressed and labeled RBCs were added to the wells, and the plate was immediately transferred to the Opera Phenix™ High-Content Screening System (PerkinElmer), maintained at 37°C with 5% CO_2. Live-cell imaging was performed for 2 h with images captured at regular intervals to monitor the uptake of RBCs, and data were analyzed using Harmony High-Content Imaging and Analysis Software (PerkinElmer).

BCAA levels

Intracellular branched-chain amino acid content was quantified in magnetically sorted $CD3^+$ T cells, $B220^+$ B cells, together with $GR1^+$ granulocytes, RPMs, peritoneal macrophages, and Kupffer cells, using the Branched Chain Amino Acid Assay Kit (Sigma-Aldrich, MAK003) following the manufacturer's instructions.

Metabolic Flux Seahorse Assay

Metabolic flux was assessed using a Seahorse XF-96 Extracellular Flux Analyzer (Agilent Technologies) Mito Stress Test (Agilent,103010-100). Magnetically sorted RPMs (8×10^4 cells/well) from IB and ID mice were plated onto poly-L-lysine-coated Seahorse XF HS Miniplates (Agilent, 103725-100). Cells were incubated in Seahorse XF RPMI medium (Agilent, 103576-100) supplemented with 2 mM L-glutamine (Agilent, 103579-100), 1 mM sodium pyruvate (Agilent, 103578-100), and 25 mM glucose (pH adjusted to 7.4; Agilent 103577-100) at 37°C in a non-CO_2 incubator for 60 min. Real-time oxygen consumption rate (OCR) was measured under basal conditions and following sequential injections of 1 µM oligomycin, 1 µM FCCP, and a mixture of 1 µM rotenone and 1 µM antimycin A.

Mitochondrial substrate utilization (MitoPlate) Assay

Mitochondrial substrate utilization was assessed using the MitoPlate S-1 assay (Biolog, 14105) according to the manufacturer's protocol. Magnetically sorted RPMs from IB, ID, and ID+ERG240 mice were pooled (four mice per condition), counted, and resuspended in MitoPlate assay medium before seeding at 8×10^4 cells per well onto the precoated 96-well Mitoplates, containing the dye mix MC. Plates were loaded into a Tecan Infinite 200 Pro maintained at 37°C, and kinetic OD_{590} measurements were collected every 10 min throughout the assay. Absolute blank-corrected OD values from the 6-h time point were used for analysis.

Voluntary Oral Drug Administration

Strawberry-flavored gelatin jellies were prepared under sterile conditions in 96-well plates (100 µL/well), with or without ENTO and ERG240. Gelatin (8% w/v, Sigma-Aldrich, G9391) was dissolved in warm, sterile water, and strawberry flavoring essence (1% v/v, OstroVit, 5903933916217) was added. Just before gelation, ENTO or ERG240 was added to the appropriate wells of a sterile 96-well plate to achieve the desired final concentration, while control wells received vehicle only. The gelatin solution (100 µL) was then added to each well, and the plates were refrigerated at 4°C until solid. To acclimate IB and ID mice, two drug-free jellies were provided per cage daily for 2-3 days (two mice per cage). This co-housing approach minimized stress associated with individual training. Following acclimation, mice readily consumed the jellies within 15-20 min. Drug-containing jellies were administered at approximately the same time each day for two or three weeks.

Generation of Ferroportin Overexpressing iRPMs

We successfully cloned the wild-type *Slc40a1* gene, encoding mouse ferroportin (FPN; Uniport ID: Q9JHI9), into the HIV SFFV lentiviral vector. Lentiviral production involved transfecting the chosen lentiviral vectors (FPN or Mock) along with the psPAX2 packaging vector and the pMD2.G envelope vector into HEK293T cells. The resulting viral supernatants were harvested and titrated to determine viral concentration. Subsequently, iRPMs were transduced on Day 1 with lentiviral vectors at a multiplicity of infection (MOI) of 1. On Days 4 and 6, the culture medium was replaced with fresh complete medium supplemented with 20 µM hemin. Expression levels of surface FPN were measured in each experiment using flow cytometry. This verification step confirmed successful FPN overexpression in iRPM population, allowing for functional analysis of the consequences in subsequent experiments.

Hepcidin Measurement with ELISA

Serum hepcidin levels were measured using the Hepcidin-Murine Compete ELISA Kit (Intrinsic LifeSciences, HMC-001) following the manufacturer's instructions. Optical density was determined with a microplate reader at a wavelength of 450 nm.

Erythropoietin (EPO) Measurement with ELISA

Serum EPO levels were measured using the Mouse Erythropoietin/EPO Quantikine ELISA Kit (R&D Systems, MEP00B) following the manufacturer's instructions. Optical density was determined with a microplate reader at a wavelength of 450 nm.

Transferrin Saturation and Tissue Iron Measurements

The levels of serum iron and unsaturated iron-binding capacity were quantified using SFBC (Biolabo, 80008) and UIBC (Biolabo, 97408) kits per the manufacturer's instructions. Transferrin saturation was determined using the formula SFBC/(SFBC+UIBC) x 100. Tissue non-heme iron content was measured using the bathophenanthroline method, and the results were calculated based on tissue dry weight, as previously described[89].

RT-qPCR

RNA from cell pellets was isolated using an RNA purification kit (Eurex) according to the manufacturer's instructions. RNA from liver, heart and kidney tissues was isolated using TRIzol™ reagent according to the manufacturer's instructions. 400 ng of RNA was subjected to reverse transcription. In the first stage of the reaction, RNA was denatured, and random primers were attached. For this purpose, a mixture consisting of 400 ng RNA, 1 µL of random primers at a concentration of 200 ng/µL, and nuclease-free water was prepared so that the total reaction volume was 17.7 µL. The mixture was incubated at 70°C for 10 min and then cooled to 4°C. The next step was to add the reaction mixture to the tubes, which contained: 0.3 µl RevertAid H Minus reverse transcriptase, 1 µL of 10 mM dNTP solution, and 5 µL of reaction buffer. The total reaction volume was 25 µL. The reaction was carried out for 60 min at 42°C, 70°C, 10 min. The obtained cDNA was diluted 9x and then used for quantitative polymerase chain reaction (qPCR). The reaction mixture consisted of 4 µL cDNA, 7.5 µL SG qPCR Master Mix (2x), and 1.5 µL of a 5 µM solution of forward and reverse primers. The whole was supplemented with nuclease-free water to a final reaction volume of 15 µL. The qPCR reaction was carried out using the LightCycler 96 Real-Time PCR System (Roche). The reaction was pre-incubated at 95°C for 600 s, and then two-step amplification was performed 40x (95°C x 15 s, 60°C x 60 s).

Immunohistochemistry of Spleen Tissues

The spleen was fixed in 4% PFA at 4°C for 24 h. Tissues were washed with PBS (3x30min) and incubated for 2 h in 12.5% and then in 25% sucrose solution for 48 h. Subsequently, spleen tissue fragments were embedded in the Cryomatrix medium, frozen in liquid nitrogen, and cut into 10 µm thick sections using a cryo microtome (Leica). The sections were mounted on glass slides and stored at -20°C. Before staining, the sections were warmed at room temperature for 30 min, and then their edges were surrounded using a Pap Pen Liquid Blocker. Next, the slides with sections were washed in PBS for 10 min and permeabilized in 0.1% Triton X-100 solution for 20 min.

Nonspecific antibody binding was blocked by incubating the sections in 3% BSA solution for 1 h at room temperature. To visualize RPMs, the tissues were incubated with FITC-conjugated F4/80 antibody (1:100), and for FPN, with Alexa Fluor 647-conjugated FPN antibody (1:100) in 3% BSA for 2 h at room temperature in the dark. After incubation with antibodies, the tissues were washed 5 x 5 min in 0.1% Triton X-100 solution to remove unbound antibodies. To stain cell nuclei, the sections were incubated with Hoechst 33342 diluted in 0.1% Triton X-100 solution (final concentration 1 µg/ml) for 10 min at room temperature in the dark. Then, the sections were washed for 3 x 5 min in 0.1% Triton X-100 solution, incubated in PBS for 10 min, and mounted with a coverslip using ProLong™ Glass Antifade Mountant. Samples were imaged on a confocal microscope with a Plan-Apochromat 40x/1.3 NA oil immersion objective (Zeiss) LSM 800.

Histological and Histochemical Analysis

Following fixation in 10% formalin for 24 h, spleens were stored in 70% ethanol before further preparation. The tissue was embedded in paraffin and 7 µm cross-sections were cut with a microtome (Reichert-Jung, Germany). Sections were prepared as described above. After mounting on glass slides, sections were deparaffinized, incubated with a working solution containing Perls' Prussian Blue for 30 min, counterstained with pararosaniline solution for 2 min, and analyzed under standard light microscopy (Olympus CH2).

Transcriptome analysis by RNA-seq

RNA-seq libraries were generated from FACS-sorted RPMs (minimum 100,000 cells per sample) using the Smart-seq2 protocol[90], which is optimized for low-input total mRNA sequencing. RNA integrity and library quality were checked by a Bioanalyzer. Sequencing was performed on an Illumina NextSeq500 platform, producing 75-bp single-end reads at ~50 million reads per sample. RNA-seq was carried out at the EMBL GeneCore facility (Heidelberg, Germany). Sequence reads were trimmed to remove possible adapter sequences and nucleotides with poor quality using Trimmomatic v.0.36. The trimmed reads were mapped to the Mus musculus GRCm38 reference genome available on ENSEMBL using the STAR aligner v.2.5.2b. Unique gene hit counts were calculated by using featureCounts from the Subread package v.1.5.2. Normalization and differential expression analysis were performed using DESeq2. The Wald test was used to generate p-values and log2 fold changes. Genes with an adjusted p-value < 0.05 and absolute log2 fold change > 1 were called as differentially expressed genes.

Proteomic analysis of RPMs

Sample Preparation. Magnetically isolated RPMs were obtained from the spleens of IB and ID female C57BL/6J mice. The cells were lysed using RIPA buffer. Proteins were precipitated using a chloroform/methanol method, washed with methanol, and reconstituted in 100 mM HEPES (pH 8.0) containing 10 mM TCEP and 10 mM chloroacetamide.

LC-MS/MS Analysis. 10 µg of each lysate was subjected to an in-solution tryptic digest using a modified version of the Single-Pot Solid-Phase-enhanced Sample Preparation (SP3) protocol[91,92]. To this end, lysates were added to Sera-Mag Beads (Thermo Scientific, #4515-2105-050250, 6515-2105-050250) in 10 µl 15% formic acid and 30 µl of ethanol. The binding of proteins was achieved by shaking for 15 min at room temperature. SDS was removed by 4 subsequent washes with 200 µl of 70% ethanol. Proteins were digested overnight at room temperature with 0.4 µg of sequencing grade modified trypsin (Promega, V5111) in 40 µl Hepes/NaOH, pH 8.4 in the presence of 1.25 mM TCEP and 5 mM chloroacetamide (Sigma-Aldrich, C0267). Beads were separated and washed with 10 µl of an aqueous solution of 2% DMSO, and the combined eluates were dried down.

Up to 10 µg of peptides per sample were labeled with TMT10plex™ reagents following established protocols[93]. Briefly, 0.8 mg of TMT reagent was dissolved in 45 µL of anhydrous acetonitrile, and 4 µL of this solution was added to each peptide sample. Labeling was carried out at room temperature for 1 h. The reaction was quenched by adding 4 µL of 5% hydroxylamine in water, followed by a 15-minute incubation at room temperature. Labeled peptides were pooled for multiplexing, desalted using an Oasis® HLB µElution Plate (Waters #186001828BA) according to the manufacturer's instructions, and dried by vacuum centrifugation.

Offline high-pH reversed-phase fractionation was performed as described previously[94], using an Agilent 1200 Infinity HPLC system equipped with a Gemini C18 analytical column (3 µm particle size, 110 Å pore size, 100 × 1.0 mm; Phenomenex) and a matching Gemini C18 SecurityGuard pre-column (4 × 2.0 mm; Phenomenex). Peptides were separated at a flow rate of 0.1 mL/min using mobile phase A (20 mM ammonium formate, pH 10.0) and mobile phase B (100% acetonitrile). The chromatographic gradient was as follows: 100% A for 2 min, linear increase to 35% B over 59 min, ramp to 85% B in 1 min, held at 85% B for 15 min, followed by re-equilibration at 100% A for 13 min. A total of 48 fractions were collected and subsequently pooled into 12 final fractions. Nanoflow LC-MS/MS analysis was performed on an UltiMate 3000 RSLCnano system (Thermo Fisher Scientific) coupled to an Orbitrap Fusion™ Lumos™ Tribrid™ mass spectrometer (Thermo

Fisher Scientific). Peptides were initially loaded onto a µ-Precolumn C18 PepMap™ 100 trap cartridge (300 µm i.d. × 5 mm, 5 µm particles, 100 Å; Thermo) at 30 µL/min with 0.05% TFA in water for 6 min. Analytical separation was carried out using a nanoEase™ M/Z HSS T3 column (75 µm i.d. × 250 mm, 1.8 µm particles, 100 Å; Waters), equilibrated with solvent A (3% DMSO, 0.1% formic acid in water). Peptides were eluted at 0.3 µL/min using a gradient of solvent B (3% DMSO, 0.1% formic acid in acetonitrile) as follows: 2–8% B over 6 min, 8–25% over 99 min, 25–40% over 5 min, ramp to 85% in 0.1 min, held at 85% for 3.9 min, followed by re-equilibration to 2% B for 6 min. Mass spectrometry was performed using a Pico-Tip emitter (360 µm OD × 20 µm ID, 10 µm tip; CoAnn Technologies) with a spray voltage of 2.4 kV and a capillary temperature of 275 °C. Full MS scans were acquired in the Orbitrap at a resolution of 120,000 (at m/z 200), over a mass range of m/z 375–1,500, with an AGC target set to 'standard' and a maximum injection time of 50 ms. The instrument operated in data-dependent acquisition (DDA) mode. MS/MS spectra were acquired in the Orbitrap at a resolution of 30,000, with a maximum injection time of 94 ms and an AGC target of 200%. Precursors were fragmented using higher-energy collisional dissociation (HCD) at 36% normalized collision energy. A quadrupole isolation window of 0.7 m/z was used, with dynamic exclusion set to 60 s. Only precursor ions with charge states between 2 and 7 were selected for fragmentation.

Acquired data were analyzed using IsobarQuant and Mascot V2.4 (Matrix Science) using a reverse UniProt FASTA Mus musculus database (UP000000589), including common contaminants. The following modifications were considered: Carbamidomethyl (C, fixed), TMT10plex (K, fixed), Acetyl (N-term, variable), Oxidation (M, variable), and TMT10plex (N-term, variable). The mass error tolerance for full scan MS spectra was set to 10 ppm, and for MS/MS spectra to 0.02 Da. A maximum of 2 missed cleavages were allowed. A minimum of 2 unique peptides with a peptide length of at least seven amino acids and a false discovery rate below 0.01 were required on the peptide and protein level.

Data Processing. The data were processed using MaxQuant 2.1.3.0, with peptides identified from MS/MS spectra searched against the Uniprot Mouse Reference Proteome (UP000000589) using the built-in Andromeda search engine. Fixed modifications included cysteine carbamidomethylation, while variable modifications included methionine oxidation, glutamine/asparagine deamination, and protein N-terminal acetylation. In silico digests allowed for cleavages of arginine or lysine followed by any amino acid (trypsin/P), with up to two missed cleavages permitted. The false discovery rate (FDR) was set to 0.01 for peptides, proteins, and

sites. Match between runs was enabled, and other parameters were used as preset in the software. Protein identification and intrasample quantification were performed using the iBAQ algorithm in MaxQuant.

Transmission Electron Microscopy (TEM) of the Spleen

Fresh spleen samples, approximately 3 mm^2 in size, were fixed in 2.5% glutaraldehyde for 24 h at 4°C. Following fixation, the samples were washed in PBS and postfixed with 1% osmium tetroxide for 1 h. After rinsing with water, the samples were incubated in 1% aqueous uranyl acetate for 12 h at 4°C. The samples were then dehydrated at room temperature using increasing concentrations of ethanol, infiltrated with epoxy resin (Sigma-Aldrich, 45-359-1EA-F), and polymerized for 48 h at 60°C. The polymerized resin blocks were trimmed using a tissue processor (Leica EM TP) and sectioned into ultrathin slices (65 nm thick) with an ultramicrotome (EM UC7, Leica). These ultrathin sections were collected on nickel grids with 200 mesh (Agar Scientific, G2200N). The specimen grids were examined with a Tecnai T12 BioTwin transmission electron microscope (FEI, Hillsboro, OR, USA) equipped with a 16-megapixel TemCam-F416 camera (TVIPS GmbH) at the in-house Microscopy and Cytometry Facility.

Preparation of Schematic Figures

The graphical abstract was created in BioRender. Mleczko-Sanecka, K. (2025) https://BioRender.com/y54j6da.

Statistical Analysis

Female mice of the same age were randomly assigned to experimental groups. Samples derived from mice were collected and assessed/measured randomly, and harvested in a different order across individual experiments. The sample size, typically ranging from 5 to 9 mice per group or independent biological cell-based experiments, was determined based on power analysis, prior experience with similar experiments, and previously published studies in the field of RPM biology. Statistical analysis was conducted using GraphPad Prism (GraphPad Software, Version 9). Data are presented as mean ± SEM unless otherwise noted. Student's t-test with Welch's correction was employed when comparing the two groups. For comparisons involving more than two groups, one-way ANOVA was used, or two-way ANOVA when the simultaneous effects of two factors were being evaluated. Tukey's test was implemented for post-hoc analysis following ANOVA. The following notation was used to indicate statistically significant differences between means: ns for

non-significant ($p > 0.05$), * for $p < 0.05$, ** for $p < 0.01$, *** for $p < 0.001$, and **** for $p < 0.0001$.

Data availability

Mass spectrometry proteomics data were deposited to the ProteomeXchange Consortium via the PRIDE partner repository with the dataset identifiers: Project accession: PXD064719 (access secured by a token: lKilHQArXhhB). RNA sequencing data are available in Gene Expression Omnibus GEO under the accession number GSE312948, and metadata were deposited to SRA (PRJNA1274426).

Authorship Contributions

KMS, PKM, RM, KC and PS conceived and planned the experiments; PKM, RM, KC, PS, GZ, MN, AJ, and ML performed research; PKM, RM, KC, PS, GZ, KMS and ML analyzed and visualized data; EN, ZL and FG provided critical reagents/models, KC and KMS curated data; KMS, WP, and EN supervised the study; KC edited the manuscript; PKM, RM and KMS wrote the manuscript.

Conflict of interest

EN is a shareholder and scientific advisor of Intrinsic LifeSciences and Silarus Therapeutics, and a consultant for Disc Medicine, Ionis Pharmaceuticals, Protagonist, GSK and Vifor. Other authors have declared that no conflict of interest exists.

Acknowledgments

We thank the EMBL Proteomics Core Facility (EMBL, Heidelberg) for performing RPM proteomic profiling and data analysis, and the GeneCore team (EMBL, Heidelberg) for performing RNA sequencing. We thank Tara Arvedson (Amgen Inc., USA) for the anti-ferroportin antibody, Elizabeta Nemeth (UCLA, USA) for PR73, Florent Ginhoux for access to Ms4a3-Cre mice, and Aneta Suwińska for sharing UBI-GFP/BL6 mice, and Vania Manolova (CSL Vifor) for providing vamifeport. Many thanks to Agnieszka Popielska and Anna Kosson, and the staff of the Experimental Medicine Centre (Bialystok, Poland) and Mossakowski Medical Research Institute (Warsaw, Poland) for their technical support. We thank Sylwia Herman for her assistance with the histological analyses and Enrico Tatti for consulting on the MitoPlates profiling data. Mouse-based experiments and animal housing were supported by the Rodent Facility, EM, and Opera Phenix imaging were performed at the Microscopy Facility, and lentiviral DNA constructs were generated

at the Genome Engineering Facility of IIMCB (IN-MOL-CELL Infrastructure) funded by the European Union – NextGenerationEU under the National Recovery and Resilience Plan. IN-MOL-CELL Infrastructure was also funded by the European Union under Horizon Europe (Project 101059801 - RACE) and by the RACE-PRIME project carried out within the IRAP programme of the Foundation for Polish Science, co-financed by the European Union under the European Funds for Smart Economy 2021-2027 (FENG). Pratik Kumar Mandal gratefully acknowledges funding from the National Science Centre PRELUDIUM 22 grant, which supported experiments involving lentiviral-mediated FPN overexpression (UMO-2023/49/N/NZ3/04232). This work was funded by the National Science Centre Sonata Bis grant (UMO-2020/38/E/NZ4/00511).

During the preparation of this work, the authors used ChatGPT 5.2 to assist with language editing in a limited number of instances. After using this tool, the authors reviewed and edited the content as needed and take full responsibility for the content of the published article.

References

1. Boada-Romero, E., Martinez, J., Heckmann, B.L., and Green, D.R. (2020). The clearance of dead cells by efferocytosis. Nat Rev Mol Cell Biol *21*, 398–414. https://doi.org/10.1038/s41580-020-0232-1.

2. Doran, A.C., Yurdagul, A., and Tabas, I. (2020). Efferocytosis in health and disease. Nat Rev Immunol *20*, 254–267. https://doi.org/10.1038/s41577-019-0240-6.

3. Moon, B., Yang, S., Moon, H., Lee, J., and Park, D. (2023). After cell death: the molecular machinery of efferocytosis. Exp Mol Med *55*, 1644–1651. https://doi.org/10.1038/s12276-023-01070-5.

4. Sheng, Y.R., Hu, W.T., Chen, S., and Zhu, X.Y. (2024). Efferocytosis by macrophages in physiological and pathological conditions: regulatory pathways and molecular mechanisms. Front Immunol *15*, 1275203. https://doi.org/10.3389/fimmu.2024.1275203.

5. Schilperoort, M., Ngai, D., Sukka, S.R., Avrampou, K., Shi, H., and Tabas, I. (2023). The role of efferocytosis-fueled macrophage metabolism in the resolution of inflammation. Immunol Rev *319*, 65–80. https://doi.org/10.1111/imr.13214.

6. Mukundan, L., Odegaard, J.I., Morel, C.R., Heredia, J.E., Mwangi, J.W., Ricardo-Gonzalez, R.R., Goh, Y.P.S., Eagle, A.R., Dunn, S.E., Awakuni, J.U.H., et al. (2009). PPAR-delta senses and orchestrates clearance of apoptotic cells to promote tolerance. Nat Med *15*, 1266–1272. https://doi.org/10.1038/nm.2048.

7. A-Gonzalez, N., Bensinger, S.J., Hong, C., Beceiro, S., Bradley, M.N., Zelcer, N., Deniz, J., Ramirez, C., Díaz, M., Gallardo, G., et al. (2009). Apoptotic cells promote their own clearance and immune tolerance through activation of the nuclear receptor LXR. Immunity *31*, 245–258. https://doi.org/10.1016/j.immuni.2009.06.018.

8. Mota, A.C., Dominguez, M., Weigert, A., Snodgrass, R.G., Namgaladze, D., and Brüne, B. (2021). Lysosome-Dependent LXR and PPARδ Activation Upon Efferocytosis in Human Macrophages. Front Immunol *12*, 637778. https://doi.org/10.3389/fimmu.2021.637778.

9. Schilperoort, M., Ngai, D., Katerelos, M., Power, D.A., and Tabas, I. (2023). PFKFB2-mediated glycolysis promotes lactate-driven continual efferocytosis by macrophages. Nat Metab *5*, 431–444. https://doi.org/10.1038/s42255-023-00736-8.

10. Morioka, S., Perry, J.S.A., Raymond, M.H., Medina, C.B., Zhu, Y., Zhao, L., Serbulea, V., Onengut-Gumuscu, S., Leitinger, N., Kucenas, S., et al. (2018). Efferocytosis induces a novel SLC program to promote glucose uptake and lactate release. Nature *563*, 714–718. https://doi.org/10.1038/s41586-018-0735-5.

11. Zhang, S., Weinberg, S., DeBerge, M., Gainullina, A., Schipma, M., Kinchen, J.M., Ben-Sahra, I., Gius, D.R., Yvan-Charvet, L., Chandel, N.S., et al. (2019). Efferocytosis Fuels Requirements of Fatty Acid Oxidation and the Electron Transport Chain to Polarize Macrophages for Tissue Repair. Cell Metab *29*, 443-456.e5. https://doi.org/10.1016/j.cmet.2018.12.004.

12. Wang, Y., Subramanian, M., Yurdagul, A., Barbosa-Lorenzi, V.C., Cai, B., de Juan-Sanz, J., Ryan, T.A., Nomura, M., Maxfield, F.R., and Tabas, I. (2017). Mitochondrial Fission Promotes the Continued Clearance of Apoptotic Cells by Macrophages. Cell *171*, 331-345.e22. https://doi.org/10.1016/j.cell.2017.08.041.

13. Jiang, S., Park, D.W., Stigler, W.S., Creighton, J., Ravi, S., Darley-Usmar, V., and Zmijewski, J.W. (2013). Mitochondria and AMP-activated protein kinase-dependent mechanism of efferocytosis. J Biol Chem *288*, 26013–26026. https://doi.org/10.1074/jbc.M113.489468.

14. Tsai, T.-L., Zhou, T.-A., Hsieh, Y.-T., Wang, J.-C., Cheng, H.-K., Huang, C.-H., Tsai, P.-Y., Fan, H.-H., Feng, H.-K., Huang, Y.-C., et al. (2022). Multiomics reveal the central role of pentose phosphate pathway in resident thymic macrophages to cope with efferocytosis-associated stress. Cell Rep *40*, 111065. https://doi.org/10.1016/j.celrep.2022.111065.

15. He, D., Mao, Q., Jia, J., Wang, Z., Liu, Y., Liu, T., Luo, B., and Zhang, Z. (2021). Pentose Phosphate Pathway Regulates Tolerogenic Apoptotic Cell Clearance and Immune Tolerance. Front Immunol *12*, 797091. https://doi.org/10.3389/fimmu.2021.797091.

16. Yurdagul, A., Subramanian, M., Wang, X., Crown, S.B., Ilkayeva, O.R., Darville, L., Kolluru, G.K., Rymond, C.C., Gerlach, B.D., Zheng, Z., et al. (2020). Macrophage Metabolism of Apoptotic Cell-Derived Arginine Promotes Continual Efferocytosis and Resolution of Injury. Cell Metab *31*, 518-533.e10. https://doi.org/10.1016/j.cmet.2020.01.001.

17. Ampomah, P.B., Cai, B., Sukka, S.R., Gerlach, B.D., Yurdagul, A., Wang, X., Kuriakose, G., Darville, L.N.F., Sun, Y., Sidoli, S., et al. (2022). Macrophages use apoptotic cell-derived

methionine and DNMT3A during efferocytosis to promote tissue resolution. Nat Metab *4*, 444–457. https://doi.org/10.1038/s42255-022-00551-7.

18. Sukka, S.R., Ampomah, P.B., Darville, L.N.F., Ngai, D., Wang, X., Kuriakose, G., Xiao, Y., Shi, J., Koomen, J.M., McCusker, R.H., et al. (2024). Efferocytosis drives a tryptophan metabolism pathway in macrophages to promote tissue resolution. Nat Metab *6*, 1736–1755. https://doi.org/10.1038/s42255-024-01115-7.

19. Merlin, J., Ivanov, S., Dumont, A., Sergushichev, A., Gall, J., Stunault, M., Ayrault, M., Vaillant, N., Castiglione, A., Swain, A., et al. (2021). Non-canonical glutamine transamination sustains efferocytosis by coupling redox buffering to oxidative phosphorylation. Nat Metab *3*, 1313–1326. https://doi.org/10.1038/s42255-021-00471-y.

20. Muckenthaler, M.U., Rivella, S., Hentze, M.W., and Galy, B. (2017). A Red Carpet for Iron Metabolism. Cell *168*, 344–361. https://doi.org/10.1016/j.cell.2016.12.034.

21. Slusarczyk, P., and Mleczko-Sanecka, K. (2021). The Multiple Facets of Iron Recycling. Genes (Basel) *12*, 1364. https://doi.org/10.3390/genes12091364.

22. Klei, T.R.L., Meinderts, S.M., van den Berg, T.K., and van Bruggen, R. (2017). From the Cradle to the Grave: The Role of Macrophages in Erythropoiesis and Erythrophagocytosis. Front Immunol *8*, 73. https://doi.org/10.3389/fimmu.2017.00073.

23. Nemeth, E., Tuttle, M.S., Powelson, J., Vaughn, M.B., Donovan, A., Ward, D.M., Ganz, T., and Kaplan, J. (2004). Hepcidin regulates cellular iron efflux by binding to ferroportin and inducing its internalization. Science *306*, 2090–2093. https://doi.org/10.1126/science.1104742.

24. Aschemeyer, S., Qiao, B., Stefanova, D., Valore, E.V., Sek, A.C., Ruwe, T.A., Vieth, K.R., Jung, G., Casu, C., Rivella, S., et al. (2018). Structure-function analysis of ferroportin defines the binding site and an alternative mechanism of action of hepcidin. Blood *131*, 899–910. https://doi.org/10.1182/blood-2017-05-786590.

25. Mleczko-Sanecka, K., and Silvestri, L. (2021). Cell-type-specific insights into iron regulatory processes. Am J Hematol *96*, 110–127. https://doi.org/10.1002/ajh.26001.

26. Kohyama, M., Ise, W., Edelson, B.T., Wilker, P.R., Hildner, K., Mejia, C., Frazier, W.A., Murphy, T.L., and Murphy, K.M. (2009). Role for Spi-C in the development of red pulp macrophages and splenic iron homeostasis. Nature *457*, 318–321. https://doi.org/10.1038/nature07472.

27. Slusarczyk, P., Mandal, P.K., Zurawska, G., Niklewicz, M., Chouhan, K., Mahadeva, R., Jończy, A., Macias, M., Szybinska, A., Cybulska-Lubak, M., et al. (2023). Impaired iron recycling from erythrocytes is an early hallmark of aging. Elife *12*, e79196. https://doi.org/10.7554/eLife.79196.

28. Okreglicka, K., Iten, I., Pohlmeier, L., Onder, L., Feng, Q., Kurrer, M., Ludewig, B., Nielsen, P., Schneider, C., and Kopf, M. (2021). PPARγ is essential for the development of bone marrow erythroblastic island macrophages and splenic red pulp macrophages. J Exp Med *218*, e20191314. https://doi.org/10.1084/jem.20191314.

29. Delaby, C., Pilard, N., Puy, H., and Canonne-Hergaux, F. (2008). Sequential regulation of ferroportin expression after erythrophagocytosis in murine macrophages: early mRNA induction by haem, followed by iron-dependent protein expression. Biochem J *411*, 123–131. https://doi.org/10.1042/BJ20071474.

30. Bian, Z., Shi, L., Guo, Y.-L., Lv, Z., Tang, C., Niu, S., Tremblay, A., Venkataramani, M., Culpepper, C., Li, L., et al. (2016). Cd47-Sirpα interaction and IL-10 constrain inflammation-induced macrophage phagocytosis of healthy self-cells. Proc Natl Acad Sci U S A *113*, E5434-5443. https://doi.org/10.1073/pnas.1521069113.

31. Bennett, L.F., Liao, C., Quickel, M.D., Yeoh, B.S., Vijay-Kumar, M., Hankey-Giblin, P., Prabhu, K.S., and Paulson, R.F. (2019). Inflammation induces stress erythropoiesis through heme-dependent activation of SPI-C. Sci Signal *12*, eaap7336. https://doi.org/10.1126/scisignal.aap7336.

32. Ma, S., Dubin, A.E., Zhang, Y., Mousavi, S.A.R., Wang, Y., Coombs, A., Loud, M., Andolfo, I., and Patapoutian, A. (2021). A role of PIEZO1 in iron metabolism in mice and humans. Cell *184*, 969-982.e13. https://doi.org/10.1016/j.cell.2021.01.024.

33. Camaschella, C. (2019). Iron deficiency. Blood *133*, 30–39. https://doi.org/10.1182/blood-2018-05-815944.

34. Pasricha, S.-R., Tye-Din, J., Muckenthaler, M.U., and Swinkels, D.W. (2021). Iron deficiency. Lancet *397*, 233–248. https://doi.org/10.1016/S0140-6736(20)32594-0.

35. GBD 2021 Anaemia Collaborators (2023). Prevalence, years lived with disability, and trends in anaemia burden by severity and cause, 1990-2021: findings from the Global Burden of Disease Study 2021. Lancet Haematol *10*, e713–e734. https://doi.org/10.1016/S2352-3026(23)00160-6.

36. Atkinson, S.H., Suchdev, P.S., Bode, M., Carducci, B., Cerami, C., Mwangi, M.N., Namaste, S., Winichagoon, P., Leung, S., Mutua, A.M., et al. (2025). Getting back on track to meet global anaemia reduction targets: a Lancet Haematology Commission. Lancet Haematol *12*, e717–e767. https://doi.org/10.1016/S2352-3026(25)00146-2.

37. Camaschella, C., and Girelli, D. (2020). The changing landscape of iron deficiency. Mol Aspects Med *75*, 100861. https://doi.org/10.1016/j.mam.2020.100861.

38. Al-Naseem, A., Sallam, A., Choudhury, S., and Thachil, J. (2021). Iron deficiency without anaemia: a diagnosis that matters. Clin Med (Lond) *21*, 107–113. https://doi.org/10.7861/clinmed.2020-0582.

39. Theurl, I., Hilgendorf, I., Nairz, M., Tymoszuk, P., Haschka, D., Asshoff, M., He, S., Gerhardt, L.M.S., Holderried, T.A.W., Seifert, M., et al. (2016). On-demand erythrocyte disposal and iron recycling requires transient macrophages in the liver. Nat Med *22*, 945–951. https://doi.org/10.1038/nm.4146.

40. Klei, T.R.L., Dalimot, J., Nota, B., Veldthuis, M., Mul, F.P.J., Rademakers, T., Hoogenboezem, M., Nagelkerke, S.Q., van IJcken, W.F.J., Oole, E., et al. (2020). Hemolysis in the spleen drives erythrocyte turnover. Blood *136*, 1579–1589. https://doi.org/10.1182/blood.2020005351.

41. Zurawska, G., Sas, Z., Jończy, A., Mahadeva, R., Slusarczyk, P., Chwałek, M., Seehofer, D., Damm, G., Mazgaj, R., Skórzyński, M., et al. (2026). Liver sinusoidal endothelial cells constitute a major route for hemoglobin clearance. EMBO Rep. https://doi.org/10.1038/s44319-025-00673-5.

42. Akilesh, H.M., Buechler, M.B., Duggan, J.M., Hahn, W.O., Matta, B., Sun, X., Gessay, G., Whalen, E., Mason, M., Presnell, S.R., et al. (2019). Chronic TLR7 and TLR9 signaling drives anemia via differentiation of specialized hemophagocytes. Science *363*, eaao5213. https://doi.org/10.1126/science.aao5213.

43. Liu, Z., Gu, Y., Chakarov, S., Bleriot, C., Kwok, I., Chen, X., Shin, A., Huang, W., Dress, R.J., Dutertre, C.-A., et al. (2019). Fate Mapping via Ms4a3-Expression History Traces Monocyte-Derived Cells. Cell *178*, 1509-1525.e19. https://doi.org/10.1016/j.cell.2019.08.009.

44. Palmieri, M., Impey, S., Kang, H., di Ronza, A., Pelz, C., Sardiello, M., and Ballabio, A. (2011). Characterization of the CLEAR network reveals an integrated control of cellular clearance pathways. Hum Mol Genet *20*, 3852–3866. https://doi.org/10.1093/hmg/ddr306.

45. Bussi, C., and Gutierrez, M.G. (2024). One size does not fit all: Lysosomes exist in biochemically and functionally distinct states. PLoS Biol *22*, e3002576. https://doi.org/10.1371/journal.pbio.3002576.

46. Rovira, M., Sereda, R., Pladevall-Morera, D., Ramponi, V., Marin, I., Maus, M., Madrigal-Matute, J., Díaz, A., García, F., Muñoz, J., et al. (2022). The lysosomal proteome of senescent cells contributes to the senescence secretome. Aging Cell *21*, e13707. https://doi.org/10.1111/acel.13707.

47. Vinchi, F., Costa da Silva, M., Ingoglia, G., Petrillo, S., Brinkman, N., Zuercher, A., Cerwenka, A., Tolosano, E., and Muckenthaler, M.U. (2016). Hemopexin therapy reverts heme-induced proinflammatory phenotypic switching of macrophages in a mouse model of sickle cell disease. Blood *127*, 473–486. https://doi.org/10.1182/blood-2015-08-663245.

48. Pfefferlé, M., Ingoglia, G., Schaer, C.A., Yalamanoglu, A., Buzzi, R., Dubach, I.L., Tan, G., López-Cano, E.Y., Schulthess, N., Hansen, K., et al. (2020). Hemolysis transforms liver macrophages into antiinflammatory erythrophagocytes. J Clin Invest *130*, 5576–5590. https://doi.org/10.1172/JCI137282.

49. Pereira, M., Chen, T.-D., Buang, N., Olona, A., Ko, J.-H., Prendecki, M., Costa, A.S.H., Nikitopoulou, E., Tronci, L., Pusey, C.D., et al. (2019). Acute Iron Deprivation Reprograms Human Macrophage Metabolism and Reduces Inflammation In Vivo. Cell Rep *28*, 498-511.e5. https://doi.org/10.1016/j.celrep.2019.06.039.

50. Pagani, A., Nai, A., Corna, G., Bosurgi, L., Rovere-Querini, P., Camaschella, C., and Silvestri, L. (2011). Low hepcidin accounts for the proinflammatory status associated with iron deficiency. Blood *118*, 736–746. https://doi.org/10.1182/blood-2011-02-337212.

51. Diskin, C., and Pålsson-McDermott, E.M. (2018). Metabolic Modulation in Macrophage Effector Function. Front Immunol *9*, 270. https://doi.org/10.3389/fimmu.2018.00270.

52. Luo, B., Gan, W., Liu, Z., Shen, Z., Wang, J., Shi, R., Liu, Y., Liu, Y., Jiang, M., Zhang, Z., et al. (2016). Erythropoeitin Signaling in Macrophages Promotes Dying Cell Clearance and Immune Tolerance. Immunity *44*, 287–302. https://doi.org/10.1016/j.immuni.2016.01.002.

53. Finberg, K.E., Heeney, M.M., Campagna, D.R., Aydinok, Y., Pearson, H.A., Hartman, K.R., Mayo, M.M., Samuel, S.M., Strouse, J.J., Markianos, K., et al. (2008). Mutations in TMPRSS6 cause iron-refractory iron deficiency anemia (IRIDA). Nat Genet *40*, 569–571. https://doi.org/10.1038/ng.130.

54. Folgueras, A.R., de Lara, F.M., Pendás, A.M., Garabaya, C., Rodríguez, F., Astudillo, A., Bernal, T., Cabanillas, R., López-Otín, C., and Velasco, G. (2008). Membrane-bound serine protease matriptase-2 (Tmprss6) is an essential regulator of iron homeostasis. Blood *112*, 2539–2545. https://doi.org/10.1182/blood-2008-04-149773.

55. Silvestri, L., Pagani, A., Nai, A., De Domenico, I., Kaplan, J., and Camaschella, C. (2008). The serine protease matriptase-2 (TMPRSS6) inhibits hepcidin activation by cleaving membrane hemojuvelin. Cell Metab *8*, 502–511. https://doi.org/10.1016/j.cmet.2008.09.012.

56. Nai, A., Pagani, A., Mandelli, G., Lidonnici, M.R., Silvestri, L., Ferrari, G., and Camaschella, C. (2012). Deletion of TMPRSS6 attenuates the phenotype in a mouse model of β-thalassemia. Blood *119*, 5021–5029. https://doi.org/10.1182/blood-2012-01-401885.

57. Finberg, K.E., Whittlesey, R.L., Fleming, M.D., and Andrews, N.C. (2010). Down-regulation of Bmp/Smad signaling by Tmprss6 is required for maintenance of systemic iron homeostasis. Blood *115*, 3817–3826. https://doi.org/10.1182/blood-2009-05-224808.

58. Manolova, V., Nyffenegger, N., Flace, A., Altermatt, P., Varol, A., Doucerain, C., Sundstrom, H., and Dürrenberger, F. (2019). Oral ferroportin inhibitor ameliorates ineffective erythropoiesis in a model of β-thalassemia. Journal of Clinical Investigation *130*, 491–506. https://doi.org/10.1172/JCI129382.

59. Zumerle, S., Calì, B., Munari, F., Angioni, R., Di Virgilio, F., Molon, B., and Viola, A. (2019). Intercellular Calcium Signaling Induced by ATP Potentiates Macrophage Phagocytosis. Cell Rep *27*, 1-10.e4. https://doi.org/10.1016/j.celrep.2019.03.011.

60. Shen, J., Wilbon, A.S., Zhou, M., and Pan, Y. (2023). Mechanism of Ca2+ transport by ferroportin. Elife *12*, e82947. https://doi.org/10.7554/eLife.82947.

61. Wang, Y.-T., Trzeciak, A.J., Rojas, W.S., Saavedra, P., Chen, Y.-T., Chirayil, R., Etchegaray, J.I., Lucas, C.D., Puleston, D.J., Keshari, K.R., et al. (2023). Metabolic adaptation supports enhanced macrophage efferocytosis in limited-oxygen environments. Cell Metab *35*, 316-331.e6. https://doi.org/10.1016/j.cmet.2022.12.005.

62. Bhutia, Y.D., and Ganapathy, V. (2016). Glutamine transporters in mammalian cells and their functions in physiology and cancer. Biochimica et Biophysica Acta (BBA) - Molecular Cell Research *1863*, 2531–2539. https://doi.org/10.1016/j.bbamcr.2015.12.017.

63. Beard, J. (2003). Iron deficiency alters brain development and functioning. J Nutr *133*, 1468S-72S. https://doi.org/10.1093/jn/133.5.1468S.

64. Badaracco, M.E., Ortiz, E.H., Soto, E.F., Connor, J., and Pasquini, J.M. (2008). Effect of transferrin on hypomyelination induced by iron deficiency. J Neurosci Res *86*, 2663–2673. https://doi.org/10.1002/jnr.21709.

65. Jiang, Y., Li, C., Wu, Q., An, P., Huang, L., Wang, J., Chen, C., Chen, X., Zhang, F., Ma, L., et al. (2019). Iron-dependent histone 3 lysine 9 demethylation controls B cell proliferation and humoral immune responses. Nat Commun *10*, 2935. https://doi.org/10.1038/s41467-019-11002-5.

66. Zhu, L., Li, G., Liang, Z., Qi, T., Deng, K., Yu, J., Peng, Y., Zheng, J., Song, Y., and Chang, X. (2023). Microbiota-assisted iron uptake promotes immune tolerance in the intestine. Nat Commun *14*, 2790. https://doi.org/10.1038/s41467-023-38444-2.

67. Frost, J.N., Wideman, S.K., Preston, A.E., Teh, M.R., Ai, Z., Wang, L., Cross, A., White, N., Yazicioglu, Y., Bonadonna, M., et al. (2022). Plasma iron controls neutrophil production and function. Sci Adv *8*, eabq5384. https://doi.org/10.1126/sciadv.abq5384.

68. Frost, J.N., Tan, T.K., Abbas, M., Wideman, S.K., Bonadonna, M., Stoffel, N.U., Wray, K., Kronsteiner, B., Smits, G., Campagna, D.R., et al. (2021). Hepcidin-Mediated Hypoferremia Disrupts Immune Responses to Vaccination and Infection. Med *2*, 164-179.e12. https://doi.org/10.1016/j.medj.2020.10.004.

69. Wang, L., Johnson, E.E., Shi, H.N., Allan Walker, W., Wessling-Resnick, M., and Cherayil, B.J. (2008). Attenuated inflammatory responses in hemochromatosis reveal a role for iron in the regulation of macrophage cytokine translation. J Immunol *181*, 2723–2731.

70. Agoro, R., Taleb, M., Quesniaux, V.F.J., and Mura, C. (2018). Cell iron status influences macrophage polarization. PLoS One *13*, e0196921. https://doi.org/10.1371/journal.pone.0196921.

71. Xu, W., Barrientos, T., Mao, L., Rockman, H.A., Sauve, A.A., and Andrews, N.C. (2015). Lethal Cardiomyopathy in Mice Lacking Transferrin Receptor in the Heart. Cell Rep *13*, 533–545. https://doi.org/10.1016/j.celrep.2015.09.023.

72. Papathanassiu, A.E., Ko, J.-H., Imprialou, M., Bagnati, M., Srivastava, P.K., Vu, H.A., Cucchi, D., McAdoo, S.P., Ananieva, E.A., Mauro, C., et al. (2017). BCAT1 controls metabolic reprogramming in activated human macrophages and is associated with inflammatory diseases. Nat Commun *8*, 16040. https://doi.org/10.1038/ncomms16040.

73. Lu, M., Luo, D., Zhang, Z., Ouyang, F., Shi, Y., Hu, C., Su, H., Li, Y., Zhang, J., Gui, Q., et al. (2024). Branched-chain amino acid catabolism promotes M2 macrophage polarization. Front. Immunol. *15*, 1469163. https://doi.org/10.3389/fimmu.2024.1469163.

74. Yan, H., Liu, Y., Li, X., Yu, B., He, J., Mao, X., Yu, J., Huang, Z., Luo, Y., Luo, J., et al. (2024). Leucine alleviates cytokine storm syndrome by regulating macrophage polarization via the mTORC1/LXRα signaling pathway. eLife *12*, RP89750. https://doi.org/10.7554/eLife.89750.

75. Banerjee, S., Lu, S., Jain, A., Wang, I., Tao, H., Srinivasan, S., Nemeth, E., and He, P. (2024). Targeting PKCa alleviates iron overload in diabetes and hemochromatosis through the inhibition of ferroportin. Blood, blood.2024023829. https://doi.org/10.1182/blood.2024023829.

76. Ennerfelt, H., Frost, E.L., Shapiro, D.A., Holliday, C., Zengeler, K.E., Voithofer, G., Bolte, A.C., Lammert, C.R., Kulas, J.A., Ulland, T.K., et al. (2022). SYK coordinates neuroprotective microglial responses in neurodegenerative disease. Cell *185*, 4135-4152.e22. https://doi.org/10.1016/j.cell.2022.09.030.

77. Wang, S., Sudan, R., Peng, V., Zhou, Y., Du, S., Yuede, C.M., Lei, T., Hou, J., Cai, Z., Cella, M., et al. (2022). TREM2 drives microglia response to amyloid-β via SYK-dependent and -independent pathways. Cell *185*, 4153-4169.e19. https://doi.org/10.1016/j.cell.2022.09.033.

78. Kobayashi, A., Azuma, K., Takeiwa, T., Kitami, T., Horie, K., Ikeda, K., and Inoue, S. (2023). A FRET-based respirasome assembly screen identifies spleen tyrosine kinase as a target to improve muscle mitochondrial respiration and exercise performance in mice. Nat Commun *14*, 312. https://doi.org/10.1038/s41467-023-35865-x.

79. Canton, J., Khezri, R., Glogauer, M., and Grinstein, S. (2014). Contrasting phagosome pH regulation and maturation in human M1 and M2 macrophages. Mol Biol Cell *25*, 3330–3341. https://doi.org/10.1091/mbc.E14-05-0967.

80. Das Gupta, K., Shakespear, M.R., Curson, J.E.B., Murthy, A.M.V., Iyer, A., Hodson, M.P., Ramnath, D., Tillu, V.A., von Pein, J.B., Reid, R.C., et al. (2020). Class IIa Histone Deacetylases Drive Toll-like Receptor-Inducible Glycolysis and Macrophage Inflammatory Responses via Pyruvate Kinase M2. Cell Rep *30*, 2712-2728.e8. https://doi.org/10.1016/j.celrep.2020.02.007.

81. Codo, A.C., Davanzo, G.G., Monteiro, L. de B., de Souza, G.F., Muraro, S.P., Virgilio-da-Silva, J.V., Prodonoff, J.S., Carregari, V.C., de Biagi Junior, C.A.O., Crunfli, F., et al. (2020). Elevated Glucose Levels Favor SARS-CoV-2 Infection and Monocyte Response through a HIF-1α/Glycolysis-Dependent Axis. Cell Metab *32*, 437-446.e5. https://doi.org/10.1016/j.cmet.2020.07.007.

82. Van den Bossche, J., O'Neill, L.A., and Menon, D. (2017). Macrophage Immunometabolism: Where Are We (Going)? Trends Immunol *38*, 395–406. https://doi.org/10.1016/j.it.2017.03.001.

83. Divakaruni, A.S., Hsieh, W.Y., Minarrieta, L., Duong, T.N., Kim, K.K.O., Desousa, B.R., Andreyev, A.Y., Bowman, C.E., Caradonna, K., Dranka, B.P., et al. (2018). Etomoxir Inhibits Macrophage Polarization by Disrupting CoA Homeostasis. Cell Metab *28*, 490-503.e7. https://doi.org/10.1016/j.cmet.2018.06.001.

84. Liu, P.-S., Wang, H., Li, X., Chao, T., Teav, T., Christen, S., Di Conza, G., Cheng, W.-C., Chou, C.-H., Vavakova, M., et al. (2017). α-ketoglutarate orchestrates macrophage activation through metabolic and epigenetic reprogramming. Nat Immunol *18*, 985–994. https://doi.org/10.1038/ni.3796.

85. Mills, E.L., Kelly, B., Logan, A., Costa, A.S.H., Varma, M., Bryant, C.E., Tourlomousis, P., Däbritz, J.H.M., Gottlieb, E., Latorre, I., et al. (2016). Succinate Dehydrogenase Supports Metabolic Repurposing of Mitochondria to Drive Inflammatory Macrophages. Cell *167*, 457-470.e13. https://doi.org/10.1016/j.cell.2016.08.064.

86. Chia, X.X., Ozols, E., Nikolic-Paterson, D.J., and Tesch, G.H. (2025). Spleen tyrosine kinase signaling in myeloid cells promotes macrophage infiltration, glomerulosclerosis, and interstitial fibrosis in diabetic kidney disease. Am J Physiol Renal Physiol *329*, F872–F882. https://doi.org/10.1152/ajprenal.00289.2025.

87. Chen, L., Zhu, F., Gao, X., Yang, Y., Jin, G., Zhou, Y., Dong, G., and Zhou, G. (2025). Spleen tyrosine kinase aggravates intestinal inflammation through regulating inflammatory responses of macrophage in ulcerative colitis. Int Immunopharmacol *148*, 114122. https://doi.org/10.1016/j.intimp.2025.114122.

88. Rohila, D., Park, I.H., Pham, T.V., Weitz, J., Hurtado de Mendoza, T., Madheswaran, S., Ishfaq, M., Beaman, C., Tapia, E., Sun, S., et al. (2023). Syk Inhibition Reprograms Tumor-Associated Macrophages and Overcomes Gemcitabine-Induced Immunosuppression in Pancreatic Ductal Adenocarcinoma. Cancer Res *83*, 2675–2689. https://doi.org/10.1158/0008-5472.CAN-22-3645.

89. Torrance, J.D., and Bothwell, T.H. (1968). A simple technique for measuring storage iron concentrations in formalinised liver samples. S Afr J Med Sci *33*, 9–11.

90. Picelli, S., Björklund, Å.K., Faridani, O.R., Sagasser, S., Winberg, G., and Sandberg, R. (2013). Smart-seq2 for sensitive full-length transcriptome profiling in single cells. Nat Methods *10*, 1096–1098. https://doi.org/10.1038/nmeth.2639.

91. Moggridge, S., Sorensen, P.H., Morin, G.B., and Hughes, C.S. (2018). Extending the Compatibility of the SP3 Paramagnetic Bead Processing Approach for Proteomics. J Proteome Res *17*, 1730–1740. https://doi.org/10.1021/acs.jproteome.7b00913.

92. Hughes, C.S., Foehr, S., Garfield, D.A., Furlong, E.E., Steinmetz, L.M., and Krijgsveld, J. (2014). Ultrasensitive proteome analysis using paramagnetic bead technology. Mol Syst Biol *10*, 757. https://doi.org/10.15252/msb.20145625.

93. Werner, T., Sweetman, G., Savitski, M.F., Mathieson, T., Bantscheff, M., and Savitski, M.M. (2014). Ion coalescence of neutron encoded TMT 10-plex reporter ions. Anal Chem *86*, 3594–3601. https://doi.org/10.1021/ac500140s.

94. Yang, F., Shen, Y., Camp, D.G., and Smith, R.D. (2012). High-pH reversed-phase chromatography with fraction concatenation for 2D proteomic analysis. Expert Rev Proteomics *9*, 129–134. https://doi.org/10.1586/epr.12.15.

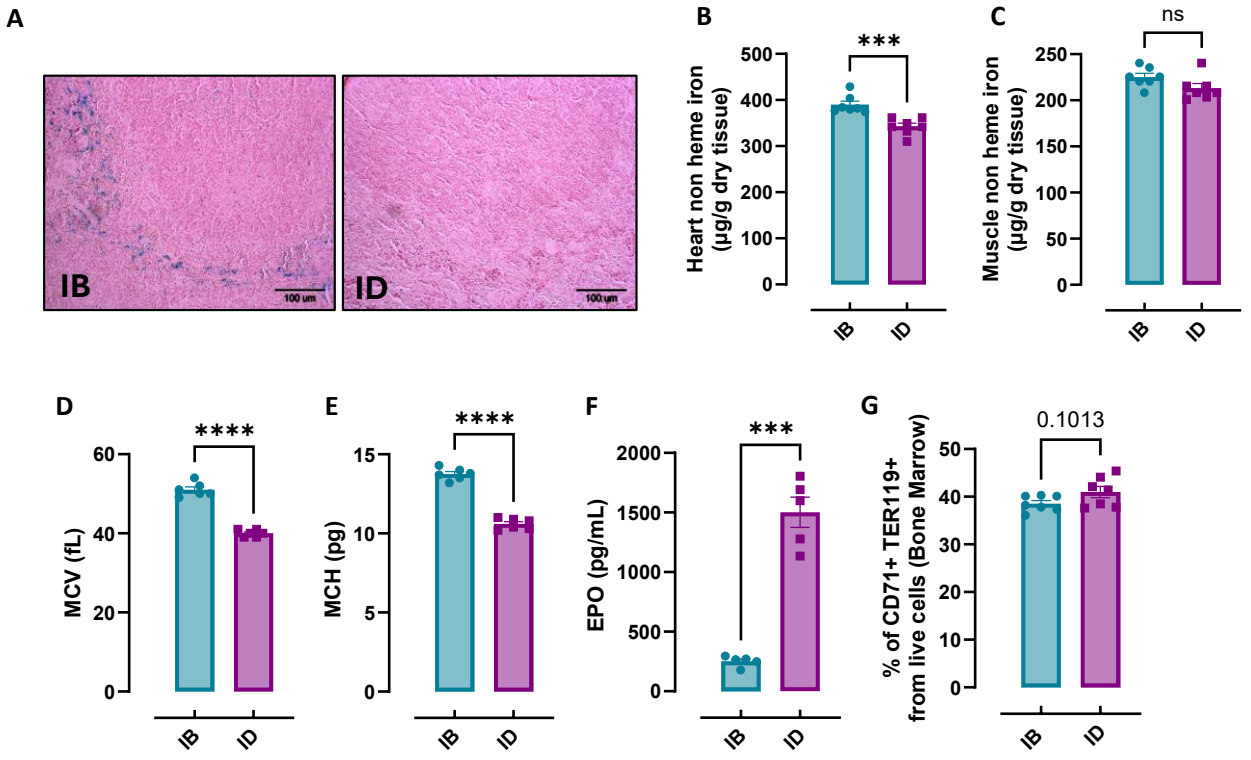

Figure S1. **Body iron indices and hematological parameters of nutritional iron-deficient mice.**
(A) Perls' Prussian Blue staining of the splenic red pulp in IB and ID mice. (B) Heart and (C) muscle non-heme iron content was determined in IB and ID mice. (D) Mean corpuscular volume (MCV), and (E) mean corpuscular hemoglobin (MCH) were determined in IB and ID mice. (F) EPO concentration in the serum of IB and ID mice was measured by Mouse Erythropoietin/EPO Quantikine ELISA Kit. (G) Shown is the percentage of erythroid progenitor cells (TER119+ CD71+) present in the bone marrow of IB and ID mice. Each dot represents one mouse. Data are represented as mean ± SEM. Welch's unpaired t-test determined statistical significance between the two groups. ns $p>0.05$, *** $p<0.001$ and **** $p<0.0001$.

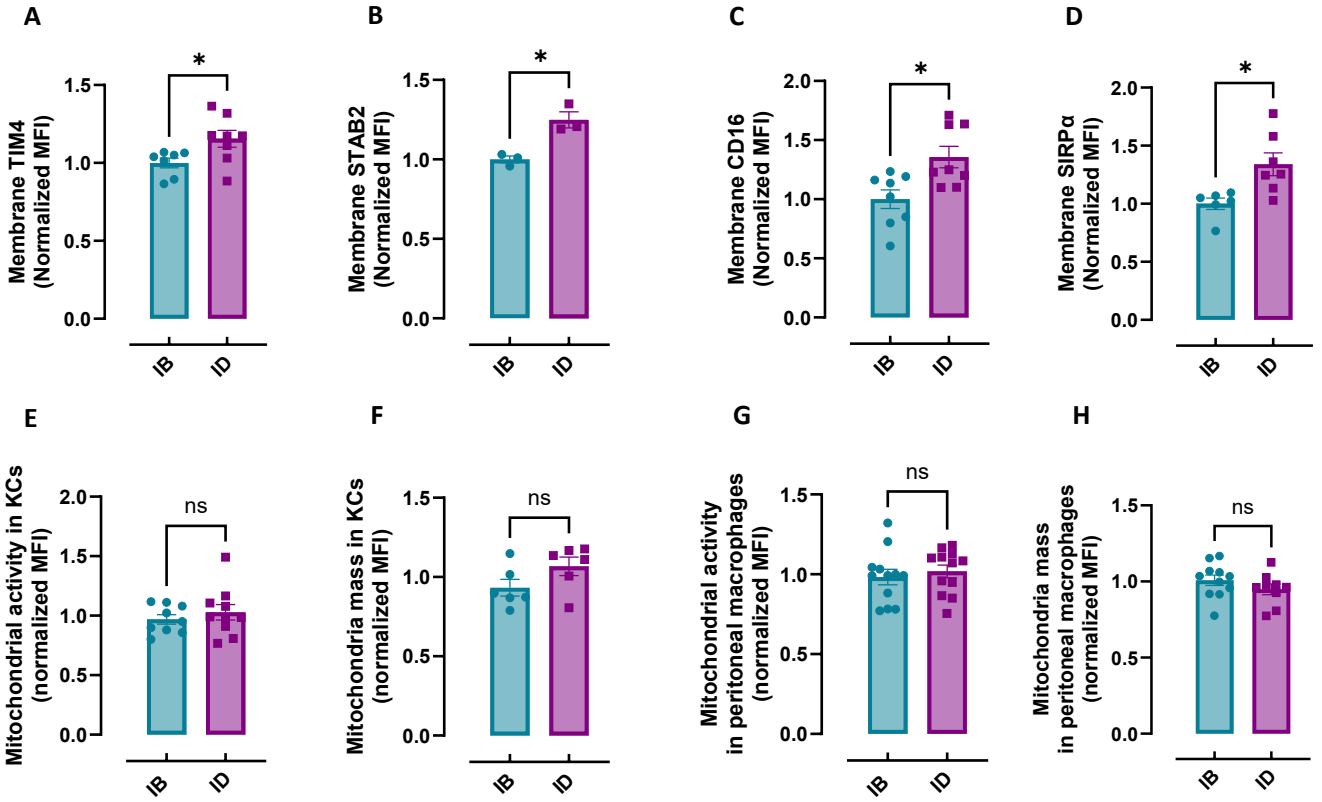

Figure S2.1: **Apoptotic cell receptors in RPMs and mitochondrial profiling of Kupffer cells and peritoneal macrophages.**
Cell membrane expression levels of (A) TIM4, (B) STAB2, (C) the Fc receptor CD16, and (D) SIRPα of RPMs in IB and ID mice were determined by using fluorescently labelled antibodies and flow cytometry. (E) Mitochondrial activity and (F) mitochondrial mass were determined in Kupffer cells (KCs) derived from IB and ID mice using TMRE probes and MitoTracker Green, respectively, with flow cytometry. (G) Mitochondrial activity and (H) mitochondrial mass were determined in peritoneal macrophages derived from IB and ID mice using TMRE probes and MitoTracker Green, respectively, with flow cytometry. Each dot represents one mouse. Data are represented as mean ± SEM. Welch's unpaired t-test determined statistical significance between the two groups. ns $p>0.05$, *$p<0.05$, **$p<0.01$, ***$p<0.001$ and ****$p<0.0001$.

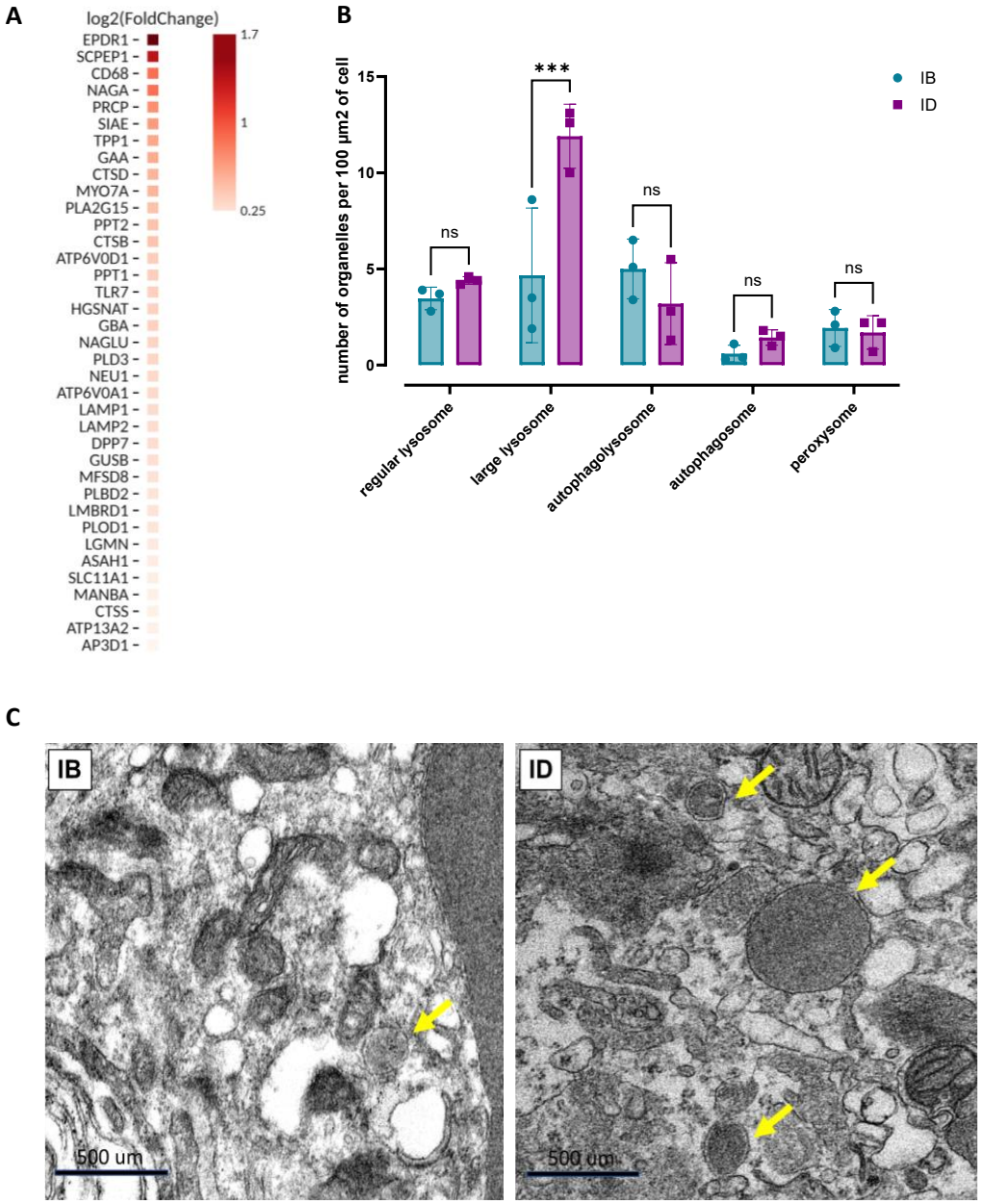

Figure S2.2. **Characterization of increased lysosomal function in RPMs of ID mice.**

(A) Heatmap showing $\log_2$ fold changes of lysosome-related proteins upregulated in RPMs from ID versus IB mice. (B) Quantification of regular lysosomes, large lysosomes, autophagolysosomes, autophagosomes, and peroxisomes per 100 µm² of cell area in RPMs from IB and ID mice. (C) Representative images of enlarged lysosomes in RPMs of IB and ID mice. Yellow arrows indicate enlarged lysosomes. Each dot represents one mouse. Data are represented as mean ± SEM. Welch's unpaired t-test determined statistical significance between the two groups. ns $p>0.05$, *$p<0.05$, **$p<0.01$, ***$p<0.001$ and ****$p<0.0001$.

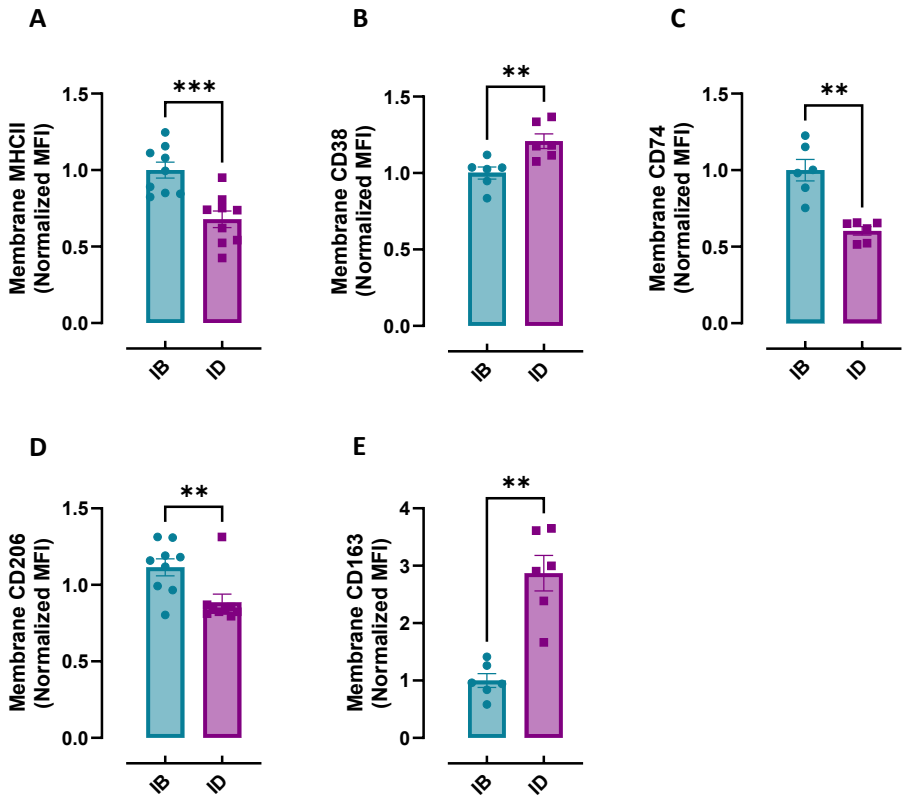

Figure S2.3. **Profiling of macrophage polarization markers in RPMs under ID conditions.**

Cell membrane expression levels of (A) MHCII, (B) CD38, (C) CD74, (D) CD206 and (E) CD163 of RPMs in IB and ID mice were determined by using fluorescently labelled antibodies and flow cytometry. Each dot represents one mouse. Data are represented as mean ± SEM. Welch's unpaired t-test determined statistical significance between the two groups. ns $p>0.05$, *$p<0.05$, **$p<0.01$, ***$p<0.001$ and ****$p<0.0001$.

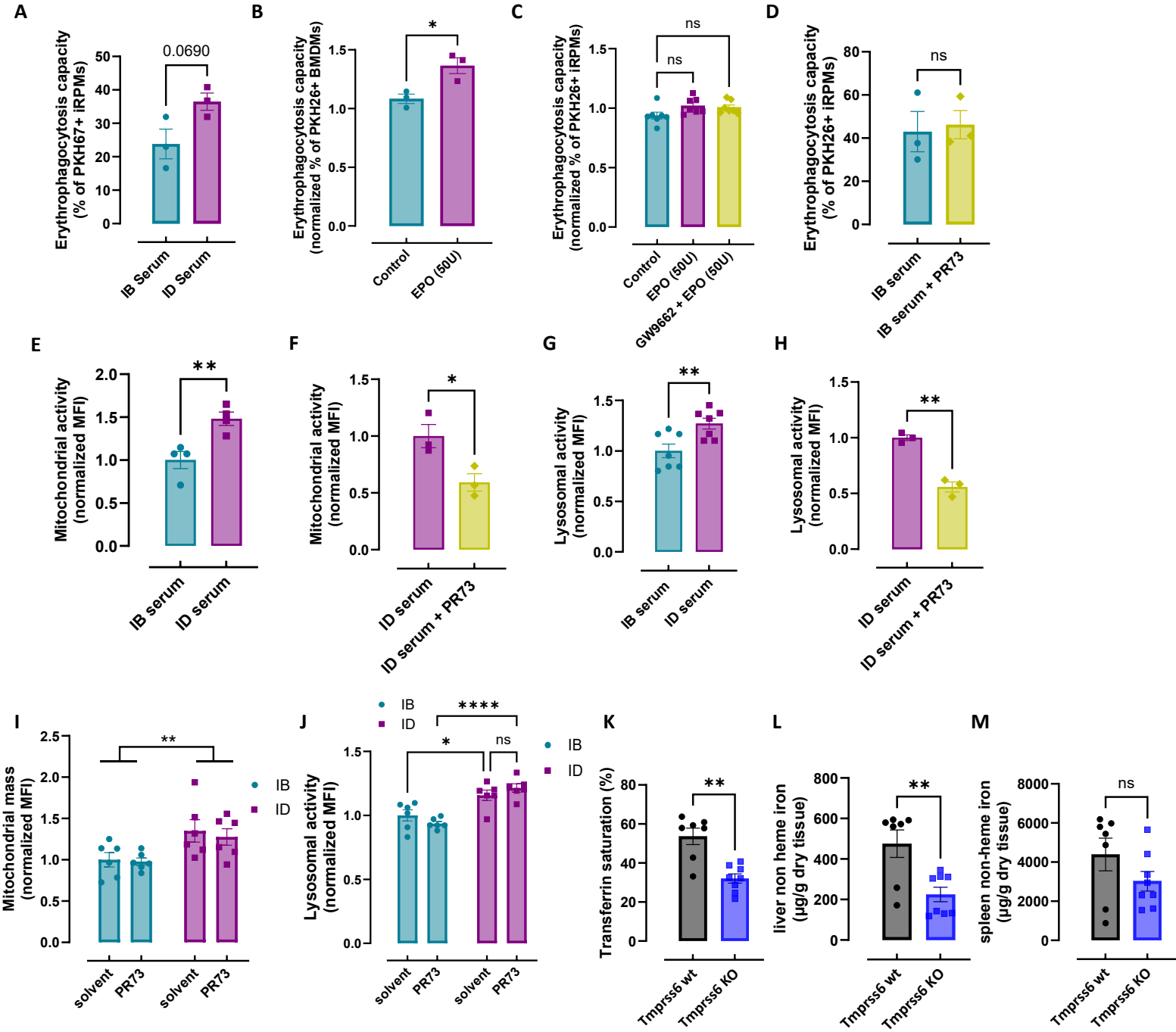

Figure S3: **The hepcidin-FPN axis regulates functional adaptations of RPMs during iron deficiency – extended data**

(A) The EP capacity in iRPMs treated with serum from IB or ID mice determined using flow cytometry by measuring the percentage of cells that phagocytosed transfused PKH26-labeled RBCs. (B) Normalized EP capacity of PKH26 sRBCs by cultured iRPMs treated with EPO determined using flow cytometry. (C) Normalized EP capacity of PKH26 sRBCs by cultured iRPMs with EPO (25 units, 24 h) treated alone or in combination with GW9662 (1µM, 25 h), a selective PPARγ antagonist determined using flow cytometry. (D) The EP capacity in iRPMs treated with serum from IB mice and serum from IB mice treated with the hepcidin agonist PR73 (50 nmol/mouse, 4 h) determined using flow cytometry by measuring the percentage of cells that phagocytosed transfused PKH26-labeled RBCs. (E) Mitochondrial activity was determined in iRPMs treated with serum from IB or ID mice using TMRE probe, with flow cytometry. (F) Mitochondrial activity was determined in iRPMs treated with serum from ID mice and serum from ID mice treated with the hepcidin agonist PR73 (50 nmol/mouse, 4 h) using TMRE probe determined using flow cytometry. (G) Lysosomal activity was determined in iRPMs treated with serum from IB or ID mice using the Lysosomal Intracellular Activity Assay Kit, with flow cytometry. (H) Lysosomal activity was determined in iRPMs treated with serum from ID mice and serum from ID mice treated with the hepcidin agonist PR73 (50 nmol/mouse, 4 h) using the Lysosomal Intracellular Activity Assay Kit determined using flow cytometry. (I) Mitochondrial mass was determined in RPMs from IB and ID mice using MitoTracker Green with flow cytometry after PR73 administration. (J) Flow cytometric assessment of lysosomal activity in RPMs from IB and ID mice using the Lysosomal Intracellular Activity Assay Kit following PR73 administration. (K) Plasma transferrin saturation was determined in Tmprss6 wt and Tmprss6 KO mice. (L) Liver and (M) spleen non-heme iron content was determined in wild type and Tmprss6 KO mice. Each dot represents one mouse or an independent cell-based experiment. Data are represented as mean ± SEM. Welch's unpaired t-test determined statistical significance in A-B, D, E-H and K-M, while two-way ANOVA with Tukey's Multiple Comparison tests was used in I-J. A one-way ANOVA test with Dunnett's or Tukey's Multiple Comparison tests was used in C. ns $p>0.05$, *$p<0.05$, **$p<0.01$, ***$p<0.001$ and ****$p<0.0001$.

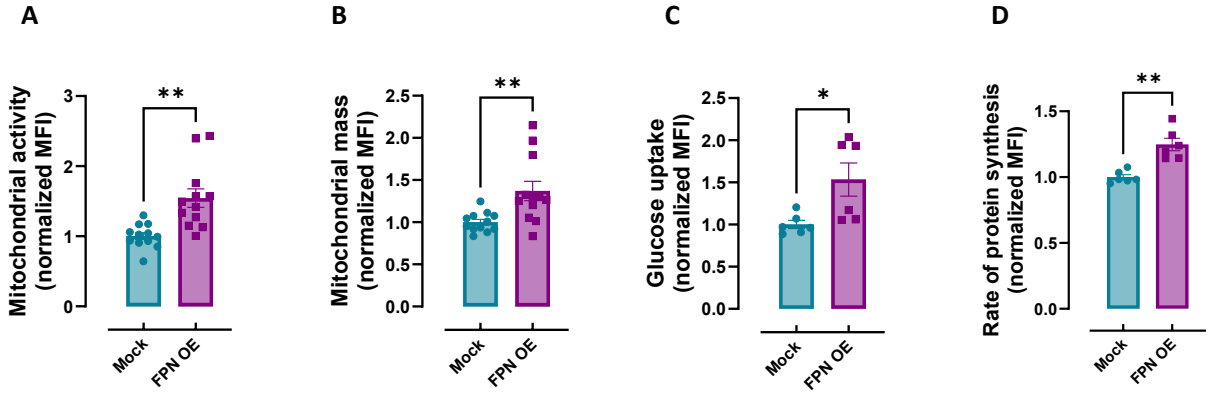

Figure S4. **Consequences of FPN overexpression on iRPMs functions in culture without sRBCs exposure.**

(A) Mitochondrial activity was determined in mock and FPN-iRPMs using TMRE probe, with flow cytometry. (B) Mitochondrial mass was determined in mock and FPN-iRPMs using MitoTracker Green, with flow cytometry. (C) Quantification of glucose uptake via flow cytometry in mock and FPN-iRPMs using a fluorescent glucose analog. (D) Flow cytometric detection of newly synthesized proteins in mock and FPN-iRPMs using Click-iT Plus OPP Alexa Fluor 488 Protein Synthesis Assay. Each dot represents an independent cell-based experiment. Data are represented as mean ± SEM. Welch's unpaired t-test determined statistical significance. ns $p>0.05$, *$p<0.05$ and **$p<0.01$.

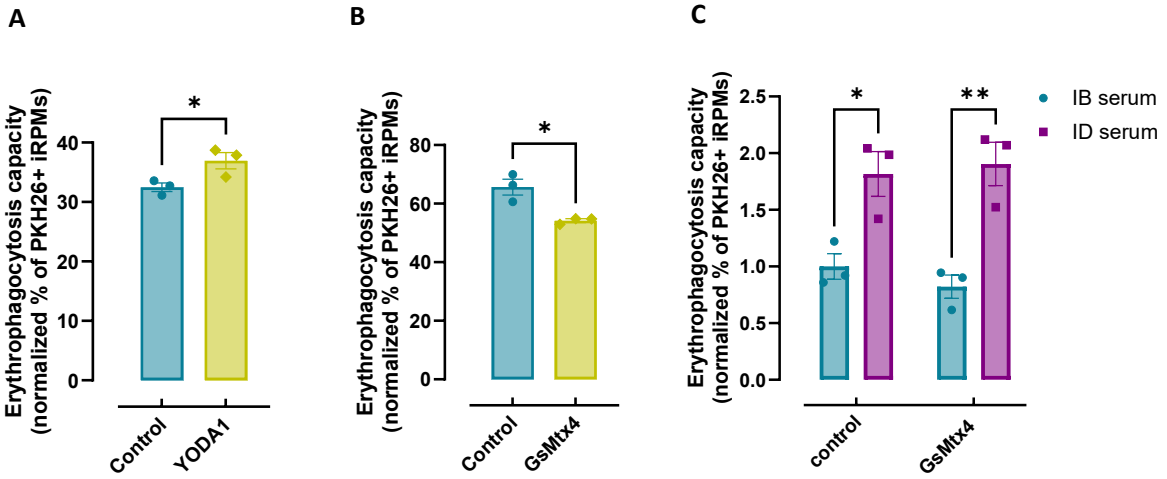

Figure S5.1. **The effects of PIEZO1 modulation in rewiring of RPMs in ID-like conditions.**

(A-B) EP capacity was assessed by flow cytometry as the percentage of iRPMs that internalized PKH26-labeled sRBCs, after treatment with (A) the PIEZO1 activator YODA1 (10 µM, 1h) or (B) the PIEZO1 inhibitor GsMTx4 (10 µM, 1h). (C) EP capacity was measured in iRPMs cultured with IB and ID serum by flow cytometry as the percentage of cells that phagocytosed PKH26-labeled sRBCs, upon treatment with GsMTx4. Each dot represents an independent cell-based experiment. Data are represented as mean ± SEM. Welch's unpaired t-test determined statistical significance in A-B. Two-way ANOVA with Tukey's Multiple Comparison tests was used in C. ns $p>0.05$, *$p<0.05$, **$p<0.01$,.

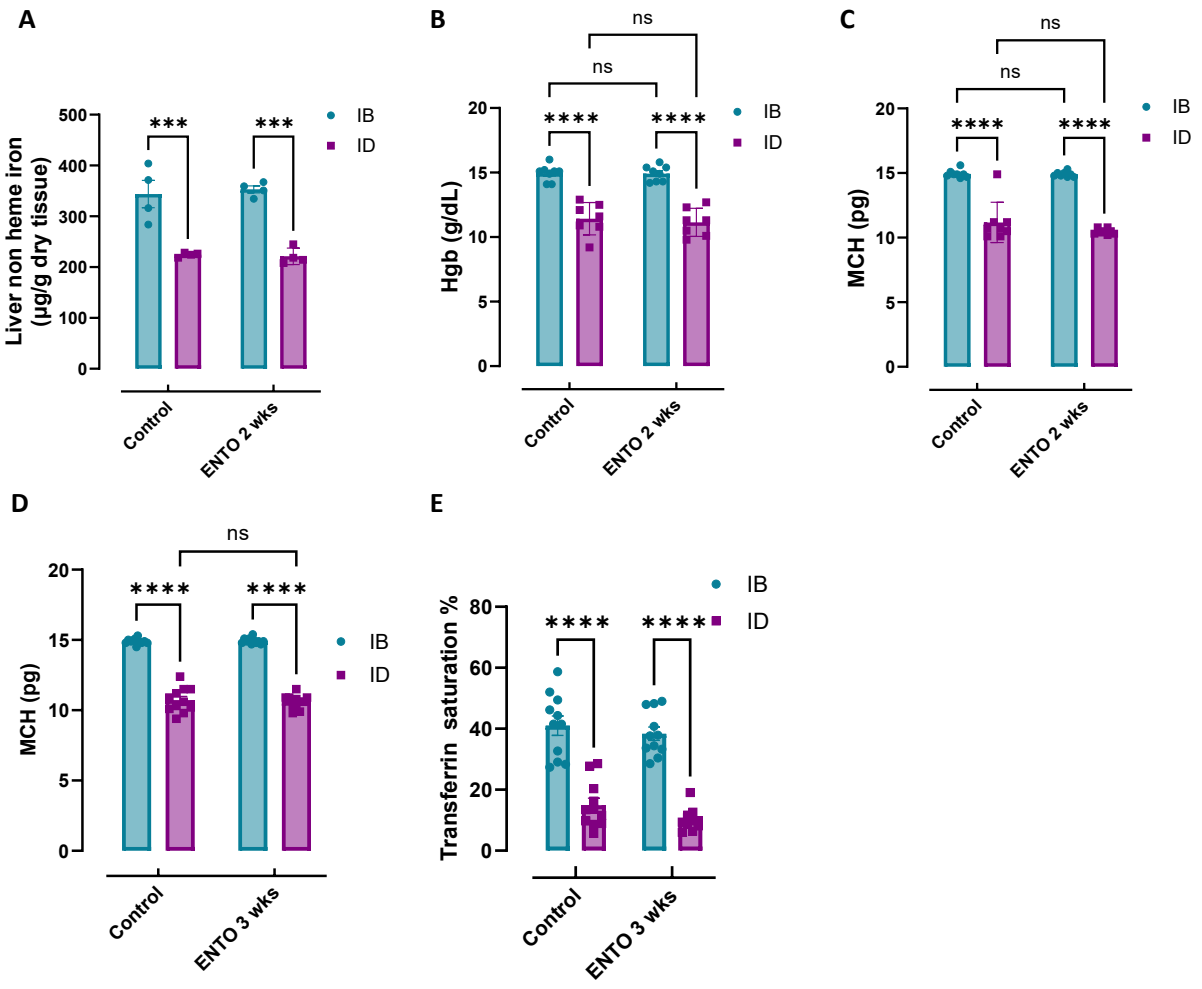

Figure S5.2. **SYK kinase inhibition disrupts the adaptation of RPMs to ID conditions in mice – extended data.**

(A) Liver non-heme iron content measured in IB and ID mice following 2 weeks of dietary intervention with or without ENTO jelly supplementation. (B) Blood hemoglobin (Hgb) levels in IB and ID mice after 2 weeks of ENTO jelly or control treatment. (C) Mean corpuscular hemoglobin (MCH) levels in IB and ID mice following 2 weeks of supplementation with ENTO jelly. (D) Mean corpuscular hemoglobin (MCH) levels in IB and ID mice following 3 weeks of supplementation with ENTO jelly. (E) Plasma transferrin saturation levels were measured in IB and ID mice after 3 weeks of supplementation with ENTO jelly. Each dot represents one mouse. Data are represented as mean ± SEM. Two-way ANOVA with Tukey's Multiple Comparison tests was used to determine statistical significance. ns $p>0.05$, *$p<0.05$, **$p<0.01$, ***$p<0.001$ and ****$p<0.0001$.

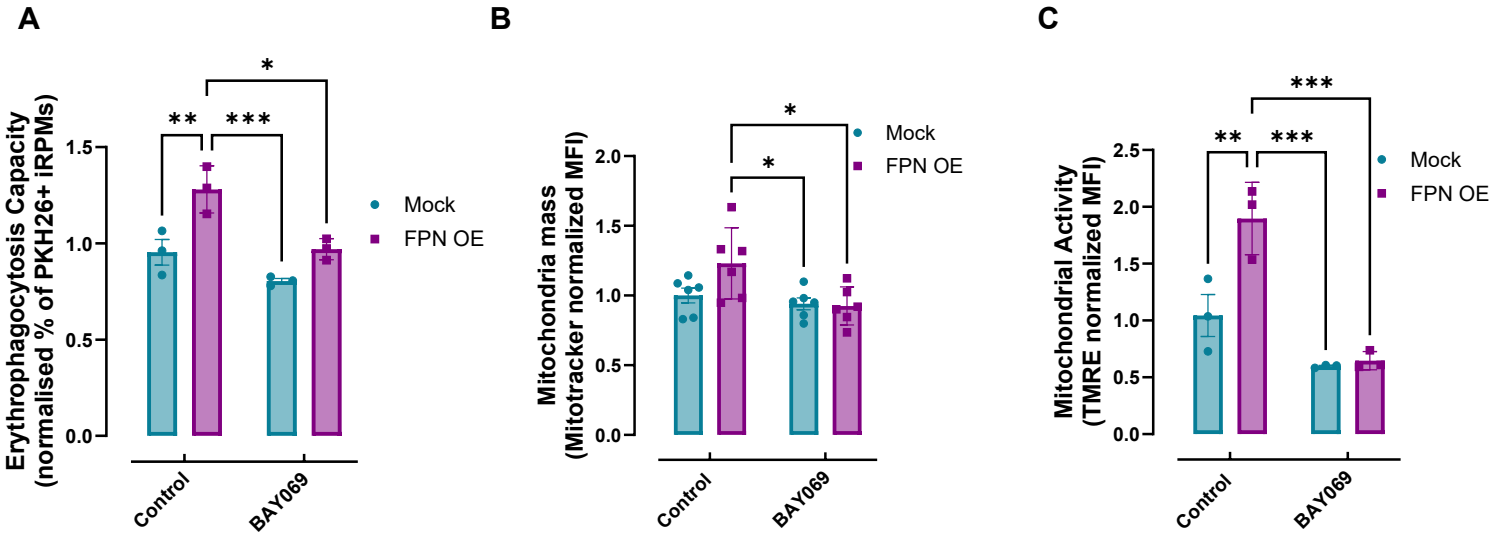

Figure S6.1. **Enhanced phagocytic and metabolic function of ID-like RPMs are reversed by BCAT inhibitor BAY069.**

(A) Normalized EP capacity of mock and FPN OE iRPMs upon treatment with BAY069 (10 µM, 15 h) measured by uptake of PKH26-labeled sRBCs. (B) Mitochondrial mass was determined in mock and FPN OE iRPMs upon treatment with BAY069 using MitoTracker Green, with flow cytometry (C) Mitochondrial activity was determined in mock and FPN OE iRPMs upon treatment with BAY069 using TMRE probe, with flow cytometry. Each dot represents an independent cell-based experiment. Data are represented as mean ± SEM. Two-way ANOVA with Tukey's Multiple Comparison tests was used to determine statistical significance. ns $p>0.05$, *$p<0.05$, **$p<0.01$, ***$p<0.001$ and ****$p<0.0001$.

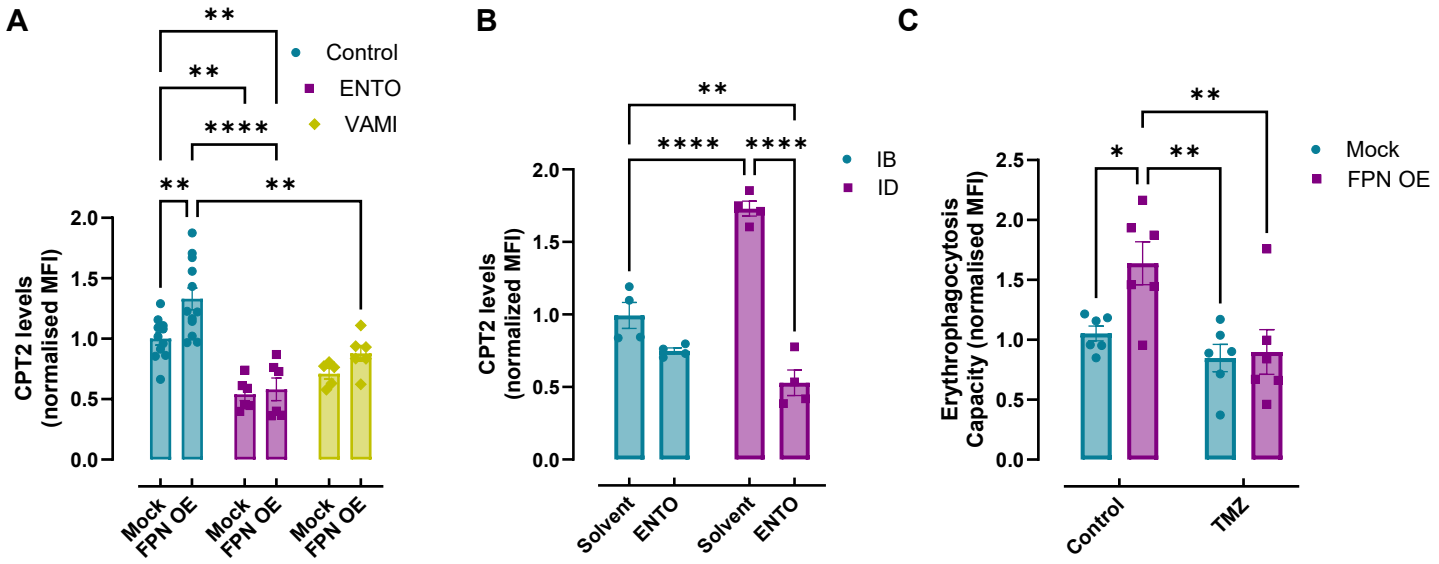

Figure S6.2. **Enhanced β-oxidation supports RPM adaptation to ID conditions.**

(A) Intracellular CPT2 levels in mock and FPN OE iRPMs upon treatment with Entospletinib (ENTO) (10 µM, 1 h) and vamifeport (VAMI) (20 µM, 15 h), determined using flow cytometry. (B) Intracellular CPT2 levels of RPMs from IB and ID mice supplemented with ENTO via jelly feeding (3 weeks), determined using flow cytometry. (C) Normalized EP capacity towards PKH26-sRBCs by mock and FPN OE iRPMs upon Trimetazidine (TMZ) treatment (10 µM, 15 h). Each dot represents one mouse or an independent cell-based experiment. Data are represented as mean ± SEM. Two-way ANOVA with Tukey's Multiple Comparison tests was used to determine statistical significance. ns $p>0.05$, *$p<0.05$, **$p<0.01$, ***$p<0.001$ and ****$p<0.0001$.

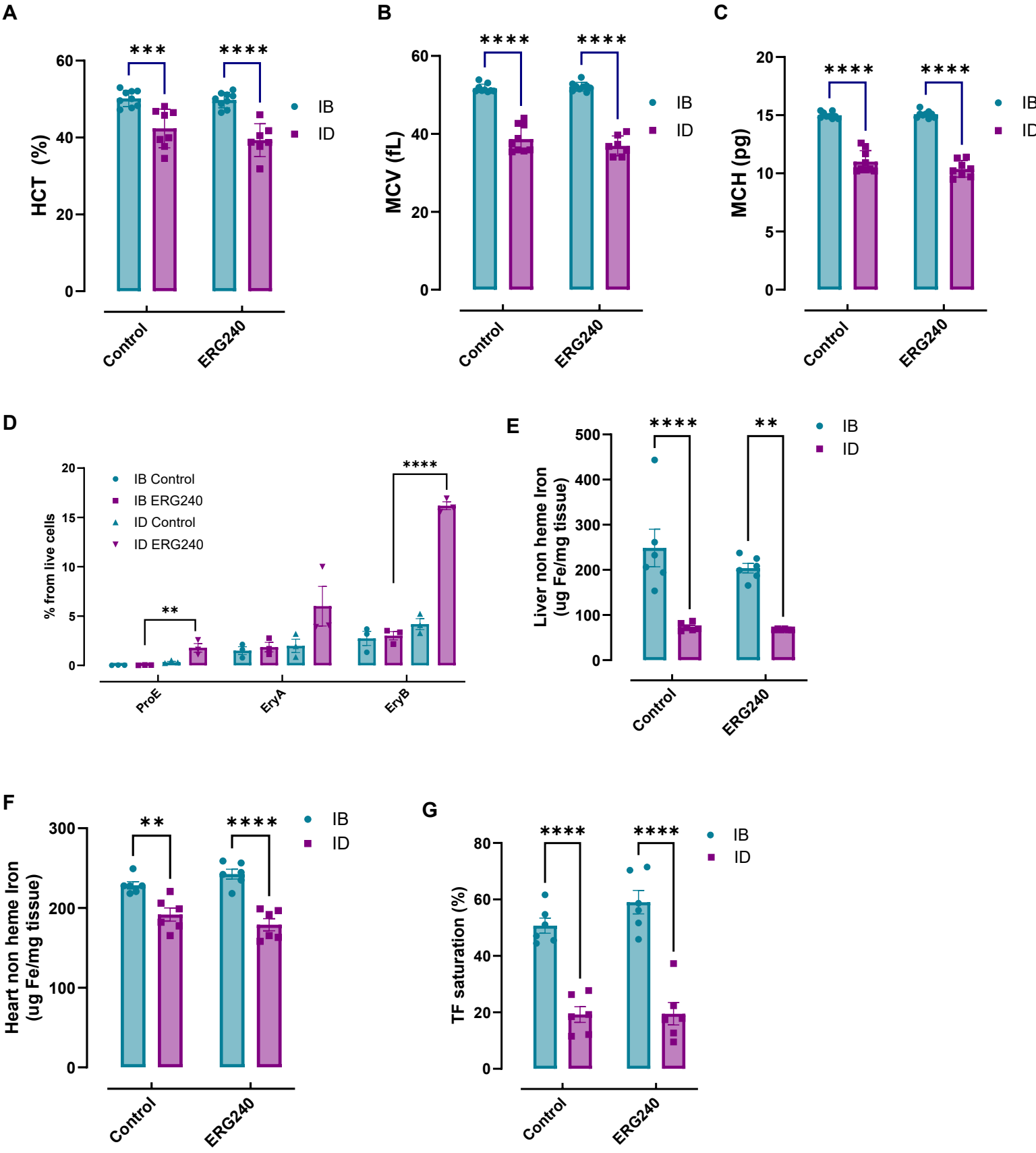

Figure S7. **In vivo inhibition of BCAA catabolism alters erythrophagocytic capacity and metabolic remodeling of RPMs in ID mice – extended data.**

(A) Hematocrit (HCT), (B) Mean corpuscular volume (MCV) and (C) mean corpuscular hemoglobin (MCH) were determined in IB and ID mice following 3 weeks of dietary ERG240 supplementation. (D) Proerythroblasts, EryA, and EryB erythroblast representations in the spleens of IB and ID mice supplemented with ERG240. (E) Liver and (F) heart non-heme iron content measured in IB and ID mice following 3 weeks of dietary ERG240 supplementation. (G) Plasma transferrin saturation was determined in IB and ID mice supplemented with ERG240. Each dot represents one mouse. Data are represented as mean ± SEM. Two-way ANOVA with Tukey's Multiple Comparison tests was used to determine statistical significance. ns $p>0.05$, *$p<0.05$, **$p<0.01$, ***$p<0.001$ and ****$p<0.0001$.

Appendix 2

Manuscript 2:

Gabriela Zurawska*, Zuzanna Sas*, Aneta Jończy*, **Raghunandan Mahadeva**, Patryk Slusarczyk, Marta Chwałek, Daniel Seehofer, Georg Damm, Rafał Mazgaj, Marcin Skórzyński, Maria Kulecka, Izabela Rumieńczyk, Morgane Moulin, Kamil Jastrzębski, Kevin Waldron, Michal Mikula, Anders Etzerodt, Remigiusz Serwa, Marta Miączyńska, Tomasz P Rygiel & Katarzyna Mleczko-Sanecka. Liver sinusoidal endothelial cells constitute a major route for hemoglobin clearance. EMBO Reports (2026). DOI: https://doi.org/10.1038/s44319-025-00673-5

*Authors contributed equally

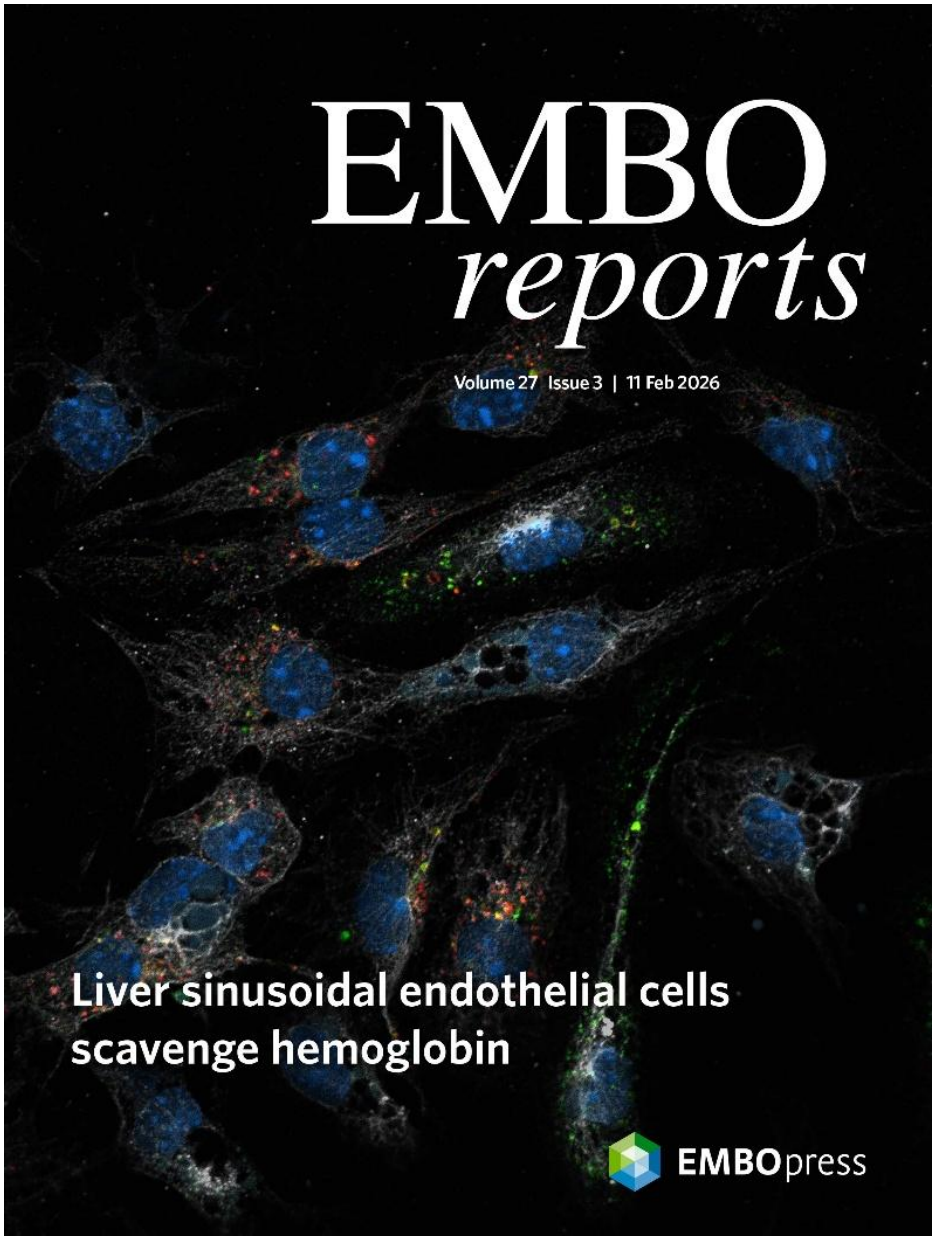

Warsaw, 19-12-2025

Raghunandan Mahadeva

Laboratory of Iron Homeostasis

International Institute of Molecular
and Cell Biology in Warsaw
Ks. Trojdena 4 Street
02-109 Warsaw

Candidate's Contribution Statement

Article's title: Liver sinusoidal endothelial cells constitute a major route for hemoglobin clearance

Authors: Gabriela Zurawska#, Zuzanna Sas#, Aneta Jończy#, **Raghunandan Mahadeva**, Patryk Slusarczyk, Marta Chwałek, Daniel Seehofer, Georg Damm, Maria Kulecka, Izabela Rumieńczyk, Morgane Moulin, Kamil Jastrzębski, Michal Mikula, Anders Etzerodt, Remigiusz Serwa, Marta Miączyńska, Tomasz P Rygiel, Katarzyna Mleczko-Sanecka

# - equal contribution

Journal: bioRxiv, EMBO Reports (in press)

Date of publishing: 14/11/2023 (first version; bioRxiv); 07/01/2025 (latest version; bioRxiv)

DOI: https://doi.org/10.1101/2023.11.14.566925

I hereby declare that I, Raghunandan Mahadeva, made a substantive contribution to the development of this publication. My contribution consisted of:

I largely supported the experiments that delineated and quantified the contributions of splenic and hepatic myeloid and endothelial cells to the uptake of intact erythrocytes, erythrocyte ghosts, and free hemoglobin (Figure 5A–D). My work involved methodological optimization, assistance in the execution of these experiments, and participation in the interpretation of the resulting data. These findings were important for resolving the functional crosstalk between the liver and spleen in iron recycling from erythrocytes. In addition, I contributed to basic data analysis and preparation of visualizations that aided in presenting the results clearly within the manuscript.

Candidate's Signature

Signature of the Corresponding Author

INTERNATIONAL INSTITUTE OF MOLECULAR AND CELL BIOLOGY IN WARSAW
4 Ks. Trojdena Street, 02-109 Warsaw, Poland; phone: +48 22 597 07 00, fax: +48 22 597 07 15
e-mail: secretariat@iimcb.gov.pl, **www.iimcb.gov.pl**

Article

SOURCE DATA | TRANSPARENT PROCESS | OPEN ACCESS | CHECK FOR UPDATES

EMBO reports

Liver sinusoidal endothelial cells constitute a major route for hemoglobin clearance

Gabriela Zurawska[1,9], Zuzanna Sas[2,9], Aneta Jończy[1,9], Raghunandan Mahadeva[1], Patryk Slusarczyk[1], Marta Chwałek[1], Daniel Seehofer[3], Georg Damm[3], Rafał Mazgaj[4], Marcin Skórzyński[5], Maria Kulecka[6], Izabela Rumieńczyk[6], Morgane Moulin[7], Kamil Jastrzębski[1], Kevin Waldron[4], Michal Mikula[6], Anders Etzerodt[7], Remigiusz Serwa[8], Marta Miączyńska[1], Tomasz P Rygiel[5,10]✉ & Katarzyna Mleczko-Sanecka[1,10]✉

Abstract

Mild rupture of aged erythrocytes occurs in the spleen, resulting in hemoglobin (Hb) release, whereas pathological hemolysis characterizes several diseases. Hb detoxification is attributed to macrophages, but other routes of Hb clearance remain elusive. Here, we uncover that Hb uptake is chiefly executed by liver sinusoidal endothelial cells (LSECs) via macropinocytosis. Consistently, LSECs display proteomic signatures indicative of heme catabolism, ferritin iron storage, antioxidant defense, and macropinocytic capacity, alongside high iron content and expression of the iron exporter ferroportin. Erythrocyte/Hb transfusion assays demonstrate that splenic macrophages excel in erythrophagocytosis, while LSECs and Kupffer cells scavenge the spleen-borne hemolysis products Hb and erythrocyte membranes, respectively. High Hb doses result in transient hepatic iron retention, LSEC-specific induction of heme-catabolizing *Hmox1*, along with the iron-sensing *Bmp6*-hepcidin axis culminating in hypoferremia. Transcriptional induction of *Bmp6* in LSECs is phenocopied by erythrocyte lysis upon phenylhydrazine and elicits a distinct transcriptional signature compared to iron. Collectively, we identify LSECs as key Hb scavengers, a function that establishes the spleen-to-liver axis for iron recycling and contributes to heme detoxification during hemolysis.

Keywords Hemoglobin; Hemolytic Disease; LSEC; Macropinocytosis; RBC
Subject Categories Autophagy & Cell Death; Haematology; Immunology
https://doi.org/10.1038/s44319-025-00673-5
Received 20 February 2025; Revised 20 November 2025;
Accepted 3 December 2025
Published online: 6 January 2026

Introduction

Internal iron recycling from senescent red blood cells (RBCs) satisfies most of the body's iron needs (Muckenthaler et al, 2017; Slusarczyk and Mleczko-Sanecka, 2021) and relies mainly on the phagocytic clearance of aged RBCs by splenic red pulp macrophages (RPMs) (Ma et al, 2021; Youssef et al, 2018). However, recent evidence suggests that some aged RBCs escape erythrophagocytosis and lyse locally in the spleen, thus releasing hemoglobin (Hb) (Klei et al, 2020). Several inherited and acquired disorders, including hereditary anemias, autoimmune hemolytic diseases, or infections, are characterized by compromised erythrocyte stability and an increased risk of hemolysis (Kato et al, 2017; Schaer et al, 2014). Free Hb is captured by the acute-phase plasma protein haptoglobin (Wang et al, 2001). The Hb-haptoglobin complexes are sequestered via CD163 (Kristiansen et al, 2001), a receptor that is highly expressed by both splenic RPMs and liver macrophages, Kupffer cells (KCs) (Klei et al, 2020; Slusarczyk and Mleczko-Sanecka, 2021). However, the role of these macrophage populations in Hb uptake has not been well characterized. Interestingly, pharmacokinetic studies in non-rodent mammals have shown that the clearance rate of the Hb-haptoglobin complex is significantly slower than that of free Hb (Boretti et al, 2014), and that Hb sequestration may occur independently of haptoglobin and/or CD163 (Etzerodt et al, 2013; Schaer et al, 2006b). These observations are clinically relevant as enhanced erythrophagocytosis and prolonged erythrolytic conditions lead to the partial loss of the CD163-expressing iron-recycling macrophages (Theurl et al, 2016; Youssef et al, 2018) and are characterized by depletion of the plasma haptoglobin pool (Schaer et al, 2014; Vinchi et al, 2013; Vinchi et al, 2021). Collectively, this evidence suggests that macrophages may be dispensable for Hb clearance. It is well established that free Hb undergoes renal glomerular filtration (Fagoonee et al, 2005; Marro et al, 2007). However, it remains

[1]International Institute of Molecular and Cell Biology in Warsaw, Warsaw, Poland. [2]Medical University of Warsaw, Warsaw, Poland. [3]Department of Hepatobiliary Surgery and Visceral Transplantation, Clinic for Visceral, Transplant, Thoracic and Vascular Surgery, Leipzig University Medical Center, Leipzig, Germany. [4]Institute of Biochemistry and Biophysics, Polish Academy of Sciences, Warsaw, Poland. [5]Mossakowski Medical Research Institute, Polish Academy of Sciences, Warsaw, Poland. [6]Maria Sklodowska-Curie National Research Institute of Oncology, Warsaw, Poland. [7]Department of Biomedicine, Aarhus University, Aarhus, Denmark. [8]ReMedy International Research Agenda Unit, IMol Polish Academy of Sciences, Warsaw, Poland. [9]These authors contributed equally: Gabriela Zurawska, Zuzanna Sas, Aneta Jończy. [10]These authors contributed equally: Tomasz P Rygiel, Katarzyna Mleczko-Sanecka. ✉E-mail: trygiel@imdik.pan.pl; kmsanecka@iimcb.gov.pl

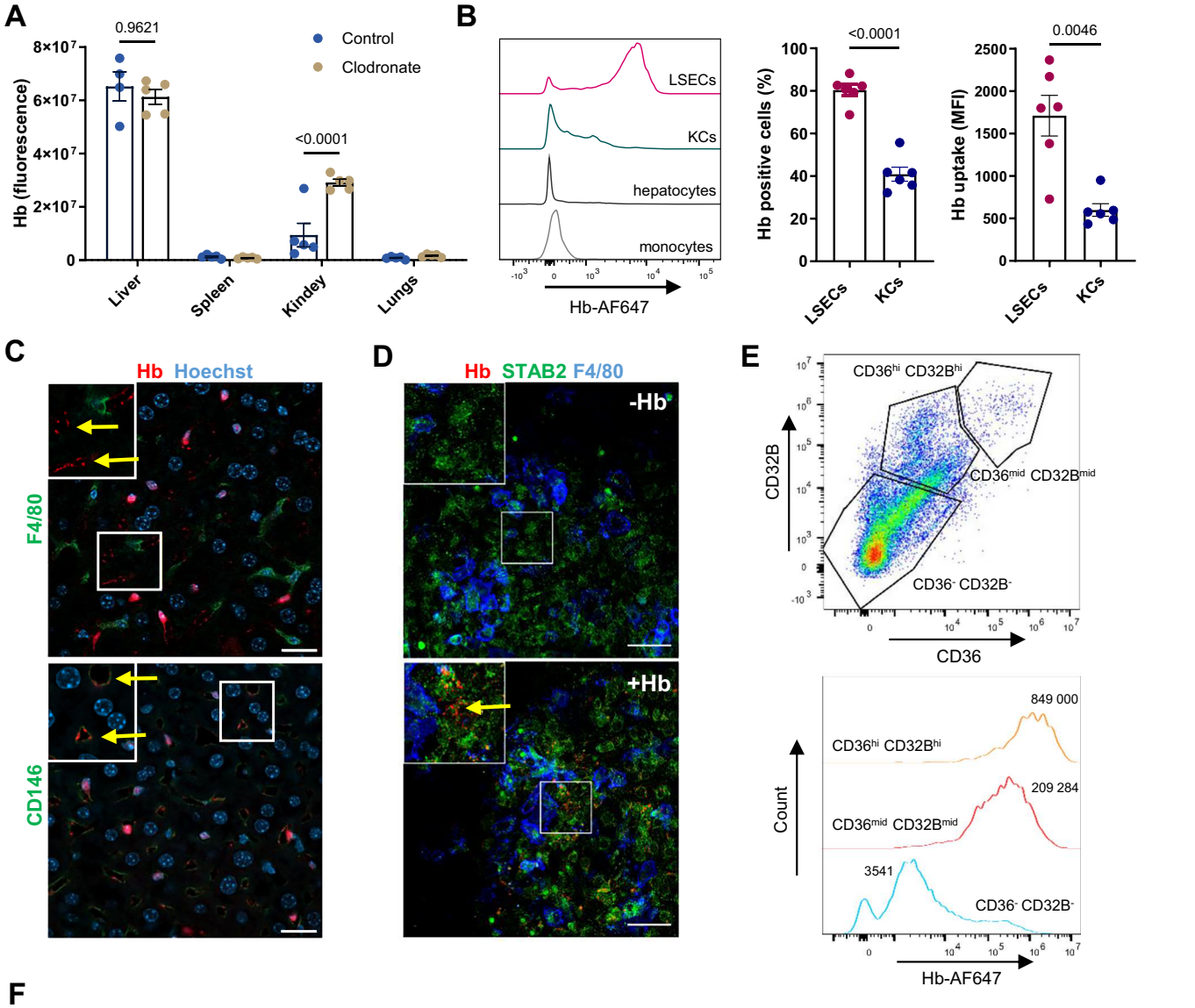

unclear whether other specialized routes of extra-renal and macrophage-independent Hb clearance operate in the body.

The liver receives approximately 25% of the cardiac output and is exposed to blood from the portal circulation, which drains the gastrointestinal tract and the spleen (Poisson et al, 2017). The hepatic capillary network, which is composed of venous sinusoids, is specialized for monitoring and filtering blood components. Liver sinusoidal endothelial cells (LSECs), along with KCs, constitute the most efficient dual scavenging system in the body (Sorensen et al, 2012). While KCs engulf large particles, LSECs remove macromolecules and nanoparticles, a function that protects the body from waste by-products and noxious blood factors (Koch et al, 2021; Schledzewski et al, 2011). The maintenance of appropriate iron homeostasis adds to the growing spectrum of homeostatic functions of LSECs. Importantly, LSECs are the sensors of body iron levels and the major producers of inducible angiokine bone morphogenetic protein 6 (BMP6), and homeostatic BMP2 (Canali et al, 2017; Koch et al, 2017). BMPs function as upstream activators of hepcidin, a key iron-regulatory hormone produced by liver hepatocytes (Muckenthaler et al, 2017). Hepcidin

Figure 1. LSECs represent the major cell type that sequesters Hb.

(**A**) Hemoglobin (Hb) distribution in control and macrophage-depleted mice (clodronate) injected with AlexaFluor 750-labeled Hb (Hb-AF750, 10 µg/mouse), imaged with Bruker in vivo Imaging System. Results are presented as total fluorescent counts from the isolated organs. (**B**) AF750 fluorescence from the indicated liver cell populations isolated from Hb-AF750-injected mice was analyzed with flow cytometry. (**C**) Frozen liver slices from mice injected with Hb-AF647 (red) were processed and stained for Kupffer cells (KCs) (F4/80, green) or LSECs (CD146, green) and nuclei (blue). Single-channel images for this figure are presented in Fig. EV1C. (**D**) Murine liver primary non-parenchymal cells (NPCs) were treated in vitro with Hb-AF750 (red) (0.5 µg/ml) and stained for F4/80 (blue) and the LSEC marker STAB2 (green). (**C**, **D**) Areas in the highlighted rectangles are shown at 5× higher magnification. (**E**) Flow cytometric analysis of human freshly isolated primary NPCs, exposed in culture to human Hb-AF647 and stained with the human LSEC markers CD36 and CD32B. The intensity of Hb-A647 uptake was measured in two LSEC subpopulations, $CD36^{hi}CD32B^{hi}$ and $CD36^{mid}CD32B^{mid}$, as compared to other NPCs $CD36^{-}CD32B^{-}$. Numbers indicate MFI. Data are representative of three independent donors of human NPCs. (**F**) Hb-AF647 (green) uptake was imaged in freshly isolated human liver NPCs stained for the LSEC markers CD36 and CD32B (orange). (**C**, **D**, **F**) Arrows indicate Hb presence in LSECs; Scale bars, 20 µm. Numerical data are expressed as mean ± SEM; each data point represents one biological replicate (individual mouse or independent cell-based experiment), $n = 4$–5 (**A**), 6 (**B**). Two-way ANOVA with Tukey's Multiple Comparison tests was used in (**A**), and Welch's unpaired *t* test was used to determine statistical significance in (**B**); exact *P* values are shown on graphs. Source data are available online for this figure.

suppresses iron release into the bloodstream via the sole known iron exporter ferroportin (FPN), thereby limiting iron availability under iron-rich conditions (Mleczko-Sanecka and Silvestri, 2021). However, it remains unclear how different types of iron signals are sensed and detoxified in the liver microenvironment, and whether the emerging scavenging functions of LSECs cross-talk with their role in maintaining iron homeostasis. Here, we show that LSECs constitute a major route for Hb clearance. They contribute to steady-state iron recycling from spleen-derived Hb that enters the liver via the portal vein and participate in heme detoxification during hemolysis, timely coupled with induction of the iron-sensing BMP6–hepcidin axis.

Results

LSECs engage macropinocytosis to sequester Hb

Studies using radiolabeled Hb have shown that the clearance of injected hemoglobin is rapid (Fagoonee et al, 2005) and mainly mediated by the liver, kidney, and spleen (Fagoonee et al, 2005; Marro et al, 2007). To address the involvement of macrophages in Hb uptake, we first performed experiments using clodronate liposomes, a well-established strategy for depleting tissue macrophages, including hepatic KCs. Using a whole-organ imaging system, we observed that regardless of the presence of KCs, the liver emerged as the major organ sequestering fluorescently-labeled mouse Hb (Figs. 1A and EV1A,B). Next, using flow cytometry and confocal microscopy imaging of mouse liver sections, we identified $CD146^{+}STAB2^{+}$ LSECs as the major hepatic cell type that takes up Hb, surpassing KCs, hepatocytes, and monocytes (Figs. 1B,C and EV1C; see Appendix for gating strategies). We found that murine primary LSEC cultures recapitulated the high capacity of this cell type for Hb uptake, as validated by confocal microscopy and flow cytometry (Figs. 1D and EV1D). We further confirmed that freshly isolated human primary LSECs, distinguished by CD36 and CD32B markers, as previously reported (Ganesan et al, 2012; Strauss et al, 2017) and confirmed by the Human Liver Cell Atlas (Guilliams et al, 2022) (Fig. EV1E), outperformed other NPCs in human Hb uptake (Fig. 1E,F). Notably, flow cytometric analysis revealed that cells with high CD36 and CD32B expression, albeit not highly abundant, showed the highest capacity for Hb scavenging (Fig. 1E).

To better understand the mechanism of Hb uptake, we used mouse primary liver cell cultures. In contrast to murine KCs, LSECs were negative for the Hb-haptoglobin complex receptor, CD163 (Fig. 2A), and took up free Hb to a comparable extent as haptoglobin-bound Hb (Hb:Hp; Fig. 2B). Therefore, we hypothesized that LSECs may sequester Hb in a receptor-independent manner, possibly via macropinocytosis, which is a non-specific internalization of extracellular fluid (Canton, 2018). Staining of primary murine LSECs with an early endosome marker, EEA1, revealed many constitutively formed intracellular vesicles of macropinosome size (1–2 µm) (Figs. 2C and EV2A). Fluorescently-labeled Hb was entrapped, though not exclusively, within such vesicles (Figs. 2C and EV2A), and co-localized with high-molecular-weight dextran, a known macropinocytic cargo (Figs. 2D and EV2B) (Commisso et al, 2013; Zdzalik-Bielecka et al, 2021). Human primary CD36-high LSECs likewise displayed numerous macropinosome-like vesicles and efficiently sequestered dextran (Fig. 2E,F). Consistently, ethyl-isopropyl amiloride (EIPA), a well-established blocker of macropinocytosis, in contrast to an inhibitor of clathrin-mediated endocytosis, chlorpromazine (CPZ), abolished Hb uptake in murine primary LSECs (Figs. 2G and EV2C) and decreased Hb scavenging by their human counterparts (Fig. 2H). Notably, EIPA was less potent in inhibiting Hb uptake in human LSECs, indicating possible species differences in sensitivity or compensatory uptake pathways. Furthermore, Hb internalization by murine LSECs was partially dependent on actin remodeling (suppressed by latrunculin A, LAT-A), and Cdc42 activity (inhibited by ML141), both of which are important for macropinosome formation (Zdzalik-Bielecka et al, 2021). Hb uptake also required canonical Wnt signaling via β-catenin (blocked by PRI-724), a pathway that is active in LSECs (Klein et al, 2008) and has previously been shown to activate macropinocytosis (Fig. 2G) (Redelman-Sidi et al, 2018; Tejeda-Munoz et al, 2019). Similarly, Hb uptake by human primary LSECs was suppressed by LAT-A (Fig. 2H), supporting the conclusion that Hb uptake in LSECs is at least partially dependent on macropinocytosis rather than classical clathrin-mediated endocytosis, even though the degree of sensitivity to EIPA may differ between species. Noteworthy, Hb uptake was not altered by the micropinocytosis blocker, nystatin (Fig. 2G). Interestingly, close to 100% of LSECs actively sequestered Hb even at low doses, and the capacity for the uptake did not show saturation with higher cargo presence, implying a receptor-independent entry route (Fig. EV2D). However, the same doses

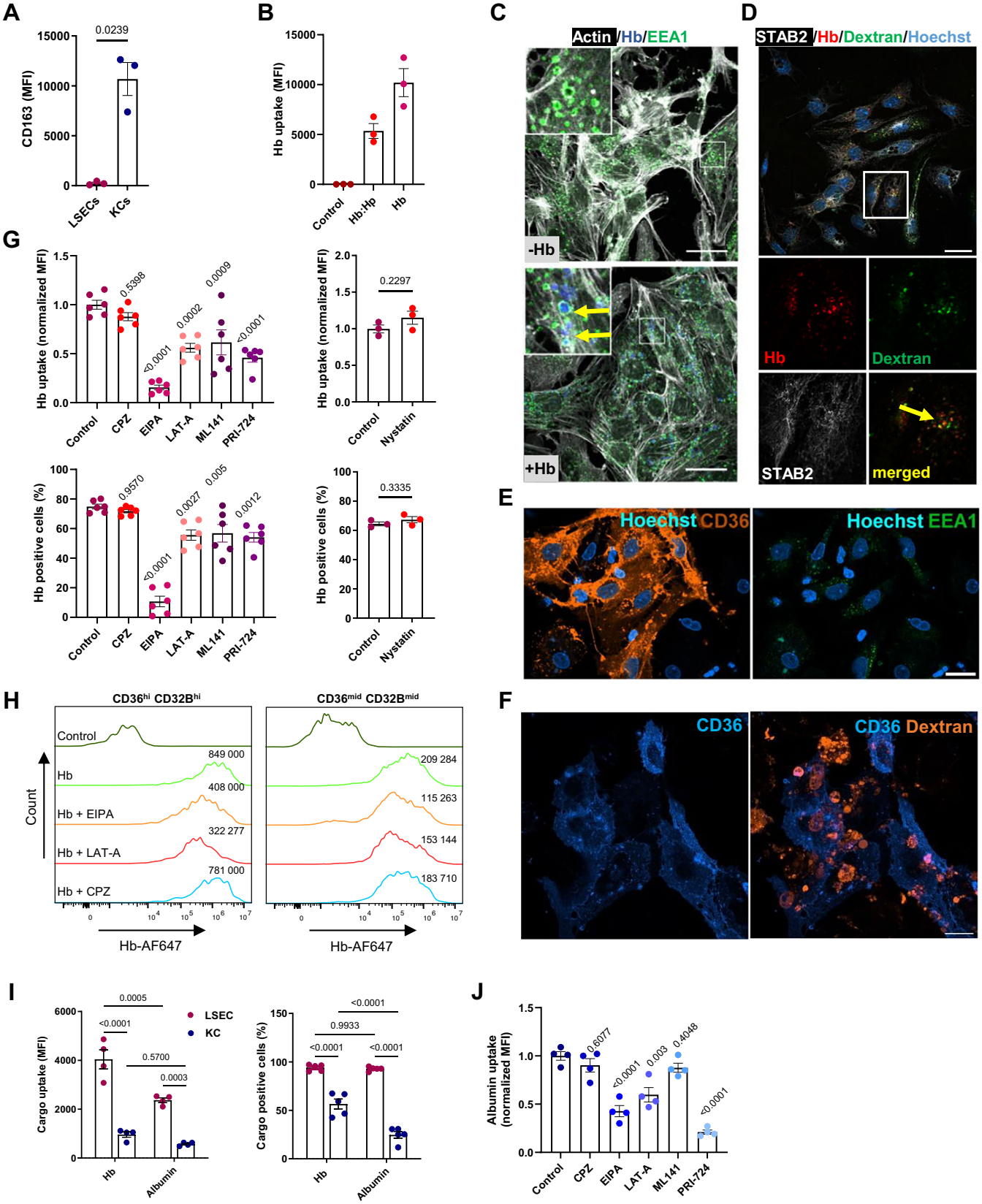
A
CD163 (MFI)
0.0239
LSECs
KCs
B
Hb uptake (MFI)
Control
Hb:Hp
Hb
C
Actin /Hb/EEA1
-Hb
+Hb
D
STAB2 /Hb/Dextran/Hoechst
Hb
Dextran
STAB2
merged
E
Hoechst CD36
Hoechst EEA1
F
CD36
CD36 Dextran
G
Hb uptake (normalized MFI)
Control
CPZ
EIPA
LAT-A
ML141
PRI-724
Nystatin
Hb positive cells (%)
H
CD36hi CD32Bhi
CD36mid CD32Bmid
Control
Hb
Hb + EIPA
Hb + LAT-A
Hb + CPZ
849 000
408 000
322 277
781 000
209 284
115 263
153 144
183 710
Count
Hb-AF647
I
Cargo uptake (MFI)
LSEC
KC
Cargo positive cells (%)
Hb
Albumin
J
Albumin uptake (normalized MFI)

Figure 2. LSECs engage macropinocytosis to sequester Hb.

(A) Cell-surface expression of the CD163 receptor on LSECs and KCs was measured by flow cytometry and presented as fluorescence intensity. **(B)** Uptake of free Hb or Hb in the presence of haptoglobin (Hp, Hb:Hp) in primary murine LSEC cultures was measured with flow cytometry. **(C)** Hb-AF647 vesicle localization was imaged with microscopy in NPCs in vitro cultures depleted of macrophages. Arrows indicate Hb-AF647 (blue) presence in the EEA1$^+$ (green) and Actin$^+$ (white) vesicles. Areas in the highlighted rectangles are shown at a higher 5× magnification (left corner). Scale bars, 20 µm. Single-channel images for this figure are presented in Fig. EV2A. **(D)** Co-localization of Hb-AF647 (red) with rhodamine-dextran (green) was imaged with microscopy in STAB2$^+$ LSECs (white); nuclei are stained in blue. The arrow indicates colocalization of Hb and rhodamine-dextran. The area in the highlighted rectangle is shown at a higher 5× magnification in separate channels below. Scale bar, 20 µm. Single-channel images for this figure are presented in Fig. EV2B. **(E)** EEA1$^+$ vesicles (green) were imaged with microscopy in human NPCs cultures stained with the LSEC marker CD36 (orange); nuclei are stained in blue. **(F)** Texas red-dextran uptake (orange) was imaged with microscopy in human NPCs cultures stained with the LSEC marker CD36 (blue). **(G)** NPCs were pre-treated with the clathrin-mediated endocytosis inhibitor chlorpromazine (CPZ), the macropinocytosis blocker EIPA, actin polymerization blocker latrunculin A (LAT-A), inhibitor of Cdc42 GTPase ML141, β-catenin inhibitor PRI-724, and with micropinocytosis blocker nystatin before Hb-AF750 treatment for 10 min. Flow cytometry was used to determine Hb uptake by the LSECs. **(H)** Flow cytometric analysis of CD36^{hi}CD32B^{hi} and CD36^{mid}CD32B^{mid} human primary LSECs, treated with Hb-AF647 and exposed to EIPA, LAT-1, and CPZ. Numbers indicate MFI. Data are representative of three independent donors of human NPCs. **(I)** Mice were injected for 1 h with Hb-AF750 or albumin-AF750, both at 10 µg/mouse. The fluorescence intensity of AF750, the percentage of AF750$^+$ LSECs, and KCs populations were measured with flow cytometry. **(J)** NPCs were pre-treated with CPZ, EIPA, LAT-A, ML141, and PRI-724 before albumin-AF647 treatment for 10 min. Flow cytometry was used to determine albumin uptake by the LSECs. **(C–F)** Scale bars, 20 µm. Numerical data are expressed as mean ± SEM, each data point represents one biological replicate (individual mouse or independent cell-based experiment), $n = 3$ **(A, B)**, 3–6 **(G)**, 4–5 **(I)**, 4 **(J)**. Welch's unpaired *t* test was used to determine statistical significance in **(A, G)** for nystatin, two-way ANOVA with Tukey's Multiple Comparison tests was used in **(I)**; while one-way ANOVA with Tukey's Multiple Comparison tests was used in **(G, J)**. Exact *P* values are shown on graphs; values above bars in **(G, J)** indicate comparison with untreated controls. Source data are available online for this figure.

of dextran, a cargo of similar molecular weight, were internalized by LSECs with far lower efficiency (Fig. EV2D). This implied a certain specialization of LSECs towards Hb scavenging, even though the uptake of dextran by LSECs was likewise abolished by the macropinocytosis inhibitor EIPA or actin remodeling blocker (Fig. EV2E). Confirming the high macropinocytic capacity of LSECs in vivo, we demonstrated their ability for efficient uptake of fluorescently-labeled albumin, another known macropinocytic cargo (Fig. 2I) (Commisso et al, 2013). Furthermore, albumin clearance by primary LSECs was inhibited by EIPA, LAT-A, and PRI-724, further supporting the high macropinocytic activity of these specialized cells (Fig. 2J). Of note, we observed that the uptake of Hb by primary murine KCs was not affected by the clathrin endocytosis inhibitor CPZ, and appeared to be dependent on macropinocytosis (Fig. EV2F). Interestingly, the uptake of the Hb:Hp complex by LSECs and KCs was suppressed by both EIPA and CPZ, implying the involvement of both clathrin-dependent endocytosis and macropinocytosis routes in this process (Fig. EV2G). Taken together, our data identify LSECs as efficient scavengers of both free and haptoglobin-bound Hb and implicate macropinocytosis as an important alternative pathway for Hb uptake, which also extends to KC-mediated Hb scavenging.

LSECs outperform other endothelial and macrophage populations in Hb uptake

Similar to the liver, sinusoidal endothelial cells are also present in the spleen and bone marrow (Koch et al, 2021), organs that perform critical functions in systemic iron metabolism owing to the presence of CD163$^+$ iron-recycling RPMs and erythroblastic island macrophages, respectively. Therefore, we sought to accurately compare the Hb-scavenging capacity of endothelial and macrophage populations from the spleen and bone marrow with those of hepatic LSECs and KCs over a wide range of Hb doses. Thus, we intravenously injected mice with 1 µg of Hb, which is below the binding capacity of circulating haptoglobin (10–20 µg/ml plasma), an intermediate dose of 10 µg, and 100 µg (injected together with 10 mg of unlabeled Hb), which saturates the haptoglobin pool and mimics hemolytic conditions. We also injected mice with 1 µg of Hb bound to haptoglobin. Myeloid cells and ECs from the bone marrow were not capable of efficient Hb sequestration (Appendix Fig. S1A). Strikingly, we observed the extraordinary ability of LSECs to internalize Hb as compared to the other cell types analyzed, as exemplified by the 70–99% of Hb-positive cells depending on the dose (Fig. 3A) and the highest mean intensity of the Hb signal per cell as compared to KCs, splenic ECs, or RPMs (Fig. 3B,D,F,H). The scavenging capacity of KCs and splenic ECs gradually increased with the Hb dose (Fig. 3C–F), whereas RPMs contributed, albeit slightly, to Hb clearance only at the highest dose, mimicking hemolysis (Fig. 3G,H). Finally, using flow cytometry and whole-organ imaging, we did not detect Hb accumulation in the aorta, lined by non-sinusoidal ECs (Appendix Fig. S1B,C). In conclusion, our data suggest that LSECs outperform other cell types for Hb clearance over a wide range of circulating Hb concentrations.

LSECs constitutively express proteins critical for iron recycling from heme

We were intrigued by the fact that LSECs efficiently scavenged low doses of Hb. To further explore their specialization, we examined data from single-cell RNA sequencing of ECs from different mouse organs (Kalucka et al, 2020). Interestingly, both *Hmox1* [encoding heme oxygenase 1 (HO-1)] and *Blrvb* (encoding biliverdin reductase b, BLRVB), which are important for heme catabolism, together with important antioxidant enzymes such as *Gclc*, *Gpx4*, and *Nqo1*, were identified by Kalucka et al (Kalucka et al, 2020) as metabolic markers exclusively specific for liver EC. Using the EC Atlas, we visualized the expression levels of *Hmox1* and *Blvrb*, as well as *Slc40a1*, the gene encoding the iron exporter FPN, and found a clear signature for the high expression of these transcripts in liver ECs compared to other organs (Appendix Fig. S2A). Consistently, by employing dedicated single-cell RNA-seq databases, we observed high expression levels of *Slc40a1*, *Hmox1*, and *Hmox2* in pig liver ECs and *Slc40a1* in human LSECs (Appendix Fig. S2B,C) (Guilliams et al, 2022; Wang et al, 2022). Following up

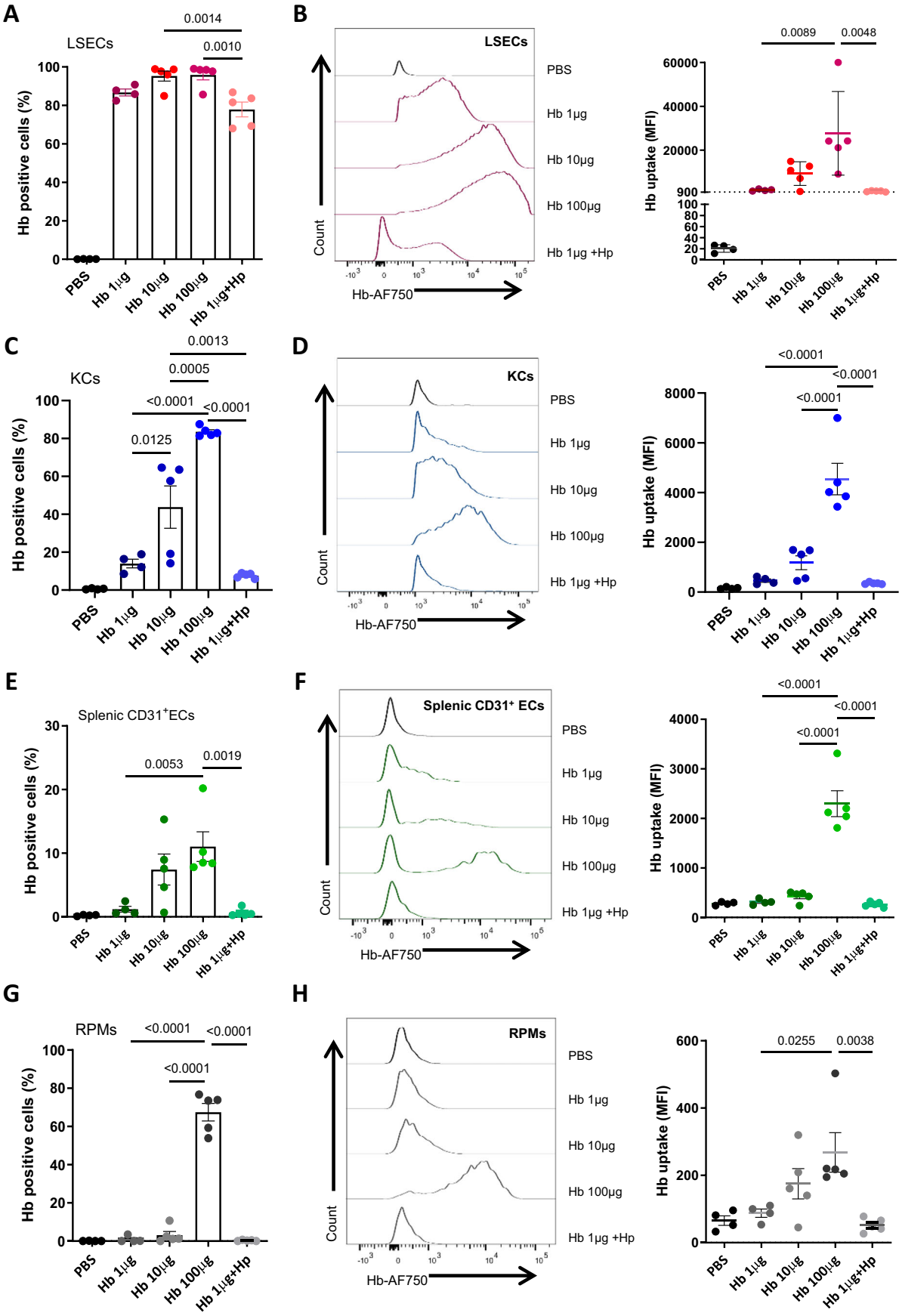
A
LSECs
0.0014
0.0010
Hb positive cells (%)
PBS
Hb 1µg
Hb 10µg
Hb 100µg
Hb 1µg+Hp
B
LSECs
PBS
Hb 1µg
Hb 10µg
Hb 100µg
Hb 1µg +Hp
Count
Hb-AF750
0.0089
0.0048
Hb uptake (MFI)
C
KCs
0.0013
0.0005
<0.0001
<0.0001
0.0125
D
KCs
<0.0001
<0.0001
<0.0001
E
Splenic CD31+ECs
0.0053
0.0019
F
Splenic CD31+ ECs
<0.0001
<0.0001
<0.0001
G
RPMs
<0.0001
<0.0001
<0.0001
H
RPMs
0.0255
0.0038

Figure 3. LSECs outperform other endothelial populations and macrophages in Hb uptake.

Mice received intravenous injections of fluorescently labeled hemoglobin (Hb-AF750) at increasing doses, either alone or complexed with haptoglobin, as indicated. Samples were collected after 1 h. The percentage of Hb-AF750-positive cells and fluorescence intensity of Hb-AF750 are shown for LSECs (**A**, **B**), KCs (**C**, **D**), splenic CD31^{+} endothelial cells (ECs) (**E**, **F**), and RPMs (**G**, **H**). Both parameters were analyzed with flow cytometry. Data are expressed as mean ± SEM, and each data point represents one biological replicate (individual mouse), $n = 4$–5 (**A–H**). One-way ANOVA with Tukey's Multiple Comparison tests was used to determine statistical significance; exact *P* values are shown on graphs. Source data are available online for this figure.

on these transcriptomic signatures, we detected protein expression of FPN and HO-1 in mouse liver sections (Fig. 4A) and primary murine LSECs (Fig. 4B). Flow cytometry confirmed clear expression of cell-surface FPN on LSECs, reaching approximately 40% of cells, albeit at lower levels compared to KCs (Fig. 4C). Furthermore, close to 100% of LSECs were positive for HO-1, although the expression levels appeared lower than those in KCs (Fig. 4D). Next, to obtain comprehensive information on LSEC adaptation to Hb clearance, we performed label-free proteomic profiling of FACS-sorted LSECs in comparison with iron recycling macrophages (RPMs and KCs) and splenic and heart ECs. This analysis identified 417 protein groups that were significantly more abundant in LSECs than in splenic and cardiac ECs (Fig. 4E; Dataset EV1). In addition to well-established LSEC markers (STAB1, STAB2, CD206), intriguingly, these included L and H ferritin, HO-1 and BLVRB, heme binding protein HEBP1, and enzymes involved in the antioxidant response (e.g., NQO1, GCLC, or PRDX1). Interestingly, the hits also included several known macropinocytosis effectors, such as Rabankirin-5, ATP6V0A1, RAB5 or septin 2 (Dolat and Spiliotis, 2016; Maxson et al, 2021; Ramirez et al, 2019; Schnatwinkel et al, 2004), and several putative players identified by previous RNAi screens (Ramirez et al, 2019) (Dataset EV1). This proteomic signature of LSEC, indicating their steady-state involvement in Hb uptake and iron recycling from heme, was consistent with their iron/heme indices. As measured by ICP-OES, FACS-sorted LSECs showed total iron levels intermediate between KCs and heart or spleen ECs. Moreover, LSECs exhibited higher labile iron levels compared to other ECs, as determined with Fe^{2+}-specific fluorescent probe and flow cytometry (Fig. 4F,G). Likewise, magnetically-sorted LSECs showed slightly lower, though not statistically significant, heme content compared with KCs and splenic RPMs (Fig. 4H). The purity of LSECs and KCs obtained by magnetic separation is shown in Appendix Fig. S3. FPN was robustly induced in LSECs under conditions of systemic iron deficiency, mimicking the response observed in KCs (Fig. 4I), suggesting a tight control of LSECs' FPN by circulating hepcidin. Confirming the iron export function of LSEC FPN, we detected a significant increase in labile iron in LSECs in response to mini-hepcidin PR73 injection, a response that was comparable to that found in KCs (Fig. 4J). Collectively, these data indicate that LSECs are equipped with protein machinery that drives iron recycling from heme, suggesting their role in steady-state iron turnover.

LSECs and KCs support iron recycling by removing hemolysis products from the spleen

Next, we sought to understand how LSECs may be involved in physiological iron recycling. The hemolysis-driven iron recycling model proposed by Klei et al implied but did not formally demonstrate that RPMs likely sequester spleen-derived Hb via highly expressed CD163 (Klei et al, 2020). However, CD163 knockout mice did not show major differences in systemic and splenic iron parameters (Fig. EV3). Inspired by the high capacity of LSECs for Hb scavenging, we hypothesized that hepatic cells may play a role in the clearance of splenic hemolytic products delivered via portal circulation. Therefore, we extended previous studies by quantifying the contributions of splenic and hepatic myeloid and endothelial cells to the uptake of intact RBCs, RBCs devoid of cytoplasm (RBC ghosts), and free Hb. To this end, we injected mice with temperature-stressed RBCs, derived from UBI-GFP transgenic mice, a model where GFP is expressed ubiquitously under the human ubiquitin C promoter. GFP-positive stressed RBCs were additionally stained with the membrane label PKH26 (Fig. 5A,B). This approach revealed that RPMs outperformed other splenic cell types, F4/80^{high} CD11b^{high} pre-RPMs, CD11c^{+} dendritic cells (DCs), monocytes, and splenic ECs in the sequestration of PKH26^{+}GFP^{+} intact RBCs. An equal percentage of RPMs (approximately 30% of the population) was effective in removing PKH26^{+}GFP^{-} RBC ghosts, a function that was efficiently supported by splenic pre-RPMs and, to a lesser extent, by DCs, monocytes, or ECs. Interestingly, we found that in the liver, phagocytosis of intact RBCs by KCs was less efficient than the uptake of RBC ghosts (Fig. 5B). Erythrophagocytosis of intact RBCs was negligible in hepatic DCs and LSECs, but they showed some capacity for the sequestration of RBC membranes, albeit lower than that of KCs. Independently, injection of fluorescently labeled RBC ghosts along with free Hb confirmed that KCs and LSECs, rather than RPMs or splenic ECs, respectively, are specialized in the clearance of these two major hemolysis products (Fig. 5C,D). Corroborating these data, we detected an increase in heme levels in the portal vein plasma, and we identified hemoglobin α (HBA) and β (HBB) chains as top proteins upregulated in LSECs at the proteome-wide level after injection of stressed RBCs compared to control PBS-injected mice (Fig. 5E,F; Dataset EV2). Interestingly, among the five proteins that were significantly increased along with HBA and HBB in LSECs following RBC transfusion, we detected two dehydrogenases ALDH1A1 and ALDH1L1 (Fig. 5F), the former with established roles in the detoxification of aldehydes formed by lipid peroxidation (Makia et al, 2011).

Next, we sought to determine whether the ability of LSECs to sequester Hb could be modulated by the altered capacity of splenic RPMs to fully execute erythrophagocytosis. First, we observed that LSECs were more effective at Hb uptake in response to macrophage depletion after clodronate injection (Fig. 5G). Consistently, plasma and kidney heme levels did not significantly differ between control and clodronate-injected mice at the early 1-hour time point following intravenous Hb administration (Fig. 5H,I). Second, we took advantage of the physiological difference in iron parameters between the BALB/c and C57BL/6 J (BL/6 J) mice. We observed a lower erythrophagocytic capacity of RPMs from BALB/c mice

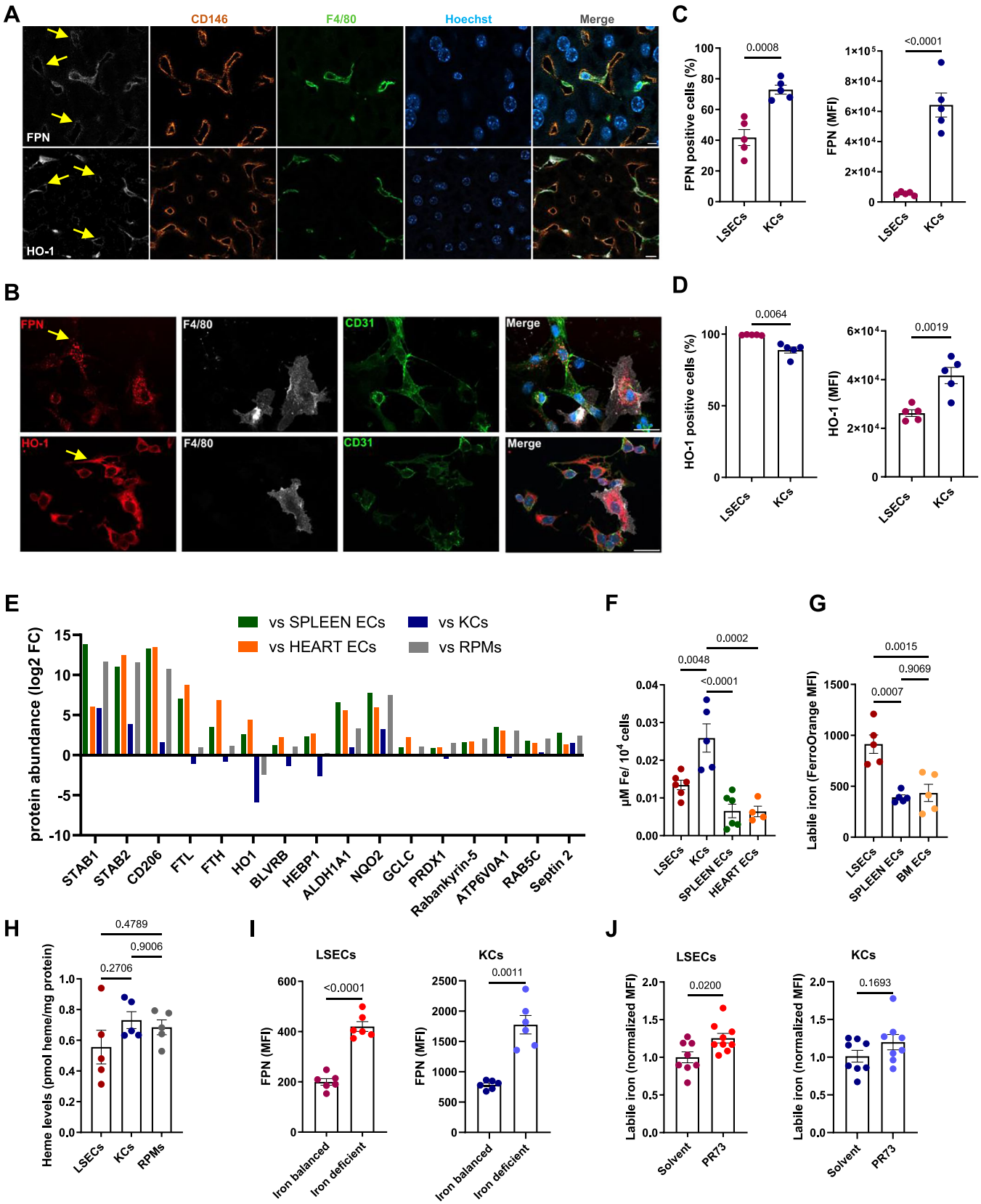
A
CD146
F4/80
Hoechst
Merge
FPN
HO-1
B
FPN
F4/80
CD31
Merge
HO-1
C
FPN positive cells (%)
0.0008
FPN (MFI)
<0.0001
LSECs
KCs
D
HO-1 positive cells (%)
0.0064
HO-1 (MFI)
0.0019
E
vs SPLEEN ECs
vs KCs
vs HEART ECs
vs RPMs
protein abundance (log2 FC)
STAB1
STAB2
CD206
FTL
FTH
HO1
BLVRB
HEBP1
ALDH1A1
NQO2
GCLC
PRDX1
Rabankyrin-5
ATP6V0A1
RAB5C
Septin 2
F
µM Fe/ 10^4 cells
0.0002
0.0048
<0.0001
LSECs
KCs
SPLEEN ECs
HEART ECs
G
Labile iron (FerroOrange MFI)
0.0015
0.9069
0.0007
LSECs
SPLEEN ECs
BM ECs
H
Heme levels (pmol heme/mg protein)
0.4789
0.9006
0.2706
LSECs
KCs
RPMs
I
LSECs
KCs
FPN (MFI)
<0.0001
0.0011
Iron balanced
Iron deficient
J
LSECs
KCs
Labile iron (normalized MFI)
0.0200
0.1693
Solvent
PR73

Figure 4. LSECs constitutively express proteins critical for iron recycling and macropinocytosis.

(A) Frozen mouse liver slices were processed and stained for FPN or HO-1 (white) in KCs (F4/80, green) or LSECs (CD146, orange) and imaged using confocal microscopy. Scale bars, 5 µm (upper panel) and 10 µm (bottom panel) **(B)** FPN and HO-1 presence in F4/80$^+$ (white) KCs and CD31$^+$ endothelial cells (green) imaged by confocal microscopy in murine NPC in vitro cultures. **(A, B)** Nuclei (blue), scale bars, 20 µm. Arrows indicate ECs positive for FPN or HO-1. **(C)** Flow cytometry analysis of FPN expression in LSECs and KCs. **(D)** Flow cytometry analysis of HO-1 expression in LSECs and KCs. **(E)** Shown are selected proteins that are statistically significantly ($P < 0.01$) more abundant in mouse FACS-sorted LSECs than in spleen and heart endothelial cells (ECs). Log2 fold change (from three independent cell isolates) in protein abundance in LSECs versus the indicated cell type is presented. Data are retrieved from Dataset EV1, where individual label-free quantification values of protein abundance and calculated *P* values are included. **(F)** Total iron content in FACS-sorted cells was determined by ICP-OES and normalized to cell numbers. **(G)** Cytosolic ferrous iron (Fe^{2+}) levels in the indicated endothelial cells were measured with a FerroOrange probe and flow cytometry. **(H)** Heme levels were quantified in magnetically-sorted cells using the Heme Assay Kit and normalized to the protein content. **(I)** Flow cytometry analysis of FPN expression in LSEC and KCs isolated from mice maintained on balanced or iron-deficient diets. **(J)** Cytosolic ferrous iron (Fe^{2+}) content was measured with a FerroOrange probe and flow cytometry in LSECs and KCs derived from mice injected with mini-hepcidin (PR73). Numerical data are expressed as mean ± SEM, and each data point represents one biological replicate (individual mouse), $n = 5$ **(C, D, G, H)**, 5–6 **(F)**, 6 **(I)**, 8–9 **(J)**. Welch's unpaired *t* test was used to determine statistical significance in **(C, D, I, J)**; one-way ANOVA with Tukey's Multiple Comparison tests was used in **(F, G, H)**; exact *P* values are shown on graphs. Source data are available online for this figure.

compared to BL/6 J mice (Fig. 5J), which was likely underlain by higher iron levels and reduced RPM FPN expression (Fig. EV4A,B), two interconnected factors that were previously shown to affect erythrophagocytosis (Slusarczyk et al, 2023). This led to heme accumulation in the extracellular space of the spleen and portal plasma (Figs. 5K and EV4C,D). This phenotype was coupled with elevated levels of labile iron, a higher percentage of HO-1-positive LSECs in the liver, and increased FPN expression in the LSECs of BALB/c mice (Figs. 5L–N and EV4E,F), indicating their enhanced activity in iron recycling from Hb. Taken together, our findings support the physiological role of LSECs in the sequestration of endogenous spleen-derived Hb, thereby establishing a spleen-liver axis for effective iron recycling from senescent RBCs.

LSECs detoxify hemoglobin upon hemolysis and trigger the iron-sensing BMP6 angiokine

We next investigated the response of LSECs to hemolytic conditions. To this end, we first injected mice with 10 mg of mouse Hb (equivalent to the RBC fraction in approximately 100 µl of blood) in a time-dependent manner. We detected a significant increase in heme iron content in the liver at the early time point, which was normalized by the 24-hour endpoint (Fig. 6A). Consistently, we observed a transient increase in iron levels in the liver, but not in the spleen (Figs. 6B and EV5A). Notably, the kidney also accumulated iron that could not be mobilized and remained elevated throughout the experiment (Fig. EV5B). Hemoglobin clearance in the liver resulted in a strong transcriptional induction of the heme catabolizing enzyme *Hmox1*, a response that could be attributed specifically to LSECs (Fig. 6C,D). At the protein level, we found that 6 h after intravenous Hb injection, HO-1, which under control conditions was predominantly expressed by KCs, appeared mildly reduced in these cells, while levels in LSECs became more comparable, indicating a greater contribution of LSECs to liver HO-1 expression under Hb exposure (Fig. 6E). Notably, although HO-1 was detected in structures resembling sinusoids, the CD146 signal decreased following Hb delivery, an observation that may warrant further investigation. Consistently, we observed that 20 min after high-dose intravenous Hb administration, LSECs, but not KCs or RPMs, showed a significant increase in total iron content, as determined by ICP-OES in magnetically sorted populations (Fig. 6F). The rapid induction of *Hmox1* in LSECs upon intravenous Hb delivery was phenocopied by injecting the mice with the hemolytic agent phenylhydrazine (PHZ), exceeding the transcriptional response of KCs, splenic cells, and the aorta (Fig. 6G,H). PHZ also caused significant, albeit mild, iron accumulation in the liver (Fig. 6I), but not in other organs (Fig. EV5C,D).

Hemoglobin challenge rapidly increased the hepatic expression of the iron-sensing gene *Bmp6*, attributable to FACS-sorted LSECs, accompanied by transient upregulation of the BMP target gene hepcidin (*Hamp*) in the liver (Fig. 7A–C). As expected, induction of the BMP6–hepcidin axis caused serum hypoferremia at the 15-h timepoint, which normalized after 24 h (Fig. 7D), reflecting the changes in liver iron content (Fig. 6B). PHZ-induced hemolysis likewise led to the activation of *Bmp6* transcription in sorted LSECs (Fig. 7E). Finally, we aimed to determine whether LSECs induce a specific response when exposed to Hb compared with non-heme iron. To this end, we performed RNA sequencing to assess global gene expression signatures upon injection of 10 mg of Hb and compared these to a previously reported response to a quantitatively matched dose of iron citrate (Zurawska et al, 2024). Both stimuli induced *Bmp6* at very comparable levels and triggered an ETS1-controlled transcriptional program, as previously reported for iron citrate response (Zurawska et al, 2024) (Appendix Fig. S4). However, the two iron sources elicited different responses of LSECs at the transcriptome-wide level (Fig. 7F). While only 64 genes, mainly attributable to the response to oxidative stress and iron, were co-induced by Hb and iron citrate, as many as 372 and 202 genes increased their expression specifically upon Hb and iron citrate injection, respectively (Fig. 7F). These differences were reflected by a distinct functional enrichment within the Hb- and iron-induced transcriptional signature (Fig. 7G). Interestingly, Hb-exposed LSECs specifically induced genes associated with immune and inflammatory responses, such as the phagocyte marker *Cd68*, the chemokines *Ccl24*, *Ccl6*, and *Ccl9*, and importantly, *Il18*, a cytokine implicated in the pathogenesis of hemolytic sickle cell disease (Gupta et al, 2021). Furthermore, Hb ingestion activated gene expression signatures associated with phagocytosis, the PI3K-Akt pathway, growth factor activity, and intracellular signaling, enriched categories with several links to actin remodeling and, in some cases, directly to macropinocytosis. Indeed, several genes induced by Hb, such as the receptors *Axl*, *Csf1r*, and *Met*, the growth factors *Hgf* and *Pdgfa*, and the actin cytoskeleton-interacting factors *Evl* and *Coro1a* are known to play a role in the regulation and/or execution of macropinocytosis (BoseDasgupta et al, 2015; Recouvreux and Commisso, 2017; Visweshwaran et al, 2022; Zdzalik-Bielecka et al, 2021).

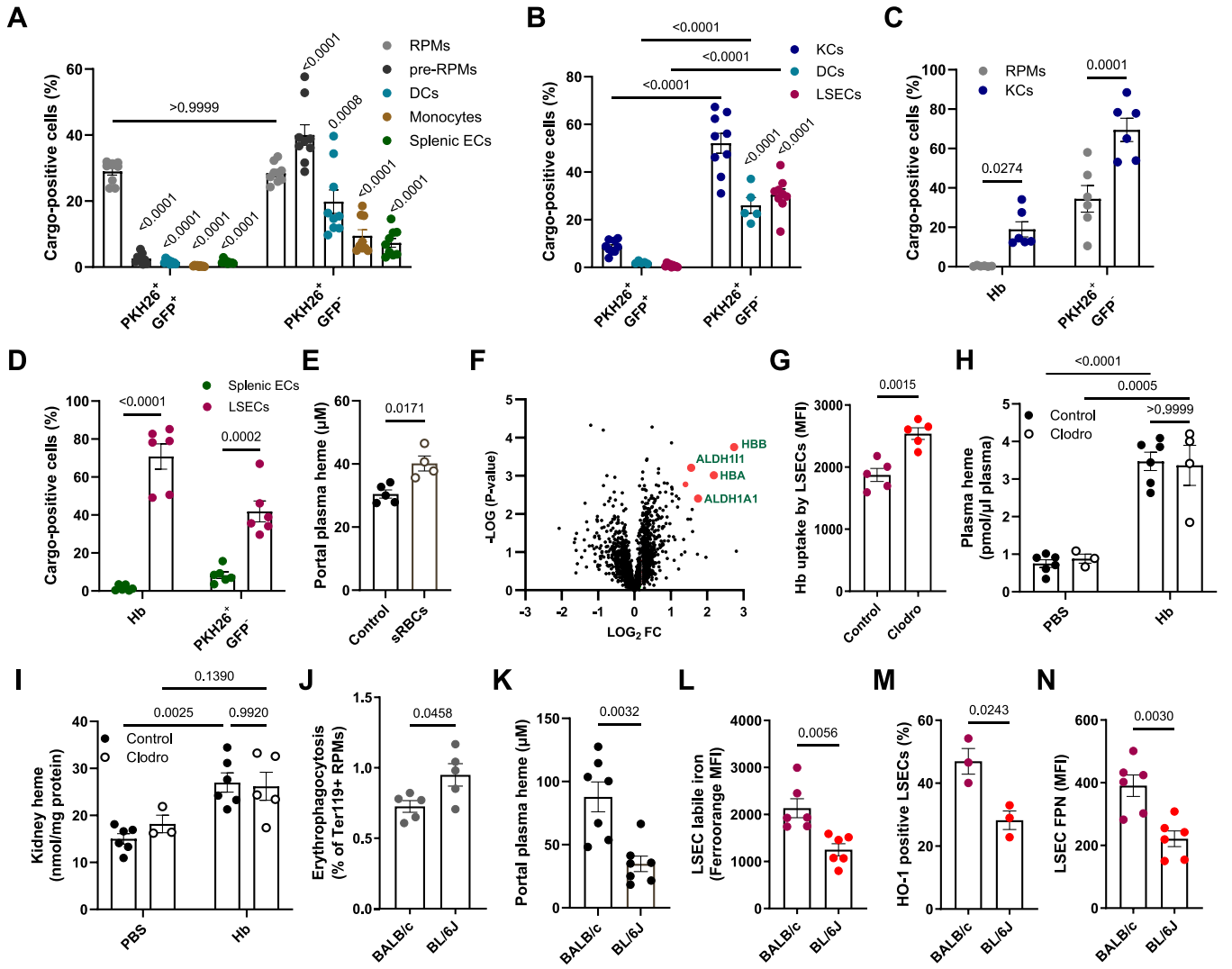

Figure 5. LSECs and KCs support iron recycling by removing hemolysis products from the spleen.

(**A–D**) Mice were administered i.v. with (**A**, **B**) stressed GFP$^+$ RBCs stained with a membrane marker PKH26 or (**C**, **D**) Hb-AF750 and PKH26$^+$ RBCs devoid of cytoplasm (RBC ghosts). Splenic and liver cells were isolated, stained, and analyzed by flow cytometry. (**A**) The percentage of cells positive for markers of intact RBCs (PKH26$^+$GFP$^+$) and RBC ghosts (PKH26$^+$GFP$^-$) in splenic RPMs, pre-RPMs, dendritic cells (DCs), monocytes, and endothelial cells (ECs). (**B**) The percentage of PKH26$^+$GFP$^+$ and PKH26$^+$GFP$^-$ cells in liver KCs, dendritic cells (DCs), and LSECs. (**C**, **D**) The percentage of cells positive for Hb (AF750) and RBC ghosts. (**E**) Heme levels from the portal vein plasma of control mice and mice transfused with temperature-stressed RBCs, measured by Heme Assay Kit. (**F**) Volcano plot illustrating the changes in the proteome of FACS-sorted LSECs 90 min after i.v. transfusion of stressed RBCs. Proteins significantly upregulated are marked in red. Data are included in the Dataset EV2. (**G**) Hb-AF750 uptake by LSECs derived from control and macrophage-depleted mice (Clodro). (**H**, **I**) Heme levels in the plasma (**H**) and kidney (**I**) of control and macrophage-depleted mice (Clodro), measured by Heme Assay Kit. (**J–N**) BALB/c and C57BL/6J (BL/6J) mice phenotype comparison. (**J**) The capacity of endogenous erythrophagocytosis was assessed by intracellular staining of the erythrocytic marker (Ter119) in RPMs. (**K**) Heme levels in the portal vein were measured with the Heme Assay Kit. (**L**) Cytosolic ferrous iron (Fe^{2+}) levels in LSECs were measured with a FerroOrange probe and flow cytometry. (**M**) The percentage of HO-1-positive LSECs was measured with flow cytometry. (**N**) FPN levels in LSECs were measured by flow cytometry. Data are expressed as mean ± SEM, and each data point represents one biological replicate (individual mouse), $n = 8$–9 (**A**, **B**), 6 (**C**, **D**, **L**, **N**), 4–5 (**E**), 5 (**F**, **G**, **J**), 3–6 (**H**, **I**), 7 (**K**), 3 (**M**). Welch's unpaired *t* test was used to determine statistical significance in (**E**, **G**, **J–N**); while two-way ANOVA with Tukey's Multiple Comparison tests was used in (**A–D**, **H**, **I**); exact *P* values are shown on graphs, values above bars in (**A**, **B**) indicate comparison with RPMs and KCs, respectively, within the same group. Source data are available online for this figure.

Collectively, these findings support the role of LSECs in Hb clearance and demonstrate their high capacity to trigger the iron-sensing *Bmp6* angiokine in response to excessive Hb, along with specific pro-inflammatory markers and factors associated with actin remodeling.

Discussion

Recent advances have revealed the critical role of specialized hepatic sinusoidal endothelium in maintaining systemic and liver homeostasis. The scavenging activity of LSECs is essential

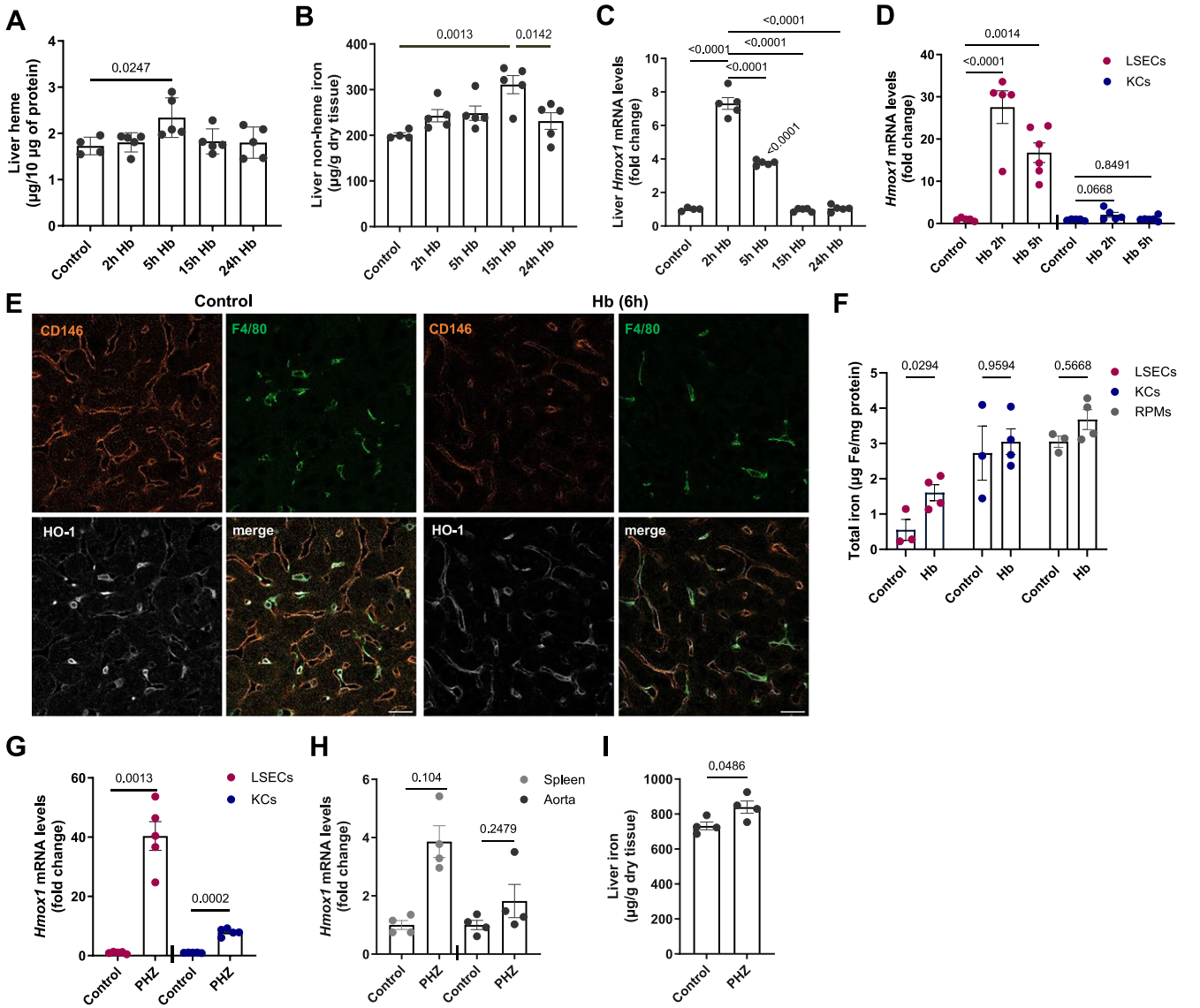

Figure 6. LSECs detoxify hemoglobin upon hemolysis.

(**A–D**) Mice were injected with native hemoglobin (Hb, 10 mg/mouse) and analyzed at the indicated time points. (**A**) Heme iron levels in the liver were determined with the Heme Assy Kit and normalized to protein content. (**B**) Non-heme iron content in the liver was measured by bathophenanthroline colorimetric assay. (**C**, **D**) *Hmox1* gene expression measurement by RT-PCR in (**C**) the liver and (**D**) FACS-sorted KC and LSEC populations. (**E**, **F**) Mice were injected i.v. with high-dose Hb (10 mg). (**E**) Frozen mouse liver slices were processed and stained for HO-1 (white), the LSEC marker CD146 (orange), and F4/80 identifying KCs (green) and imaged using confocal microscopy. Scale bars, 20 µm. (**F**) Total iron content in magnetically-sorted cells was determined 20 min after injection by ICP-OES and normalized to protein content. (**G**, **H**) Hemolysis was induced in mice by i.p. injection of phenylhydrazine (PHZ, 0.125 mg/g) 6 h before analysis. *Hmox1* gene expression in (**G**) FACS-sorted cell populations of KCs and LSECs, and (**H**) spleen and aorta. (**I**) Non-heme iron content in the liver. Data are expressed as mean ± SEM, and each data point represents one biological replicate (individual mouse), $n = 4$–5 (**A–C**), 5–6 (**D**), 3–4 (**F**), 5 (**G**), 4 (**H**, **I**). One-way ANOVA with Tukey's Multiple Comparison tests was used in (**A–C**), and separately for KCs and LSECs in (**D**); two-way ANOVA with Tukey's Multiple Comparison tests was used in (**F**), and Welch's unpaired *t* test was used to determine statistical significance in (**G–I**), separately for each cell type/organ; exact *P* values are shown on graphs, a value above the bar in (**C**) indicates comparison with control mice. Source data are available online for this figure.

for the hepatic clearance of biological macromolecules, such as denatured collagen, glycans/glycation end products, modified low-density lipoproteins, small immune complexes, lipopolysaccharides, and viruses (Ganesan et al, 2012; Koch et al, 2021; Malovic et al, 2007; Schledzewski et al, 2011; Shetty et al, 2018). In addition, LSECs regulate the vascular tone in the liver, balance the tolerogenic immune milieu with the onset of immune responses, ensure physiological zonation of hepatic immune cells (Gola et al, 2021; Shetty et al, 2018), and control iron balance by producing the angiokines BMP2 and BMP6 (Canali et al, 2017; Koch et al, 2017). Our study identified the novel homeostatic role of LSECs in the clearance of free Hb, an activity in which their scavenging and iron-regulatory functions converge.

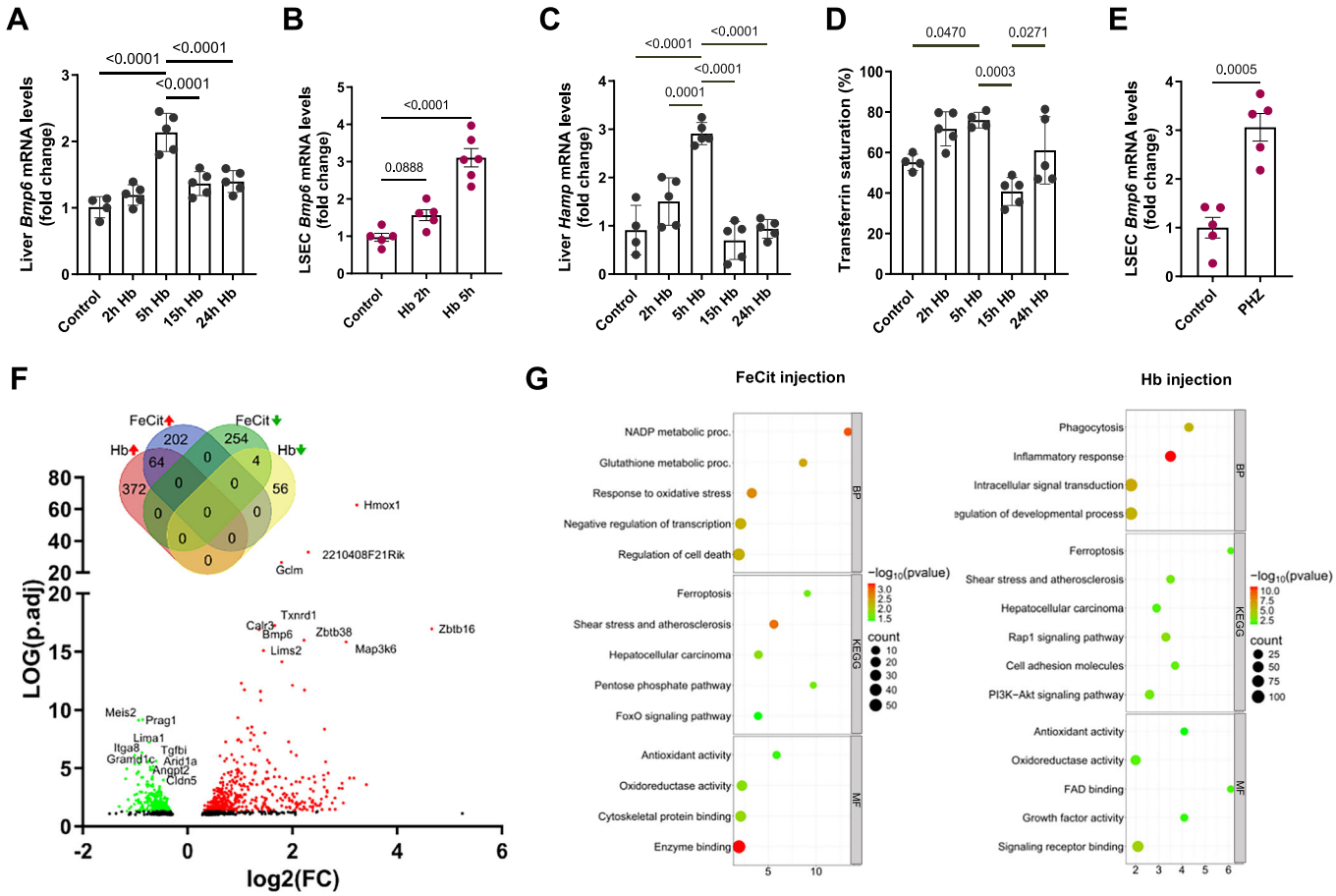

Figure 7. LSECs trigger the iron-sensing BMP6 angiokine upon hemolysis.

(**A–D**) Mice were injected with native hemoglobin (Hb, 10 mg/mouse) and analyzed at the indicated time points. (**A**, **B**) *Bmp6* and (**C**) *Hamp* gene expression measured by RT-qPCR in whole livers or FACS-sorted LSECs, as indicated. (**D**) Plasma iron levels were determined by transferrin saturation measurements. (**E**) *Bmp6* expression in FACS-sorted LSECs in mice injected with (PHZ, 0.125 mg/g, 6 h). (**F**, **G**) Mice were injected with Hb (10 mg) or Ferric citrate (FeCit, 150 µg) for 5 h. (**F**) A volcano plot of differentially regulated genes identified by the RNA-seq transcriptomic analysis in FACS-sorted LSECs. The green color indicates negatively, and the red color positively-regulated genes. A Venn diagram shows genes regulated by Hb and FeCit. (**G**) functional enrichment among genes induced by Hb or FeCit. The *x* axis represents the fold of enrichment. The *y* axis represents GO terms of biological processes (BP), Kyoto Encyclopedia of Genes and Genomes terms (KEGG), and GO terms of molecular function (MF). The size of the dot represents the number of genes under a specific term. The color of the dots represents the adjusted *P*-value. Data are expressed as mean ± SEM, and each data point represents one biological replicate (individual mouse), $n = 4$–5 (**A**, **C**, **D**), 5–6 (**B**), 5 (**E**), 4 (**F**). One-way ANOVA with Tukey's Multiple Comparison tests was used in (**A–D**), while Welch's unpaired *t* test was used to determine statistical significance in (**E**); exact *P* values are shown on graphs. Source data are available online for this figure.

The clearance functions of LSECs have been attributed to their extraordinary endocytic activity and surface expression of scavenger receptors (Koch et al, 2021). We discovered that LSECs have a remarkable and constitutive capacity for macropinocytosis, similar to that of macrophages, which use this pathway for antigen presentation, and in contrast to the inducible macropinocytosis of cancer cells, which is critical for nutrient acquisition (Canton, 2018; Commisso et al, 2013). We showed that this capability distinguishes LSECs from ECs of other organs, thus significantly expanding the scarce knowledge on the macropinocytic activity of ECs (Lin et al, 2020) and assigning physiological significance to early observations that LSECs can engage macropinocytosis for antigen capture (Connolly et al, 2010). We propose that the macropinocytosis of LSECs likely contributes to their scavenging function. While this possibility merits future studies, macropinocytosis has recently been identified as a major driver of LDL uptake by macrophages, leading to foam cell formation in atherosclerosis (Lin et al, 2022). Hence, our findings aid in shifting the paradigm from the sole role of scavenger receptor-mediated endocytosis in the clearance of blood-borne macromolecules, emphasizing the importance of macropinocytic uptake. Finally, our data also demonstrated that the macropinocytic activity of KCs supports their uptake of both free Hb and Hb complexed with Hp, broadening the significance of this route in Hb clearance.

Our study employed in vivo approaches to verify the role of macrophages in Hb uptake and revealed that LSECs qualitatively and quantitatively outcompete CD163-expressing KCs and RPMs in this task. These provocative findings may be explained by the fact that the role of CD163 in Hb uptake has been mainly investigated by its ectopic expression in non-macrophage cells and by using polyclonal anti-CD163 blocking antibodies in cultured macrophages (Kristiansen et al, 2001; Schaer et al, 2006a; Schaer

et al, 2006b). It is noteworthy that CD163-expressing macrophages play important anti-inflammatory roles, such as in the tumor microenvironment or arthritis, but these tissue-specific roles do not appear to be related to Hb clearance (Etzerodt et al, 2020; Etzerodt et al, 2019; Svendsen et al, 2020).

Most importantly, our study defined and quantified the individual contributions of splenic and hepatic cell types to physiological iron recycling. Consistent with previous studies (Ma et al, 2021; Youssef et al, 2018), we provide evidence that RPMs are efficient at phagocytosis of intact stressed RBCs, whereas the liver is the site of scavenging steady-state hemolytic products. KCs were efficient in the uptake of RBC ghosts and outperformed RPMs in Hb uptake. LSECs, owing to their anatomical location, exceptional macropinocytic activity, and expression of iron-recycling proteins, have emerged as a novel cell type involved in the maintenance of iron homeostasis, specialized for the removal of spleen-derived Hb. Consistent with this newly proposed role of LSECs, endothelial-specific FPN knock-out mice have been reported to exhibit marked iron deficiency, anemia, and iron loading in liver NPCs (Zhang et al, 2014).

Importantly, our study has several limitations. Although we propose that macropinocytosis may contribute to the scavenging function of LSECs, this possibility requires further validation. In addition to β-catenin, additional signaling pathways and effector proteins are likely to support the high macropinocytic activity of LSECs. Defining these regulatory mechanisms would allow for their genetic or pharmacological blockage in mice, thereby revealing the consequences of such intervention for LSEC scavenging functions, elimination of body waste products, and iron homeostasis. Furthermore, our study cannot exclude the long-term contribution of iron-recycling macrophages in Hb uptake under hemolytic conditions, nor can we rule out that other tissues or endothelial cell populations may be affected by prolonged or pathological exposure to free Hb and heme. The extent to which LSEC-mediated Hb uptake protects other organs in hemolytic disorders, such as sickle cell disease or thalassemia, remains unresolved. Future studies employing cell-type-specific genetic deletions of proteins involved in iron recycling will be essential to precisely define the relative contributions of RPMs, KCs, and LSECs to systemic iron homeostasis. Finally, the contribution of LSECs to Hb clearance is expected to depend on the degree of splenic hemolysis, which may be modulated by sex, age, pathological conditions, and disease states that affect RPM fitness, factors that remain to be fully elucidated.

Methods

Reagents and tools table

Reagent/resource	Reference or source	Identifier or catalog number
Experimental models		
BALB/c (*M. musculus*)	Experimental Medicine Centre of the Medical University of Bialystok or Mossakowski Medical Research Institute	N / A
C57BL/6J (*M. musculus*)	Experimental Medicine Centre of the Medical University of Bialystok	N / A
C57BL/6-Tg(UBC-GFP) 30Scha/J (*M. musculus*)	Faculty of Biology, University of Warsaw	IMSR_JAX:004353
Cd163−/− (*M. musculus*)	Department of Biomedicine, Aarhus University	N / A
Primary mouse hepatic cells	This study	N / A
Primary human hepatic cells	This study	N / A
Antibodies		
Anti-mouse CD45 Pe-Cy7	BioLegend	#103114
Anti-mouse CD45 Pacific Blue	BioLegend	#103126
Anti-mouse CD45 APC-Cy7	BioLegend	#103116
Anti-mouse CD45 PerCP	BioLegend	#103129
Anti-mouse F4/80 APC-Cy7	BioLegend	#123118
Anti-mouse CD11b PerCP	BioLegend	#1012300
Anti-mouse CD11b BrilliantViolet 605	BioLegend	#101237
Anti-mouse CD146 PE	BioLegend	#134704
Rabbit anti-mouse STAB2 AF647	St John's Laboratory	#STJ192359
Anti-mouse VCAM PE	BioLegend	#105713
Anti-mouse CD31 FITC	BioLegend	#102506
Anti-mouse CD31 APC	BioLegend	#102509
Anti-mouse CD31 PE-Cy7	BioLegend	#102524
Anti-CD45R/B220 Pacific Blue	BioLegend	#103227
Anti-CD3 Pacific Blue	BioLegend	#100213
Anti-Gr1 Pacific Blue	BioLegend	#108430
Anti-mouse F4/80 PE	BioLegend	#123110
Anti-mouse HO1	Enzo	#ADI-OSA-150-F
Anti-mouse BLVRB	Proteintech	#17727-1-AP
Anti-mouse EEA1	Enzo Life Sciences	#ALX-210-239
Anti-mouse FPN	Amgen	clone 1C7
Anti-mouse Ter-119	BioLegend	#116201
Anti-mouse Ter-119 488	BioLegend	#116215
Anti-mouse Ter-119 Pacific Blue	BioLegend	#116231
Donkey anti-rabbit AlexaFluor 647	Thermo Fisher Scientific	#A-31571
donkey anti-rabbit AlexaFluor 488	Thermo Fisher Scientific	#A-21206
Anti-human CD36 PE	BioLegend	#336206
Anti-human CD32B PE	BioLegend	#398404
Anti-human CD36 BUV421	BioLegend	# 336230

Reagent/resource	Reference or source	Identifier or catalog number
Donkey anti-rabbit IgG 488	Thermo Fisher Scientific	#A-21206
Oligonucleotides and other sequence-based reagents	**Primer Fw (5′- > 3′)**	**Primer Rev (5′- > 3′)**
Rpl19	AGGCATATGGG CATAGGGAAGAG	TTGACCTTCAGG TACAGGCTGTG
Bmp6	ATGGCAGGAC TGGATCATTGC	CCATCACAGT AGTTGGCAGCG
Hmox-1	AGGCTAAGAC CGCCTTCCT	TGTGTTCCTCT GTCAGCATCA
Hamp	ATACCAATGCA GAAGAGAAGG	AACAGATACCA CACTGGGAA
Random primers	Thermo Fisher Scientific	#48190011
Chemicals, enzymes and other reagents		
Clodronate liposomes	LIPOSOMA B.V.	#C-SUV-005
Iron citrate solution (FeCit)	Sigma-Aldrich	#F3388
Mini-hepcidin (PR73)	gift from Elizabeta Nemeth, UCLA	N/A
Phenylhydrazine (PHZ)	Sigma-Aldrich	#P26252
PKH26	Sigma-Aldrich	#MINI26-1KT
HBSS	Capricorn	#HBSS-1A
Liver Perfusion Medium	Gibco	#17701038
Liver Digest Medium	Gibco	#17703034
Hepatocyte Wash Medium	Gibco	#17704024
Percoll solution	Sigma-Aldrich	#GE17-0891-01
RBCs Lysis Buffer	BioLegend	#420301
Williams E Medium	Sigma-Aldrich	#W1878
FBS	Sigma-Aldrich	# F9665
Penicillin/streptomycin	Thermo Fisher Scientific	# 15140122
Glutamax	Gibco	#35050061
Insulin (human)	Sigma-Aldrich	#I9278
Human Hp	Sigma-Aldrich	#SRP6506
Human hemoglobin	Sigma-Aldrich	#H7379
Collagen I	Corning	# 354236
DPBS	Sigma-Aldrich	# D1408
PBS with Mg^{2+}/Ca^{2+}	Gibco	#14040174
EGTA	Sigma-Aldrich	#03777
HBSS	Thermo Fisher Scientific	#14025092
Collagenase P	Roche, Switzerland	#11213873001
Trypan blue	Sigma-Aldrich	#T8154
Chill Protec Plus	Merck	#F2295
AlexaFluor 467 NHS Ester	Thermo Fisher Scientific	#A20006
AlexaFluor 750 NHS Ester	Thermo Fisher Scientific	#A20011
AlexaFluor 647 Conjugation Kit	Abcam	#ab269823
AlexaFluor 488 Conjugation Kit	Abcam	#ab236553
Dextran Tetramethylrhodamine	Thermo Fisher Scientific	#D1818
Dextran, Texas Red™, 70,000 MW, Lysine Fixable	Thermo Fisher Scientific	#D1864
Dextran, Fluorescein, 70,000 MW, Anionic	Thermo Fisher Scientific	# D1823
Wnt/βcatenin inhibitor PRI-724	Selleckchem	#S8968
Chlorpromazine (inhibitor of clathrin-mediated endocytosis)	Sigma-Aldrich	#C8138
EIPA (inhibitor of macropinocytosis)	MedChemExpress	#HY-101840
ML141 (Cdc42 inhibitor)	Selleckchem	#S7686
Latrunculin A (actin-depolymerizing agent)	Tocris	#3973
Nystatin (inhibitor of caveolae-mediated endocytosis)	Sigma-Aldrich	# N1638
Human hemoglobin	Sigma-Aldrich	#H7379
Human TruStain FcX™ (Fc Block)	BioLegend	#422302
Anti-F4/80 magnetic beads	Miltenyibiotec	#130-110-443
BSA	Bioshop	#ALB001.250
Mouse TruStain FcX (Fc Block)	BioLegend	#101320
TRIzol™ Reagent	Thermo Fisher Scientific	#15596026
TRIzol™ LS Reagent	Thermo Fisher Scientific	#10296028
Glycogen	Thermo Fisher Scientific	#R0551
RevertAid H Minus Reverse Transcriptase	Thermo Fisher Scientific	#EP0452
SG qPCR Master Mix	Eurex	#E0401-01
RPMI 1640 medium	CAPRICORN	#RPMI-STA
Collagenase, Type IV	Sigma-Aldrich	#C5318
DNAse	Sigma-Aldrich	#DN25
Type I collagenase	Thermo Fisher Scientific	# 17100017
Type XI collagenase	Sigma-Aldrich	# C7657
Type I-s hyaluronidase	Sigma-Aldrich	# H3506
Saponin	Sigma-Aldrich	# SAE0073
Gelatin	Sigma-Aldrich	# G7041
Rat serum	Sigma-Aldrich	# R9759
PFA	Thermo Fisher Scientific	#J19943.K2
DMSO	Sigma-Aldrich	#D8418
Sodium bicarbonate	Sigma-Aldrich	#S6014

Reagent/resource	Reference or source	Identifier or catalog number
Hoechst 33342	Thermo Fisher Scientific	#H3570
Triton X-100	Thermo Fisher Scientific	#85111
Phalloidin Atto 390	Sigma-Aldrich	#50556
ProLong™ Glass Antifade Mountant	Thermo Fisher Scientific	#P36980
Cryomatrix medium	Epredia	#6769006
Citrate-phosphate-dextrose solution with adenine	Sigma-Aldrich	#C4431
Pap Pen Liquid Blocker	Ted Pella	#22311
Lymphosep	Biowest	#L0560-500
DNase I	Sigma-Aldrich	# DN25
Zombie Aqua™ Fixable Viability Kit	BioLegend	#423101
LIVE/DEAD™ Fixable Aqua Cell Stain Kit	Thermo Fisher Scientific	#L34957
LIVE/DEAD™ Fixable Violet Cell Stain Kit	Thermo Fisher Scientific	#L34955
Unsaturated iron-binding kit	Biolabo	#97408
FerroOrange	DojinD	#F374
Heme Assay Kit	Sigma-Aldrich	#MAK316
Collagen I – coated plates	Ibidi	#80841
Amicon Ultra Centrifugal Filter, 10 kDa	Sigma-Aldrich	#UFC9010
Software		
Prism software	https://www.graphpad.com	
FlowJo Software v10	https://www.flowjo.com	
CytExpert	https://www.mybeckman.pl/	
ZEN 2011 software	https://www.zeiss.com/microscopy/en/products/software/zeiss-zen.html	
Adobe Photoshop	https://www.adobe.com/	
ImageJ	https://imagej.net/ij/	

Mice and in vivo procedures

Female BALB/c and C57BL/6J mice (8–10 weeks old) were obtained from the Experimental Medicine Centre of the Medical University of Bialystok or the Mossakowski Medical Research Institute of the Polish Academy of Sciences. Female C57BL/6-Tg(UBC-GFP)30Scha/J (JAX strain #: 004353; UBI-GFP/BL6), which express GFP under control of the human ubiquitin C promoter from a transgenic cassette integrated in chromosome 17, were kindly provided by Aneta Suwińska (Faculty of Biology, University of Warsaw, Poland). Female and male (8–12 weeks old) WT C57BL/6J and *Cd163*$^{-/-}$ mice were kindly provided by Anders Etzerodt (Department of Biomedicine, Aarhus University, Denmark). For the dietary experiment, C57BL/6J females (4 weeks old) were obtained from the Experimental Medicine Centre of the Medical University of Bialystok. Mice were fed a standard iron diet of 200 mg/kg (control) or a low iron diet containing <6 mg/kg (iron-deficient) for 5 weeks before analysis. All mice were maintained at the SPF facility under standard conditions (20 °C, humidity 60%, 12-h light/dark cycle). All data on Hb uptake by LSECs were obtained using female mice or primary female LSECs, in line with the previous studies investigating iron recycling mechanisms (Slusarczyk et al; Klei et al). Although we expect these findings to be relevant for both sexes, a detailed comparison of LSEC contribution to iron recycling between sexes would require an independent study. No formal randomization procedure was used; animals/samples were allocated based on the order of collection. No blinding was performed during allocation, conduct, or analysis of the experiments. Experimental design, conduct, and reporting followed the ARRIVE guidelines to ensure transparent reporting of animal research.

Procedures involving BALB/c mice

Proteins or their conjugates were dissolved in PBS and administered intravenously (i.v.) at doses indicated in the figure legends. For macrophage depletion, mice received an i.v. solution of liposomes containing clodronic acid (LIPOSOMA, #C-SUV-005) (5 ml/kg) or control empty liposomes for 24 h. A sterile aqueous iron citrate (FeCit, 150 µg/mouse) solution (Sigma-Aldrich, #F3388) or sterile citric acid buffer (0.05 M, Sigma-Aldrich, #251275) was normalized to pH 7.0 and administered i.v.; tissues were collected 5 h after injection. Mini-hepcidin (PR73, 50 nmol/mouse) (Stefanova et al, 2017) (kind gift from Elizabeta Nemeth, UCLA, USA) was injected intraperitoneally (i.p.); tissues were harvested 4 h post-injection. To induce hemolysis, a sterile solution of phenylhydrazine (PHZ, Sigma-Aldrich, #P26252) in PBS was administered i.p. at a dose of 0.125 mg/g body weight, and tissues were collected after 6 h.

Procedures involving C57BL/6J mice

PKH26-stained (Sigma-Aldrich, #PKH26GL-1KT) temperature-stressed UBI-GFP RBCs were resuspended to 50% hematocrit in HBSS (Capricorn, #HBSS-1A) and administered i.v. for 1.5 h in a 100 µl. An equal dose of PKH26-stained RBC ghosts was mixed with fluorescently labeled Hb (10 µg/mouse) and administered i.v. for 1.5 h in a 100 µl. For proteomics analysis of LSECs, wild-type unstained RBCs were resuspended to 50% hematocrit in HBSS and administered i.v. for 1.5 h in a 100 µl.

Isolation of human non-parenchymal liver cells

Liver tissue samples were obtained from the Department of Hepatobiliary Surgery and Visceral Transplantation at Leipzig University Medical Center. Specimens were collected from macroscopically healthy tissue adjacent to resected segments in patients with primary or secondary liver tumors or benign local liver diseases. During resections, both diseased and surrounding unaffected liver tissue were removed; a portion of this unaffected tissue was used for liver cell isolation. Cells obtained from a total of four patients: a male, aged 73; two females, aged 60; and a female, aged 68, supported the data presented in the figures. Primary human NPCs (hNPCs) were isolated using a two-step collagenase perfusion technique (Damm et al, 2019; Kegel et al, 2016). Briefly,

liver tissue was perfused first with a buffer containing ethylenediaminetetraacetic acid (EGTA) (Sigma-Aldrich, USA, #03777-10 g), followed by a digestion buffer with collagenase P (Roche, Switzerland, #11213873001). Hepatocytes were separated by washing and centrifuging the cell suspension twice at 50 g in PBS with Mg^{2+}/Ca^{2+} (Gibco, USA, #14040174). The supernatants containing hNPCs were then united and centrifuged at 300× *g* and subsequently at 650× *g* (Zimmermann et al, 2021). Cell pellets containing hNPCs were resuspended in PBS with Mg^{2+}/Ca^{2+}, and the hNPC fraction was counted and checked for viability using the Trypan blue (Sigma-Aldrich, #T8154) exclusion method. Finally, the hNPC fraction was prepared for shipment by centrifugation, resuspension in Chill Protec Plus (Merck, Germany, #F2295), and transfer into cryovials (Sarstedt, Nümbrecht, Germany, #72.379). After overnight transport at 4 °C, the hNPCs pellet was washed with Williams E Medium (Sigma-Aldrich, #W1878-500ML), containing 10% FBS, and centrifuged for 5 min, 650 g, RT (room temperature). The pellet was resuspended in RBC Lysis Buffer (BioLegend, #420301) and incubated for 5 min. The hNPCs were then washed and centrifuged again at 650 g for 10 min at RT. The cell pellet was resuspended in Williams E Medium (Sigma-Aldrich, #W1878-500ML), containing 10% FBS, 1% Penicillin/Streptomycin, 1% Glutamax (Gibco, #35050061), and human insulin at a concentration of 5 µg/ml (Capricorn, # INS-K) and seeded for experiments on collagen-I-coated plates.

Primary murine cell culture

Murine liver cells were isolated from female BALB/c mice according to the standard two-step perfusion method with minor modifications. Briefly, mice were euthanized, and livers were perfused in situ (5 ml/min) with Liver Perfusion Medium (Gibco, #17701038) for 3 min through the inferior vena cava after transection of the portal vein. Next, the medium was exchanged for prewarmed (37 °C) Liver Digest Medium (Gibco, #17703034), and perfusion continued for the next 15 min. Digested livers were gently disintegrated in Hepatocyte Wash Medium (Gibco, #17704024) and filtered through a 100-µm cell strainer. The cell suspension was then centrifuged at 50 g for 3 min to separate hepatocytes from the supernatant containing non-parenchymal cells (NPCs). Hepatocytes were further purified by layering them on 1.06 g/mL Percoll solution (Sigma-Aldrich, #GE17-0891-01) and centrifugation at 750× *g* for 20 min without a break. NPCs were centrifuged two more times at 50× *g* for 3 min and spun at 650× *g* for 15 min, 4 °C. The pellet was resuspended in RBCs Lysis Buffer, incubated for 3 min, washed, and centrifuged again for 10 min, 650× *g*, 4 °C. Subsequently, the NPCs were resuspended in Williams E Medium (Sigma-Aldrich, #W1878-500ML), containing 10% FBS, 1% Penicillin/Streptomycin, 1% Glutamax (Gibco, #35050061), and insulin at a concentration of 10 µg/ml (Sigma-Aldrich, #I9278). Cells were seeded on collagen I-coated (Corning, # 354236) plates or glass microscope slides at a density of 30,000 cells/cm^2. After 3 h, the cells were washed with PBS, and the medium was replaced with Williams E Medium supplemented with 4% FBS, 1% Penicillin/Streptomycin, and 1% Glutamax.

Cell culture treatments

Murine NPCs primary cells were cultured in Williams E medium supplemented with 4% FBS, 1% Penicillin/Streptomycin, and 1% Glutamax. The day after cell seeding, the cells were stimulated with freshly prepared fluorescently stained hemoglobin (Hb-AF647 or Hb-AF750, 0.5 µg/ml), hemoglobin-haptoglobin complex (Hb-AF750:Hp, 0.5 µg:15 µg/ml), Dextran Tetramethylrhodamine, 70,000 MW, Lysine Fixable (1 mg/ml, ThermoScientific, #D1818), Dextran, Texas Red, 70,000 MW, Neutral (0.25 mg/ml, ThermoScientific, # D1830) or Albumin from Bovine Serum (BSA-AF647) (1 µg/ml, ThermoScientific, # A34785) for 1 h. When indicated, the following compounds were used for pre-treatments: Wnt/beta-catenin inhibitor PRI-724 (5 µM, for 24 h, Selleckchem, #S8968); inhibitor of clathrin-mediated endocytosis, chlorpromazine (2 µM, for 1 h, Sigma-Aldrich, #C8138); inhibitor of macropinocytosis, EIPA (25 µM, for 1 h, MedChemExpress, #HY-101840); inhibitor of Cdc42 GTPase, ML141 (10 µM, for 1 h, Selleckchem, #S7686), an actin-depolymerizing agent, latrunculin A (1 µM, for 30 min, Tocris, #3973) and inhibitor of caveolae-mediated endocytosis, nystatin (240 U/ml for 30 min, Sigma-Aldrich, # N1638).

The day after seeding, hNPCs were stimulated with freshly prepared fluorescently stained human hemoglobin (Sigma, #H7379; Hb-AF647, 0.5 µg/ml for immunofluorescence imaging, 5 µg/ml for flow cytometry analysis) or Dextran, Texas Red™, 70,000 MW, Lysine Fixable (1 mg/ml, ThermoScientific, # D1864) for 1 h. When indicated, the following compounds were used for pre-treatments: chlorpromazine (2 µM, for 1 h, Sigma-Aldrich, #C8138); EIPA (25 µM, for 1 h, MedChemExpress, #HY-101840), and latrunculin A (1 µM, for 30 min, Tocris, #3973).

Preparation of single-cell suspension for flow cytometry

For flow cytometry analysis of the liver cells, mice were euthanized, and liver lobes were dissected. Next, liver lobes were perfused with PBS until blood removal, minced with scissors, and enzymatically digested in RPMI 1640 medium (CAPRICORN, #RPMI-STA) containing type IV collagenase (1 mg/ml, Sigma-Aldrich, #C5318-5G) and DNAse (20 mg/ml, Sigma-Aldrich, #DN25-1G) for 40 min at 37 °C with shaking. Next, the cell suspension was passed through a 100 µm cell strainer, washed with PBS, and centrifuged 2× at 50× *g*, 3 min, RT to remove hepatocyte pellets. Next, the supernatant was centrifuged at 650× *g*, 15 min, and 4 °C. Cells were suspended in RBCs Lysis Buffer, incubated for 5 min, RT, then washed with PBS and centrifuged at 650× *g*, 15 min, 4 °C. For the splenocytes, the spleen was minced with scissors and subjected to digestion under similar conditions as the liver, but with a shorter incubation time of 20 min at 37 °C. Next, the organ pieces were passed through a 100 µm cell separation strainer, washed with PBS, and centrifuged at 500× *g*, 5 min, and 4 °C. Cells were suspended in RBCs Lysis Buffer, incubated for 7 min, RT, then washed with PBS and centrifuged at 500× *g*, 5 min, 4 °C. For the analysis of femurs and tibias, the epiphysis of the dissected bones was cut off, and the bones were placed vertically in a specially cut tip for an automatic pipette placed in an Eppendorf tube, so that the bone did not touch the bottom. The tubes were centrifuged at 1000× *g*, 1 min, RT. The cell pellet was suspended in RBCs Lysis Buffer and incubated for 5 min at RT, washed with PBS, and centrifuged at 500× *g*, 5 min, 4 °C. The cell pellet was resuspended in the same enzymatic mixture used for liver and spleen digestion and incubated for 15 min at 37 °C with shaking. The cells were then washed with PBS and centrifuged at 500× *g*, 5 min, and 4 °C. The aorta was dissected and minced with scissors. Next tissue was enzymatically digested with a mix of enzymes: type I collagenase, type XI collagenase, type

I-s hyaluronidase, and DNase I according to the protocol published previously (Gjurich et al, 2015). The organ pieces were then filtered through a 100 µm cell separation strainer, rinsed with PBS, and centrifuged at 500× *g*, 5 min, and 4 °C.

Isolation of liver non-parenchymal cells, spleen, and heart endothelial cells for FACS sorting

For FACS-sorting of murine LSECs and KCs, livers were perfused as described above with an additional step of purification. Briefly, NPCs depleted of RBCs were mixed with 1.06 g/mL Percoll (Sigma-Aldrich, #GE17-0891-01) solution (1:1) and centrifuged at 800× *g*, 30 min at RT (without brake). Cell pellets were resuspended in PBS and stained with LIVE/DEAD™ Fixable Violet Cell Stain Kit (ThermoScientific, #L34955) according to the manufacturer's instructions, and centrifuged at 650 g, 5 min, 4 °C. Next, cells were resuspended with FACS buffer (1% BSA in PBS) and incubated with TruStain FcX™ (Fc block; BioLegend, #101320) 1:100 for 5 min. Next, cells were stained with the following antibodies (BioLegend): rat anti-mouse CD45 Pe-Cy7 (#103114), F4/80 APC-Cy7 (#123118), CD11b PerCP (#1012300), CD146 PE (#134704) and unconjugated rabbit-anti-mouse STAB2 (St John's Laboratory, #STJ192359) for 30 min at 4 °C, in 1:100 dilution. Cells were washed and stained with the secondary antibodies donkey-anti-rabbit AlexaFluor 647 (ThermoScientific, #A-31571, dilution 1:200) or donkey-anti-rabbit AlexaFluor 488 (ThermoScientific, #A-21206, dilution 1:200). Next, cells were washed and sorted using BD FACS Aria II sorter (BD Biosciences). For gene expression analysis, cells were sorted directly into TRIzol™ LS Reagent (ThermoScientific, #10296028) at a quantity of 20,000–50,000 cells, with a maximum flow rate of 2000 events per second using an 85 or 100 µm nozzle. The sorting purity was approximately 90% from $CD45^+$ cells. For quantification of cellular total iron levels (ICP-OES), cells were sorted into PBS and spun for 5 min at 1000× *g* (at a quantity of 40,000–200,000 cells).

For FACS sorting of spleen and heart endothelial cells, mice were euthanized and perfused via heart with ice cold PBS containing heparin (1:100). Next, organs were minced with scissors and enzymatically digested in RPMI 1640 medium containing type IV collagenase (1 mg/ml) and DNAse (20 mg/ml) for 20 (spleen) or 40 (heart) min at 37 °C with shaking. Next, the cell suspension was passed through a 100 µm cell strainer, washed with PBS, and resuspended in RBCs Lysis Buffer. After 5 min of incubation, the cells were washed with PBS and centrifuged at 650× *g*, 5 min at 4 °C. The Fc block was added at a 1:100 dilution in FACS buffer and incubated at 4 °C for 10 min. The cells were then stained with the following antibody panel for 30 min at 4 °C in the dark in 1:100 dilution: CD45 (Biotin, BioLegend, #103104), together with a trace "spike-in" of CD45 (PE-Cy7, BioLegend, #103114) to monitor depletion efficiency by flow cytometry. CD3 (BV421, BioLegend, #100227), Gr-1 (BV421, BioLegend, #108433), and B220 (BV421, BioLegend, #103245), F4/80 (PE, BioLegend, #123110), and CD11b (FITC, BioLegend, #101206) and CD31 (APC, BioLegend, #102410) to identify endothelial cells. Following incubation, the cells were washed with cold PBS containing 0.5% BSA (sorting buffer) and centrifuged at 650× *g* for 5 min. The pellet was resuspended in 200 µL of sorting buffer containing 50 µL of MojoSort Streptavidin Nanobeads (BioLegend, #480016) and incubated at 4 °C in the dark for 20 min. After incubation, 2.5 mL of sorting buffer was added, and the tube was placed on an EasyEights EasySep Magnet (STEMCELL, #18103) for 10 min. The supernatant, corresponding to the $CD45^-$ fraction, was transferred to a fresh 5 mL tube and centrifuged at 650× *g* for 5 min, and resuspended in sorting buffer. For quantification of cellular total iron levels (ICP-OES), cells were sorted into PBS and spun for 5 min at 1000× *g*. Gating strategy details are reported in the Appendix.

Flow cytometry

Murine cell pellets were resuspended in PBS and stained with LIVE/DEAD™ Fixable Violet/Aqua Cell Stain Kit (ThermoScientific, #L34955, # L34957) or Zombie Aqua™ Fixable Viability Kit (BioLegend, #423101) according to the manufacturer's instructions, and centrifuged at 650× *g*, 5 min, 4 °C. Next, cells were resuspended with FACS buffer (1% BSA in PBS) and incubated with rat serum (5%) and Fc block 1:100 for 5 min. In the next step, liver cells were stained with the following rat anti-mouse antibodies (BioLegend): anti-CD45 Pe-Cy7 (#103114), anti-F4/80 APC-Cy7 (#123118), anti-CD11b PerCP (#1012300), anti-CD146 PE (#134704) and unconjugated rabbit-anti-mouse STAB2 (St John's Laboratory, #STJ192359) for 30 min at 4 °C, in 1:100 dilution. Secondary antibody staining was performed with donkey-anti-rabbit IgG AlexaFluor 647 (ThermoScientific, #A-31571, dilution 1:200) or donkey-anti-rabbit IgG AlexaFluor 488 (ThermoScientific, #A-21206, dilution 1:200). After discrimination of dead cells and doublets, LSEC cells were gated as a population moderately expressing CD45, lacking macrophage-specific proteins F4/80 and CD11b, and expressing STAB2 and CD146 receptors. KCs were gated as a population with high expression of CD45 and F4/80 and moderate expression of CD11b.

For analysis of the splenic cell populations, the following surface rat anti-mouse BioLegend antibodies were used: anti-CD45 PerCP (#103129), anti-F4/80 PE (#123109), anti-CD11b BrilliantViolet 605 (#101237), anti-CD45R/B220 Pacific Blue (#103227), anti-CD3 Pacific Blue (#100213), anti-Gr1 Pacific Blue (#108430), anti-Ter119 Pacific Blue (#116231) and anti-CD31 PE-Cy7 (#102524). Splenic RPMs were gated as a population negative for CD3, Gr1, B220 and Ter119, with high expression of CD45, F4/80, and moderate expression of CD11b. Splenic endothelial cells were gated as a population negative for CD45, expressing CD31. For analysis bone marrow macrophages and endothelial cells (ECs) the following surface rat anti-mouse BioLegend antibodies were used: anti-CD45 PerCP (#103129), anti-CD11b BrilliantViolet 605 (#101237), anti-VCAM PE (#105713), anti-CD45R/B220 Pacific Blue (#103227), anti-CD3 Pacific Blue (#100213), anti-Gr1 Pacific Blue (#108430), anti-Ter119 Pacific Blue (#116231) and anti-CD31 PE-Cy7 (#102524). Macrophages were gated as a population negative for CD3, Gr1, B220, and Ter119, with high expression of CD45, VCAM, and moderate expression of CD11b. ECs were gated as a population negative for CD45, expressing CD31. Immediately before the analysis, the cell suspension was transferred to tubes with a sieve with a pore diameter of 35 µm.

The content of intracellular ferrous iron (LIP, Fe^{2+}) was measured using FerroOrange (DojinD, #F374). Briefly, surface-stained cells were incubated with 1 µM FerroOrange in HBSS for 30 min at 37 °C and analyzed directly by flow cytometry without further washing. Detection of FPN was performed with a non-commercial antibody that recognizes the extracellular loop of

mouse FPN [rat monoclonal antibody, Amgen, clone 1C7; directly conjugated using AlexaFluor 488 Labeling Kit (Abcam, ab236553)] (Slusarczyk et al, 2023). For intracellular HO-1 staining, surface-stained cells were fixed with 4% PFA and permeabilized with 0.5% Triton-X in PBS. Next, cells were stained for 30 min at 4 °C with primary anti-HO-1 (ENZO, #ADI-OSA-150-F) conjugated with AlexaFluor 488. Conjugation was performed with the Conjugation Kit (Abcam, #ab236553) according to the manufacturer's protocol. Erythrophagocytosis capacity in RPMs was determined by intracellular staining of the erythrocytic marker using anti-Ter-119 (BioLegend, #116201 and #116215) as described previously (Slusarczyk et al, 2023). The panel of antibodies used for FPN and HO-1 staining consisted of anti-CD45 PE-Cy7, anti-F4/80 anti-APC-Cy7, anti-CD11b PerCP, anti-CD146 PE, and anti-STAB2-AlexaFluor 647 (Gbiosciences, #ITN 2255-647). Due to the wide emission spectrum, the panel employed for experiments involving FerroOrange was modified by omitting anti-CD11b and anti-CD146 markers: for liver NPCs, it included anti-CD45 Pacific Blue (#103126), anti-F4/80 APC-Cy7 (#123118), anti-STAB2-AlexaFluor 647 (Gbiosciences, #ITN 2255-647) or anti-STAB2 (St John's Laboratory, # STJ192359), while for splenic and bone marrow ECs, it included anti-CD45 APC-Cy7 (#103116), anti-CD31 APC (#102509), anti-CD45R/B220 Pacific Blue (#103227), anti-CD3 Pacific Blue (#100213), anti-Gr1 Pacific Blue (#108430), and anti-Ter119 Pacific Blue (#116231).

After hemoglobin treatment, human hNPCs were washed with FACS buffer and centrifuged at 650× *g*, 5 min, 4 °C. hNPCs pellets were stained with LIVE/DEAD™ Fixable Aqua Cell Stain Kit (ThermoScientific, # L34957) according to the manufacturer's instructions, and centrifuged at 650× *g*, 5 min, 4 °C. Next, cells were resuspended with FACS buffer and incubated with Human TruStain FcX™ (BioLegend, # 422302) 1:100 for 5 min. In the next step, human liver cells were stained with mouse anti-human CD36 BUV421 (Biolegend, # 336230) 1:100 and CD32B PE (Biolegend, #398404) 1:100 antibodies for 1 h at 4 °C. After staining, cells were washed with FACS buffer and centrifuged at 650× *g*, 5 min, 4 °C. Pellets were fixed with 4% PFA for 15 min at RT, washed with FACS buffer, and centrifuged at 750× *g*, 5 min, 4 °C.

Analyses were performed using BD LSRFortessa X-20 (BD Biosciences), BD Canto II (BD Biosciences), BD Aria II sorter (BD Biosciences) or CytoFLEX (Beckman Coulter) flow cytometers and were analyzed with FlowJo or CytExpert, respectively. The geometric mean fluorescence intensities (MFI) corresponding to the probes/target protein levels were determined. For quantifications, the MFI of the adequate fluorescence minus one (FMO) control was subtracted from the sample's MFI, and data were further normalized. All gating strategy details are reported in the Appendix.

Magnetic sorting of liver sinusoidal endothelial cells, Kupffer cells and red pulp macrophages

NPC pellets obtained after liver perfusion were resuspended in RBCs Lysis Buffer, incubated for 4 min, washed with sorting buffer (0,5% BSA/PBS), and centrifuged for 10 min, 650× *g*, 4 °C. NPCs were further purified using the Percoll gradient centrifugation protocol. Briefly, NPCs pellet was resuspended in 3 ml of sorting buffer, layered on the top of a two-layer Percoll gradient (3 ml of 50% Percoll on the bottom, 3 ml of 25% Percoll on the top) and centrifuged at 800 g without brake, 20 min, RT. NPCs were mainly localized and collected from the interphase between 25% and 50% Percoll, washed with sorting buffer, and spun at 700× *g* for 10 min. The pellet was resuspended in 180 µl of sorting buffer containing Fc block 1:100 and incubated on ice for 5 min. Next, cells were mixed with 30 µl of anti-F4/80 MicroBeads UltraPure magnetic beads (Miltenyi Biotec, #130-110-443) and incubated for 15 min on ice with regular shaking. After that, cells were washed and spun for 5 min, 400× *g*, 4 °C. The cell pellet was resuspended in sorting buffer and passed through a magnetized LS Separation Column (Miltenyi Biotec, # 130-042-401). F4/80 positive cells (Kupffer cells) were eluted from the demagnetized column, washed with sorting buffer, and spun for 5 min, 400× *g*, 4 °C. The flow-through suspension containing F4/80 negative cells was collected and centrifuged for 5 min at 400× *g*, 4 °C. Next, the cell pellet was incubated in the mixture of 180 µl of sorting buffer and 30 µl anti-CD146 (LSEC) MicroBeads (Miltenyi Biotec, # 130-092-007) for 15 min on ice with regular shaking. Cells were washed, spun for 5 min, 400× *g*, 4 °C, and resuspended in sorting buffer. The suspension was loaded on the LS Separation Column to obtain a pure population of LSECs. F4/80$^-$ CD146$^+$ LSECs were eluted from the demagnetized column, washed, and centrifuged for 5 min at 400× *g*, 4 °C. Pellets were washed twice with PBS and incubated with RIPA buffer containing Protease Inhibitor Cocktail (Sigma,#4693124001), followed by centrifugation for 15 min at 12,000× *g*. Supernatant was further collected and saved for heme level or total iron content analysis.

To obtain a magnetically sorted population of red pulp macrophages (RPMs), single-cell suspensions of spleens were prepared. The Fc block was added at a 1:100 dilution in FACS buffer (1% BSA/PBS) and incubated at 4 °C for 10 min. The cells were then labelled with the following antibodies: anti-F4/80 (APC, Biolegend, #123116), anti-Ly-6G/Ly-6C (Gr-1) (Biotin, Biolegend, # 108403), anti-CD3 (Biotin, Biolegend, #100243), and anti-B220 (Biotin, Biolegend, #103204), in the dilution 1:100 for 30 min at 4 °C in the dark. After incubation, cells were washed with cold PBS containing 0.5% BSA (sorting buffer) and centrifuged at 650× *g* for 5 min. The pellet was resuspended in 200 µL of sorting buffer containing 50 µL of MojoSort Streptavidin Nanobeads (Biolegend, #480016) and incubated at 4 °C in the dark for 20 min. Subsequently, 2.5 mL of sorting buffer was added, and the tube was placed on an EasyEights EasySep Magnet (STEMCELL, #18103) for 10 min. The supernatant was transferred to a fresh 5 mL tube and centrifuged at 650× *g* for 5 min. The resulting pellet was resuspended in 175 µL of sorting buffer, and 25 µL of MojoSort Mouse anti-APC Nanobeads (Biolegend, #480072) were added. The suspension was gently mixed and incubated for 20 min at 4 °C in the dark. After incubation, 2.5 mL of sorting buffer was added, and the tube was placed on the magnet for 10 min. The bead-bound F4/80$^+$ cells were washed twice with PBS and incubated with RIPA buffer as mentioned above for heme level and total iron content analysis.

Isolation of murine hemoglobin (Hb) and conjugation of mouse Hb, human Hb and bovine serum albumin (BSA)

To isolate hemoglobin (Hb) from mouse erythrocytes, peripheral blood was collected after euthanasia by cardiac puncture into heparinized tubes. Blood was centrifuged at 500× *g* for 5 min, RT;

the plasma fraction and the buffy coat were discarded. Erythrocytes were suspended in PBS and centrifuged at 500× *g*, 5 min, and 4 °C, and this washing was repeated four times. Erythrocytes were then centrifuged at 3000× *g*, 5 min, 4 °C. The pellet was resuspended in 20 ml of cold sterile deionized water and incubated overnight at 4 °C. Finally, the solution was centrifuged at 3000× *g*, 5 min, 4 °C, and concentrated using an Amicon® Ultra-15 filter unit with a 10 kDa cutoff (Sigma-Aldrich, # UFC901008D). Hb concentration was calculated from the Beer-Lambert law and heme extinction coefficient (167,000 M − 1·cm−1) at 415 nm, which was measured using a NanoDrop 2000 spectrophotometer (Thermo Fisher Scientific).

AlexaFluor NHS esters AlexaFluor 647 (#A20006) or AlexaFluor 750 (#A20111) (Thermo Fisher Scientific) were dissolved in DMSO and diluted in 0.1 M $NaHCO_3$, pH 8.3. Isolated murine hemoglobin, human hemoglobin (Sigma-Aldrich, # H7379), or BSA were dissolved in 0.1 M $NaHCO_3$, pH 8.3. Protein and ester solutions were mixed in a volume ratio of 1:1 at a molar ratio of 1:2.5 and incubated at 25 °C in the dark for 1 h with shaking. Then the conjugate was washed with 0.1 M $NaHCO_3$, pH 8.3, and concentrated using an Amicon® Ultra-15 filter unit with 10 kDa cut-off at 4000× *g*, 15 min, 4 °C. Hb concentration was calculated from the Beer-Lambert law and heme extinction coefficient (167,000 M^{-1}·cm^{-1}) at 415 nm, which was measured using a NanoDrop 2000 spectrophotometer (Thermo Fisher Scientific). BSA concentration was measured using standard methods. The effectiveness of conjugation was confirmed by mass spectrometry analysis. To prepare of Hb-haptoglobin (Hp) complex, Hb-AF750 and human Hp (Sigma-Aldrich, #SRP6506) solutions were mixed in a molar ratio (Hb-AF750:Hp) of 1:6 and incubated for 30 min at 4 °C in the dark. Then the complex was purified from free Hb or Hp by centrifugation using an Amicon® Ultra-0.5 filter unit with 100 kDa cutoff (Sigma-Aldrich, # UFC510024) at 4000× *g*, 3 min, 4 °C.

RBC preparation and staining

RBC isolation, labeling, and RBC ghost preparations were performed as described previously (Slusarczyk et al, 2023) with some modifications. Briefly, whole blood obtained from the wild-type C57BL/6 J and UBI-GFP/BL6 mice was collected in CPDA-1 solution (Sigma-Aldrich, #C4431). The suspensions were mixed with HBSS, loaded on Lymphosep (Biowest, #L0560-500), and centrifuged at 400× *g* for 15 min at RT. The buffy coat was removed, and the suspension of RBCs was washed with HBSS twice. When indicated, RBCs were stressed (sRBCs) by heating for 30 min at 48 °C with shaking. In total, 1×10^{10} RBC were resuspended in 1 ml diluent C, mixed with 1 ml diluent C containing 7.5 µM PKH26 (Sigma-Aldrich, #MINI26-1KT), and incubated in the dark for 5 min at 37 °C. The reaction was stopped by adding 2 ml HBSS/1% BSA, and the suspension was washed with HBSS. For in vivo experiments, RBCs were resuspended to 50% hematocrit in HBSS. RBC ghosts were obtained by lysis of stressed PKH26-stained RBCs derived from C57BL/6J mice (volume of the suspension was two times more than PKH26-stained UBI-GFP/BL6 RBCs) with PBS to water (1:15) mixture, followed by at least three centrifugations at 13,000× *g*, 5 min each, until the pellet became brighter. The final pellet was resuspended in HBSS.

Immunofluorescence

The mouse liver was fixed in 4% PFA at 4 °C for 24 h. Tissues were washed with PBS (3 × 30 min) and soaked in 12.5% and 25% sucrose for 1.5 h and 48 h, respectively. Liver samples were embedded in Cryomatrix medium (Epredia™, #6769006), frozen in liquid nitrogen, sectioned in 10-µm slices using a cryo-microtome (Leica), and stored at −20 °C. Before staining, the sections were left in RT for 20 min, surrounded with Pap Pen Liquid Blocker (Ted Pella, 22311), washed in PBS for 10 min, and permeabilized with PBS/0.1% Triton X-100 (Thermo Fisher, #85111) for 20 min. Non-specific antibody binding was blocked by incubating sections in PBS/3% BSA (Bioshop, #ALB001.250) for 2 h at RT. For LSEC detection, tissues were incubated with anti-CD146 PE (BioLegend, #134704) 1:100 in PBS/3% BSA for 2 h at RT. For KCs detection, tissues were incubated with anti-F4/80 PE (BioLegend, #123110) 1:100 in PBS/3% BSA for 2 h at RT. After antibody incubation, tissues were washed 5 × 5 min with PBS/0.1% Triton X-100 to remove unbound antibodies. For nuclear staining, sections were incubated with Hoechst 33342 (ThermoFisher, #H3570) diluted in PBS/0.1% Triton X-100 (final concentration—1 µg/ml) for 10 min at RT. Next, sections were washed 3×5 min with PBS/0.1% Triton X-100, incubated in PBS for 10 min, and mounted with ProLong™ Glass Antifade Mountant (Thermo Fisher, #P36982). For immunofluorescence staining of in vitro cultured NPCs, cells were seeded on round coverslips coated with collagen I (Corning, #354236). For macropinosomes visualization, seeding of NPCs was performed with an additional step of macrophage depletion with anti-F4/80 magnetic beads (Miltenyibiotec, #130-110-443) according to the manufacturer's protocol. For Hb and dextran intracellular colocalization, cells were fixed with 4% PFA for 10 min at RT, washed with PBS, and incubated in PBS/5% BSA for 1 h at RT for blocking. After blocking, cells were incubated overnight at 4 °C with anti-F4/80 PE and/or anti-STAB2 (St John's Laboratory, #STJ192359, 1:100). After incubation with primary antibody, cells were washed with PBS, and incubated with secondary antibody: donkey-anti-rabbit IgG AlexaFluor 488 (Thermo Fisher Scientific, #A-31571, 1:300) for 1 h at RT. For FPN staining, NPCs were washed with PBS and blocked with 1% BSA/PBS for 1 h at RT. After blocking, cells were stained with anti-CD31 FITC (Biolegend, #102506, 1:50), anti-F4/80 PE (Biolegend, #123110, 1:100), and anti-FPN (Kind gift from Tara Arvedson, Amgen, 1:100 -conjugated with AF647 fluorescent dye—Abcam, #ab269823) for 45 min at RT. NPCs were washed with PBS and fixed with 4% PFA for 10 min at RT. After fixation, cells were washed with PBS, stained with Hoechst 33342 for 10 min at RT, and mounted on the slides with ProLong™ Glass Antifade Mountant.

For intracellular HO1 staining, NPCs were washed with PBS and blocked with 1%BSA/PBS for 1 h at RT. After blocking, cells were stained with anti-CD31 FITC (Biolegend, #102506, 1:50) and anti-F4/80 PE (Biolegend, #123110, 1:100), washed with PBS, and fixed with 4% PFA for 10 min at RT. After fixation, NPCs were washed with PBS, permeabilized with PBS/0.1% Triton X-100 for 5 min at RT, and blocked again with 1%BSA/PBS for 1 h at RT. After blocking, cells were incubated overnight at 4 °C with anti-HO1 (Enzo, #ADI-OSA-150-F, 1:100) primary antibody. After incubation, cells were washed and incubated with donkey anti-rabbit IgG

AlexaFluor 647 (Thermo Fisher Scientific, #A-31571, 1:300) for 1 h at RT. NPCs were washed, stained with Hoechst 33342 for 10 min at RT, and mounted on the slides with ProLong™ Glass Antifade Mountant. Samples were imaged using a confocal microscope LSM 800 (Zeiss), equipped with an EC Plan-Neofluar 40x/1.30 Oil DIC M27 oil objective and T-PMT detectors. Images were acquired with a resolution of 2101 ×2101 pixels. The images were processed using ImageJ software with linear adjustments of contrast and brightness, equally across the whole image area and in comparison to the blank samples. For macropinosomes visualization, fixed cells were permeabilized and blocked with solution I—PBS/ 0,1% w/v Saponin, 0,2% w/v/gelatin, 5 mg/ml BSA for 10 min RT. After blocking, cells were incubated in solution II—PBS 0.01% Saponin, 0,2% gelatin with primary antibody anti-EEA1 (Enzo Life Sciences, #ALX-210-239, 1:1000) for 1 h at RT. After washing in solution II, cells were incubated with secondary antibody donkey anti-rabbit IgG 488 (Thermo Fisher Scientific, #A-21206, 1:500) for 1 h at RT. Phalloidin Atto 390 (Sigma-Aldrich, #50556, 1:500) to stain actin was added during incubation with fluorescent secondary antibodies. After incubation with antibodies, cells were washed with PBS and mounted on the slides with Moviol. Sections and slides were visualized with a Zeiss LSM 710 equipped with an Objective Plan-Apochromat 63×/1.4 Oil DIC M27 oil objective and T-PMT detectors. Macropinosome size was determined with ZEN 2011 software. The remaining images were processed using Adobe Photoshop software with linear adjustments of contrast and brightness.

Human non-parenchymal cells seeded on collagen I-coated plates (Ibidi, #80841) were washed with PBS and fixed with 4% PFA for 15 min at RT. After fixation, cells were washed with PBS and blocked in 2% BSA for 1 h. After blocking, cells were incubated with anti-human CD36 PE (Biolegend, #336206, 1:50), anti-human CD32B PE (Biolegend, #398404, 1:50), or anti-human CD36 BUV421 (Biolegend, # 336230, 1:50) antibodies for 1 h. For intracellular EEA1 staining, cells were additionally permeabilized and blocked with PBS/0.1% w/v Saponin, 0.2% w/v/gelatin, 5 mg/ml BSA solution for 10 min RT. After blocking, cells were incubated in PBS 0.01% Saponin +0.2% gelatin solution with primary antibody anti-EEA1 (Enzo Life Sciences, #ALX-210-239, 1:1000) for 1 h at RT. After washing, cells were incubated with secondary antibody donkey anti-rabbit IgG 488 (Thermo Fisher Scientific, #A-21206, 1:500) for 1 h at RT, washed with PBS and directly visualized using a confocal microscope LSM 800 (Zeiss).

Proteomics

Cell pellets were lysed in lysis buffer (2% SDS, 100 mM TRIS, pH 8.5). Samples were subjected to chloroform/methanol precipitation, and the resulting protein pellets were washed twice with methanol, air-dried, and resuspended in 100 mM HEPES (pH 8) by vigorous vortexing and sonication. Proteins were reduced and alkylated with 10 mM TCEP/40 mM CAA and digested with trypsin in a 1:100 (w/w) enzyme-to-protein ratio at 37 °C overnight. Digestion was stopped by the addition of trifluoroacetic acid (TFA) to a final concentration of 1%, and peptides were desalted on C18-StageTips. Chromatographic separation was performed on an UltiMate 3000 nano-LC system (Thermo Fisher Scientific) coupled to a Q Exactive HF-X mass spectrometer via an Easy-Spray source. The Q Exactive HF-X was operated in data-dependent mode, and MS data were processed with MaxQuant v. 1.6.17.0 (Cox and Mann, 2008). Peptides were identified against the mouse reference proteome UP000000589 using the Andromeda search engine. Cysteine carbamidomethylation was set as a fixed modification, and methionine oxidation, glutamine/asparagine deamidation, and protein N-terminal acetylation were set as variable modifications. For in silico digests of the reference proteome, cleavages of arginine or lysine followed by any amino acid were allowed (trypsin/P), and up to two missed cleavages were allowed. False discovery rate (FDR) was set to 0.01 at the peptide, protein, and site levels. Match between runs was enabled. Quantification was based on unique and razor peptides. Processed data were imported into Perseus v. 1.6.10.0 (Tyanova et al, 2016) for downstream statistical analysis.

For the absolute quantification of protein abundance in LSECs compared to splenic and heart ECs and iron-recycling macrophages, peptides were separated on an Easy-Spray Acclaim PepMap column (2 µm, 100 Å, 75 µm × 50 cm) with a 180 min acetonitrile gradient at a flow rate of 300 nl/min. Survey scans were acquired at a resolution of 120,000 (*m/z* 200), with MS/MS spectra collected at 15,000 resolution. The top 12 most abundant ions (charge states 2–5) were isolated with a 1.3 *m/z* window and fragmented by HCD (27 NCE), with a dynamic exclusion of 40 s. Maximum ion injection times were 45 ms (MS) and 96 ms (MS/MS), with target values of 3e6 and 1e5, respectively; the MS/MS intensity threshold was set to 1e4. Both LFQ and iBAQ values were log2-transformed in Perseus. Standard filtering was applied to remove reverse hits, contaminants, and proteins only identified by site. For relative comparisons between LSEC and other cell types, a minimum of two LFQ values per group was required; missing values were imputed from a normal distribution (downshift = 1.8 SD, width = 0.3 SD). Two-sided Student's *t* tests (permutation-based FDR = 0.01, S0 = 0.2) identified proteins significantly altered between groups. Data are reported in Dataset EV1.

For the comparison of proteomic changes in LSECs upon stressed RBCs injection in mice, peptides were separated on an Easy-Spray Acclaim PepMap column (2 µm, 100 Å, 50 µm × 15 cm) with a 60 min acetonitrile gradient at a flow rate of 300 nl/min. Survey scans were acquired at a resolution of 60,000 (*m/z* 200), with MS/MS spectra collected at 15,000 resolution. The top 12 most abundant ions (charge states 2–5) were isolated with a 1.3 *m/z* window and fragmented by HCD (27 NCE), with a dynamic exclusion of 30 s. Maximum ion injection times were 50 ms (MS) and 28 ms (MS/MS), with target values of 3e6 and 1e5, respectively; the MS/MS intensity threshold was set to 3.6e4. LFQ intensity values were log2-transformed, and filtering was applied as above. Two-sided Student's *t* tests (permutation-based FDR = 0.05, S0 = 0.2) identified proteins significantly altered between RBC-injected and control samples. Data are reported in Dataset EV2.

Heme analysis and iron quantification

Tissue non-heme iron content was measured using the bathophenanthroline colorimetric method and calculated against dry tissue weight. Serum iron content (SFBC) and unsaturated iron-binding capacity (UIBC) were measured with the SFBC and the UIBC kit (Biolabo, #97408). Transferrin saturation was calculated using the formula SFBC/(SFBC + UIBC) × 100. Heme content was measured as described previously (Slusarczyk et al, 2023). Briefly, to determine the extracellular heme content in the spleen, the entire

spleen was dissected, weighed, and gently mashed through a 100 µm strainer, rinsed with 3 ml of HBSS (ThermoScientific, #14025092). The resulting suspension was centrifuged at 400× *g* for 10 min at 4 °C, and the supernatant was collected. To eliminate the remaining cells and membranes, the supernatant was centrifuged again at 1000× *g* for 10 min at 4 °C, and the supernatant was transferred to a fresh tube. To determine heme content in the kidneys, organs were incubated in RIPA buffer containing Protease Inhibitor Cocktail, followed by centrifugation for 15 min at 12,000× *g*. The obtained lysate was further used for heme quantification. To determine heme content in the blood, blood from the circulation and portal vein was collected into the heparin-coated tube, centrifuged at 400× *g* for 10 min at 4 °C, and plasma was transferred to a fresh tube. Heme concentrations in the plasma, kidney, or supernatant collected from magnetically sorted LSECs, KCs, and RPMs were determined using the Heme Assay Kit (Sigma-Aldrich, #MAK316), following the instructions provided by the manufacturer. The absorbance was measured at a wavelength of 400 nm. The amount of heme was calculated against Heme Calibrator and additionally normalized to the initial weight of fresh spleens (for splenic extracellular heme content) or protein concentration (for kidney and magnetically sorted cells).

RNA isolation and qPCR

RNA from tissues was extracted using TRIzol™ Reagent (ThermoScientific, #15596026) and from sorted cells using TRIzol™ LS Reagent (ThermoScientific, #10296028) according to the manufacturer's instructions with an additional step of RNA precipitation with glycogen (ThermoScientific, #R0551). RNA (100–400 ng) was reverse transcribed into cDNA using random primers (ThermoScientific, #48190011) and RevertAid H Minus Reverse Transcriptase (ThermoScientific, #EP0452). The cDNA products were amplified by quantitative polymerase chain reaction (qPCR) using the SG qPCR Master Mix (2×) (Eurex, #E0401-01). Real-time qPCR (RT-qPCR) was run in LightCycler 96 Real-Time PCR System (Roche), using the following primer sequences: *Rpl19*- AGGCATATGGGCATAGGG AAGAG (forward primer); TTGACCTTCAGGTACAGGCTGTG (reverse primer). *Bmp6* – ATGGCAGGACTGGATCATTGC (forward primer); CCATCACAGTAGTTGGCAGCG (reverse primer). *Hmox-1* – AGGCTAAGACCGCCTTCCT (forward primer); TGTGTTCCT CTGTCAGCATCA (reverse primer). *Hamp* – ATACC AATGCAGAAGAGAAGG (forward primer); AACAGATACCAC ACTGGGAA (reverse primer).

RNA sequencing

Transcriptome analysis of LSECs was conducted using the AmpliSeq method. RNA integrity was assessed using Agilent RNA 6000 Nano Kit on Agilent™ 2100 Bioanalyzer™, and cDNA library preparation was performed using a commercially available kit (Ion AmpliSeq™ Transcriptome Mouse Gene Expression Kit, ThermoScientific, # A36554) following the manufacturer's recommendations. Targeted cDNA fragments were amplified using the Ion AmpliSeq™ Library Kit 2.0. cDNA libraries were measured using Agilent™ 2100 Bioanalyzer™. Raw reads were processed using the Torrent Suite tool and mapped to the mouse genome mm10 AmpliSeqTranscriptome version using Torrent Mapping Alignment Program (TMAP).

Elemental analysis by inductively coupled plasma optical emission spectrometry (ICP-OES) of liver non-parenchymal cells and red pulp macrophages

Samples were digested overnight in 65% ultrapure nitric acid (Merck, #1004410250) and diluted to a final volume of 5 mL before measuring the metal content on a iC at 0.5 L/min, and nebulizer gas pressure at 2.03 bar AP Pro ICP-OES (Thermo-Fisher Scientifics) instrument equipped with a iSC-65 autosampler, a Torch Duo (Slot) Rev 02 argon plasma torch and a Qutegra software, which was used to calculate the metal concentration in measured sample. The wavelengths for Fe (259.940 nm) and S (180.731 nm) were selected to minimize overlapping emissions. Samples were measured in Aqueous-Axial_iFR mode with RF power set to 1250 W, nebulizer gas flow at 0.5 L/min, and nebulizer gas pressure at 2.03 bar. Final metal concentration was calculated according to the dilution of the sample and normalized to the protein level/number of cells used for digestion.

Graphics

The synopsis image and graphical abstract were created using BioRender.com.

Statistical analysis

Statistical analyses were conducted using GraphPad Prism software (Version 9.4.1). Data are represented as the mean ± SEM. The number of mice/samples per group or the number of independent cell-based experiments is shown in the figures and reflects biological replicates. Sample size was determined based on power analysis, prior experience of performing similar experiments, and previously published papers in the field. Although no formal tests for normality or homogeneity of variance were performed, sample sizes and distributions were consistent with standard practice in the field. Statistical tests were chosen according to data type. When two groups were compared, a two-tailed unpaired Welch's *t* test was applied, whereas for comparisons involving more than two groups, one-way or two-way analysis of variance (ANOVA) was performed, depending on the experimental design. Post-hoc Tukey's test was used to correct for multiple comparisons between groups. Results were considered significant for $P < 0.05$; the exact *P* values are shown in the figures.

Ethics declarations

All animal experiments were conducted following the guidelines of European Directive 2010/63/EU and the Federation for Laboratory Animal Science Associations. The procedures were approved by the Local Ethics Committee in Warsaw (No. WAW2/150/2019, WAW2/138/2019, WAW2/137/2020, WAW2/137/2021, WAW2/179/2021, WAW2/094/2021 and WAW2/067/2025), or for the dietary experiment by the local ethical committee in Olsztyn No. 26/2018. For the use of human cells, this study conformed to the principles set out in the WMA Declaration of Helsinki and the Department of Health and Human Services Belmont Report. It received approval from the Ethics Committee of the Faculty of

Medicine at Leipzig University (Biobank of Surgical Research, registration no. 322/17-ek, 2020/06/10, ratified on 2021/11/30; "Role of human LSEC in hemoglobin clearance", registration no. 057/23-ek, 2023/08/21).

Data availability

Transcriptome analysis of LSECs was conducted using the AmpliSeq method, and proteomics was performed by label-free quantification with mass spectrometry as described in the Methods. LSEC transcriptomic data for iron citrate injection have been previously deposited in the GEO repository under accession no. GSE235976, whereas data for Hb injection are accessible under no. GSE240270. Proteomics data were deposited to the ProteomeXchange Consortium via the PRIDE partner repository with the dataset identifier PXD051274. Raw flow cytometry data for Figs. 3 and 5A-D and M are deposited in the BioStudies repository under the following links: Fig. 3A and C: ; Fig. 3E and G: https://www.ebi.ac.uk/biostudies/studies/S-BSST2282; Fig. 5A: https://www.ebi.ac.uk/biostudies/studies/S-BSST2289; Fig. 5B: https://www.ebi.ac.uk/biostudies/studies/S-BSST2286; Fig. 5C: https://www.ebi.ac.uk/biostudies/studies/S-BSST2294; Fig. 5D: https://www.ebi.ac.uk/biostudies/studies/S-BSST2293; Fig. 5M: https://www.ebi.ac.uk/biostudies/studies/S-BSST2295.

The source data of this paper are collected in the following database record: biostudies:S-SCDT-10_1038-S44319-025-00673-5.

Expanded view data, supplementary information, appendices are available for this paper at https://doi.org/10.1038/s44319-025-00673-5.

Peer review information

A peer review file is available at https://doi.org/10.1038/s44319-025-00673-5

References

Boretti FS, Baek JH, Palmer AF, Schaer DJ, Buehler PW (2014) Modeling hemoglobin and hemoglobin:haptoglobin complex clearance in a non-rodent species-pharmacokinetic and therapeutic implications. Front Physiol 5:385

BoseDasgupta S, Moes S, Jenoe P, Pieters J (2015) Cytokine-induced macropinocytosis in macrophages is regulated by 14-3-3zeta through its interaction with serine-phosphorylated coronin 1. FEBS J 282:1167–1181

Canali S, Zumbrennen-Bullough KB, Core AB, Wang CY, Nairz M, Bouley R, Swirski FK, Babitt JL (2017) Endothelial cells produce bone morphogenetic protein 6 required for iron homeostasis in mice. Blood 129:405–414

Canton J (2018) Macropinocytosis: new insights into its underappreciated role in innate immune cell surveillance. Front Immunol 9:2286

Commisso C, Davidson SM, Soydaner-Azeloglu RG, Parker SJ, Kamphorst JJ, Hackett S, Grabocka E, Nofal M, Drebin JA, Thompson CB et al (2013) Macropinocytosis of protein is an amino acid supply route in Ras-transformed cells. Nature 497:633–637

Connolly MK, Bedrosian AS, Malhotra A, Henning JR, Ibrahim J, Vera V, Cieza-Rubio NE, Hassan BU, Pachter HL, Cohen S et al (2010) In hepatic fibrosis, liver sinusoidal endothelial cells acquire enhanced immunogenicity. J Immunol 185:2200–2208

Cox J, Mann M (2008) MaxQuant enables high peptide identification rates, individualized p.p.b.-range mass accuracies and proteome-wide protein quantification. Nat Biotechnol 26:1367–1372

Damm G, Schicht G, Zimmermann A, Rennert C, Fischer N, Kiessig M, Wagner T, Kegel V, Seehofer D (2019) Effect of glucose and insulin supplementation on the isolation of primary human hepatocytes. EXCLI J 18:1071–1091

Dolat L, Spiliotis ET (2016) Septins promote macropinosome maturation and traffic to the lysosome by facilitating membrane fusion. J Cell Biol 214:517–527

Etzerodt A, Kjolby M, Nielsen MJ, Maniecki M, Svendsen P, Moestrup SK (2013) Plasma clearance of hemoglobin and haptoglobin in mice and effect of CD163 gene targeting disruption. Antioxid Redox Signal 18:2254–2263

Etzerodt A, Moulin M, Doktor TK, Delfini M, Mossadegh-Keller N, Bajenoff M, Sieweke MH, Moestrup SK, Auphan-Anezin N, Lawrence T (2020) Tissue-resident macrophages in omentum promote metastatic spread of ovarian cancer. J Exp Med 217:e20191869

Etzerodt A, Tsalkitzi K, Maniecki M, Damsky W, Delfini M, Baudoin E, Moulin M, Bosenberg M, Graversen JH, Auphan-Anezin N et al (2019) Specific targeting of CD163(+) TAMs mobilizes inflammatory monocytes and promotes T cell-mediated tumor regression. J Exp Med 216:2394–2411

Fagoonee S, Gburek J, Hirsch E, Marro S, Moestrup SK, Laurberg JM, Christensen EI, Silengo L, Altruda F, Tolosano E (2005) Plasma protein haptoglobin modulates renal iron loading. Am J Pathol 166:973–983

Ganesan LP, Kim J, Wu Y, Mohanty S, Phillips GS, Birmingham DJ, Robinson JM, Anderson CL (2012) FcgammaRIIb on liver sinusoidal endothelium clears small immune complexes. J Immunol 189:4981–4988

Gjurich BN, Taghavie-Moghadam PL, Galkina EV (2015) Flow cytometric analysis of immune cells within murine aorta. Methods Mol Biol 1339:161–175

Gola A, Dorrington MG, Speranza E, Sala C, Shih RM, Radtke AJ, Wong HS, Baptista AP, Hernandez JM, Castellani G et al (2021) Commensal-driven immune zonation of the liver promotes host defence. Nature 589:131–136

Guilliams M, Bonnardel J, Haest B, Vanderborght B, Wagner C, Remmerie A, Bujko A, Martens L, Thone T, Browaeys R et al (2022) Spatial proteogenomics reveals distinct and evolutionarily conserved hepatic macrophage niches. Cell 185:379–396.e38

Gupta A, Fei YD, Kim TY, Xie A, Batai K, Greener I, Tang H, Ciftci-Yilmaz S, Juneman E, Indik JH et al (2021) IL-18 mediates sickle cell cardiomyopathy and ventricular arrhythmias. Blood 137:1208–1218

Kalucka J, de Rooij L, Goveia J, Rohlenova K, Dumas SJ, Meta E, Conchinha NV, Taverna F, Teuwen LA, Veys K et al (2020) Single-cell transcriptome atlas of murine endothelial cells. Cell 180:764–779.e20

Kato GJ, Steinberg MH, Gladwin MT (2017) Intravascular hemolysis and the pathophysiology of sickle cell disease. J Clin Invest 127:750–760

Kegel V, Deharde D, Pfeiffer E, Zeilinger K, Seehofer D, Damm G (2016) Protocol for isolation of primary human hepatocytes and corresponding major populations of non-parenchymal liver cells. J Vis Exp 109:e53069

Klei TRL, Dalimot J, Nota B, Veldthuis M, Mul FPJ, Rademakers T, Hoogenboezem M, Nagelkerke SQ, van IWFJ, Oole E et al (2020) Hemolysis in the spleen drives erythrocyte turnover. Blood 136:1579–1589

Klein D, Demory A, Peyre F, Kroll J, Augustin HG, Helfrich W, Kzhyshkowska J, Schledzewski K, Arnold B, Goerdt S (2008) Wnt2 acts as a cell type-specific, autocrine growth factor in rat hepatic sinusoidal endothelial cells cross-stimulating the VEGF pathway. Hepatology 47:1018–1031

Koch PS, Lee KH, Goerdt S, Augustin HG (2021) Angiodiversity and organotypic functions of sinusoidal endothelial cells. Angiogenesis 24:289–310

Koch PS, Olsavszky V, Ulbrich F, Sticht C, Demory A, Leibing T, Henzler T, Meyer M, Zierow J, Schneider S et al (2017) Angiocrine Bmp2 signaling in murine liver controls normal iron homeostasis. Blood 129:415–419

Kristiansen M, Graversen JH, Jacobsen C, Sonne O, Hoffman HJ, Law SK, Moestrup SK (2001) Identification of the haemoglobin scavenger receptor. Nature 409:198–201

Lin HP, Singla B, Ahn W, Ghoshal P, Blahove M, Cherian-Shaw M, Chen A, Haller A, Hui DY, Dong K et al (2022) Receptor-independent fluid-phase

macropinocytosis promotes arterial foam cell formation and atherosclerosis. Sci Transl Med 14:eadd2376

Lin XP, Mintern JD, Gleeson PA (2020) Macropinocytosis in different cell types: similarities and differences. Membranes 10:177

Ma S, Dubin AE, Zhang Y, Mousavi SAR, Wang Y, Coombs AM, Loud M, Andolfo I, Patapoutian A (2021) A role of PIEZO1 in iron metabolism in mice and humans. Cell 184:969–982.e13

Makia NL, Bojang P, Falkner KC, Conklin DJ, Prough RA (2011) Murine hepatic aldehyde dehydrogenase 1a1 is a major contributor to oxidation of aldehydes formed by lipid peroxidation. Chem Biol Interact 191:278–287

Malovic I, Sorensen KK, Elvevold KH, Nedredal GI, Paulsen S, Erofeev AV, Smedsrod BH, McCourt PA (2007) The mannose receptor on murine liver sinusoidal endothelial cells is the main denatured collagen clearance receptor. Hepatology 45:1454–1461

Marro S, Barisani D, Chiabrando D, Fagoonee S, Muckenthaler MU, Stolte J, Meneveri R, Haile D, Silengo L, Altruda F et al (2007) Lack of haptoglobin affects iron transport across duodenum by modulating ferroportin expression. Gastroenterology 133:1261–1271

Maxson ME, Sarantis H, Volchuk A, Brumell JH, Grinstein S (2021) Rab5 regulates macropinocytosis by recruiting the inositol 5-phosphatases OCRL and Inpp5b that hydrolyse PtdIns(4,5)P2. J Cell Sci 134:jcs252411

Mleczko-Sanecka K, Silvestri L (2021) Cell-type-specific insights into iron regulatory processes. Am J Hematol 96:110–127

Muckenthaler MU, Rivella S, Hentze MW, Galy B (2017) A red carpet for iron metabolism. Cell 168:344–361

Poisson J, Lemoinne S, Boulanger C, Durand F, Moreau R, Valla D, Rautou PE (2017) Liver sinusoidal endothelial cells: physiology and role in liver diseases. J Hepatol 66:212–227

Ramirez C, Hauser AD, Vucic EA, Bar-Sagi D (2019) Plasma membrane V-ATPase controls oncogenic RAS-induced macropinocytosis. Nature 576:477–481

Recouvreux MV, Commisso C (2017) Macropinocytosis: a metabolic adaptation to nutrient stress in cancer. Front Endocrinol 8:261

Redelman-Sidi G, Binyamin A, Gaeta I, Palm W, Thompson CB, Romesser PB, Lowe SW, Bagul M, Doench JG, Root DE et al (2018) The canonical Wnt pathway drives macropinocytosis in cancer. Cancer Res 78:4658–4670

Schaer CA, Schoedon G, Imhof A, Kurrer MO, Schaer DJ (2006a) Constitutive endocytosis of CD163 mediates hemoglobin-heme uptake and determines the noninflammatory and protective transcriptional response of macrophages to hemoglobin. Circ Res 99:943–950

Schaer DJ, Schaer CA, Buehler PW, Boykins RA, Schoedon G, Alayash AI, Schaffner A (2006b) CD163 is the macrophage scavenger receptor for native and chemically modified hemoglobins in the absence of haptoglobin. Blood 107:373–380

Schaer DJ, Vinchi F, Ingoglia G, Tolosano E, Buehler PW (2014) Haptoglobin, hemopexin, and related defense pathways-basic science, clinical perspectives, and drug development. Front Physiol 5:415

Schledzewski K, Geraud C, Arnold B, Wang S, Grone HJ, Kempf T, Wollert KC, Straub BK, Schirmacher P, Demory A et al (2011) Deficiency of liver sinusoidal scavenger receptors stabilin-1 and -2 in mice causes glomerulofibrotic nephropathy via impaired hepatic clearance of noxious blood factors. J Clin Invest 121:703–714

Schnatwinkel C, Christoforidis S, Lindsay MR, Uttenweiler-Joseph S, Wilm M, Parton RG, Zerial M (2004) The Rab5 effector Rabankyrin-5 regulates and coordinates different endocytic mechanisms. PLoS Biol 2:E261

Shetty S, Lalor PF, Adams DH (2018) Liver sinusoidal endothelial cells - gatekeepers of hepatic immunity. Nat Rev Gastroenterol Hepatol 15:555–567

Slusarczyk P, Mandal PK, Zurawska G, Niklewicz M, Chouhan K, Mahadeva R, Jonczy A, Macias M, Szybinska A, Cybulska-Lubak M et al (2023) Impaired iron recycling from erythrocytes is an early hallmark of aging. eLife 12:e79196

Slusarczyk P, Mleczko-Sanecka K (2021) The multiple facets of iron recycling. Genes 12:1364

Sorensen KK, McCourt P, Berg T, Crossley C, Le Couteur D, Wake K, Smedsrod B (2012) The scavenger endothelial cell: a new player in homeostasis and immunity. Am J Physiol Regul Integr Comp Physiol 303:R1217–R1230

Stefanova D, Raychev A, Arezes J, Ruchala P, Gabayan V, Skurnik M, Dillon BJ, Horwitz MA, Ganz T, Bulut Y et al (2017) Endogenous hepcidin and its agonist mediate resistance to selected infections by clearing non-transferrin-bound iron. Blood 130:245–257

Strauss O, Phillips A, Ruggiero K, Bartlett A, Dunbar PR (2017) Immunofluorescence identifies distinct subsets of endothelial cells in the human liver. Sci Rep 7:44356

Svendsen P, Etzerodt A, Deleuran BW, Moestrup SK (2020) Mouse CD163 deficiency strongly enhances experimental collagen-induced arthritis. Sci Rep 10:12447

Tejeda-Munoz N, Albrecht LV, Bui MH, De Robertis EM (2019) Wnt canonical pathway activates macropinocytosis and lysosomal degradation of extracellular proteins. Proc Natl Acad Sci USA 116:10402–10411

Theurl I, Hilgendorf I, Nairz M, Tymoszuk P, Haschka D, Asshoff M, He S, Gerhardt LM, Holderried TA, Seifert M et al (2016) On-demand erythrocyte disposal and iron recycling requires transient macrophages in the liver. Nat Med 22:945–951

Tyanova S, Temu T, Sinitcyn P, Carlson A, Hein MY, Geiger T, Mann M, Cox J (2016) The Perseus computational platform for comprehensive analysis of (prote)omics data. Nat Methods 13:731–740

Vinchi F, De Franceschi L, Ghigo A, Townes T, Cimino J, Silengo L, Hirsch E, Altruda F, Tolosano E (2013) Hemopexin therapy improves cardiovascular function by preventing heme-induced endothelial toxicity in mouse models of hemolytic diseases. Circulation 127:1317–1329

Vinchi F, Sparla R, Passos ST, Sharma R, Vance SZ, Zreid HS, Juaidi H, Manwani D, Yazdanbakhsh K, Nandi V et al (2021) Vasculo-toxic and pro-inflammatory action of unbound haemoglobin, haem and iron in transfusion-dependent patients with haemolytic anaemias. Br J Haematol 193:637–658

Visweshwaran SP, Nayab H, Hoffmann L, Gil M, Liu F, Kuhne R, Maritzen T (2022) Ena/VASP proteins at the crossroads of actin nucleation pathways in dendritic cell migration. Front Cell Dev Biol 10:1008898

Wang F, Ding P, Liang X, Ding X, Brandt CB, Sjostedt E, Zhu J, Bolund S, Zhang L, de Rooij L et al (2022) Endothelial cell heterogeneity and microglia regulons revealed by a pig cell landscape at single-cell level. Nat Commun 13:3620

Wang Y, Kinzie E, Berger FG, Lim SK, Baumann H (2001) Haptoglobin, an inflammation-inducible plasma protein. Redox Rep 6:379–385

Youssef LA, Rebbaa A, Pampou S, Weisberg SP, Stockwell BR, Hod EA, Spitalnik SL (2018) Increased erythrophagocytosis induces ferroptosis in red pulp macrophages in a mouse model of transfusion. Blood 131:2581–2593

Zdzalik-Bielecka D, Poswiata A, Kozik K, Jastrzebski K, Schink KO, Brewinska-Olchowik M, Piwocka K, Stenmark H, Miaczynska M (2021) The GAS6-AXL signaling pathway triggers actin remodeling that drives membrane ruffling, macropinocytosis, and cancer-cell invasion. Proc Natl Acad Sci USA 118:e2024596118

Zhang Z, Guo X, Herrera C, Tao Y, Wu Q, Wu A, Wang H, Bartnikas TB, Wang F (2014) Bmp6 expression can be regulated independently of liver iron in mice. PLoS ONE 9:e84906

Zimmermann A, Hansel R, Gemunden K, Kegel-Hubner V, Babel J, Blaker H, Matz-Soja M, Seehofer D, Damm G (2021) In vivo and in vitro characterization of primary human liver macrophages and their inflammatory state. Biomedicines 9:406

Zurawska G, Jonczy A, Niklewicz M, Sas Z, Rumienczyk I, Kulecka M, Piwocka K, Rygiel TP, Mikula M, Mleczko-Sanecka K (2024) Iron-triggered signaling via

ETS1 and the p38/JNK MAPK pathway regulates Bmp6 expression. Am J Hematol 99:543–554

Acknowledgements

This work was funded by the National Science Centre grant 2018/31/B/NZ4/03676 to KMS and the Foundation of Polish Science grant TEAM TECH/2016-1/8 to TPR. Additionally, TPR and MS were supported by the National Centre for Research grant 2020/39/B/NZ7/01382. Proteomic measurements were performed at the Proteomics Core Facility, IMol Polish Academy of Sciences, utilizing the equipment funded by the 'Regenerative Mechanisms for Health' project MAB/2017/2 within the International Research Agendas program of the Foundation for Polish Science, co-financed by the European Union under the European Regional Development Fund. We express gratitude to Marta Niklewicz for her substantial technical assistance in this project. We would like to thank Daria Zdżalik-Bielecka for her valuable advice during the initial phases of the project. Additionally, we extend our thanks to Damian Strzemecki for his technical assistance in performing mouse injections. We thank Tara Arvedson (Amgen Inc. USA) for the anti-ferroportin antibody, Elizabeta Nemeth for PR73, and Aneta Suwińska for sharing UBI-GFP/BL6 mice. We thank Julian Connor Eckel for his excellent technical assistance in the isolation and provision of primary human liver cells. Many thanks to Agnieszka Popielska and Anna Kosson, and the staff of the Experimental Medicine Centre (Bialystok, Poland) and Mossakowski Medical Research Institute (Warsaw, Poland) for their technical support. This research was supported by IIMCB IN-MOL-CELL Infrastructure (particularly Rodent Breeding and Microscopy Facilities) funded by the European Union-NextGenerationEU under the National Recovery and Resilience Plan. IN-MOL-CELL Infrastructure was also funded by the European Union under Horizon Europe (Project 101059801 - RACE) and by the RACE-PRIME project (FENG.02.01-IP.05-T003/23) carried out within the IRAP program of the Foundation for Polish Science, co-financed by the European Union under the European Funds for Smart Economy 2021-2027 (FENG).

Author contributions

Gabriela Zurawska: Conceptualization; Formal analysis; Validation; Investigation; Visualization; Writing—original draft; Writing—review and editing. **Zuzanna Sas**: Conceptualization; Formal analysis; Validation; Investigation; Visualization; Writing—original draft. **Aneta Jończy**: Conceptualization; Formal analysis; Validation; Investigation; Visualization; Writing—original draft; Writing—review and editing. **Raghunandan Mahadeva**: Formal analysis; Investigation. **Patryk Slusarczyk**: Formal analysis; Investigation; Visualization. **Marta Chwałek**: Formal analysis; Investigation; Visualization. **Daniel Seehofer**: Resources; Methodology. **Georg Damm**: Resources; Methodology. **Rafał Mazgaj**: Methodology. **Marcin Skórzyński**: Methodology. **Maria Kulecka**: Formal analysis. **Izabela Rumieńczyk**: Formal analysis; Investigation. **Morgane Moulin**: Investigation. **Kamil Jastrzębski**: Investigation; Visualization. **Kevin Waldron**: Methodology. **Michal Mikula**: Data curation; Visualization. **Anders Etzerodt**: Resources; Writing—review and editing. **Remigiusz Serwa**: Data curation; Formal analysis; Validation; Methodology. **Marta Miączyńska**: Conceptualization; Formal analysis; Supervision; Writing—review and editing. **Tomasz P Rygiel**: Conceptualization; Formal analysis; Supervision; Funding acquisition; Validation; Investigation; Visualization; Writing—original draft; Project administration; Writing—review and editing. **Katarzyna Mleczko-Sanecka**: Conceptualization; Formal analysis; Supervision; Funding acquisition; Validation; Investigation; Visualization; Writing—original draft; Project administration; Writing—review and editing.

Source data underlying figure panels in this paper may have individual authorship assigned. Where available, figure panel/source data authorship is listed in the following database record: biostudies:S-SCDT-10_1038-S44319-025-00673-5.

Disclosure and competing interests statement

The authors declare no competing interests.

Expanded View Figures

Figure EV1. LSECs represent the major cell type that sequesters Hb.

(**A**, **B**) Hemoglobin (Hb) distribution in control and macrophage-depleted mice (clodronate) injected with AlexaFluor 750 labeled Hb (Hb-AF750, 10 µg/mouse), imaged with Bruker in vivo Imaging System. (**A**) The efficiency of macrophage depletion in the liver was examined by the percentage of liver KCs in control and clodronate-injected mice. (**B**) Representative images of organs isolated from Hb-AF750 (10 µg/mouse, 1 h) i.v.-injected mice. (**C**) Frozen liver slices from mice injected with Hb-AF647 (red) were processed and stained for Kupffer cells (KCs) (F4/80, green) or LSECs (CD146, green) and nuclei (blue). Merged-channel images for this figure are presented in Fig. 1C. (**D**) Murine NPCs in vitro cultures were treated with Hb-AF750 (0.5 µg/ml) for 1 h. Normalized Hb-AF750 fluorescence intensity and percentage of Hb-AF750+ LSECs and KCs, measured with flow cytometry. (**E**) Plots illustrating high mRNA expression of human LCES markers CD32B and CD36 in liver ECs, visualized using the Human Liver Cell Atlas (Guilliams et al, 2022). Data are expressed as mean ± SEM, and each data point represents one biological replicate, $n = 10$ (**A**), 4 (**D**). Welch's unpaired t test was used to determine statistical significance in (**A**, **D**); exact P values are shown on graphs.

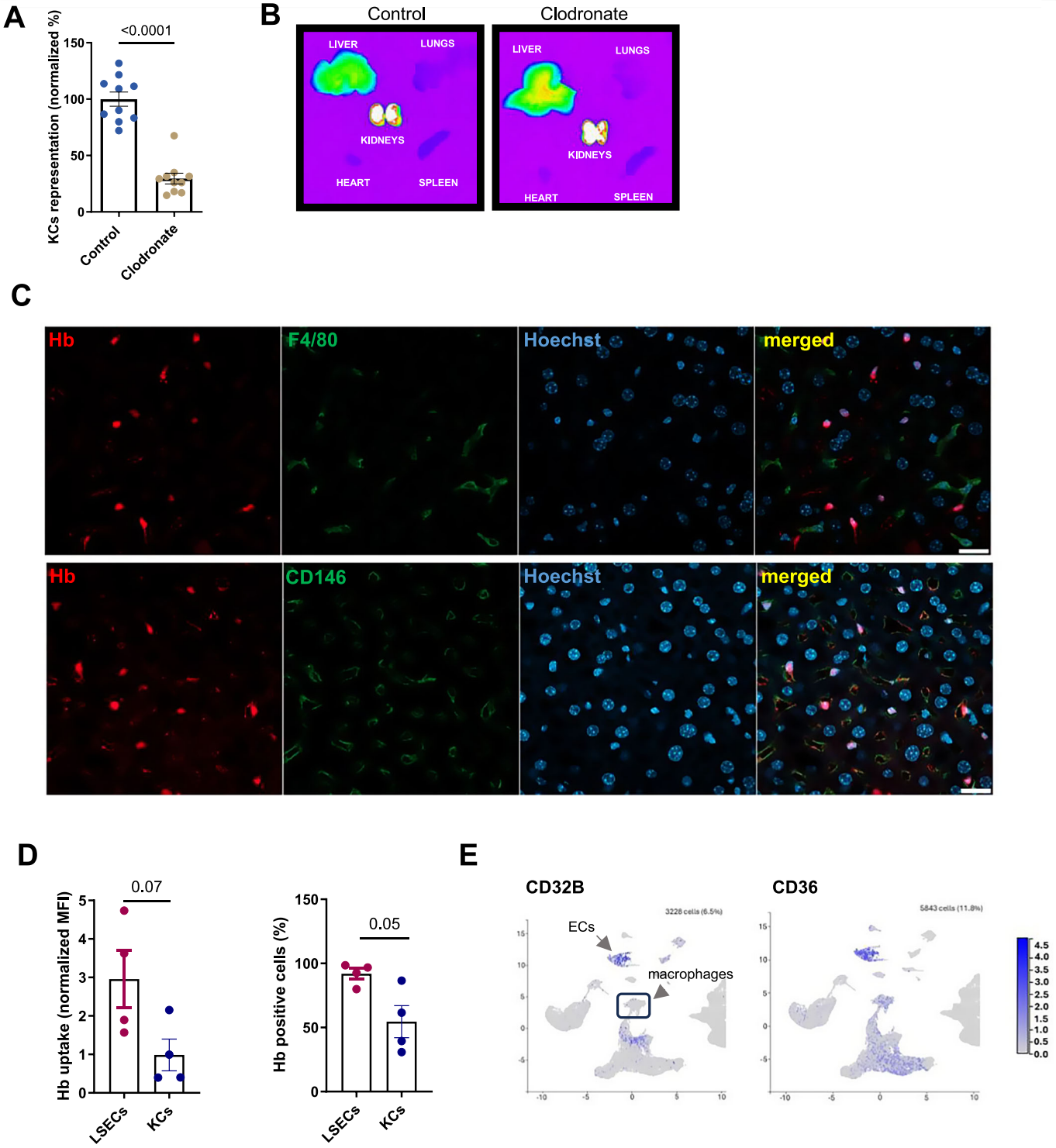
A
KCs representation (normalized %)
<0.0001
150
100
50
0
Control
Clodronate
B
Control
Clodronate
LIVER
LUNGS
KIDNEYS
HEART
SPLEEN
C
Hb
F4/80
Hoechst
merged
Hb
CD146
Hoechst
merged
D
Hb uptake (normalized MFI)
0.07
LSECs
KCs
Hb positive cells (%)
0.05
LSECs
KCs
E
CD32B
CD36
ECs
macrophages
3228 cells (6.5%)
5843 cells (11.8%)
4.5
4.0
3.5
3.0
2.5
2.0
1.5
1.0
0.5
0.0

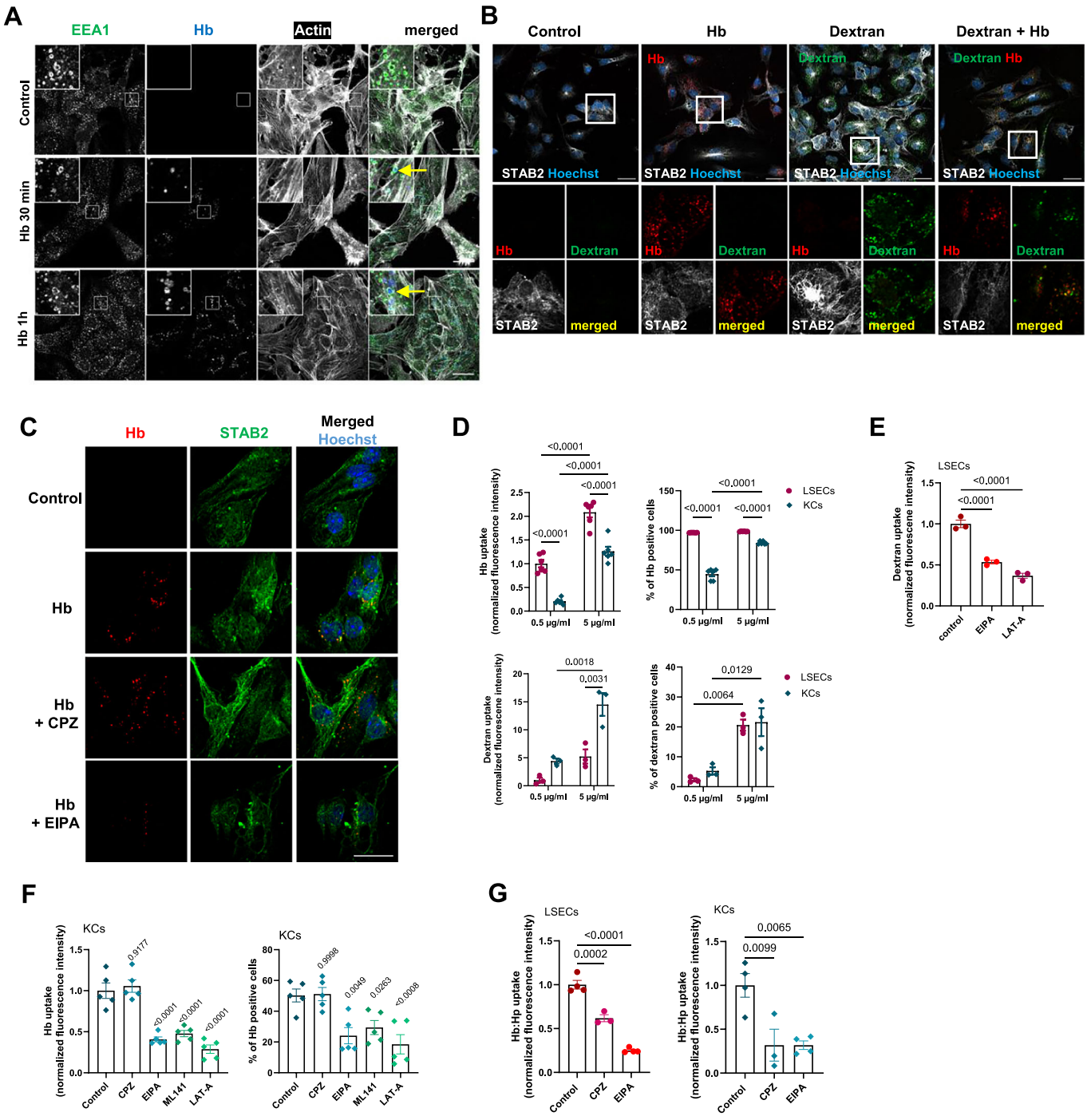
A
EEA1
Hb
Actin
merged
Control
Hb 30 min
Hb 1h
B
Control
Hb
Dextran
Dextran + Hb
STAB2 Hoechst
Dextran Hb
Hb
Dextran
STAB2
merged
C
Hb
STAB2
Merged
Hoechst
Control
Hb
Hb + CPZ
Hb + EIPA
D
Hb uptake (normalized fluorescence intensity)
% of Hb positive cells
Dextran uptake (normalized fluorescene intensity)
% of dextran positive cells
LSECs
KCs
0.5 µg/ml
5 µg/ml
<0.0001
0.0018
0.0031
0.0129
0.0064
E
LSECs
Dextran uptake (normalized fluorescene intensity)
control
EIPA
LAT-A
F
KCs
Hb uptake (normalized fluorescence intensity)
% of Hb positive cells
Control
CPZ
EIPA
ML141
LAT-A
0.9177
0.9998
0.0049
0.0263
G
LSECs
KCs
Hb:Hp uptake (normalized fluorescence intensity)
0.0002
0.0065
0.0099

Figure EV2. Primary LSECs and KCs take up Hb via macropinocytosis.

Murine NPCs in vitro cultures were treated with Hb-AF647 or fluorescently-labeled dextran (0.5 or 5 µg/ml) for 10 min, 30 min, or 1 h. (**A**) Hb-AF647 vesicle localization was imaged in NPCs in vitro cultures depleted of macrophages. Arrows indicate Hb-AF647 (blue) presence in the EEA-1+ (green) and Actin+ (white) vesicles. Areas in the highlighted rectangles are shown at higher magnification (left upper corner). Scale bars, 20 µm. Merged-channel images for this figure are presented in Fig. 2C. (**B**) Co-localization of Hb-AF647 (red) with rhodamine-dextran (green) was imaged in STAB2+ LSECs (white). The arrow indicates co-localization of Hb and rhodamine-dextran at the 10 min time-point. The area in the highlighted rectangle is shown at higher magnification in separate channels below. Nuclei were stained with Hoechst (blue). Scale bar, 20 µm. Merged-channel images for this figure are presented in Fig. 2D. (**C**) NPCs were pretreated with the inhibitor of clathrin-mediated endocytosis chlorpromazine (CPZ, 2 µM) or the macropinocytosis blocker EIPA (25 µM), before Hb-AF647 treatment for 10 min. Cells were fixed and stained for STAB2 (green) and nuclei (Hoechst, blue). Scale bars, 20 µm. (**D–F**) Hb-AF750/FITC-dextran fluorescence intensity and percentage of Hb-AF750 + /dextran+ LSECs or KCs, measured with flow cytometry 1 h after (**D**) administration of the increasing doses of the indicated cargo or (**E**, **F**) upon pretreatment with the indicated inhibitors. (**G**) Hb:Hp-AF750 fluorescence intensity in LSECs or KCs upon pretreatment with the indicated inhibitors, measured with flow cytometry 1 h after administration of Hb:Hp-AF750. Numerical data are expressed as mean ± SEM, and each data point represents one biological replicate, $n = 3$–6 (**D**), 3 (**E**), 5 (**F**), 3–4 (**G**). Two-way ANOVA with Tukey's Multiple Comparison test was used to determine statistical significance in (**D**); one-way ANOVA with Tukey's Multiple Comparison test was used to determine statistical significance in (**E–G**); exact *P* values are shown on graphs, values above bars in (**F**) indicate comparison with control cells. Source data are available online for this figure.

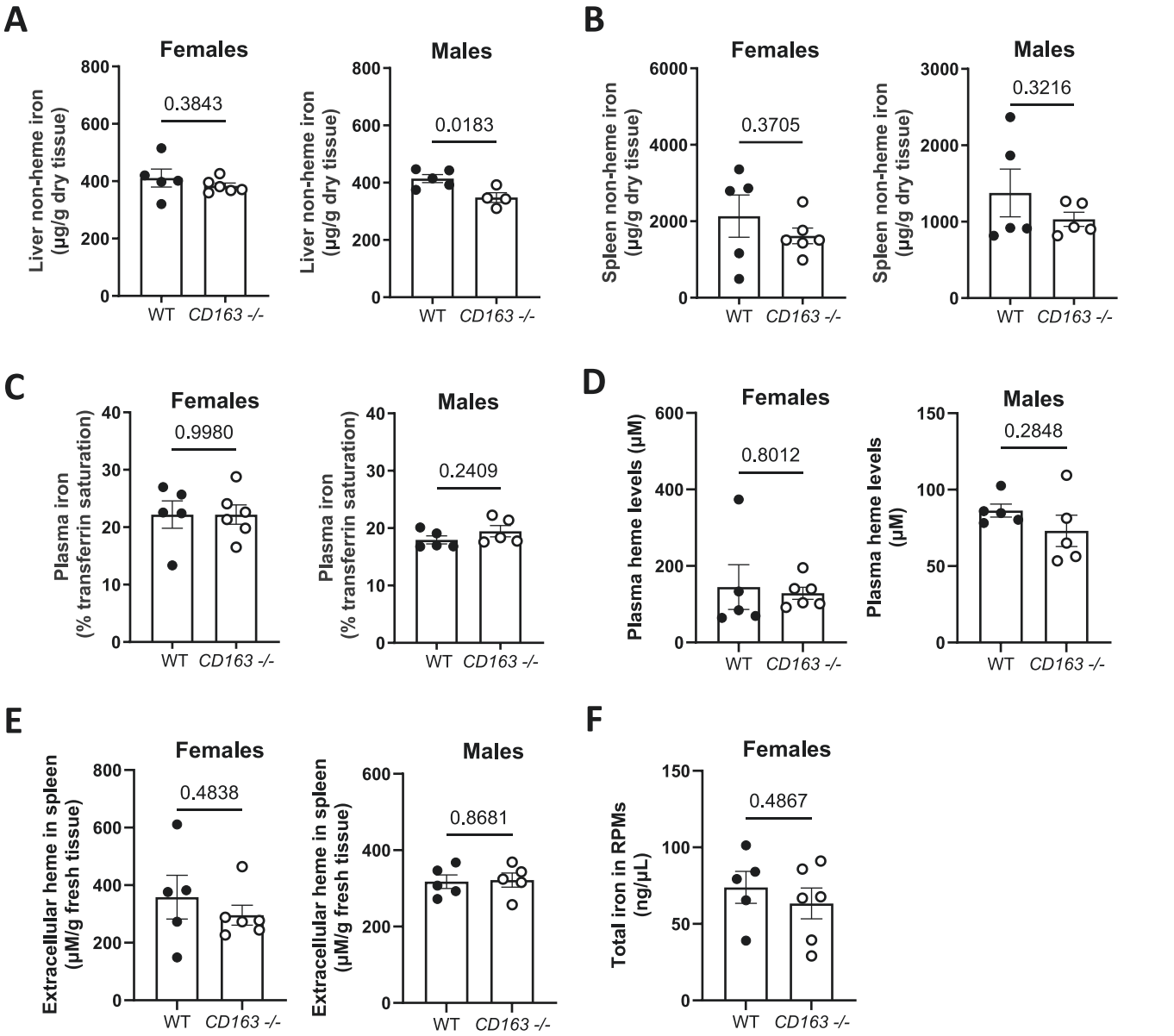

Figure EV3. CD163 KO mice show no major differences in systemic and splenic iron parameters.

(**A–E**) The phenotype of Cd163−/− mice was compared with wild-type (WT) littermates. (**A**, **B**) Non-heme iron content in (**A**) the liver and (**B**) spleen of female and male mice. (**C**) Plasma iron levels were determined by transferrin saturation measurements. (**D**, **E**) Heme levels were measured in the (**D**) plasma and (**E**) extracellular fluid from the spleen using Heme Assay Kit. (**F**) Total iron levels in magnetically-sorted RPMs were measured with Iron assay kit. Data are expressed as mean ± SEM, and each data point represents one biological replicate, $n = 4$–6 (**A**, **C**), 5–6 (**B**, **D**, **F**), 5 (**E**). Welch's unpaired *t* test was used to determine statistical significance; exact *P* values are shown on graphs.

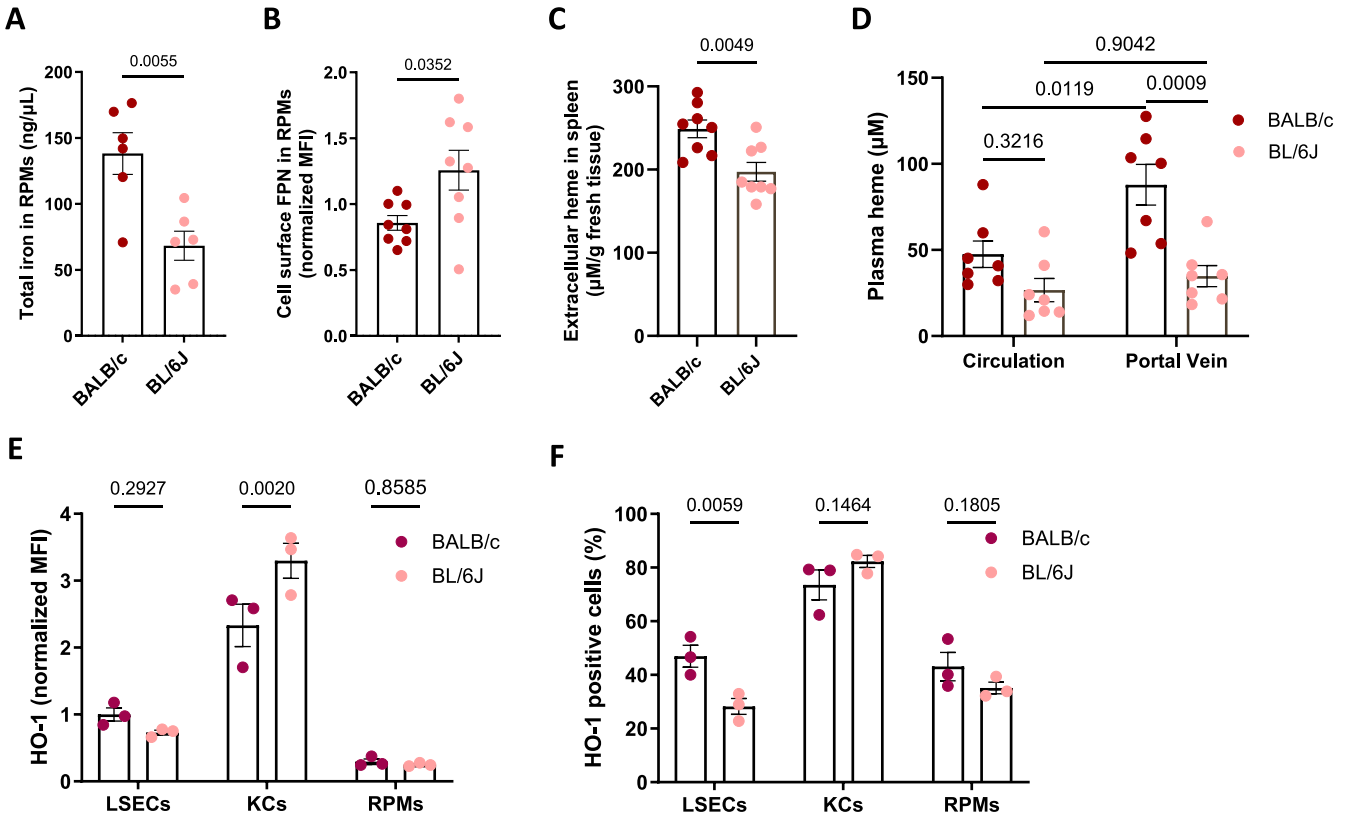

Figure EV4. Comparison of iron-recycling parameters between BALB/c and C57BL/6J mice.

(**A**) The total intracellular iron content in magnetically-sorted RPMs was assessed using the Iron Assay Kit. (**B**) FPN surface levels were measured in RPMs by flow cytometry. (**C**) Extracellular heme content in the spleen and (**D**) heme levels in the portal vein and circulating plasma were measured using Heme Assay Kit. (**E**, **F**) HO-1 levels and percentage of HO-1 positive cells in single cell suspensions from respective organs of BALB/c and C57BL/6J (BL/6J) were determined using flow cytometry. Data are expressed as mean ± SEM, and each data point represents one biological replicate, $n = 6$ (**A**), 8 (**B**, **C**), 7 (**D**), 3 (**E**, **F**). Welch's unpaired *t* test was used to determine statistical significance in (**A–C**), while two-way ANOVA with Tukey's Multiple Comparison tests was used in (**D–F**); exact *P* values are shown on graphs.

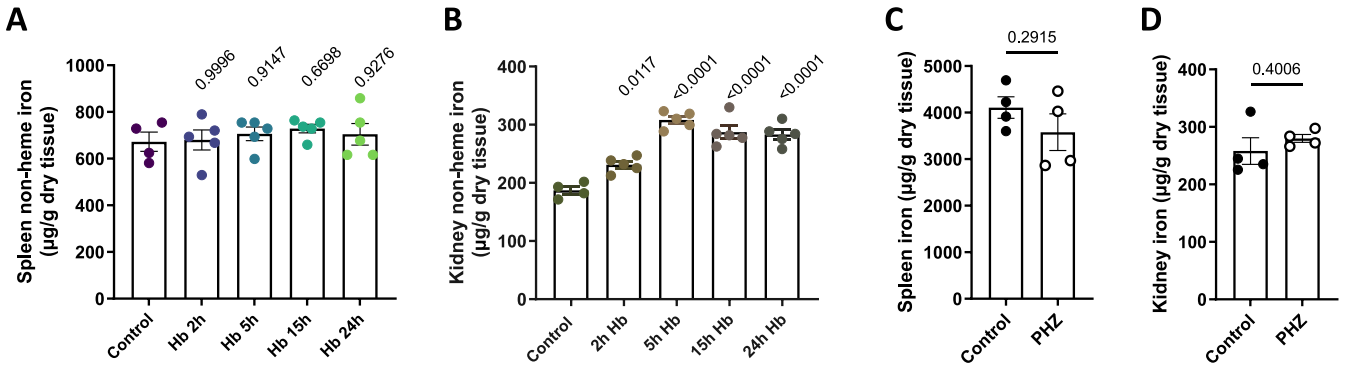

Figure EV5. Alterations of splenic and renal iron levels upon Hb injection and PHZ-induced hemolysis.

(**A**, **B**) Mice were injected with Hb (10 mg/mouse) for the indicated time points. Non-heme iron content in the (**A**) spleens and (**B**) kidneys. (**C**, **D**) Hemolysis was induced by i.p. injection of phenylhydrazine (PHZ, 0.125 mg/g) for 6 h. Non-heme iron content in the (**C**) spleens and (**D**) kidneys. Data are expressed as mean ± SEM, and each data point represents one biological replicate, $n = 4$–5 (**A**, **B**), 4 (**C**, **D**). Welch's unpaired *t* test was used to determine statistical significance in (**C**, **D**). One-way ANOVA with Tukey's Multiple Comparison test was used in (**A**, **B**); exact *P* values are shown on graphs, values above bars in (**A**, **B**) indicate comparison with control mice.

Appendix

This file contains Appendix Figures S1-S4 and Gating strategies for all figure panels.

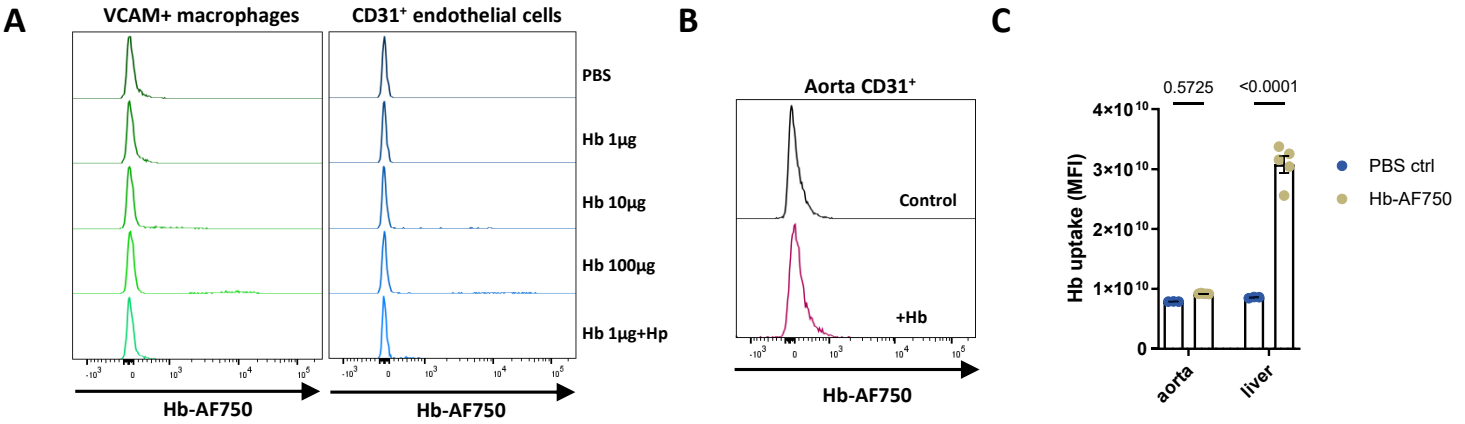

Appendix Figure S1. Bone marrow cells and aortic endothelium fail to sequester Hb.

Mice were injected i.v. with 1, 10, 100 µg of Hb-AF750 or Hb-AF750:Hp complex (1 µg: 32 µg) for 1 h. (A) Histograms of Hb-AF750 fluorescence in VCAM+ macrophages or CD31+ endothelial cells in the bone marrow. (B) Histograms of Hb-AF750 uptake by CD31+ endothelial cells from the aorta, 1 h after Hb-AF750 injection (10 µg/mouse). (C) Mice were injected with Hb-AF750 (10 µg/mouse) for 1 h, and livers and aortas were excised, and total fluorescence was measured by Bruker *in vivo* Imaging System. Quantification of the signal from Hb-AF750 in the organs is presented as total fluorescent counts. Data are expressed as mean ± SEM, and each data point represents one biological replicate. Two-way ANOVA with Tukey's Multiple Comparison tests was used to determine statistical significance in C; exact p-values are shown on the graph.

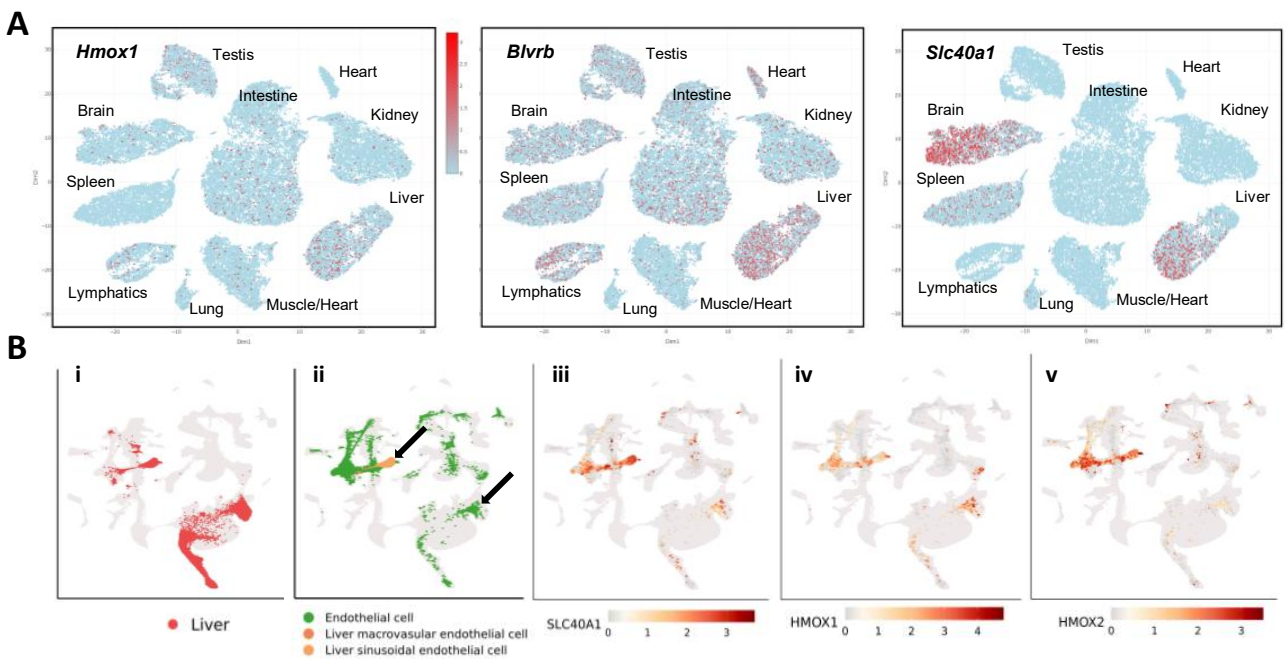

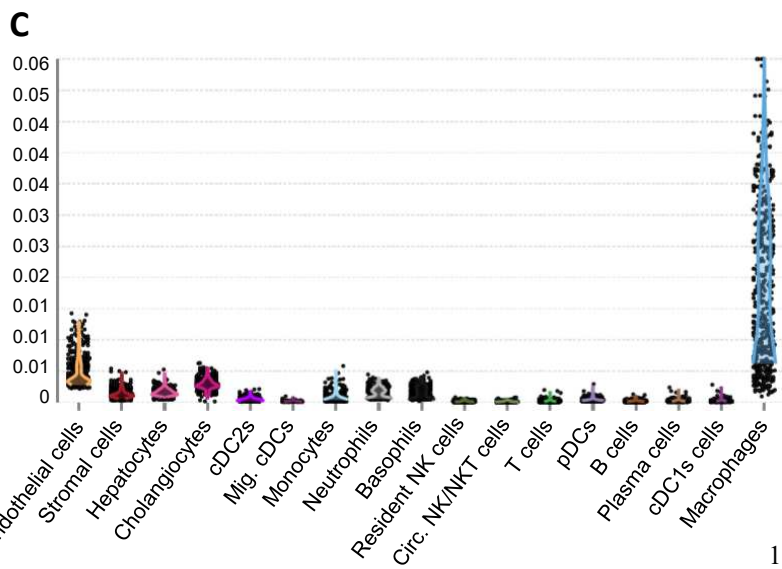

Appendix Figure S2. Liver endothelial cells are distinguished by high mRNA expression levels of genes involved in iron recycling.

(A) Visualization of the expression levels of *Hmox1*, *Blvrb*, and *Slc40a1* obtained with EC Atlas, which collects data from single-cell RNA sequencing of endothelial cells (ECs) from different mouse organs (Kalucka et al. 2020). (B) Analysis of single-cell transcriptome atlas of pig tissues: i) indicates all liver cells, ii) depicts ECs, including those in the liver – LSECs and macrovascular ECs. Arrows point to liver ECs. iii-v) visualization of the expression levels of *Slc40a1*, *Hmox1,* and *Hmox2*, respectively, in cells selected in ii) (The Pig Single Cell RNA Atlas; Wang et al. 2022). (C) Endothelial cells show second-highest expression of *Slc40a1* among all liver cells, as determined by single-cell RNA seq (Liver Cell Atlas; Guilliams et al. 2022).

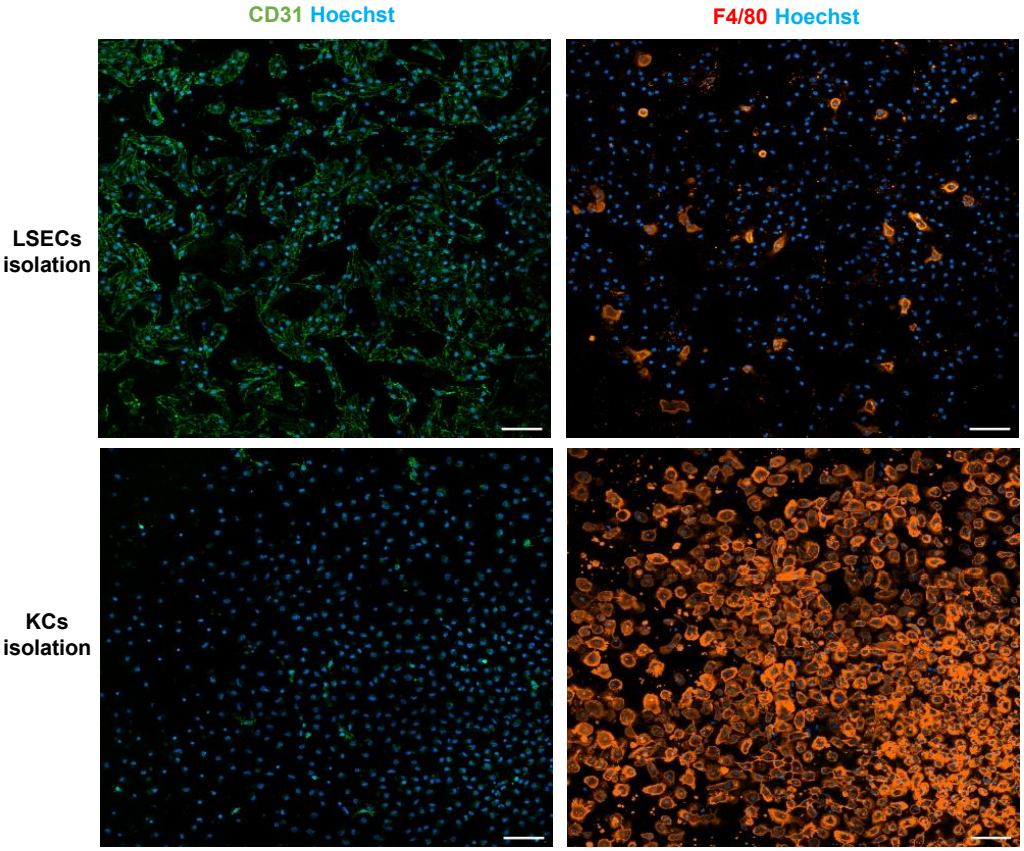

Appendix Figure S3. Purity of magnetically-sorted LSECs and KCs.

Freshly isolated murine NPCs were subjected to magnetic separation, aimed at LSECs or KCs separation. Cells were plated, fixed, and stained for CD31 (green), F4/80 (orange), and nuclei (Hoechst, blue), and evaluated for purity using confocal microscopy. Scale bars, 20 μm.

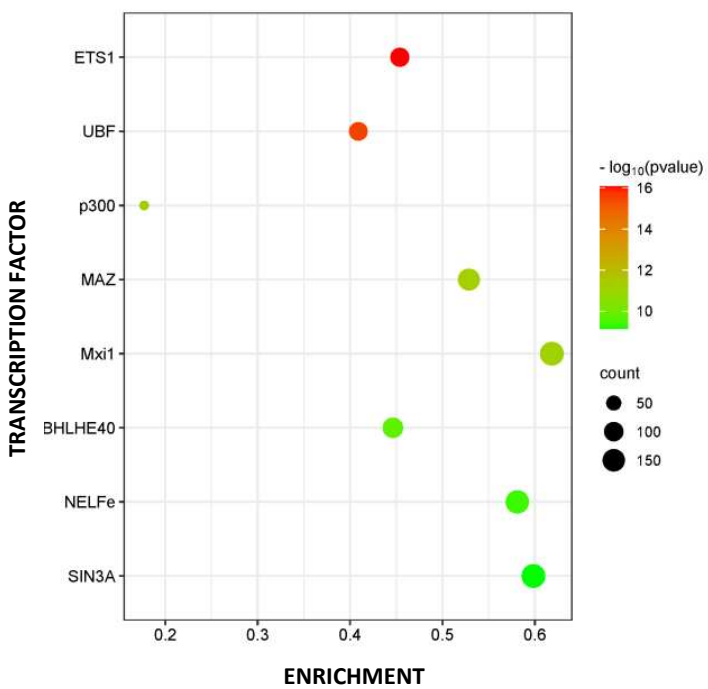

Appendix Figure S4. ETS1 emerged as a key transcription factor responsible for the LSEC transcriptome response upon Hb injection.

The set of genes induced in FACS-sorter LSECs upon injection of mice with 10 mg of Hb was compared with a genome-wide ChIP-seq dataset using the Cscan program. Potential common transcriptional regulators of input genes are shown.

Flow Cytometry Gating Strategies

This file gathers all gating strategies assigned to individual figure panels, as indicated.

Gating strategy for Figure EV1A

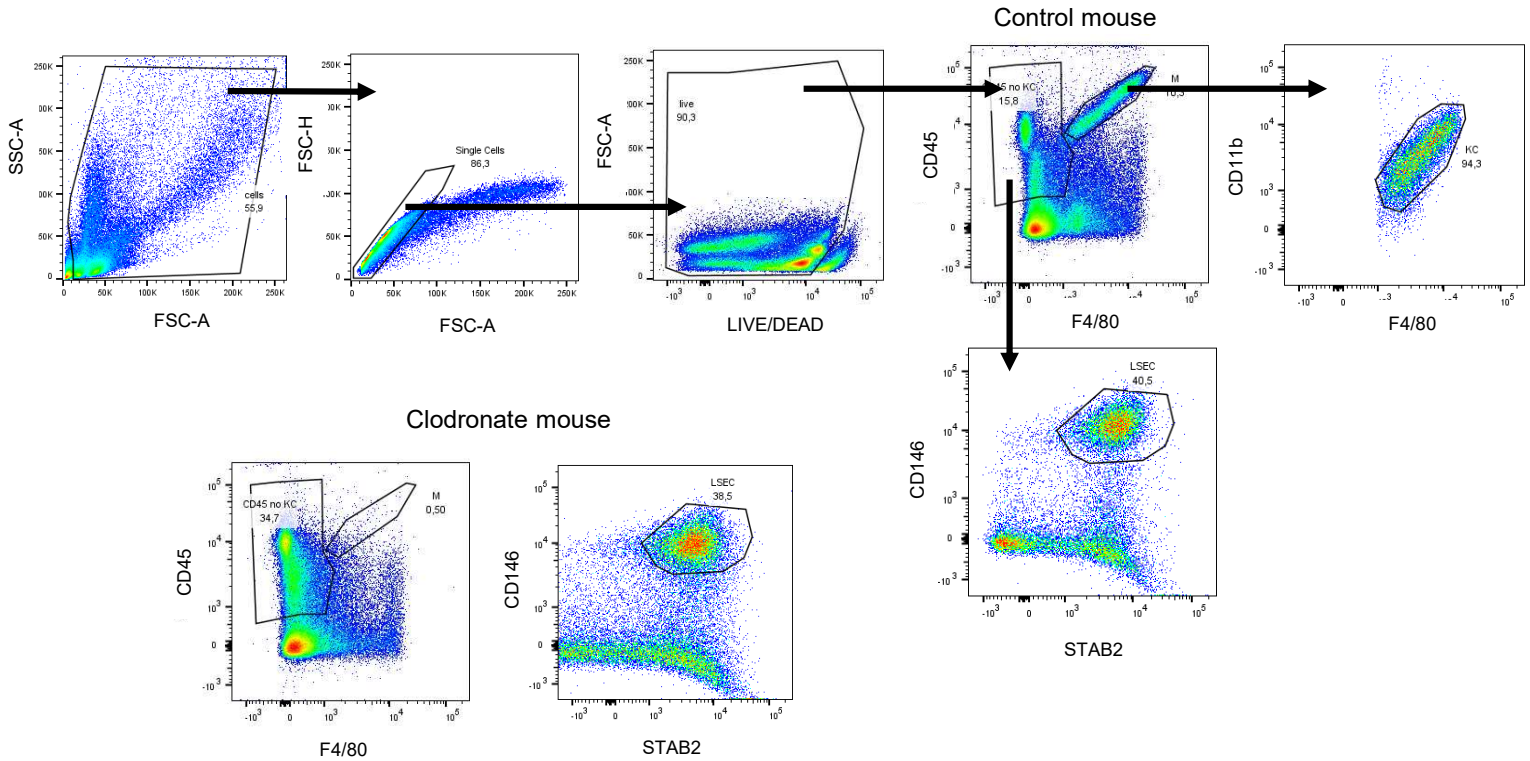

Gating strategy for Figure 1B

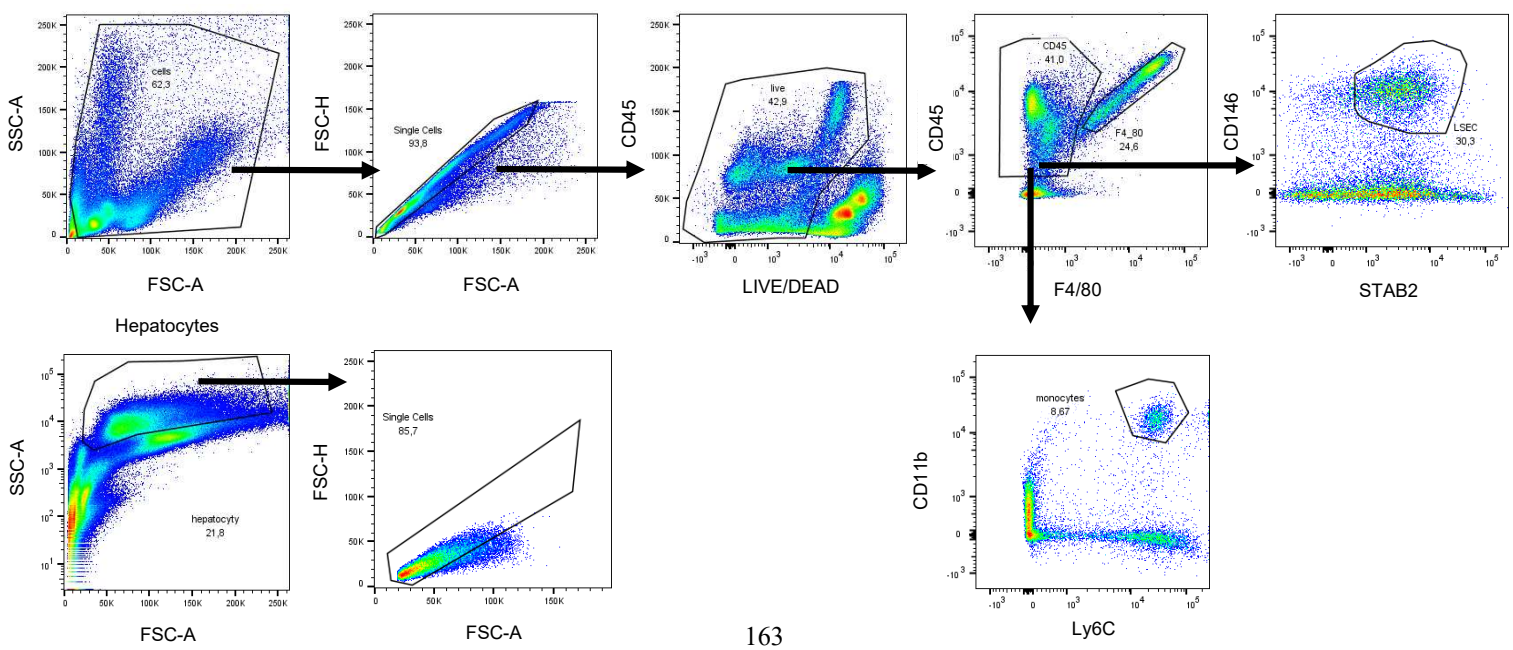

Gating strategy for Figures 1E and 2H (primary human liver NPCs cells)

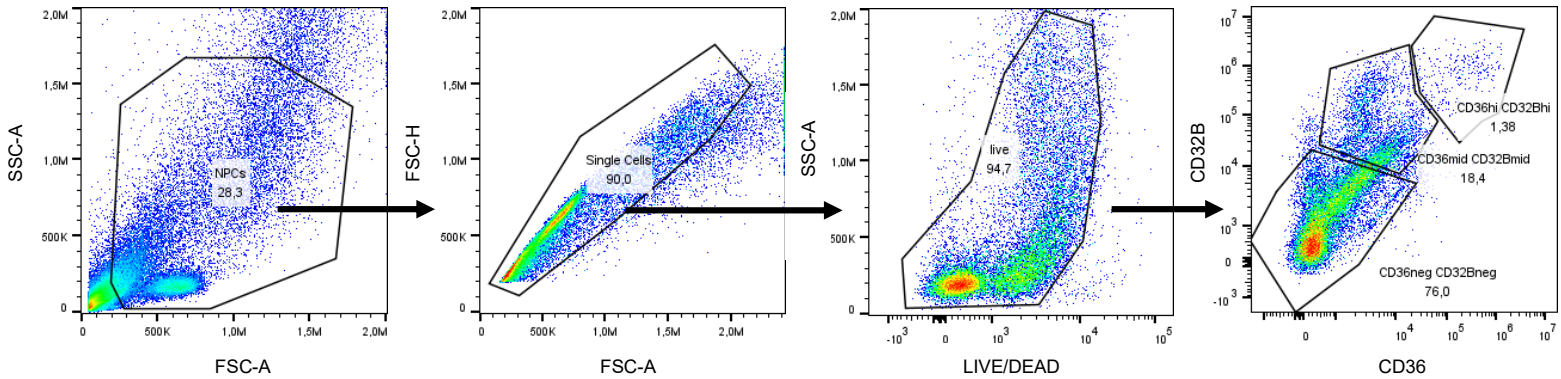

Gating strategy for Figures 2A, 2B, 2G, 2J, EV1D and EV2D-G (primary murine liver NPCs)

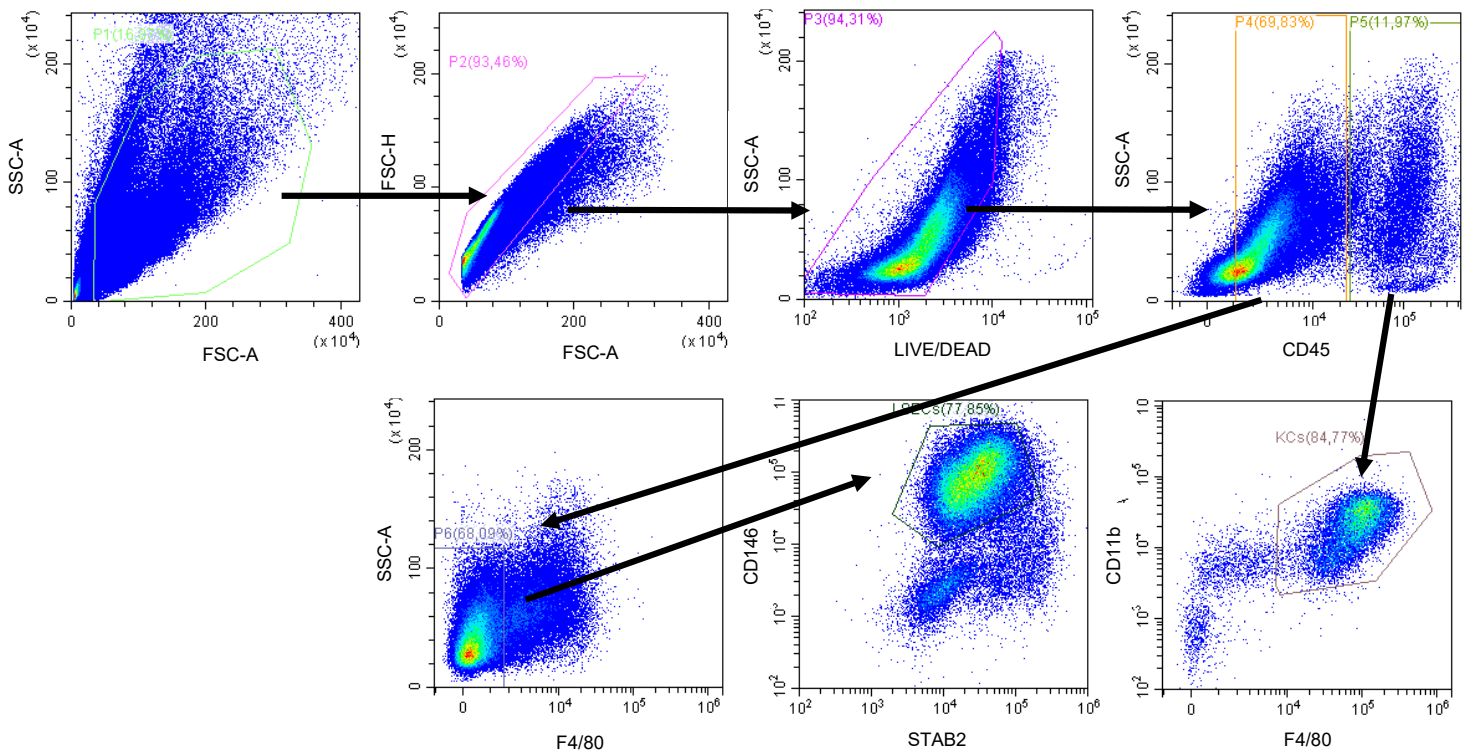

Gating strategy for Figure 2I

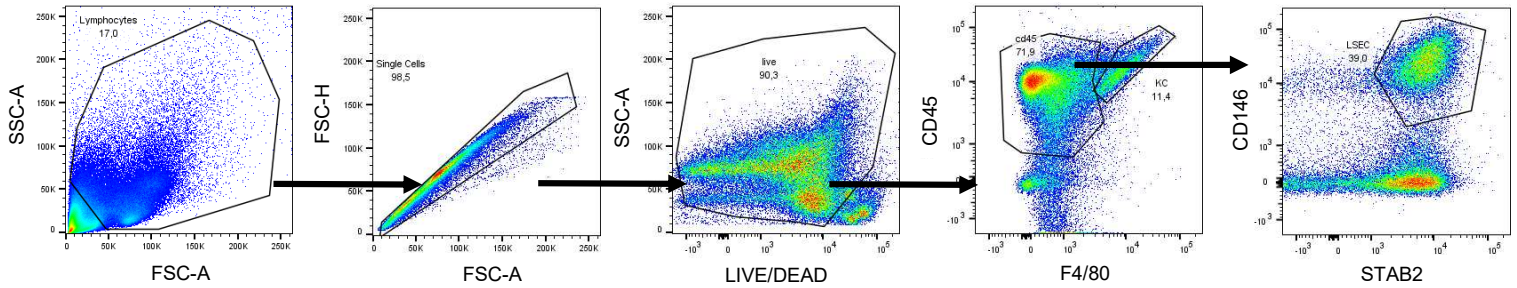

Gating strategy for Figures 3A-D

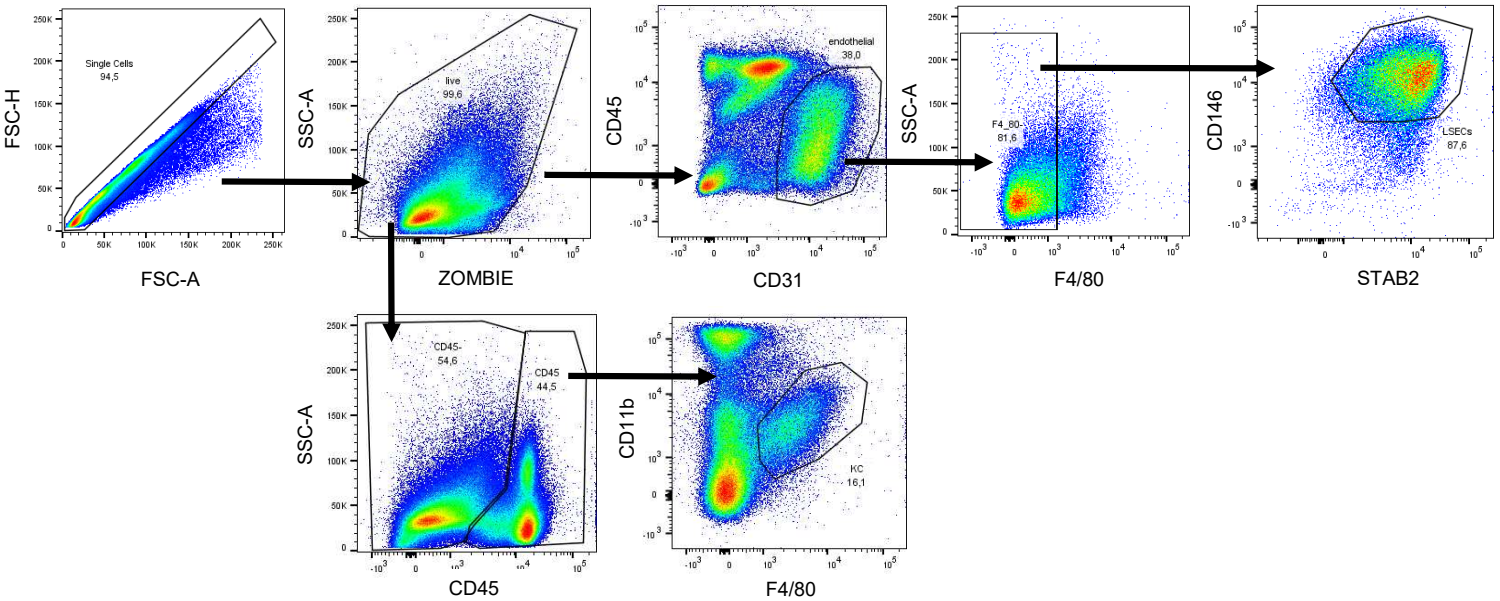

Gating strategy for Figures 3E-H

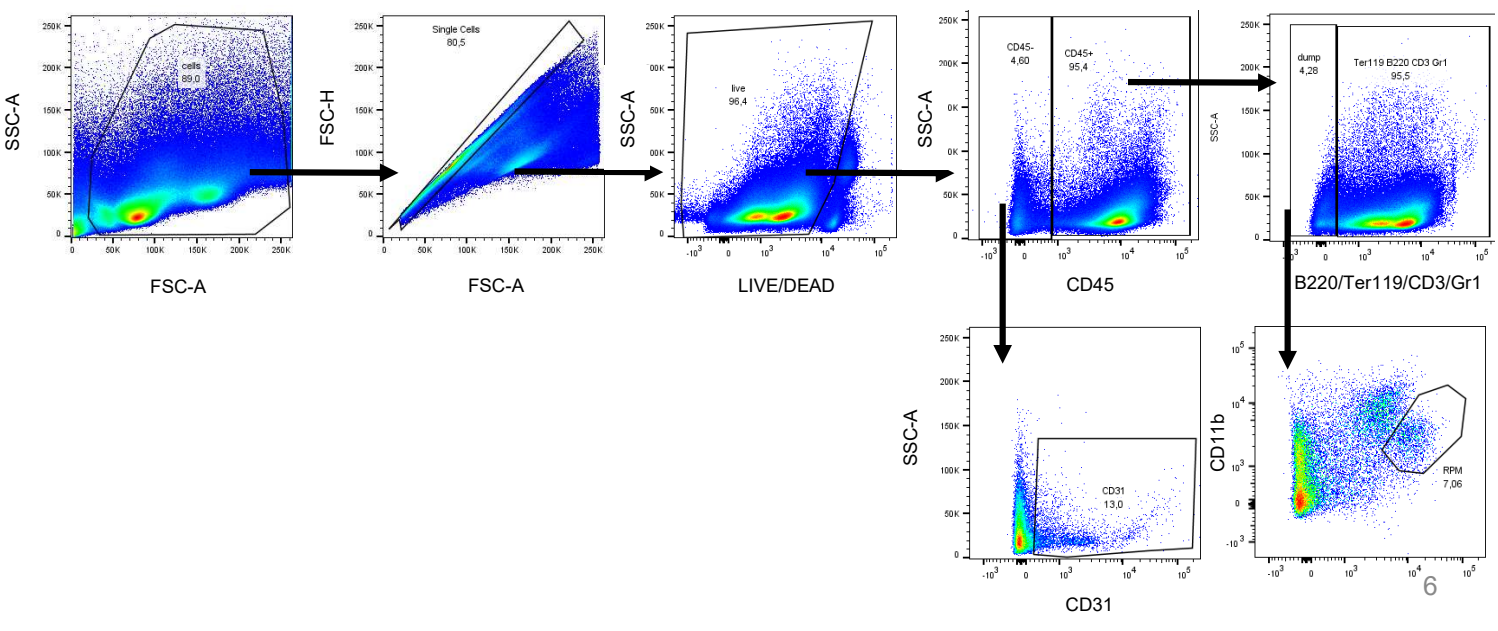

Gating strategy for Figures 4C and 4D

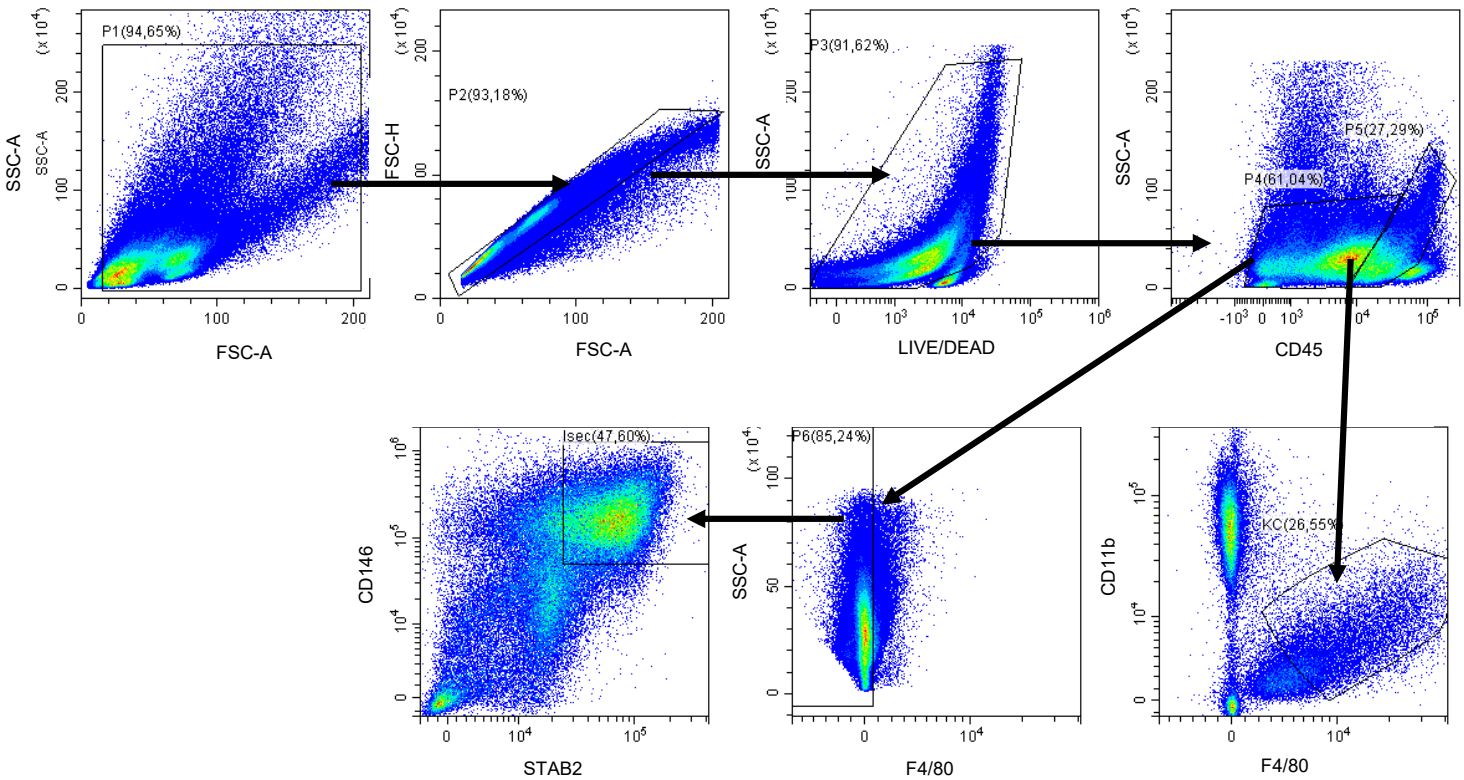

Gating strategy for Figures 4I and Figure 5N

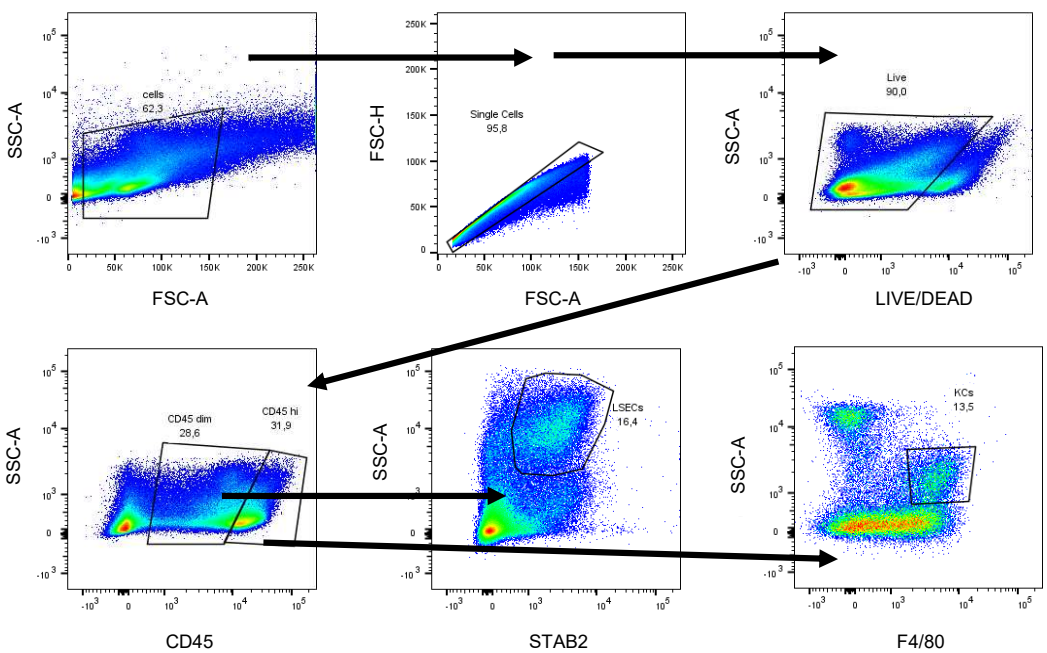

Gating strategy for Appendix Figure S1A (bone marrow)

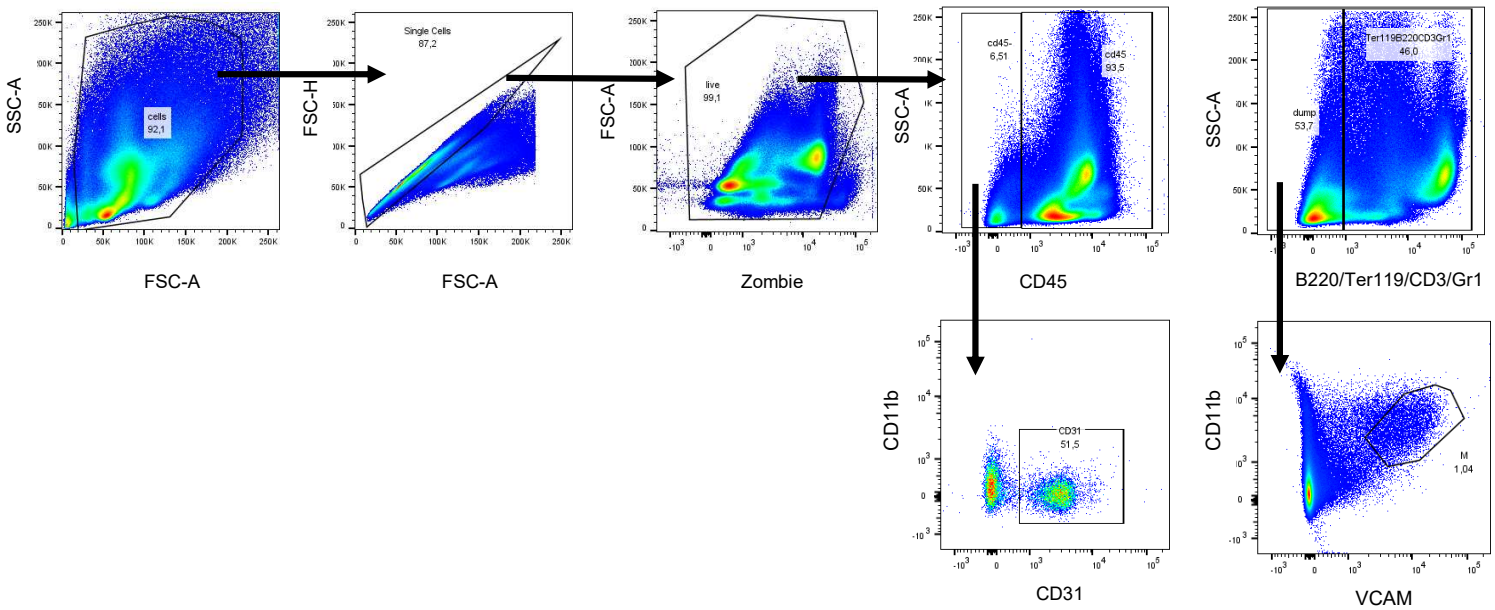

Gating strategy for Appendix Figure S1B (aorta)

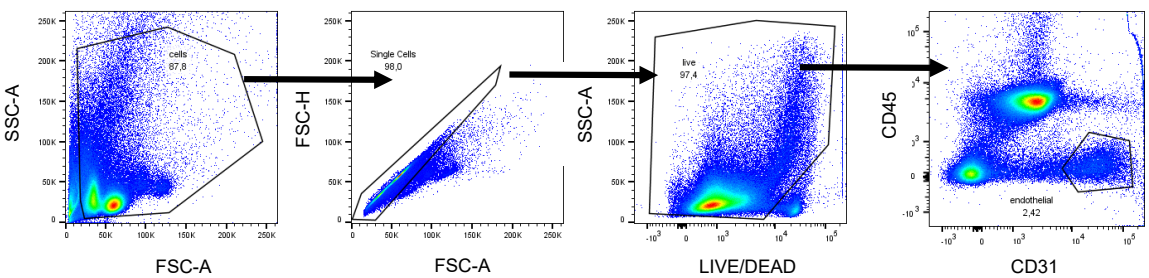

Gating strategy for Figure 4E, 4F and 5F – sorting LSECs and KCs

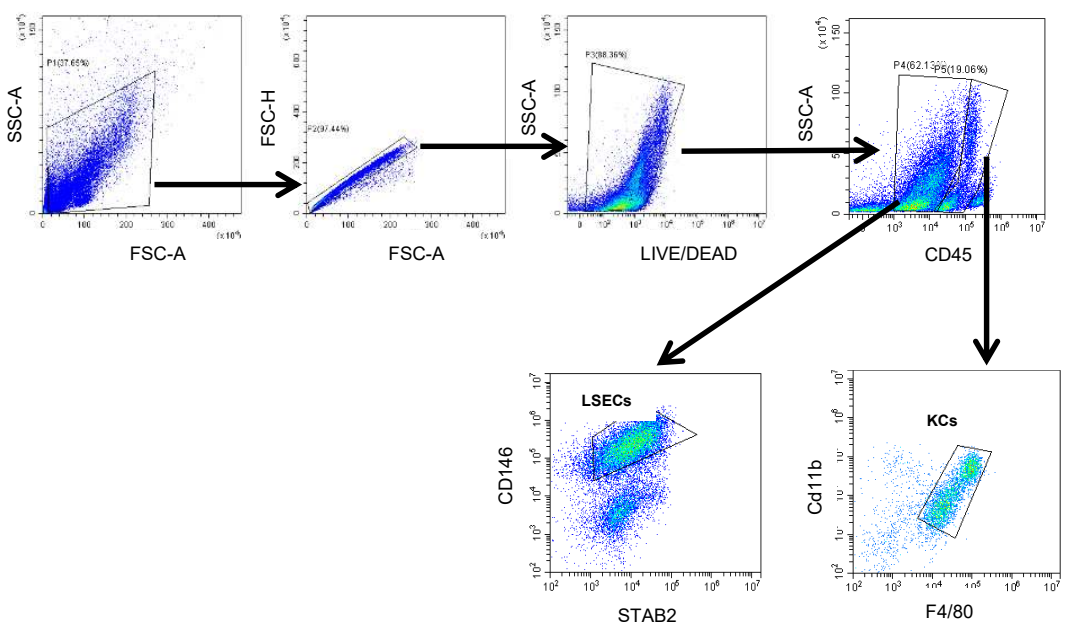

Gating strategy for Figures 4E and 4F (sorting spleen endothelial cells)

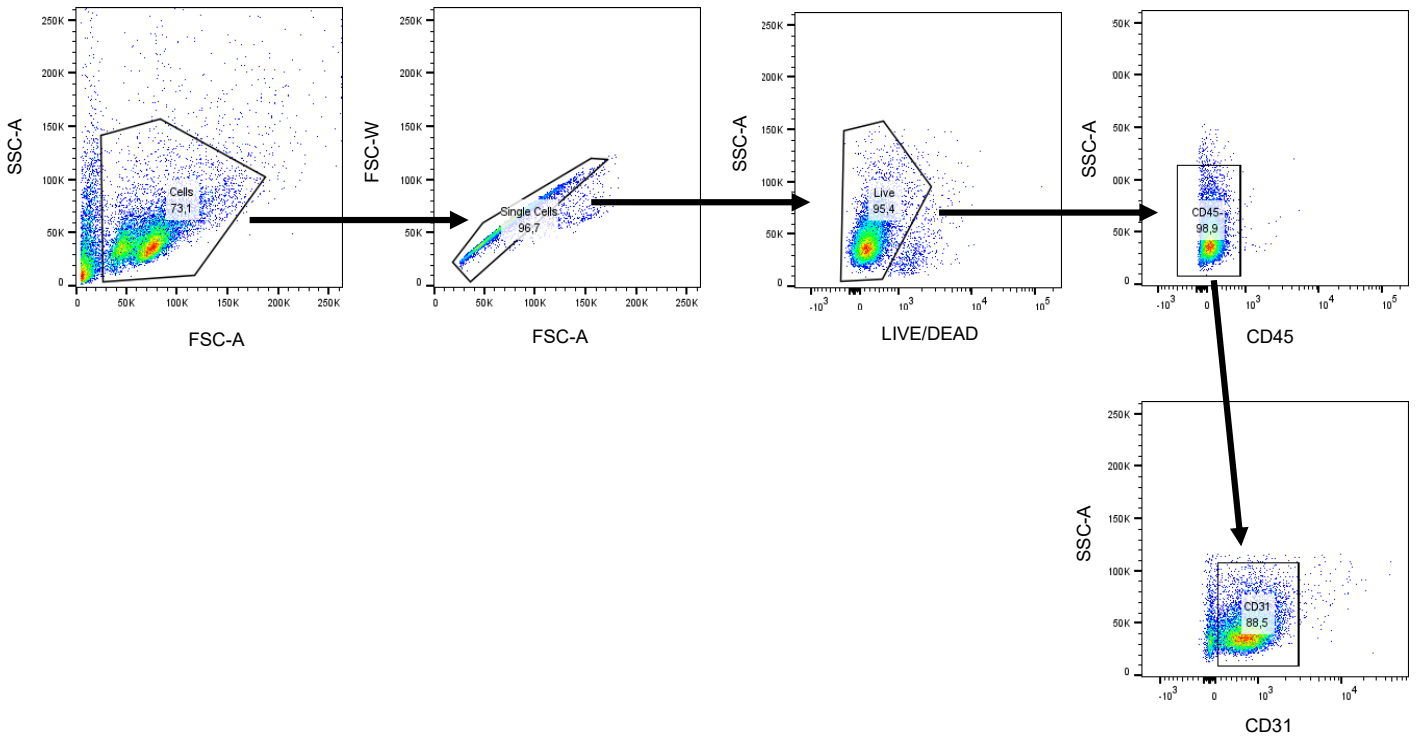

Gating strategy for Figures 4E and 4F (sorting heart endothelial cells)

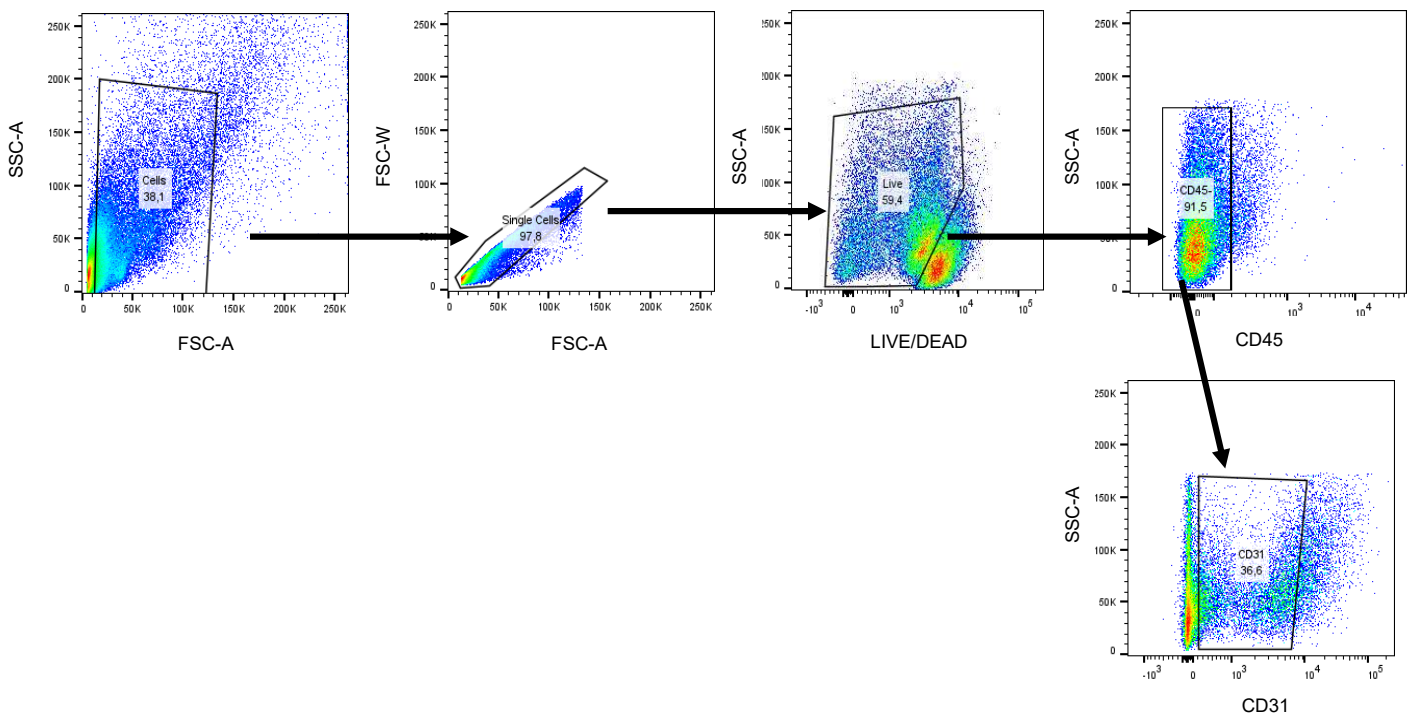

Gating strategy for Figure 4G (liver), 4J and 5L (Ferroorange)

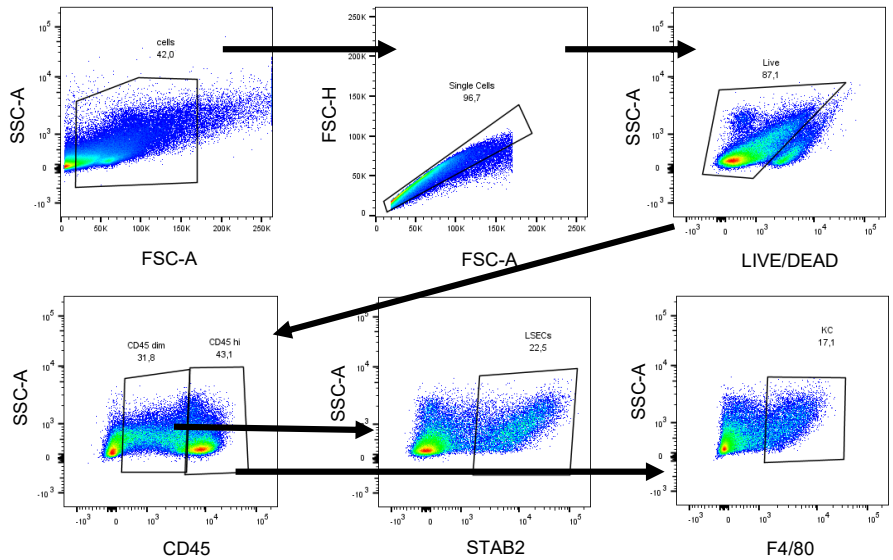

Gating strategy for Figure 4G (spleen)

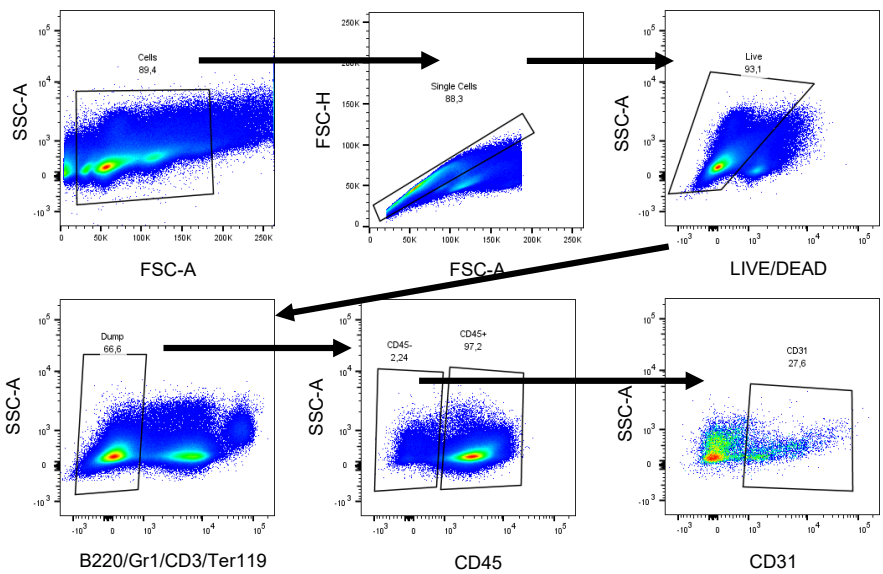

Gating strategy for Figure 4G (bone marrow)

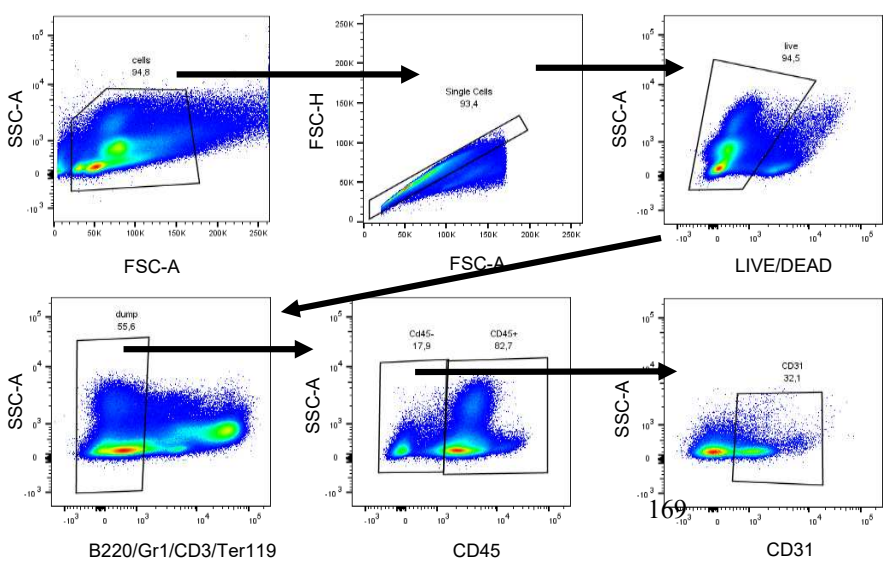

Gating strategy for Figure 5A (spleen control mouse)

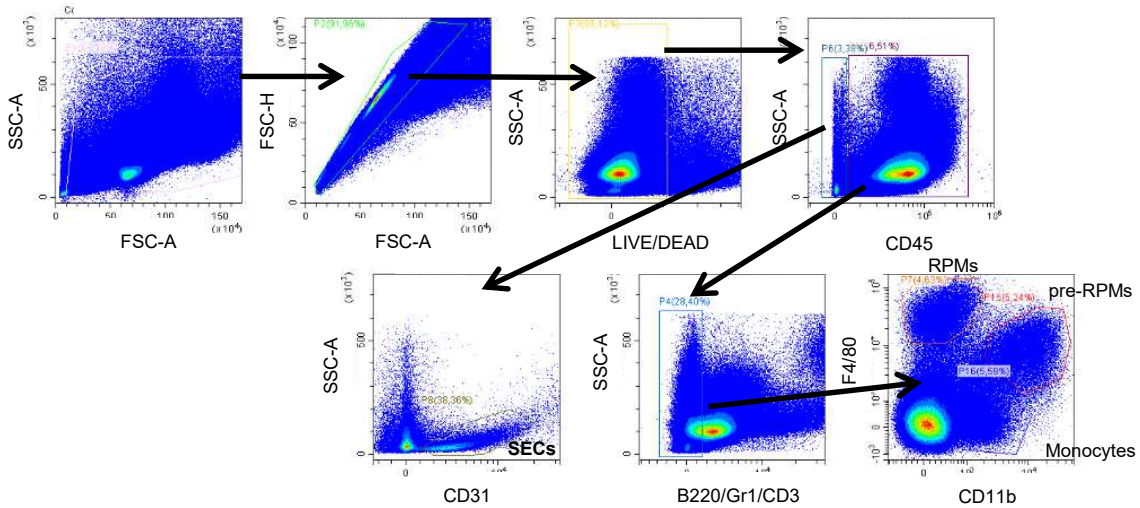

Gating strategy for Figure 5A (spleen + GFP RBCs)

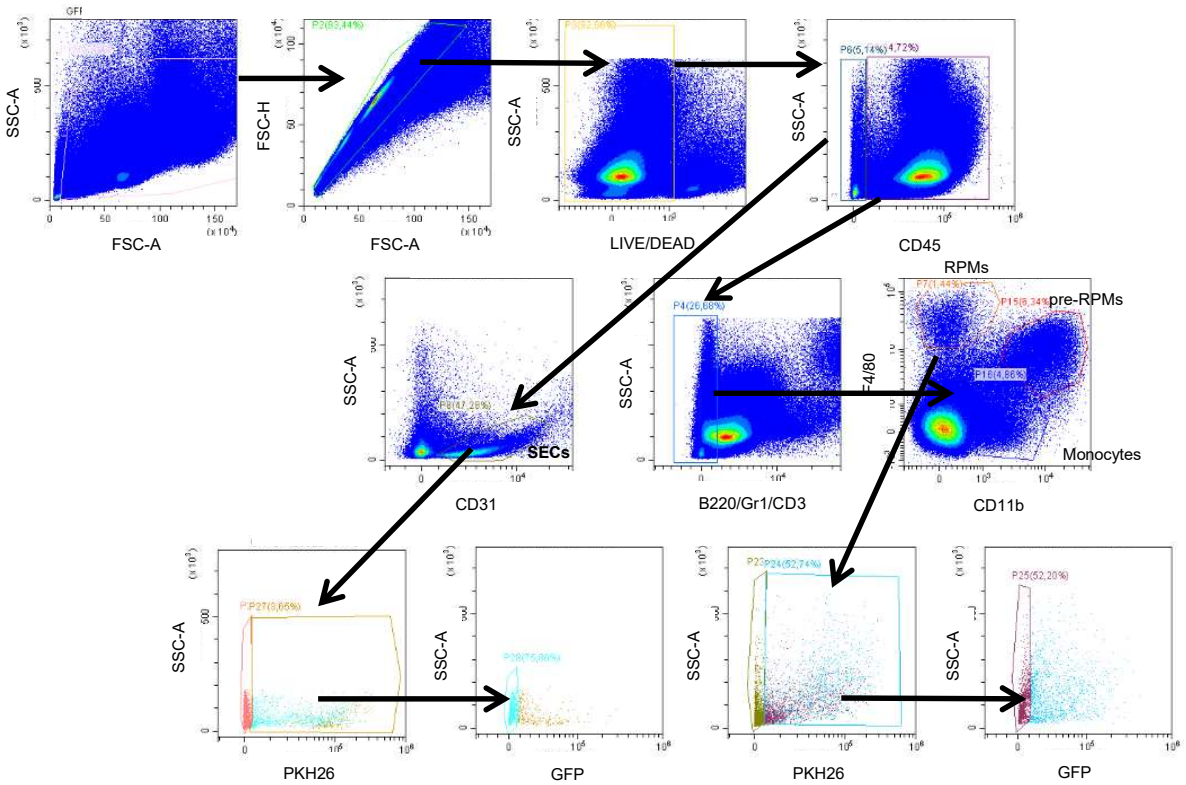

Gating strategy for Figure 5A (spleen dendritic cells)

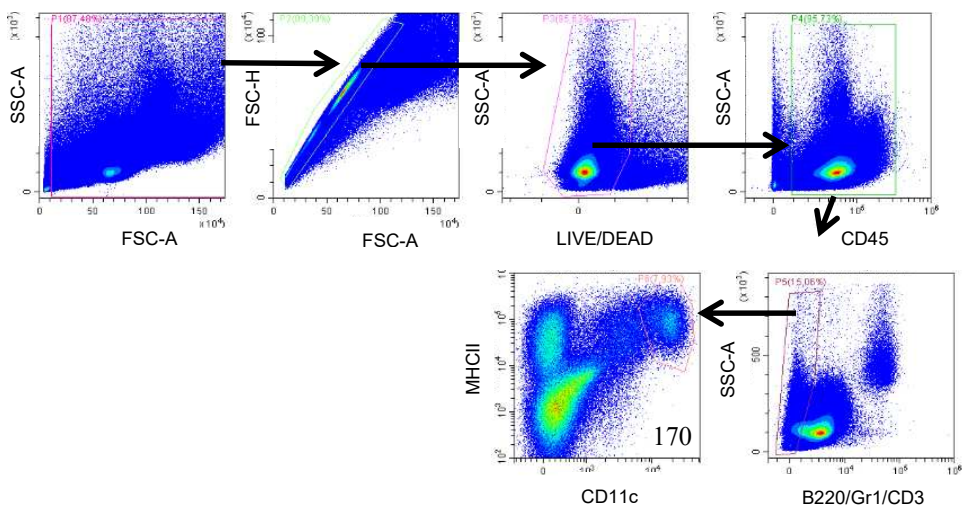

Gating strategy for Figure 5B (liver control mouse)

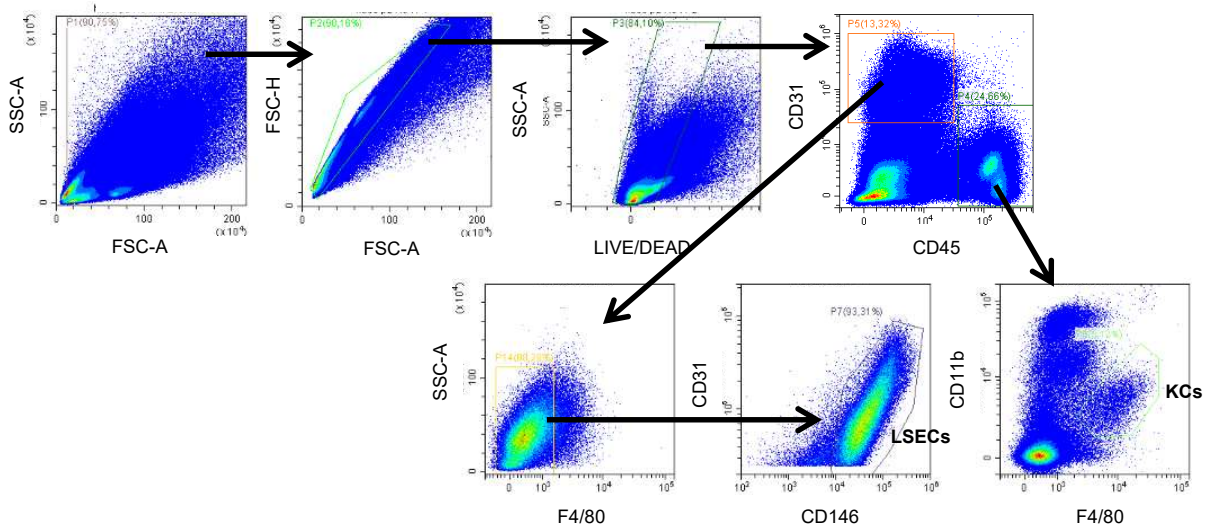

Gating strategy for Figure 5B (liver + GFP RBCs)

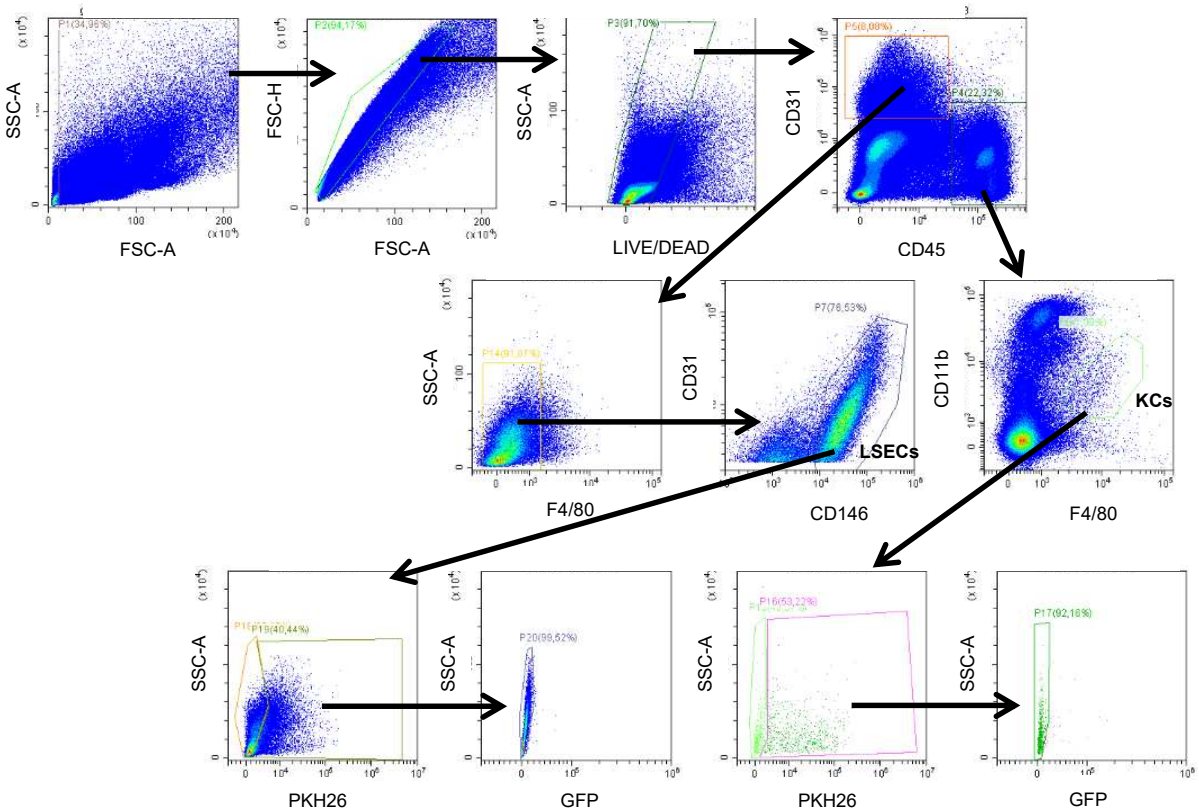

Gating strategy for Figure 5B (liver dendritic cells)

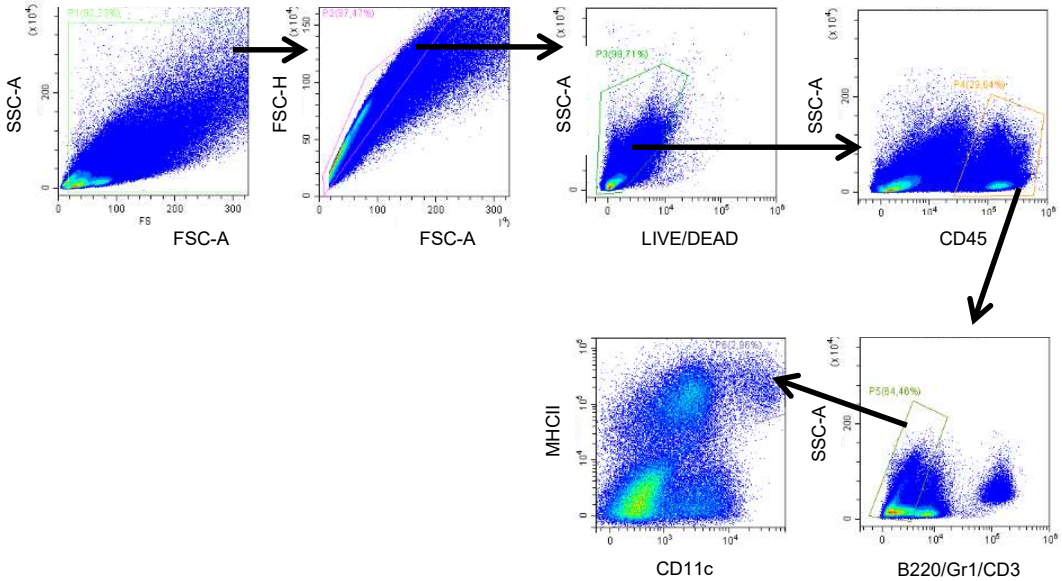

Gating strategy for Figure 5G

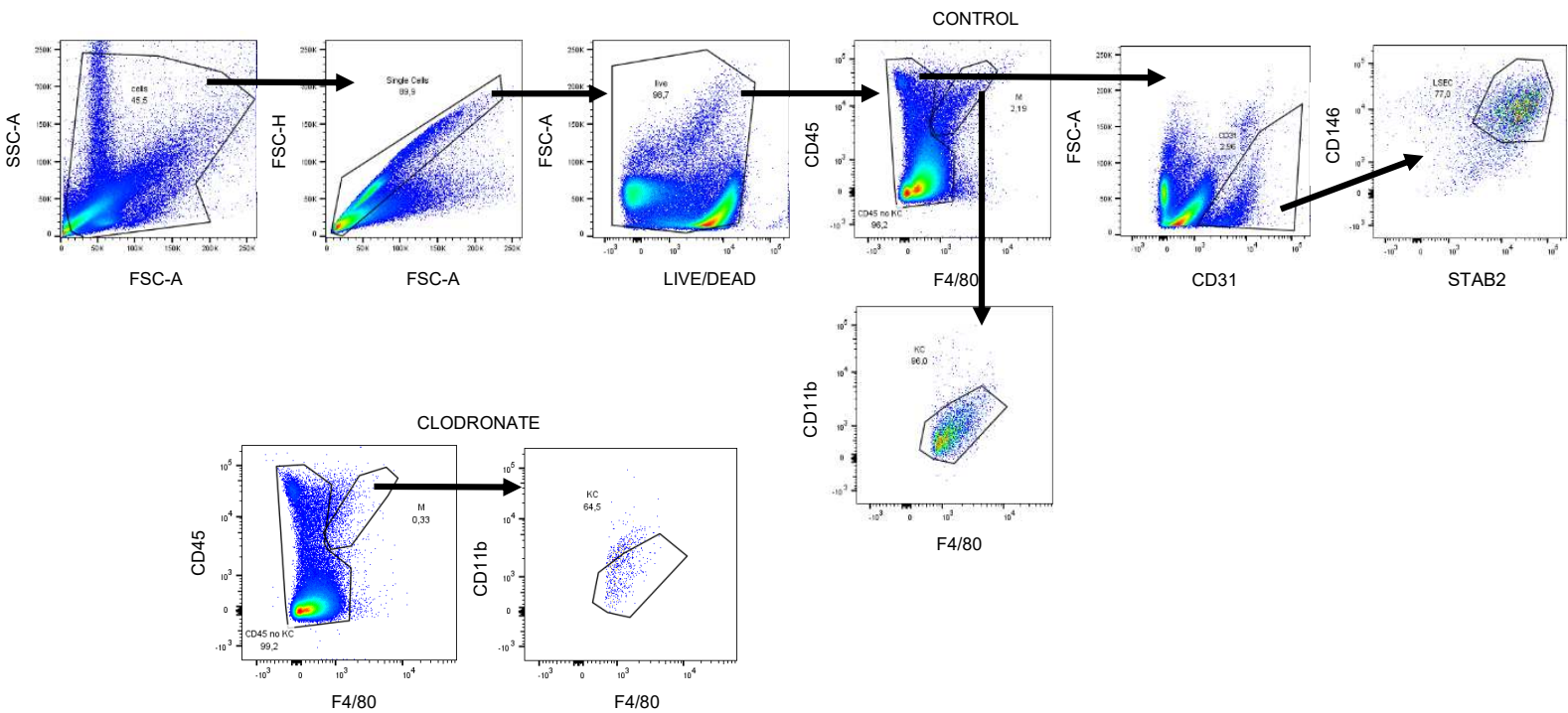

Gating strategy for Figures 5J and EV4B, E and F

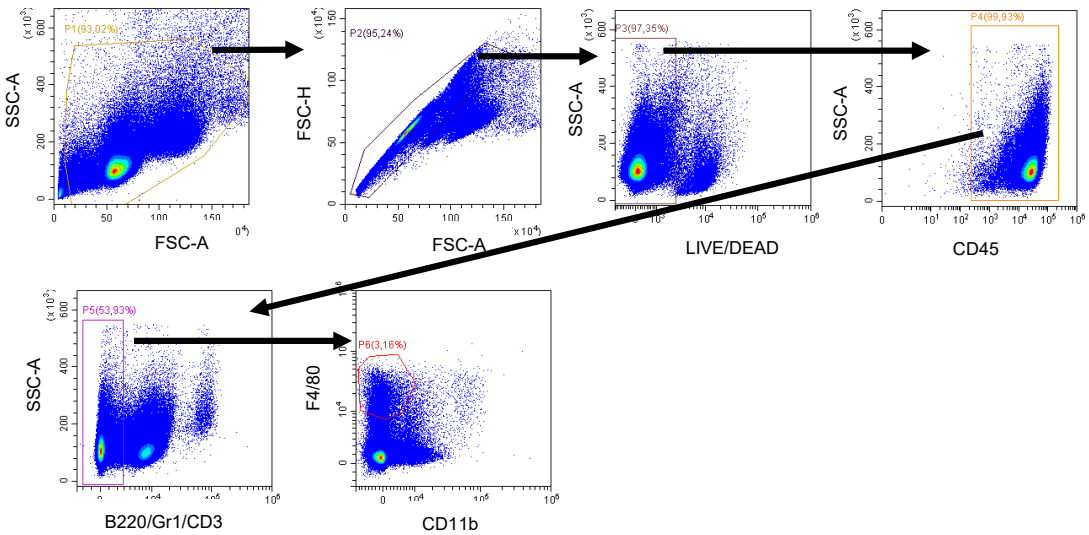

Gating strategy for Figures 5M, 6D, 6G, 7B, 7E, EV4E-F (liver cell flow analysis and FACS sorting for gene expression)